

Wave propagation in periodic buckled beams

THÈSE N° 6845 (2015)

PRÉSENTÉE LE 4 DÉCEMBRE 2015

À LA FACULTÉ DES SCIENCES ET TECHNIQUES DE L'INGÉNIEUR
LABORATOIRE DE MODÉLISATION MÉCANIQUE MULTI-ÉCHELLE
PROGRAMME DOCTORAL EN MÉCANIQUE

ÉCOLE POLYTECHNIQUE FÉDÉRALE DE LAUSANNE

POUR L'OBTENTION DU GRADE DE DOCTEUR ÈS SCIENCES

PAR

Florian Paul Robert MAURIN

acceptée sur proposition du jury:

Prof. F. Gallaire, président du jury
Prof. W. Curtin, directeur de thèse
Prof. G. van der Heijden, rapporteur
Dr G. Theocharis, rapporteur
Dr H. LISSEK, rapporteur



ÉCOLE POLYTECHNIQUE
FÉDÉRALE DE LAUSANNE

Suisse
2015

Pour

Amaia

Acknowledgements

This thesis, the greatest achievement of my professional life, would have been nothing without two persons that I would like in particular to thank. Alex, you have guided me in the maze of research from which I learned considerably, and I am sure this will benefit me considerably. I would also like to thank you for the confidence you had in me, by letting me teaching parts of your classes and participate to numerous conferences. The second person I would like to thank is Prof. Curtin who has provided me a considerable support and I really appreciated the time you have spent for improving things and making them moving on. I will never thank you enough for what you have done for me.

I am grateful to Gert van der Heijden, Georgios Theocharis and Hervé Lissek for your valuable time reading this manuscript and attending to the defense, and to François Gallaire presiding over the jury. Your comments are really constructive and definitely improve the quality of the present manuscript.

La partie expérimentale de cette thèse ne serait rien sans la participation de l'atelier qui a développé et créé un banc d'essais d'une qualité helvétique. Je remercie particulièrement Marc Jeanneret pour tes nombreux et astucieux conseils, ta disponibilité et ta bonne humeur. I also warmly acknowledge Luca Dedè for our fruitful collaboration. Your support and faith in this project was helpful to me, and your expertise on IGA was essential.

Le bon déroulement de cette thèse ne serait rien également sans un bon soutien administratif et je remercie à ce titre chaleureusement Dominique, Rosana et Géraldine.

I also thank my working colleagues Vladimir, Edgar and Bart with whom it was a pleasure to work. A special mention to Vladimir : we have done more than sharing an office for almost four years !

Je remercie également Sébastien Kohler et Joël Cugnoni du LMAF, ainsi que Kossi Agbeviade pour les prêts de matériels, vos conseils et le temps que vous m'avez accordé dans la partie expérimentale de cette thèse. I also would like to thank all the LAMMM members for your warmful welcome : Michael, Varun, Satish, Céline, Zhaoxuan, Predrag, Max, Mostafa, Wolfram, Ali, Aitor and Benjamin.

Je dois également un grand merci à toutes les personnes qui m'ont permis de passer du bon temps à l'EPFL, notamment lors de repas animés : Vlado, Laura, Mathias, Edouard, Giacomo, Gioele, Nicolas, Francesco, Andrea, Albert, Marc-Antoine, Cristobal, Pierre-Thomas, Tobias x2, Simon et Florian. Merci également à Quentin. Pour ma part, c'est souvent en allant courir que je résous des problèmes sur lesquels je planche depuis un bon moment, et à ce titre, je remercie particulièrement Sébastien qui m'a souvent accompagné lors de ces escapades. Mais

Acknowledgements

Séb, plus qu'un coureur, tu es le partenaire idéal pour des « plans foireux » mais aussi un coloc qui a su me supporter et ce, dès les premières heures du réveil! Finalement un grand merci à toutes les personnes avec qui j'ai partagé de bons moments dans Lausanne et ses montagnes environnantes.

Merci enfin à toute ma famille et à Laurianne pour ton soutien indéfectible, tendre et sincère.

Lausanne, 29 October 2015

F Maurin

Abstract

Folding of the earth's crust, wrinkling of the skin, rippling of fruits, vegetables and leaves are all examples of natural structures that can have periodic buckling. Periodic buckling is also present in engineering structures such as compressed lattices, cylinders, thin films, stretchable electronics, tissues, etc., and the question is to understand how wave propagation is affected by such media.

These structures possess geometrical nonlinearities and intrinsic dispersive sources, two conditions which are necessary to the formation of stable, nonlinear waves called solitary waves. These waves are particular since dispersive effects are balanced by nonlinear ones, such that the wave characteristics remain constant during the propagation, without any decay or modification in the shape. It is the goal of this thesis to demonstrate that solitary waves can propagate in periodic buckled structures.

This manuscript focuses specifically on periodically buckled beams that require either guided or pinned supports for stability purposes. Buckling is initially considered statically and investigations are made on stability, role played by imperfections, shape of the deflection, etc. Linear dispersion is analyzed employing the semi-analytical dispersion equation, a new method that relates the frequency explicitly to the propagation constant of the acoustic branch. This allows the quantification of the different dispersive sources and it is found that in addition to periodicity, transverse inertial and coupling effects are playing a dominant role. Modeling the system by a mass-spring chain that accounts for additional dispersive sources, homogenization and asymptotic procedures lead to the double-dispersion Boussinesq equation. Varying the pre-compression level and the support type, the main result of this thesis is to show that four different waves are possible, namely compressive supersonic, rarefaction (tension) supersonic, compressive subsonic and rarefaction subsonic solitary waves. For high-amplitude waves, models based on strongly-nonlinear PDEs as the one modeling wave propagation in granular media (Hertz power law) are more appropriate and adaptation of existing work is done. Analytical model results are then compared to finite-element simulations of the structure and experiments, and are found in excellent agreement.

In this thesis, in addition to the semi-analytical dispersion equation, two other new methods are proposed. For periodic structures by translation with additional glide symmetries (e.g. buckled beams), Bloch theorem is revisited and allows the use of a smaller unit cell. Advantages are dispersion curves easier to interpret and computational cost reduced. Finally, the last contribution of this thesis is the use of NURBS-based isogeometric analysis (IGA) to solve the extensible-elastica problem requiring at least \mathcal{C}^1 -continuous basis functions, which was not

Acknowledgements

possible before with classical finite-element methods. The formulation is found efficient to solve dynamic problems involving slender beams as buckling.

Keywords: Nonlinear periodic buckled beam, Rarefaction/compressive and supersonic/subsonic solitary wave, Experiment, Bloch theorem with glide symmetry, Isogeometric analysis of extensible-elastica

Résumé

Le plissage de la croûte terrestre, les rides de la peau, la forme ondulée des fruits, légumes ou feuilles sont des exemples de structures naturelles qui possèdent un flambage périodique. Le flambage périodique est également présent dans les structures manufacturées comme les treillis comprimés, les cylindres comprimés, les couches minces refroidies, l'électronique extensible, les tissus étirés, etc., et la question est de savoir comment la propagation d'ondes est affectée par de tels milieux.

Les structures flambées périodiquement possèdent des non-linéarités géométriques et des sources de dispersion intrinsèques, deux conditions nécessaires à la formation d'ondes non-linéaires et stables dites ondes solitaires. Ces ondes sont particulières dans la mesure où les effets dispersifs sont compensés par ceux non-linéaires, de telle sorte que la forme d'onde reste inchangée durant la propagation. L'objectif est ici de démontrer que les ondes solitaires peuvent se propager dans des structures flambées périodiquement.

Cette thèse se concentre spécifiquement sur les poutres périodiquement flambées qui exigent d'être supportées, à des fins de stabilité. Le flambage est initialement considéré en statique et l'analyse se concentre sur la stabilité, le rôle joué par les imperfections, et la forme de la déflexion. La dispersion linéaire est ensuite analysée en utilisant l'équation de la dispersion semi-analytique, un nouveau procédé qui associe de manière explicite la fréquence à la constante de propagation dans la branche acoustique, permettant la quantification des différentes sources dispersives. Il en résulte qu'en supplément de la dispersion induite par la périodicité, les effets inertiels transversaux et ceux de couplages jouent un rôle prépondérant. En modélisant la structure par un système masse-ressort prenant en compte les sources dispersives additionnelles, l'homogénéisation et l'utilisation d'une procédure asymptotique conduisent à l'équation doublement dispersive de Boussinesq. En faisant varier le niveau de flambage et le type de support, le résultat principal de cette thèse est de montrer que quatre ondes solitaires différentes sont possibles, à savoir l'onde en compression/tension et subsonique/supersonique. Les modèles analytiques sont ensuite comparés à des simulations par éléments finis puis testés expérimentalement, et les résultats se trouvent être en excellent accord.

Dans ce mémoire, en plus de l'équation de la dispersion semi-analytique, deux nouveaux procédés sont proposés. Pour les structures périodiques par réflexion glissée, le théorème de Bloch est revisité, permettant l'utilisation d'une cellule plus petite. Enfin, la dernière contribution de cette thèse est l'utilisation de l'analyse isogéométrique (IGA) pour résoudre la formulation "extensible-elastica". Cette dernière nécessite l'utilisation de fonctions de

Acknowledgements

bases ayant pour continuité minimum \mathcal{C}^1 , propriété que ne possède pas les éléments finis classiques. La formulation se trouve être efficace et appropriée pour résoudre des problèmes de dynamiques impliquant des poutres minces comme généralement rencontrés dans les problèmes de flambages.

Mots clefs : Poutre flambée périodique non-linéaire et dispersive, ondes solitaires en traction/compression et supersonique/subsonique, validation expérimentale, théorème de Bloch avec symétries par réflexion glissée, analyse isogéométrique d’“elastica” extensible

Contents

Acknowledgements	i
Abstract (English/Français)	iii
Contents	vii
1 Introduction	1
1.1 Periodic buckled structures	2
1.2 Solitary waves	6
1.3 Organization of the work	9
2 Periodic Buckled Beams: Kinematics And Stability	11
2.1 Introduction	11
2.2 Review of some two-dimensional beam formulations	11
2.3 Extensible-elastica: kinematics and constitutive law	12
2.4 Pinned-pinned column buckling	14
2.4.1 Critical load	15
2.4.2 Load-displacement relation	16
2.4.3 Analytical load-displacement equation assuming inextensibility	17
2.5 Stability and bifurcation	19
2.6 Effects of geometrical imperfections	20
2.7 Periodic buckled beam with supports	23
2.8 Conclusions	24
3 Dispersion Of Periodic Buckled Beams	25
3.1 Introduction	25
3.2 Typical sources of dispersion	26
3.2.1 Dispersion of continuous structures	26
3.2.2 Dispersion of discrete structures	27
3.3 Bloch theorem	31
3.3.1 Direct method	33
3.3.2 Inverse method	34
3.3.3 Reduced Bloch method	35
3.4 Semi-analytical dispersion relations	36

Contents

3.4.1	Semi-analytical relations including transverse-reflection symmetry . . .	37
3.4.2	Polynomial expression of the semi-analytical equation	39
3.4.3	Semi-analytical dispersion equation of buckled beams	40
3.5	Dispersion of buckled beams	41
3.5.1	Dispersion relation from Bloch theorem	43
3.5.2	Semi-analytical dispersion equation coefficients and pre-compression .	49
3.5.3	Wavemodes	50
3.6	From dispersion equation to linear wave equation	51
3.7	Conclusions	51
4	Nonlinear Wave Propagation In Buckled Beam: Models And Simulations	53
4.1	Introduction	53
4.2	Geometric, material and FE properties	54
4.3	Wave propagation described by the simple Boussinesq model	55
4.3.1	From the simple mass-spring chain to the Boussinesq equation	55
4.3.2	Comparison between the simple Boussinesq model and FE simulations	57
4.4	Solitary waves including mass and stiffness coupling	58
4.4.1	The double-dispersion Boussinesq model	58
4.4.2	Strongly nonlinear models	63
4.5	Results and discussion	69
4.5.1	Comparison of the Boussinesq model to FE simulations	69
4.5.2	Comparison of the strongly nonlinear models to FE simulations	74
4.6	Conclusions	76
5	Nonlinear Wave Propagation In Buckled Beam: Experiments	79
5.1	Introduction	79
5.2	Experimental setup and signal acquisition	80
5.2.1	Experimental setup	80
5.2.2	Signal acquisition in <i>LabView</i>	80
5.2.3	Synchronization of <i>NI</i> cards from different series via <i>LabView</i>	82
5.2.4	<i>Sylvac</i> sensor and RS-232 communications in <i>LabView</i>	84
5.3	Experimental results	86
5.3.1	Static buckling pattern	86
5.3.2	Static load-displacement relation	88
5.3.3	Wave input	88
5.3.4	Stationary wave profile	90
5.3.5	Phase speed	91
5.3.6	Period and wavelength	92
5.3.7	Effects of heterogeneities	94
5.4	Conclusions	95

6	Isogeometric Analysis Of Extensible-Elastica	97
6.1	Abstract	97
6.2	Introduction	97
6.3	Rotation-free extensible-elastica formulation	101
6.3.1	Strain measurement and constitutive law	101
6.3.2	The weak formulation	102
6.3.3	Isogeometric formulation	104
6.4	Set of static problems and exact/closed-form solutions	106
6.4.1	Test A: straight beam under pure-axial load with non-constant Young modulus	106
6.4.2	Tests B: straight and curved beams with pure-bending	107
6.4.3	Test C: cantilever straight beam under transverse tip load	107
6.4.4	Test D: buckling of a pinned-roller beam	109
6.4.5	Test E: clamped arc under a transversal tip load	109
6.5	A-priori error estimation: convergence order	110
6.5.1	Error norms	110
6.5.2	A-priori error estimation	111
6.6	Static numerical results and discussion	111
6.6.1	Convergence orders	112
6.6.2	Membrane locking	114
6.7	Dynamic problems	116
6.7.1	Solitons propagating in post buckled beams	116
6.7.2	Dynamic snap-through buckling	119
6.8	Comparison to co-rotational beam formulation	121
6.9	Conclusions	123
7	Conclusions	125
7.1	Summary of the results	125
7.2	Novel methods developed in the thesis	126
7.3	Limitations of the present research and recommendations for future work	127
7.3.1	High frequencies	127
7.3.2	Limitation in the wave amplitude: the case of snapping	128
7.3.3	Experiments	129
7.3.4	Dissipation and heterogeneity effects	129
7.3.5	Application to more complex periodic structures	129
A	Load-Displacement Series Derived From The Extensible-Elastica	131
	Bibliography	133
	Curriculum Vitae	145

1 Introduction

Periodic buckled structures (e.g. in Fig. 1.1) possess geometrical nonlinearities and intrinsic dispersive sources, both conditions necessary to host stationary, nonlinear waves called solitary waves.

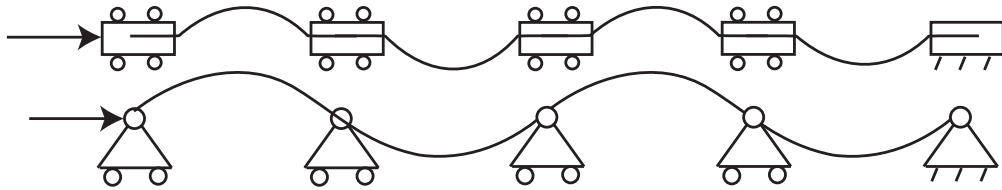


Figure 1.1: Periodic buckled beam structures investigated in this thesis.

Tsunamis are water waves created after displacement of underwater terrains, and are infamous for being associated with large disasters. What makes them dangerous is that they are solitary waves, waves that keep their amplitudes while propagating instead of being spread by dispersion. Consider now plate tectonics where subduction creates highly compressed zones on which the earth's crust can buckle (fold). If this buckling is also periodic (see Fig. 1.2a), the conditions are met for earthquake waves to act also as dangerous solitary waves but wave propagation into periodic buckled structures has not been investigated yet. Another question arising from wave propagation in periodic media is how wrinkled airway, esophagus, skin, etc. (see Fig. 1.2c-f) does affect ultrasonic waves used in medical imaging? Periodic buckling is not restricted to natural phenomena (Fig. 1.2) and is found in engineering structures too (Fig. 1.3). For engineers, the capability of a structure to host solitary waves can be undesired (e.g. in noise absorbers) or used as a tool to cancel dispersion or nonlinearity effects (e.g. optical fibers).

It is the goal the present thesis to investigate wave propagation and especially solitary waves in periodic buckled beams (Fig. 1.1), work that can be then used as a starting point to study more complex periodic buckled structures (Figs. 1.2 and 1.3). The remainder of this chapter is devoted to the state of the art of periodic buckled structures, followed by an introduction on

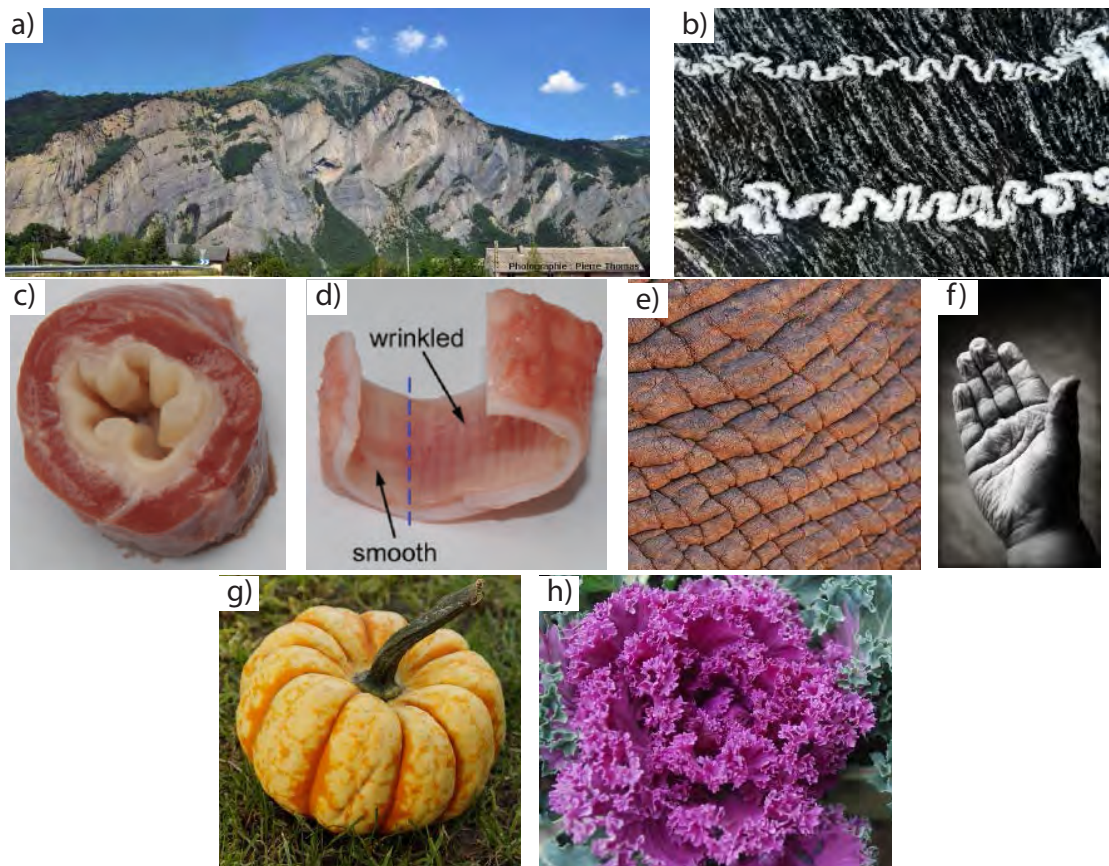


Figure 1.2: Natural periodic buckled structures: view of the mountain from La Paute (France) (a) and layers of quartz inside metamorphic rocks from the Jotun Nappe (Norway) (b). Both structures fold repeatedly due to compressive stresses. Bovine esophagus (c), porcine airway (d), elephant skin (e), and human skin (f) with wrinkles induced by the growth or the slimming of some tissues bound to some other inelastic ones. Pumpkin (g) and cabbage (h) where buckling stresses induce preferential growing directions. Photos kindly supplied by Pierre Thomas (a) and Haakon Fossen (b), reprinted from [Li et al., 2011a] with permission (c-d), and under CC0 license (e-h).

solitary waves and concluded by an overview of the work present in this manuscript.

1.1 Periodic buckled structures

From a mechanical point of view, buckling is a static instability caused by a bifurcation between a compressive to a laterally deformed state [Bazant et al., 1993]. Buckling occurs in slender structures where bending deformations are dominant, and result in large nonlinear geometrical deformations. Buckling is often awkwardly associated to failure due to the important stresses on thick post-buckled structures, but to have failure, material plasticity has to be considered as well. In this thesis, only geometrical (physical) nonlinearities are considered within the linear elastic limit of the material.

1.1. Periodic buckled structures

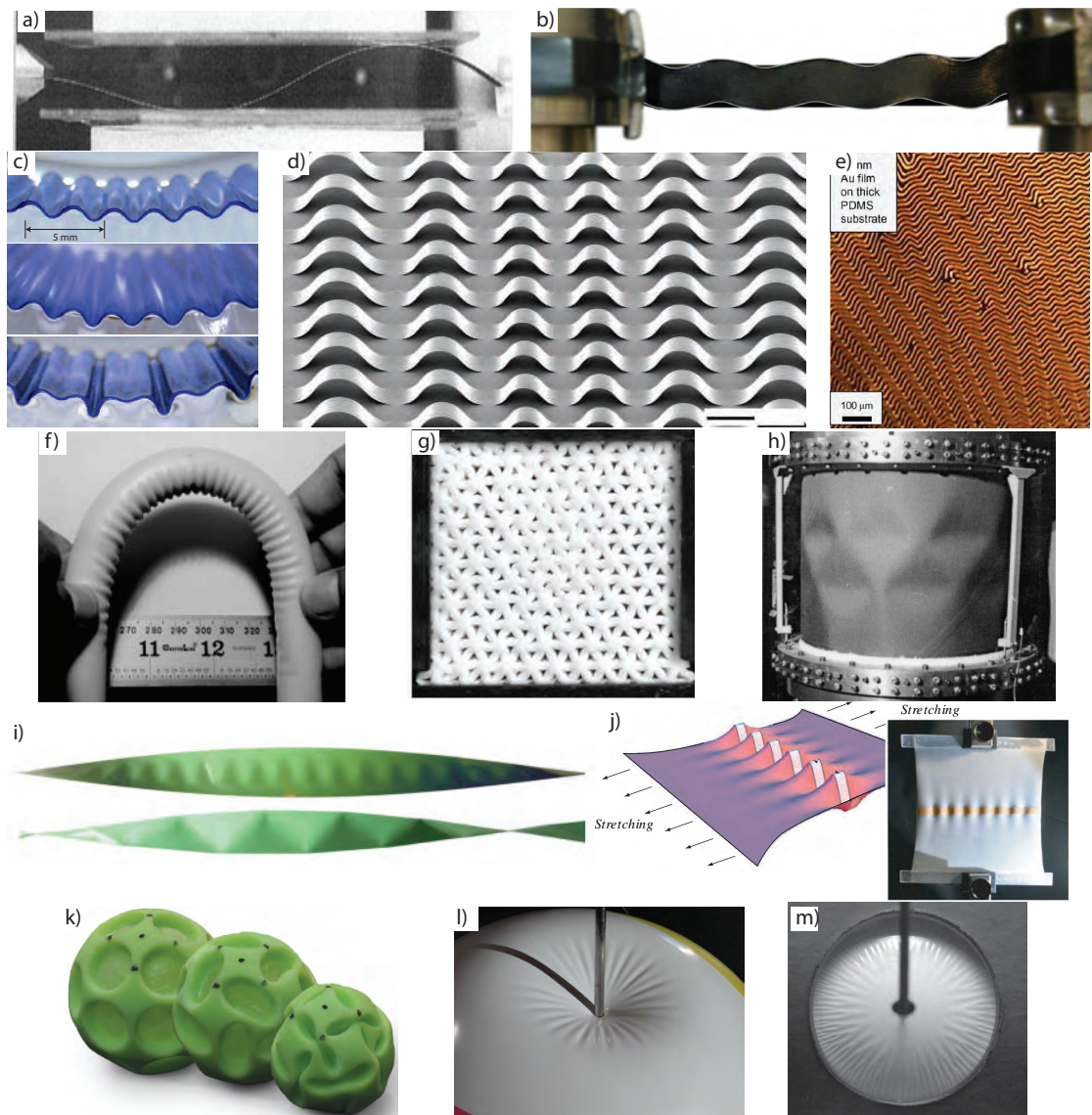


Figure 1.3: Engineered periodic buckled structures: beam compressed and constrained between two walls [Domokos et al., 1997] (a), rubber slab bound to a thin metal plate and bent [Lignon et al., 2013] (b), stiff PDMS film bound to a thick soft PDMS foundation and compressed [Brau et al., 2010] (c), electrical strips periodically clamped to a prestressed PDMS which is then released [Sun et al., 2006] (d), gold film welded to a PDMS substrate which is then cooled down [Chen and Hutchinson, 2004] (e), bent pipe [Mahadevan et al., 2004] (f), compressed triangular cellular [Kang et al., 2014] (g), compressed cylinder [Bisagni, 2000] (h), stretched and twisted strips [Chopin and Kudrolli, 2013] (i), stretched fabric [Takei et al., 2011] (j), underpressured spherical structure [Krieger, 2012] (k), local pressure applied on an inflated membrane [Vella et al., 2011] (l), and elastic plate stamped into a spherical mold [Hure et al., 2012] (m). All figures are reprinted with permission from respective references.

The classical example of buckling is the column that is compressed axially until a critical

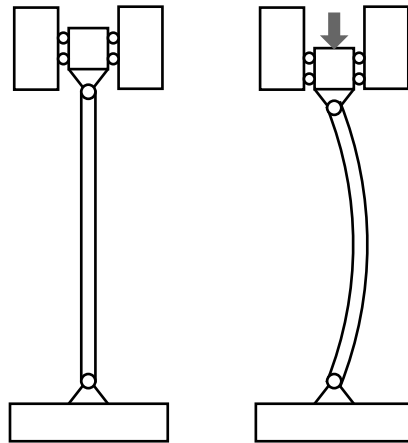


Figure 1.4: Pinned-pinned column buckling.

load where deformations become transversal (bending deformations), as shown in Fig. 1.4. Column buckling was historically the first stability problem to be solved in 1953 [Timoshenko, 1983], but only small deflections were considered. To describe large nonlinear deformations, elastica curves are required. Elastica curves were first studied by James Bernoulli in 1691, but the complete mathematical treatment is attributed to Euler in 1744 [Euler, 1744] who introduced the different families of elastica which are shown in Fig. 1.5 (see [Levien, 2008] for a complete mathematical history of the elastica). What is particularly interesting from these mathematical solutions is that they are all periodic. However, once elastica curves are considered as physical beams with non-null cross-sections, overlapping in two dimensions is not possible, and only solutions belonging to Figs. 1.5f-h remain physically possible, but are not stable. It is the reason why in this thesis, guided or pinned supports are added, as shown in Fig. 1.1.

As an alternative to the use of pinned and guided supports (Fig. 1.1), stable periodic buckled beams can be obtained by compressing a beam between two walls [Domokos et al., 1997] (Fig. 1.3a). The walls constrain large transverse displacements and force higher order buckling modes. However, high-pressure contacts between the walls and the strip induce important frictions that drastically change the dynamic behavior. Note that in [Thompson et al., 2012], straight walls are replaced by cylinders, but it involves buckling in torsion.

Like walls, elastic foundations can be used for stability purposes. For example, when a thin stiff layer is bound to a soft large layer and is compressed, stable periodic buckling of the thin layer is obtained [Brau et al., 2010] (Fig. 1.3c). The same phenomenon happens in the opposite way when a stiff layer is bound to an initially stretched substrate which is then released [Sun et al., 2006, Vella et al., 2009]. Note that in Fig. 1.3d [Sun et al., 2006], the metal strips are only locally clamped to control the buckling pattern and the resulting structure is used as a stretchable electronic device. As an alternative to force/displacement control, periodic buckling can also result from cooling down a thin film clamped to a substrate of different thermal-expansion coefficient [Chen and Hutchinson, 2004, Genzer and Groenewold, 2006] (Fig. 1.3e).

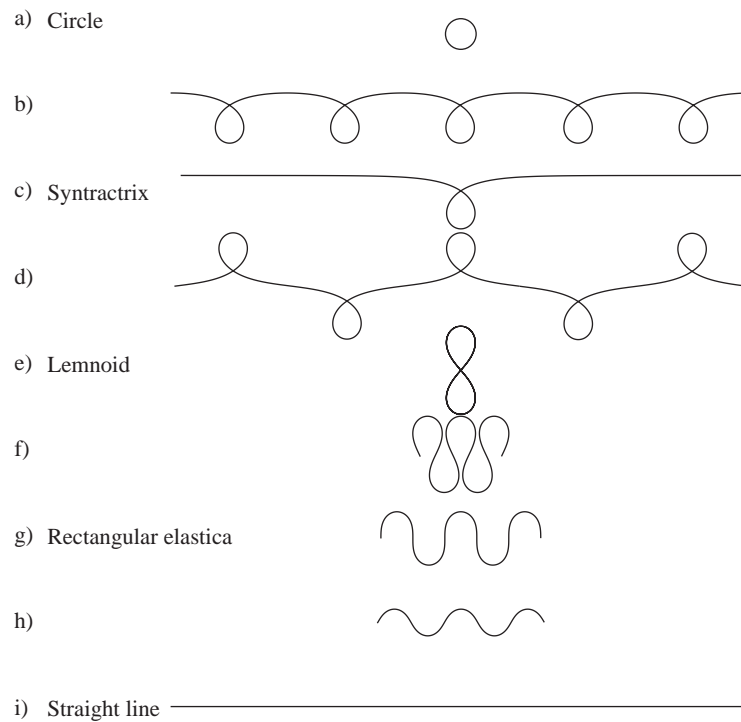


Figure 1.5: Elastica families.

The beam compressed between two walls and the beam clamped to an elastic substrate induce either dissipation (contact-friction or internal absorption of the material composing the elastic foundation) or secondary path for wave propagation. These differ from self-supported structures for which no link with the foundation exists except at extremities. For example when a rubber slab is bound to a thin metal plate, bending of the plate induces compression of the rubber that delaminates and buckles periodically [Lignon et al., 2013] (Fig. 1.3b). Bending induces buckling of the metal plate and is a global buckling mode, whereas buckling of the rubber is a local mode. Coexistence of local and global buckling modes also happen similarly in buckling of pipes [Mahadevan et al., 2004] (Fig. 1.3f) and more generally in structures which have macro-structures as sandwiches [Bazant et al., 1993, Le Grogneec and Sad Saoud, 2015, Sad Saoud and Le Grogneec, 2014]. An original beam system hosting also local/global buckling modes is composed of two pinned beams linked together by a slider, such that in compression, local high-order buckling mode can be obtained [Zaccaria et al., 2011].

In order to prevent the global buckling mode and only have local periodic buckling, one possibility is to increase the size in the transversal direction resulting to two-dimensional lattices [Kang et al., 2014, Haghpanah et al., 2014, Shan et al., 2014] (Fig. 1.3g). Alternatively, the use of a third dimension might help the structure to be self-supported with local buckling modes. This is the case of the compressed cylinders shown in Fig. 1.3h and investigated in [Bisagni, 2000, Vaziri, 2007, Seffen and Stott, 2014, Xiong et al., 2014].

Up to this point and except for the case of stresses induced by thermal drifts, buckling is obtained after the application of a compressive force at the structure extremities. However, buckling also occurs for structures under tension, and result in naturally stable systems. This is the case of the helical strip (helicoid) that buckles periodically at its centroid under torsion and tension. Indeed, stretching of the helicoid induces longitudinal compressive stresses responsible for the buckling pattern [Chopin and Kudrolli, 2013, Chopin et al., 2014, Korte et al., 2010] (Fig. 1.3i). Similarly, stretching of fabrics or plates generates buckling perpendicularly to the strip due to Poisson contraction [Audoly and Pomeau, 2010, Takei et al., 2011] (Fig. 1.3j). Another original way to get periodic buckling is by putting a conducting rod into a magnetic field [Valverde and van der Heijden, 2010, Guo et al., 2014] and find applications to electrodynamic space tethers.

In addition to structures where periodicity is by translation, cylindrical and spherical buckling patterns also exist and are found for example in underpressured spherical structures [Krieger, 2012, Shim et al., 2012, Li et al., 2011b] (Fig. 1.3k), inflated membranes on which is applied a local force [Vella et al., 2011] (Fig. 1.3l), elastic plates stamped into a spherical molds (Fig. 1.3m) [Hure et al., 2012], circular metal sheets under transversal loading [Davidovitch et al., 2011] or elastic sheet on a liquid drop [King et al., 2012, Grason and Davidovitch, 2013].

Among natural stable buckling phenomena, in addition to the aforementioned mountain folding (Fig. 1.2a), at a smaller scale, stiff layers of quartz coated into soft metamorphic rocks buckle periodically under compression, as shown in Fig. 1.2b [Hobbs and Ord, 2012]. Living organisms with pipes, skins, etc. also wrinkle periodically as shown in Figs. 1.2c-f, and these phenomena are induced by the growth or the slimming of some tissues bound to some other inelastic ones. Periodic patterns can also be observed in fruits and vegetables with thin leaves or skins. Indeed, for leaves, as growth process induce internal stresses, the cheapest way to reduce the energy elastically is by bending deformations which might result in buckling with fractal patterns [Sharon et al., 2002, Audoly and Pomeau, 2010, Li et al., 2012] (Fig. 1.2c). In spheroidal fruits/vegetables, the anisotropy resulting from fiber orientations induce stress-driven periodic buckling and various buckling patterns exist [Yin et al., 2008, Li et al., 2011b] (Fig. 1.2d).

The common point between all the aforementioned examples is periodic buckling. Moreover, buckling induces geometrical (physical) nonlinearities and periodicity induces dispersion, two phenomena necessary to the formation of solitary waves.

1.2 Solitary waves

History

Modeled by a partial differential equation (PDE), wave propagation was first studied in the linear case and solutions are well known today even in the presence of diffusion and dispersion (attenuation in time and space respectively). In the presence of dispersion, different frequency

components of a wave packet travel with different group velocity and consequences are the spreading of the wave envelope on both time and space, as shown in Fig. 1.6a. A more challenging problem is posed by nonlinearity which in general leads to amplitude-dependent behavior; shock waves, chaos or discontinuities (Fig. 1.6b). Some analytical solutions to nonlinear PDEs such as the Hopf or the Burgers equations exist but there is no general solution method [Whitham, 1974]. When nonlinearity and dispersion are both present, solitary waves may propagate and these are the kind of waves investigated in this thesis (Fig. 1.6c). A solitary wave is defined by a wave conserving its properties (speed and shape), and in contrast to linear waves, these properties depend on the wave amplitude [Whitham, 1974, Remoissenet, 1995, Ablowitz, 2011, Porubov, 2003, Samsonov and Maugin, 2001, Ablowitz and Segur, 1981].

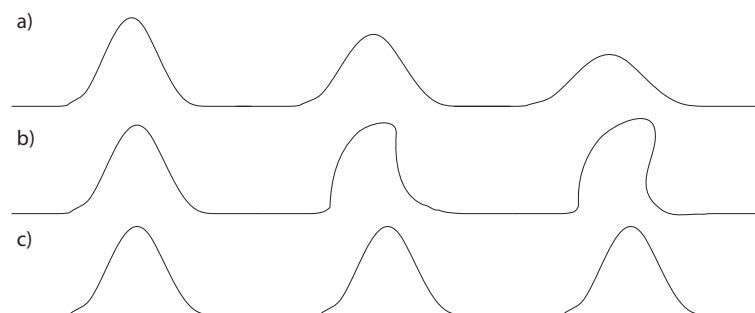


Figure 1.6: Effects of dispersion (a), nonlinearity (b) and both dispersion/nonlinearity (c) on wave propagation. The resulting wave of (c) is a solitary wave.

Solitary waves were first reported by John Scott Russell in 1834 [Dembitzer, 1965] who observed a wave traveling up a canal with a constant speed and shape for two miles (waves know now as tidal bore). In 1871, Boussinesq [Boussinesq, 1872] wrote equations including dispersion and nonlinearity. Analytical solutions in the form of solitary waves were found in 1895 by Korteweg and de Vries [Korteweg and de Vries, 1895] giving their name to the KdV equation. Later, in 1955, an unexpected discovery was made by Fermi, Pasta and Ulam (FPU) [Fermi et al., 1955] who were studying the repartition of thermal energy in a lattice ring. Instead of thermal equilibrium, quasiperiodic oscillations were found. Zabusky and Kruskal [Zabusky and Kruskal, 1965] later showed that the lattice ring used by FPU was in fact an infinite periodic chain of masses and nonlinear springs described by a KdV equation. Dispersion came from lattice periodicity and this opened the way for solitary wave studies in a large range of domains with periodic pattern as electrical networks [Ricketts and Ham, 2010], optical fibers [Hasegawa, 1998] etc. In [Remoissenet, 1995], a summary of many examples for various physical domains are given.

If in addition, solitary waves keep their properties even when interacting with other solitary waves, they are called solitons from the definition of Zabusky and Kruskal [Zabusky and Kruskal, 1965]. Specifically in physics literature, solitary waves are referred to solitons, even if these waves do not collide elastically, but in the present thesis, the distinction between these two terms is kept.

Chapter 1. Introduction

Nonlinear PDEs, which are exactly integrable in the sense of the inverse scattering (IST) methods [Ablowitz and Segur, 1981], possess an infinite number of soliton solutions, given the initial conditions. Indeed, superposition (collision) of two solitons results to a new soliton such that by repeating this operation an infinite number of times, it is possible to construct an infinite number of solutions. Examples of equations admitting soliton solutions are the Sine-Gordon, the Klein-Gordon, the nonlinear Schrödinger (NLS) and the Boussinesq equations. At the contrary, nonlinear PDEs which are not exactly integrable as the double-dispersive Boussinesq equation only admit single solitary solutions, and collision between two solitary waves results to small radiation (tail or front) [Bogolubsky, 1977, Soerensen, 1984].

Aside from this distinction, nonlinear PDEs admitting solitary waves also admit periodic solutions (cnoidal solutions) but in the present thesis, the focus is on localized solutions that are usually written under hyperbolic functions. Among localized nonlinear waves, breathers which are oscillatory solutions are also solutions of nonlinear PDEs [Ablowitz and Segur, 1981] but they are not investigated here since they are most often non-propagative.

While solitary waves are found to describe various physical phenomena, we focus here on the field of mechanics.

Solitary waves in the field of mechanics

Periodic mechanical systems are often described by discrete systems and the simplest one consists of a mass-spring chain. The momentum equation describing the displacement U of the i^{th} mass is given by

$$\ddot{U}_i = F\{U_{i-1} - U_i\} - F\{U_i - U_{i+1}\}, \quad (1.1)$$

where $(\ddot{\cdot})$ is the double derivation with respect to time and $F\{\Delta U\}$ is the nonlinear load-displacement relation. In the case of the FPU chain, this relation reads

$$F\{\Delta U\} = k_0 \Delta U + F_N\{\Delta U\}, \quad (1.2)$$

where $k_0 \in \mathbb{R}$ is the linear stiffness coefficient and $F_N\{\Delta U\}$ is a purely nonlinear function. Assuming $k_0 \Delta U \gg F_N\{\Delta U\}$, homogenization of Eq. (1.1) under the long-wave assumption leads to the Boussinesq equation which can be further recast into the KdV equation. On the contrary, if $k_0 \Delta U \ll F_N\{\Delta U\}$, the PDE resulting from Eq. (1.1) is refereed as strongly-nonlinear because no direct linear solution exist. These equations are used to describe for example wave propagation in granular media where the contact between two particles is given by the Hertz power law ($F_N\{\Delta U\} = k_N \Delta U^n$, with $\{k_N, n\} \in \mathbb{R}$) [Nesterenko, 2001, Sen et al., 2008, Theocharis et al., 2013].

In addition to the mass-spring chain in translation, the pendulum chain with torsional springs has been also investigated and the Sine-Gordon soliton is obtained [Scott, 1969, Remoissenet, 1995, Munteanu and Donescu, 2004].

While Eq. (1.1) only accounts for one-dimensional effects, more complex lattices are investigated in [Maugin, 1999, Khusnutdinova et al., 2009, Porubov and Berinskii, 2014] leading to systems of coupled equations. In addition to lattices, tensegrity structures have also been investigated in [Fraternali et al., 2012, 2014]. Recently, solitary waves have also been obtained analytically into origami-based metamaterials [Yasuda et al., 2015] and experimentally into woodpile periodic structures [Kim et al., 2015].

In all the aforementioned examples, while the systems are discrete, dispersion is induced by periodicity and nonlinearity arises from large geometrical deformations. However, in solid mechanics, solitary waves have been observed in continuous materials as well, with material nonlinearities modeled by the standard continuum theory incorporating characteristic lengths [Maugin, 1999, Destrade and Saccomandi, 2008], or having reduced dimensions as plates and rods [Coleman et al., 1995, Champneys et al., 1997, Samsonov and Maugin, 2001, Porubov, 2003, Munteanu and Donescu, 2004, Porubov and Maugin, 2005, Duričković et al., 2009, Khusnutdinova and Tranter, 2015, Samsonov et al., 2015].

Buckled beams are dispersive media and are particularly interesting since at least three length scales are present: periodicity, beam thickness and beam curvature. Combined to the fact that buckling is also geometrically nonlinear, both ingredients necessary for the structure to host solitary waves are present, and it is the goal of this thesis to characterize the wave properties.

1.3 Organization of the work

This thesis investigates wave propagation in periodic buckled beams and the framework is the following. Chapter 2 gives an overview of the static beam buckling, investigating the problem formulation, the stability, and the role played by imperfections. Using the extensible-elastica theory, a new approximated equation describing the load-displacement relation between beam extremities is developed and has the advantage compared to existing models to be valid for post-buckled regimes, where bending deformations are dominant, and for weakly-buckled states, where deformations are mainly governed by axial strains and imperfections. Moreover, this relation is valid for both support types (guided and pinned) since their behavior is identical once normalized.

In Chapter 3, linear dispersion is analyzed employing Bloch theorem which is particularly useful for complex periodic structures. While these results are numerical, a novel method has been developed in this thesis to obtain a semi-analytical dispersion equation of the acoustic branch, relating explicitly the frequency to the propagation constant. Using the fact that buckled beams possess also glide axial-reflection symmetries, Bloch theorem is revisited, reducing the unit cell to half of the translational periodicity, decreasing the computation cost and allowing for an easier representation and interpretation of results. Influence of the support type, pre-compression level, stress, curvature, dissipation, and added mass/stiffness on dispersion and wavemodes are also investigated. In addition to periodicity, additional sources of dispersion are found and are transverse inertial effects in the case of the guided-

Chapter 1. Introduction

supported beam, and also coupling effects in the case of the pinned-supported beam. These additional dispersion sources are quantified numerically in terms of the pre-compression level and the support type, and are included in a fourth-order PDE describing linear-dispersive waves.

Chapter 4 is devoted to the derivation of different models describing nonlinear wave propagation in buckled beams including all dispersive sources, and results are compared to numerical finite-element (FE) simulations of the structure. For small amplitude waves, the double-dispersion Boussinesq equation correctly describes wave propagation, whereas for large amplitude waves, models based on strongly nonlinear PDEs such as the one describing granular media are more appropriate. By varying the level of pre-compression and the support type, the structure is found to hold four different wave types, namely compressive supersonic, rarefaction supersonic, compressive subsonic and rarefaction subsonic solitary waves. In Chapter 5, experiments on weakly-buckled guided-supported beams are conducted to validate analytical models and numerical simulations.

Finally, Chapter 6 propose a solution to the use of the exact extensible-elastica formulation in FE methods. Indeed, the Galerking method applied to the extensible-elastica problem involves second order derivatives for which at least \mathcal{C}^1 -continuous basis functions are required whereas classical FE methods are maximum \mathcal{C}^0 -continuous through the geometry. NURBS-based isogeometric analysis (IGA) is proposed here, which has the advantage of requiring a limited number of degrees of freedom. After the validation of the discretization by convergence analyses, the formulation is found efficient to solve dynamic problems involving slender beams as buckling.

2 Periodic Buckled Beams: Kinematics And Stability

2.1 Introduction

The objective of this thesis is to study wave propagation in periodic buckled beams and static buckling is investigated first. Specifically, the aim is to describe the nonlinear relation between the load and the displacement of the structure extremities, which will be used in the next chapters as an effective constitutive behavior. In this thesis, concerning the beam kinematics, two main assumptions are made: (i) the beam and its deformations remain in the plane (i.e. no torsion) and (ii) the beam is assumed sufficiently slender such that shear deformations are neglected. Since buckling involves finite displacements/rotations and axial deformations before the critical load, the beam theory which is going to be used is the extensible-elastica.

The column-buckling problem admits an infinite number of modes, and stability is investigated using the energy method from which, it is found that above the critical load, only the first buckling mode is stable. Since high-order modes are required to obtain a periodic pattern, stability is ensured by the use of additional pinned or guided supports. Influence of the presence of initial geometrical imperfections on the equilibrium path (bifurcation diagram) and the load-displacement relation are also explored.

2.2 Review of some two-dimensional beam formulations

Beams are structural elements described by cross-section profiles and material parameters. In the plane, they are capable of hosting load primarily by resisting bending but can also carry axial and shear deformations. The simplest beam formulation is the Euler–Bernoulli theory that assumes that the cross section remains planar and normal to the tangent of the elastic axis (line that passes through the elastic center) after deformations, corresponding to the shear-free assumption. To account for shear deformations, Timoshenko theory has been introduced and completes the Euler–Bernoulli formulation. However, these aforementioned theories are only valid for small deformations and cannot account for finite rotations, as encountered in post-buckled beams [Wriggers, 2008]. The geometrically-exact beam formulation, firstly introduced

by Reissner [Reissner, 1972], addresses this problem since the term exact refers to the fact that the strain follows directly from geometrical considerations, without approximation.

Since beam buckling involves axial deformations before the critical buckling load and mainly bending deformations after, two regimes investigated in this thesis, shear deformations are neglected here. This is especially true since only slender beams are considered. The shear-free geometrically-exact beam formulation is also known as the extensible-elastica [Magnusson et al., 2001] and is introduced next.

2.3 Extensible-elastica: kinematics and constitutive law

In the initial configuration of the beam, \mathbf{r}_0 is the position vector of a beam material point; $\mathbf{e}_{0,i}$, $i = 1, 2$ is an orthonormal basis vector such that $\mathbf{e}_{0,1}$ represents the normal direction of the cross-section and θ_0 the orientation angle. s_0 indicates the curvilinear coordinate of the beam with l_0 its total length. Correspondingly, \mathbf{r} , \mathbf{e}_i , θ , and s represent the position vector, the orthonormal basis vectors, the rotation, and the curvilinear coordinate in the current configuration of the beam, respectively. These quantities are shown in Fig. 2.1 and are defined as

$$\begin{aligned} \mathbf{r}_0 &= \{r_{0,x}, r_{0,y}\}^T, & \mathbf{r} &= \{r_x, r_y\}^T, \\ \mathbf{e}_{0,1} &= \{\cos\theta_0, \sin\theta_0\}^T, & \mathbf{e}_1 &= \{\cos\theta, \sin\theta\}^T, \\ \mathbf{e}_{0,2} &= \{-\sin\theta_0, \cos\theta_0\}^T, & \mathbf{e}_2 &= \{-\sin\theta, \cos\theta\}^T, \end{aligned} \quad (2.1)$$

where $\mathbf{r}_0 = \mathbf{r}_0(s_0)$, $\mathbf{r} = \mathbf{r}(s) = \mathbf{r}_0 + \mathbf{u}$, $\mathbf{e}_{0,i} = \mathbf{e}_{0,i}(s_0)$, $\mathbf{e}_i = \mathbf{e}_i(s)$, $\theta_0 = \theta_0(s_0)$, $\theta = \theta(s)$ and $\mathbf{u} = \mathbf{u}(s) = \{u_x \ u_y\}^T$ is the displacement vector.

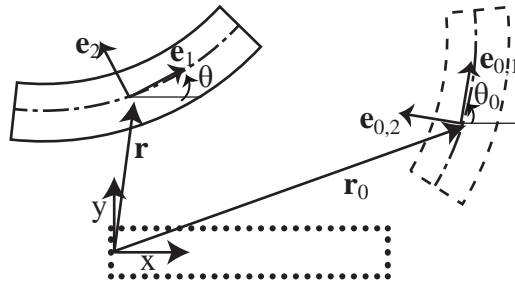


Figure 2.1: Beam kinematics: initial (dashed lines) and current configuration (full lines).

The strain relation proposed by Reissner [Reissner, 1972] for a plane beam initially free of

shear and unstretched is

$$\epsilon = \frac{dr_x}{ds_0} \cos\theta + \frac{dr_y}{ds_0} \sin\theta - 1, \quad (2.2a)$$

$$\gamma = \frac{dr_y}{ds_0} \cos\theta - \frac{dr_x}{ds_0} \sin\theta, \quad (2.2b)$$

$$\kappa = \frac{d\theta}{ds_0} - \frac{d\theta_0}{ds_0}, \quad (2.2c)$$

where ϵ is the axial strain, γ the shear strain, and κ the curvature. Neglecting shear ($\gamma = 0$), Eq. (2.2) becomes a system of two independent equations with three unknowns, such that combining Eqs. (2.2a) and (2.2b), it is possible to write the following equalities:

$$\sin\theta = \frac{1}{(\epsilon + 1)} \frac{dr_y}{ds_0}, \quad (2.3a)$$

$$\cos\theta = \frac{1}{(\epsilon + 1)} \frac{dr_x}{ds_0}, \quad (2.3b)$$

$$\epsilon + 1 = \sqrt{\left(\frac{dr_x}{ds_0}\right)^2 + \left(\frac{dr_y}{ds_0}\right)^2}. \quad (2.3c)$$

By assuming that the strain is finite but small, even for large displacements, it is possible to describe material behavior by Hooke's law. The constitutive law between the forces (internal axial force N_ϵ and bending moment N_κ) and the strain components after the integration over the beam cross section reads [Wriggers, 2008, Reissner, 1972, Irschik and Gerstmayr, 2009]

$$\begin{Bmatrix} N_\epsilon \\ N_\kappa \end{Bmatrix} = \begin{bmatrix} EA & 0 \\ 0 & EI_z \end{bmatrix} \begin{Bmatrix} \epsilon \\ \kappa \end{Bmatrix}, \quad (2.4)$$

where E is the Young modulus, and A and I_z are respectively the area and moment of inertia of the beam.

The weak formulation of the equilibrium equation is obtained from the principle of virtual work and is expressed in terms of the current configuration:

$$\int_0^{l_0} (N_\epsilon \delta\epsilon + N_\kappa \delta\kappa) ds_0 - \int_0^{l_0} (\mathbf{f}^T \delta\mathbf{u} + m\delta\theta) ds_0 - [\mathbf{F}^T \delta\mathbf{u} + M\delta\theta]_0^{l_0} = 0, \quad (2.5)$$

where \mathbf{f} and \mathbf{F} are respectively the distributed and boundary-force vectors, whereas the distributed and boundary moments are indicated respectively by m and M . The variational strain and moment are given by

$$\delta\epsilon = \frac{1}{\cos\theta} \frac{d\delta r_x}{ds_0} + (\epsilon + 1) \tan\theta \delta\theta, \quad (2.6a)$$

$$\delta\kappa = \frac{d\delta\theta}{ds_0}. \quad (2.6b)$$

In order to proceed further, the geometry and boundary conditions of the problem are required.

2.4 Pinned-pinned column buckling

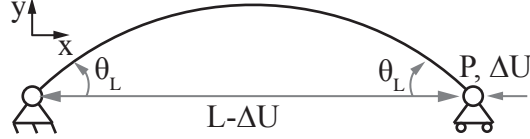


Figure 2.2: Pinned-pinned column buckling.

Consider a pinned-pinned column (straight beam) subject to a compressive axial load with constant material and geometrical properties along the length and with the initial beam length and extremity angles respectively denoted by L and θ_L (see Fig. 2.2). Noting that there is neither distributed force nor moment, and that the moment is free at extremities, the weak formulation of the beam (Eq. (2.5)) can be recast as [Magnusson et al., 2001]

$$\int_0^L \left(N_\epsilon \frac{1}{\cos \theta} \frac{d\delta r_x}{ds_0} + N_\epsilon (\epsilon + 1) \tan \theta \delta \theta + N_\kappa \frac{d\delta \theta}{ds_0} \right) ds_0 + [P\delta r_x]_0^L = 0, \quad (2.7)$$

where P is the applied force such that $F = -P$. Integrating by parts the term proportional to the moment and recasting the boundary term under integral form, the two following equalities are obtained:

$$N_\epsilon = -P \cos \theta, \quad (2.8a)$$

$$\frac{dN_\kappa}{ds_0} + (\epsilon + 1)P \sin \theta = 0, \quad (2.8b)$$

which can be recast using Eqs. (2.2) and (2.4) as

$$\frac{d^2\theta}{ds_0^2} + \frac{P}{EI_z} \sin \theta - \frac{P^2}{EAEI_z} \cos \theta \sin \theta = 0. \quad (2.9)$$

While Eq. (2.9) describes local equilibrium of the problem, the boundary conditions are given by

$$\theta|_{s_0=0} = \theta|_{s_0=L} = \theta_L \quad \text{and} \quad \frac{d\theta}{ds_0} \Big|_{s_0=0} = \frac{d\theta}{ds_0} \Big|_{s_0=L} = 0. \quad (2.10)$$

Before deriving the shape of the buckled beam, it is necessary to define the critical load at which buckling occurs.

2.4.1 Critical load

When compressed, the beam remains straight and deformations are purely axial until the load reaches a critical value for which a bifurcation occurs. In order to find this critical load denoted P_c , the beam is considered just after the bifurcation such that $\theta \rightarrow 0$ and linearization of Eq. (2.9) reads [Magnusson et al., 2001]

$$\frac{d^2\theta}{ds_0^2} + \left(\frac{P_c}{P_E} \left(\frac{\pi}{L} \right)^2 - \left(\frac{P_c}{P_E} \right)^2 \left(\frac{\pi^2}{\lambda L} \right)^2 \right) \theta = 0, \quad (2.11)$$

where

$$P_E = EI_z \left(\frac{\pi}{L} \right)^2 \quad (2.12)$$

is the critical Euler load and

$$\lambda = L \sqrt{\frac{A}{I_z}} \quad (2.13)$$

is the slenderness parameter of the beam. The eigenvalue problem Eq. (2.11), with the boundary conditions Eq. (2.10), admits eigenfunctions given by

$$\theta_n = a_n \cos \left(\frac{n\pi s_0}{L} \right), \quad (2.14)$$

where $a_n \in \mathbb{R}$ and $n \in \mathbb{N}^+$. Plugging Eq. (2.14) into Eq. (2.11),

$$\left(\frac{P_c}{P_E} \right)^2 - \frac{P_c}{P_E} \frac{\lambda^2}{\pi^2} + n^2 \frac{\lambda^2}{\pi^2} = 0, \quad (2.15)$$

for which the solution is

$$\frac{P_c}{P_E} = \frac{\lambda^2}{2\pi^2} \pm \sqrt{\frac{\lambda^4}{4\pi^4} - n^2 \frac{\lambda^2}{\pi^2}}. \quad (2.16)$$

In this thesis, since beams are assumed slender, only the minus case in Eq. (2.16) is considered next and refer to [Magnusson et al., 2001] for thick beams. Using Taylor series,

$$\frac{P_c}{P_E} = n^2 + n^4 \frac{\pi^2}{\lambda^2} + \mathcal{O} \left(n^6 \frac{\pi^4}{\lambda^4} \right), \quad (2.17)$$

and the first contribution of the extensibility is to increase the Euler critical load. Now that the critical load is defined, the load-displacement relation can be derived.

2.4.2 Load-displacement relation

Using the equation describing local equilibrium of the problem (Eq. (2.9)), the aim is to describe the axial load-displacement relation between beam extremities. Multiplying Eq. (2.9) by $\frac{d\theta}{ds_0}$ and integrating using the boundary condition $\theta\{s_0 = 0\} = \theta_L$ reads [Magnusson et al., 2001]

$$\frac{d\theta}{ds_0} = \frac{2\pi}{L} \sqrt{\frac{P}{P_E}} \sqrt{(1 - P_A) \left(q^2 - \sin^2 \frac{\theta}{2} \right) + P_A \left(q^4 - \sin^4 \frac{\theta}{2} \right)}, \quad (2.18)$$

where

$$q = \sin \frac{\theta_L}{2} \quad \text{and} \quad P_A = \frac{P}{EA} = \frac{\pi^2 P}{\lambda^2 P_E}. \quad (2.19)$$

Considering only the first buckling mode ($n = 1$), the angle at the beam extremity is found solving the integral

$$L = \int_0^L ds_0 = 2 \int_{\theta_L}^0 \frac{ds_0}{d\theta} d\theta, \quad (2.20)$$

which can be recast in terms of complete elliptical integrals of the first kind [Magnusson et al., 2001]:

$$\sqrt{\frac{P}{P_E}} = \frac{2}{\pi} \frac{1}{\sqrt{1 - P_A + 2P_A q^2}} K\{c\} \quad P > P_c, \quad (2.21)$$

where

$$c = q^2 \frac{1 + P_A q^2}{1 - P_A + 2P_A q^2}. \quad (2.22)$$

The displacement in terms of θ_L is

$$\Delta U = - \int_0^L \left(\frac{dr_x}{ds_0} - \frac{dr_{0,x}}{ds_0} \right) ds_0 = L - 2 \int_{\theta_L}^0 \left(\frac{dr_x}{ds_0} - \frac{dr_{0,x}}{ds_0} \right) \frac{ds_0}{d\theta} d\theta, \quad (2.23)$$

which can be written in terms of complete elliptical integrals of the first ($K\{c\}$) and second ($E\{c\}$) kinds [Magnusson et al., 2001]

$$\begin{aligned} \frac{\Delta U}{L} &= \frac{2}{\pi} \sqrt{\frac{P_E}{P}} \sqrt{1 - P_A + 2P_A^2} \left(\left(1 + \frac{1}{1 - P_A + 2P_A^2} \right) K\{c\} - 2E\{c\} \right) \\ &= 2 - P_A + 2P_A^2 - 2(1 - P_A + 2P_A^2) \frac{E\{c\}}{K\{c\}} \quad P > P_c. \end{aligned} \quad (2.24)$$

Eqs. (2.21) and (2.24) form a system of two independent equations with the three unknowns c , P and ΔU , and the goal is to recast this system into an expression of P in terms of ΔU only. While this work can be done easily numerically by fixing c and solving for P first and then ΔU , in order to get an analytical expression, series expansions are employed.

2.4.3 Analytical load-displacement equation assuming inextensibility

Neglecting axial deformations ($P_A = 0$), the system of Eqs. (2.24) and (2.21) simplifies to

$$\chi = 2 - 2 \frac{E\{c\}}{K\{c\}} \quad P > P_c, \quad (2.25a)$$

$$\frac{P}{P_E} = \left(\frac{2}{\pi} K\{c\} \right)^2 \quad P > P_c, \quad (2.25b)$$

where $\chi = \frac{\Delta U}{L}$. This system of two dependent equations is reduced to one after substitution of the variable c :

$$\frac{P}{P_E} = F\{c\} = G\{\chi\} \quad P > P_c, \quad (2.26)$$

where $F\{c\}$ and $G\{\chi\}$ are functions that depend only on c and χ , respectively. $G\{\chi\}$ can be found exactly only numerically and the aim is to find an analytical approximation using a Taylor expansion of $F\{c\}$ with respect to the derivative χ around the equilibrium point $\chi = c = 0$ such that

$$\begin{aligned} F\{c\} = & F\{0\} + \left(\frac{dF\{c\}}{dc} \frac{dc}{d\chi} \right) \Big|_{c \rightarrow 0} \chi + \frac{1}{2} \left(\frac{d^2F\{c\}}{dc^2} \left(\frac{dc}{d\chi} \right)^2 + \frac{dF\{c\}}{dc} \frac{d^2c}{d\chi^2} \right) \Big|_{c \rightarrow 0} \chi^2 \\ & + \frac{1}{6} \left(\frac{d^3F\{c\}}{dc^3} \left(\frac{dc}{d\chi} \right)^3 + 3 \frac{d^2F\{c\}}{dc^2} \frac{dc}{d\chi} \frac{d^2c}{d\chi^2} + \frac{dF\{c\}}{dc} \frac{d^3c}{d\chi^3} \right) \Big|_{c \rightarrow 0} \chi^3 \\ & + \frac{1}{24} \left(\frac{d^4F\{c\}}{dc^4} \left(\frac{dc}{d\chi} \right)^4 + 6 \frac{d^3F\{c\}}{dc^3} \frac{dc}{d\chi} \frac{d^2c}{d\chi^2} \right. \\ & \left. + \frac{d^2F\{c\}}{dc^2} \left(3 \left(\frac{d^2c}{d\chi^2} \right)^2 + 4 \frac{dc}{d\chi} \frac{d^3c}{d\chi^3} \right) + \frac{dF\{c\}}{dc} \frac{d^4c}{d\chi^4} \right) \Big|_{c \rightarrow 0} \chi^4 + \mathcal{O}(\chi^5) \quad P > P_c, \end{aligned} \quad (2.27)$$

where $\frac{d^{p+1}c}{d\chi^{p+1}}$ ($p \in \mathbb{N}^+$) is computed using Eq. (2.25a) and

$$\frac{d^{p+1}c}{d\chi^{p+1}} = \left(\frac{d\chi}{dc} \right)^{-1} \frac{d}{dc} \left(\frac{d^p c}{d\chi^p} \right). \quad (2.28)$$

The derivatives of the first and second elliptical integrals are:

$$\frac{dK\{c\}}{dc} = \frac{E\{c\}}{c(1-c^2)} - \frac{K\{c\}}{c} \quad \text{and} \quad \frac{dE\{c\}}{dc} = \frac{E\{c\} - K\{c\}}{c}. \quad (2.29)$$

Finally, using $F\{c\} = \left(\frac{2}{\pi}K\{c\}\right)^2$ in Eq. (2.27) gives

$$\frac{P}{P_E} = 1 + \frac{1}{2}\chi + \frac{9}{32}\chi^2 + \frac{21}{128}\chi^3 + \frac{795}{8192}\chi^4 + \mathcal{O}(\chi^5) \quad P > P_c. \quad (2.30)$$

However, the convergence of this series is not optimum and an alternative to a polynomial can be found noting that $E\{c\} + K\{c\} = \pi + \mathcal{O}(c^4)$, such that plugged into Eq. (2.25), an analytical approximation for the load-displacement relation reads

$$\frac{P}{P_E} = \left(\frac{1}{1 - \frac{1}{4}\chi} \right)^2 \quad P > P_c. \quad (2.31)$$

This equation motivates to look for an equation such that the denominator of Eq. (2.31) is the polynomial series, and using $F\{c\} = \frac{\pi}{2K\{c\}}$ in Eq. (2.27), one get

$$\frac{P}{P_E} = \left(\frac{1}{1 - \frac{1}{4}\chi - \frac{3}{64}\chi^2 - \frac{1}{64}\chi^3 - \frac{101}{16384}\chi^4 + \mathcal{O}(\chi^5)} \right)^2 \quad P > P_c. \quad (2.32)$$

As shown in Fig. 2.3, for the same order of truncation, Eq. (2.32) gives better results than Eq. (2.30) compared to the exact solution of the elastica solved numerically (Eq. (2.26)).

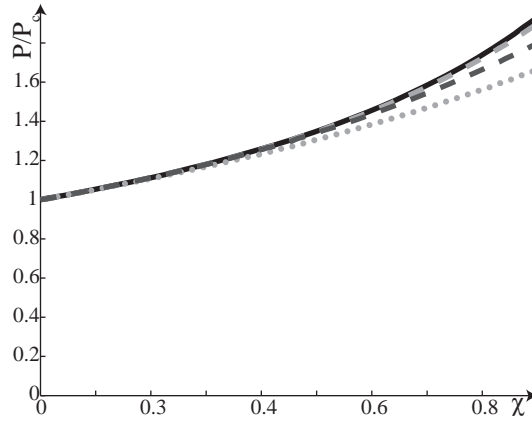


Figure 2.3: Normalized load-displacement curve from the inextensible-elastica in full black (Eq. (2.26)) and its approximations with Eq. (2.31) in dotted line, Eq. (2.32) in dashed light-gray line, and Eq. (2.30) in dashed dark-gray lines.

For the extensible case, Taylor expansions can be also employed and approximated equations of the load-displacement relation are presented in Appendix A. However, as it will be shown next, extensibility is only playing a role for really small deformations where imperfections are also present and have to be taken into account. But before introducing imperfections, stability is investigated first.

2.5 Stability and bifurcation

As shown in the derivation of the critical load, the solution of the buckling problem is not unique and an infinite number of modes exist. In order to investigate their stability, at least two different methods exist: the dynamic stability analysis for which Lyapunov criterion is used, and the energy method, valid uniquely for conservative systems and consisting in analyzing the sign of the second variation of the potential energy [Bazant et al., 1993]. Since in the considered buckling problem, applied forces are conservative (no follower forces), the energy method is used and has the advantage of not requiring the introduction of inertia. The potential energy Π of the extensible-elastica for a prismatic beam is given by [Magnusson et al., 2001]

$$\Pi = \frac{1}{2}EI_z \int_0^L \kappa^2 ds_0 + \frac{1}{2}EA \int_0^L \epsilon^2 ds_0 + P r_x|_{s_0=L}, \quad (2.33)$$

where

$$r_x|_{s_0=L} = \int_0^L \frac{du}{ds_0} ds_0 = \int_0^L (\epsilon + 1) \cos \theta ds_0. \quad (2.34)$$

Then Eq. (2.33) reads

$$\Pi = \frac{1}{2}EI_z \int_0^L \left(\frac{d\theta}{ds_0} \right)^2 ds_0 - \frac{P^2}{2EA} \int_0^L \cos^2 \theta ds_0 + P \int_0^L \cos \theta ds_0. \quad (2.35)$$

The second variation of the potential energy is given by

$$\delta^2 \Pi = EI_z \int_0^L \left(\frac{d\delta\theta}{ds_0} \right)^2 ds_0 + \frac{P^2}{EA} \int_0^L (\cos^2 \theta - \sin^2 \theta) (\delta\theta)^2 ds_0 - P \int_0^L \cos \theta (\delta\theta)^2 ds_0. \quad (2.36)$$

In order to analyze analytically the sign of $\delta^2 \Pi$, Eq. (2.36) is linearized assuming θ small:

$$\delta^2 \Pi = EI_z \int_0^L \left(\frac{d\delta\theta}{ds_0} \right)^2 ds_0 + \frac{P^2}{EA} \int_0^L (\delta\theta)^2 ds_0 - P \int_0^L (\delta\theta)^2 ds_0. \quad (2.37)$$

Assuming θ of the form of Eq. (2.14), Eq. (2.37) reads

$$\delta^2 \Pi = \left(EI_z \left(\frac{n\pi}{L} \right)^2 + \frac{P^2}{EA} - P \right) \frac{L}{2} (\delta a_n)^2. \quad (2.38)$$

Noting that solving $\delta^2 \Pi = 0$ gets back to Eq. (2.15), the straight beam is stable only when $\delta^2 \Pi > 0$ meaning that $P < P_c\{n\}$ (Eq. (2.16)) whatever n and so $P < P_c\{n = 1\}$. To summarize, the straight beam is only stable under the critical load.

While the stability analysis of the straight beam configuration is complete, stability of the different buckling modes is now investigated. Mode 1 is the buckling mode requiring the minimum energy ($P_c\{n = 1\} < P_c\{n > 1\}$) and it is expected to be the only one which is stable. Since the energy analysis of the extensible-elastica for θ finite is complex analytically, the structure is discretized using finite elements (FE) and the second variation of the potential energy is given by

$$\delta\Pi^2 = \delta\mathbf{U}^T \mathbf{K}_T \delta\mathbf{U}, \quad (2.39)$$

where \mathbf{U} is the nodal displacement vector, $\delta\mathbf{U}^T$ its transpose, $\mathbf{K}_T = \mathbf{K} + \frac{d\mathbf{K}}{d\mathbf{U}}\mathbf{U}$ is the tangent stiffness matrix, and \mathbf{K} the stiffness matrix at equilibrium. The system is stable if \mathbf{K}_T is positive definite, meaning that the real part of its eigenvalues is positive. The bifurcation diagram with the stability information is shown in Fig. 2.4 and as expected, only the first mode is stable above the critical load.

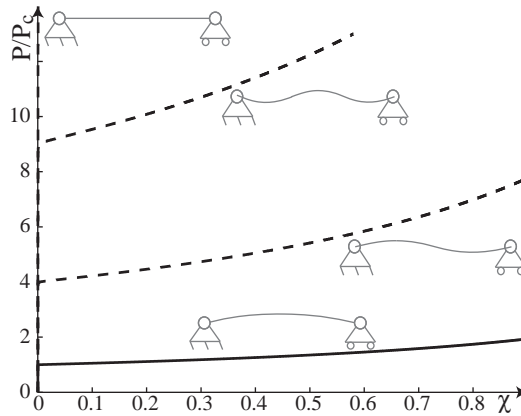


Figure 2.4: Pinned-pinned column buckling: bifurcation diagram. Stable and unstable paths respectively in full and dashed lines for the fourth first buckling modes.

Note that if the beam is initially perfectly straight, FE simulations do not follow the stable equilibrium path and the beam remains straight after the critical load. In order to follow alternative paths (first stable buckling mode or higher-order unstable ones), there are at least two possibilities. Add local forces to “help” the beam into a special direction, or add initial geometrical imperfections as it is investigated next.

2.6 Effects of geometrical imperfections

As shown previously, post-buckling of slender beams is mainly governed by bending deformations. For small compression, axial deformations have to be considered as well and modifications in the load-displacement curve are shown in Fig. 2.5. However, these results are valid only if the beam is perfectly straight without imperfections and with boundary conditions without play. If small imperfections are present, the load-displacement curve around the

critical load which was originally a sharp angle in the case of the perfect column becomes a smooth transition between the axial and bending branches, as shown in Fig. 2.5. It is the goal here to update the nonlinear load-displacement relation to include geometrical imperfection effects.

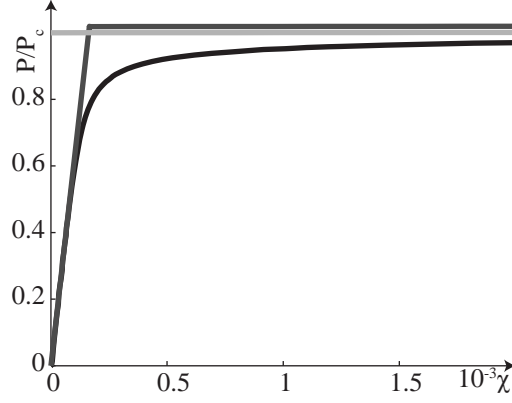


Figure 2.5: Normalized load-displacement curves for small compression: role of the extensibility and initial geometrical imperfections. Exact solution from inextensible-elastica in light-gray line, from extensible-elastica in dark-gray line, and from FE including geometrical imperfections in black line. $\lambda = 520$ and $w_0 = 10^{-2}$.

For example, for a beam initially slightly curved with a constant curvature radius R_0 , integration of the extensible-elastica Eq. (2.9) brings about an extra integration constant such that Eq. (2.18) becomes:

$$\frac{d\theta}{ds_0} = \frac{2\pi}{L} \sqrt{\frac{P}{P_E}} \sqrt{\frac{EI_z}{4R_0^2 P^2} + (1 - P_A) \left(q^2 - \sin^2 \frac{\theta}{2} \right) + e \left(q^4 - \sin^4 \frac{\theta}{2} \right)}. \quad (2.40)$$

However, for the load-displacement relation, contrary to Eq. (2.18), the additional term in Eq. (2.40) makes impossible the transformation of Eq. (2.40) into a system of complete elliptical integrals and only a complex equation involving incomplete elliptical integrals can be obtained (see handbook on elliptical integrals [Byrd and Friedman, 1971]).

An alternative to the constant curvature can be a beam with an initial deformation such that

$$w = w_0 \sin\left(\frac{s_0\pi}{L}\right), \quad (2.41)$$

where w is the transverse displacement of the beam and w_0 is the transverse displacement at midspan. An approximated solution for the load-displacement relation under small deformations is given in [Bazant et al., 1993] and reads

$$\frac{P}{P_E} = \left(1 - \frac{1}{\sqrt{1 + \frac{4}{q_0^2}(\chi - P_A)}} \right) \left(1 - \frac{q_0^2}{16} - \frac{\chi - P_A}{4} \right)^{-2}, \quad (2.42)$$

where $q_0 = \pi w_0/L$ and $P_A = P/(EA)$. Noting that $q_0^2/16 \ll 1$ (small imperfection) and that $P_A/4 \ll 1$ (small extensibility), the second term of Eq. (2.42) can be further simplified into $(1 - \chi/4)^{-2}$. Noting that this term is identical to Eq. (2.31), describing large deformation of the $P\{\Delta U\}$ curve, the first part of Eq. (2.42) describes imperfections and axial deformations. Moreover, instead of using Eq. (2.31) as the second part of Eq. (2.42), $(1 - \chi/4)^{-2}$ can be replaced by a better approximation like Eq. (2.32), such that an expression accounting for small and large compressions reads

$$\frac{P}{P_E} = \left(1 - \frac{1}{\sqrt{1 + \frac{4}{q_0^2}(\chi - P_A)}} \right) \left(1 - \frac{1}{4}\chi - \frac{3}{64}\chi^2 - \frac{1}{64}\chi^3 - \frac{101}{16384}\chi^4 \right)^{-2}. \quad (2.43)$$

First and second parts as well as the full Eq. (2.43) are plotted in Fig. 2.6 and compared to FE simulations. As expected, for small deformations, one can consider only the first part of Eq. (2.43) whereas for large buckling levels, the second part of Eq. (2.43) is sufficient.

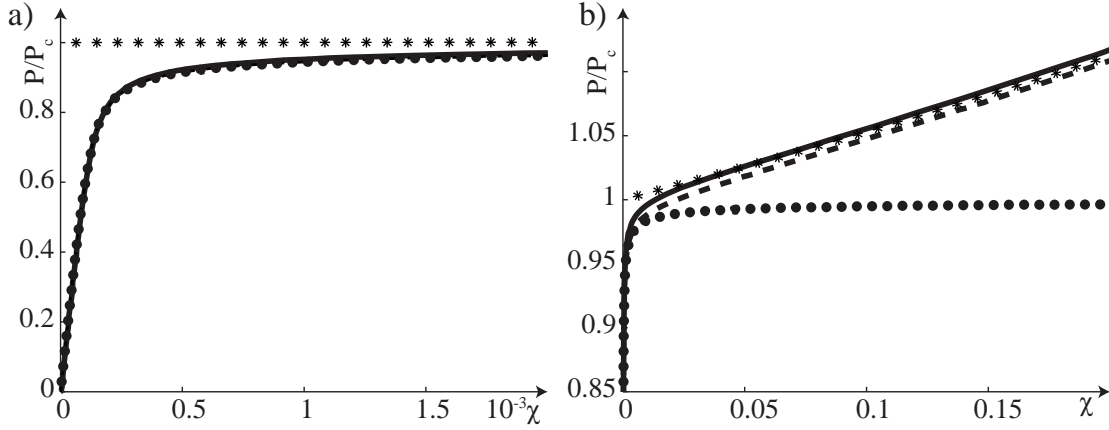


Figure 2.6: Normalized load-displacement curves for small (a) and large (b) deformations including initial imperfections and extensibility with the exact solution in full line. Full, first term and second term of Eq. (2.43) respectively in dashed, dotted and star lines. $\lambda = 520$ and $w_0 = 10^{-2}$.

The advantage of using small imperfections in FE method is to avoid the implementation of branch-switching methods [Huang and Atluri, 1995] to follow the stable equilibrium path. This is possible thanks to the transition between branches which becomes smooth with the introduction of imperfections (Fig. 2.5).

As shown in Fig. 2.7 where the influence of the imperfection size on the load-displacement curve is given, only the region around the critical load is affected for small imperfections. However if imperfections are too large, the nonlinear behavior of the load-displacement relation is almost lost. Note also that the load-displacement curves possess two different aspects which are going to be interesting for wave propagation investigation; indeed, there are inversion points in the curvature of the load-displacement curves, such that $P''\{\chi\} < 0$

before these points and $P''\{\chi\} > 0$ after, where $()''$ denotes the second derivative with respect to $\chi = \Delta U/L$ (see Fig. 2.7). This can be explained with Eq. (2.43) where its first and second terms dominate respectively for regions of $P''\{\chi\} < 0$ and $P''\{\chi\} > 0$.

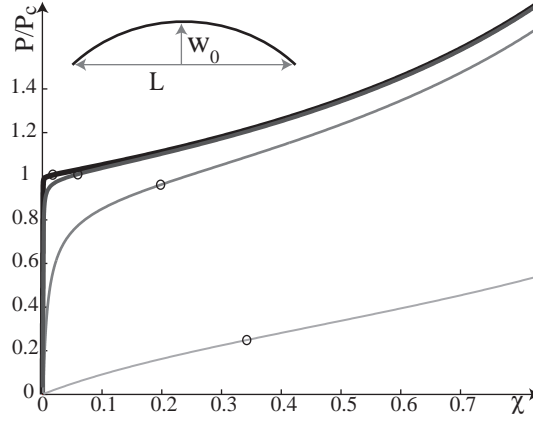


Figure 2.7: Normalized load-displacement curves for different levels of initial geometrical imperfections such that $\lambda = 520$ and $w_0/L = \{10^{-3}, 10^{-2}, 10^{-1}, 10^0\}$, respectively from dark to light gray. The circles are inversion points of the curvature.

2.7 Periodic buckled beam with supports

In this thesis, periodic buckled structures are of interest. However, although the introduction of specific imperfections can provide high-order, periodic buckled modes, these modes are unstable. In order to make them stable, additional pinned supports are placed at each wavelength, as shown in Fig. 2.8a. For the sake of clarity, in this thesis, thanks to the self-similarity of the load-deformation relation between one and several wavelengths, the length between two consecutive supports is defined as L and $n = 1$, instead of considering L the total length of the full structure, and $n \neq 1$ (Fig. 2.8a).

An alternative to pinned supports is the use of guided supports as shown in the Fig. 2.8a-b. Moreover, buckled beam with pinned and guided supports possess the same geometry (Fig. 2.8c) and the same normalized load-displacement relation [Bazant et al., 1993]. In order to generalize the previous equations to both support types, the Euler critical load (Eq. (2.12)) is redefined as

$$P_E = EI_z \left(\frac{\pi}{L_{eff}} \right)^2, \quad (2.44)$$

where $L_{eff} = L$ and $L_{eff} = L/2$, respectively in the case of pinned and guided supports, with L the original distance between two constitutive supports. Note that $\chi = \Delta U/L$ remains unchanged.

While the two support types provide the same dimensionless nonlinear load-displacement

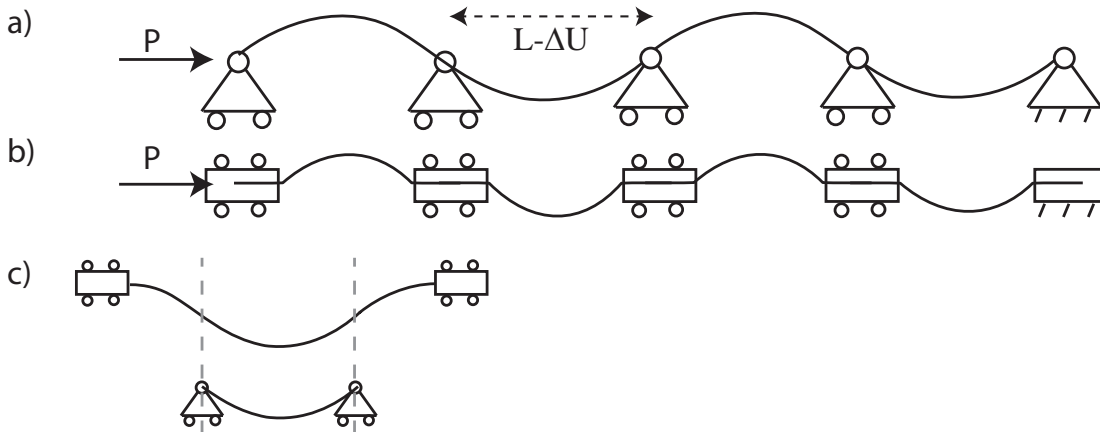


Figure 2.8: Pinned (a) and guided (b) buckled beam with 4 periods, and similitude in their geometries (c).

behavior as far as the static response, the same is not true for the dynamic response, specifically in terms of dispersion.

2.8 Conclusions

In the present chapter, starting from the extensible-elastica theory, a closed-form solution for the pinned-pinned buckled beam problem in terms of complete elliptical integrals is derived. Assuming inextensibility, which is valid for large deformations, a Taylor series of the load in terms of the axial displacements is derived (Eq. (2.32)). For small levels of compression, initial geometrical imperfections and axial deformations play a dominant role such that an additional equation describing the load-displacement behavior is given (Eq. (2.42)). By combining the two aforementioned equations, an equation describing the full buckling range is found (Eq. (2.43)), and results are validated with comparison with FE simulations.

It is also demonstrated using the energy method that above the critical buckling load, only the first buckling mode is stable. However, to follow this stable path, it is necessary to add initial imperfections and it is shown that the imperfections have to remain small for the load-displacement behavior to be nonlinear. Additionally, since high-order modes are not stable, the stability is ensured by including additional pinned or guided supports. Moreover, both support types possess the same-scaled load-displacement relation.

The dispersive characteristics of wave propagation in buckled beams are discussed next.

3 Dispersion Of Periodic Buckled Beams

Sections 3.3 to 3.4 and 3.5.3 are mainly reprinted from [Maurin and Spadoni, 2014a] with authorization of the publisher.

3.1 Introduction

Linear waves are called dispersive, if the relation between the phase speed and the frequency is nonlinear. Indeed, because the different wave frequency components propagate with different speeds, the wave spreads and its amplitude decays in time, while the total energy remains constant. In mechanics, dispersion occurs in every system where a length scale is present as in periodic structures, materials with microstructure, or continuous media with one dimension smaller than the others such as beams or plates.

Buckled beams are also a dispersive medium and are particularly interesting since at least three length scales are present: periodicity, beam thickness (bending waves) and curvature (displacement coupling). While dispersion induced by periodicity can be analyzed in the long-wave approximation by a chain of masses and linear springs, dispersion arising from the beam thickness and the curvature is more complex to model because the buckled beam is not uniformly curved or stressed. In this thesis, restriction is made to the long-wave approximation, focusing only on the acoustic branch of the dispersion, far from resonant frequencies.

In the present chapter, dispersion is analyzed employing Bloch theorem, which is particularly useful for complex periodic structures. It consists on the discretization of a periodic unit cell, and after applying periodic boundary conditions, an eigenvalue system is obtained from which the dispersion curves are extracted. While these results are numerical, a novel method has been developed in this thesis to obtain a semi-analytical dispersion equation of the acoustic branch, relating explicitly the frequency to the propagation constant. Using the fact that buckled beams possess glide axial-reflection symmetries, Bloch theorem is also revisited in this chapter by reducing the unit cell to half of the translational periodicity and updating the boundary conditions. The advantages are to decrease the computation cost and this allow an

easier interpretation of results.

This chapter is organized as follows. After reviewing different sources of dispersion in Sec. 3.2, the Bloch theorem accounting for glide-reflection symmetries is presented in Sec. 3.3 from which, semi-analytical dispersion relations are derived (Sec. 3.4). Influence of the support type, pre-compression level, stress, curvature, dissipation, and added mass/stiffness on dispersion and wavemodes are presented in Sec. 3.5, followed by the derivation of a fourth-order partial derivative equation (PDE) describing linear-dispersive waves in buckled beams.

3.2 Typical sources of dispersion

Before analyzing the dispersion of buckled beams with the Bloch theorem, some typical dispersion sources are reviewed here for continuous and discrete systems.

3.2.1 Dispersion of continuous structures

Buckled beams are complex structures involving non-constant curvature and stress, such that the exact analysis of dispersion characteristic is not possible analytically. In this section, the typical dispersion sources of simplified beam models are presented, and the frequency and the wavenumber are denoted by ω and κ , respectively. The material and geometric properties are considered constant along the length such that A and I_z are the cross-sectional area and area-moment of inertia, respectively. The material is assumed to be linear elastic and defined by Young modulus E and density ρ .

The propagation of bending waves in a compressed straight beam is [Doyle, 1997]

$$\omega^2 = -\frac{F}{\rho A}\kappa^2 + \frac{EI_z}{\rho A}\kappa^4, \quad (3.1)$$

where F is the axial compressive force, and the term proportional to κ^4 denotes bending-induced dispersion. Note that the dispersion is such that high frequencies propagate faster than lower ones, a behavior that is referred next as supersonic with respect to the long-wavelength, as shown in Fig. 3.1. In the absence of prestress ($F = 0$), the wave is purely dispersive whereas $F \neq 0$ adds a linear component to the wave. Additionally, if the beam is in compression ($F > 0$), a frequency cut-off is present [Doyle, 1997].

While Eq. (3.1) is applied to a straight beam, curvature effects can be investigated through the analysis of an infinite inextensible helix of constant radius R . For the tangential u and the

radial v displacements of the beam, governing equations are [Doyle, 1997]

$$EA \frac{d^2 u}{ds^2} + \frac{1}{R^2} \left(EI_z \frac{d^2 u}{ds^2} - EAR \frac{dv}{ds} + EI_z R \frac{d^3 v}{ds^3} \right) = \rho A \frac{d^2 u}{dt^2}, \quad (3.2a)$$

$$EI_z \frac{d^4 v}{ds^4} + \frac{1}{R^2} \left(EA v - EAR \frac{du}{ds} + EI_z R \frac{d^3 u}{ds^3} \right) = -\rho A \frac{d^2 v}{dt^2}, \quad (3.2b)$$

where s is the curvilinear coordinate. For harmonic motion, the combination of these two equations leads to the dispersion relation

$$\kappa^6 - \left(\kappa_a^2 + \frac{2}{R^2} \right) \kappa^4 - \left(\kappa_b^4 + \frac{\kappa_a^2}{R^2} - \frac{1}{R^4} \right) \kappa^2 + \left(\kappa_a^2 - \frac{1}{R^2} \right) \kappa_b^4 = 0, \quad (3.3)$$

where $\kappa_b^4 = \rho A \omega^2 / EI_z$ and $\kappa_a^2 = \rho A \omega^2 / EA$. Note that in Eq. (3.3), the term proportional to ω^4 does not have a direct physical meaning but results from displacement couplings. Bending waves and coupling effects are typical dispersion terms that will be encountered in buckled beams.

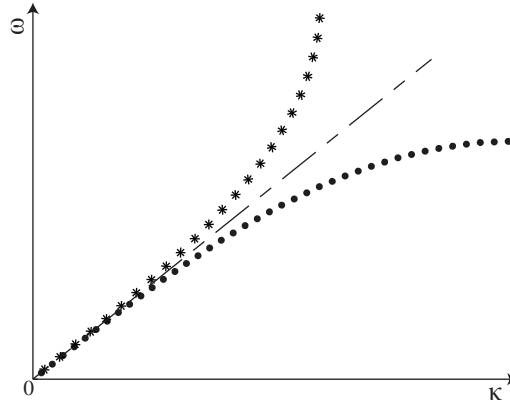


Figure 3.1: Supersonic (star line) and subsonic (dotted line) dispersion behavior, compared to non-dispersive behavior (dashed line).

3.2.2 Dispersion of discrete structures

After analyzing continuous beams where dispersion arises from the thickness and the curvature, periodic discrete structures, which also possess intrinsic length scales, are investigated here. The three different mass-spring systems shown in Fig. 3.2, which can be used as approximated models of buckled beams, are considered.

Simple chain of masses and springs

The simplest discrete periodic structure is the chain of masses and springs in series showed in Fig. 3.2a. Its dispersion equation is derived from the linear momentum equation of the n^{th}

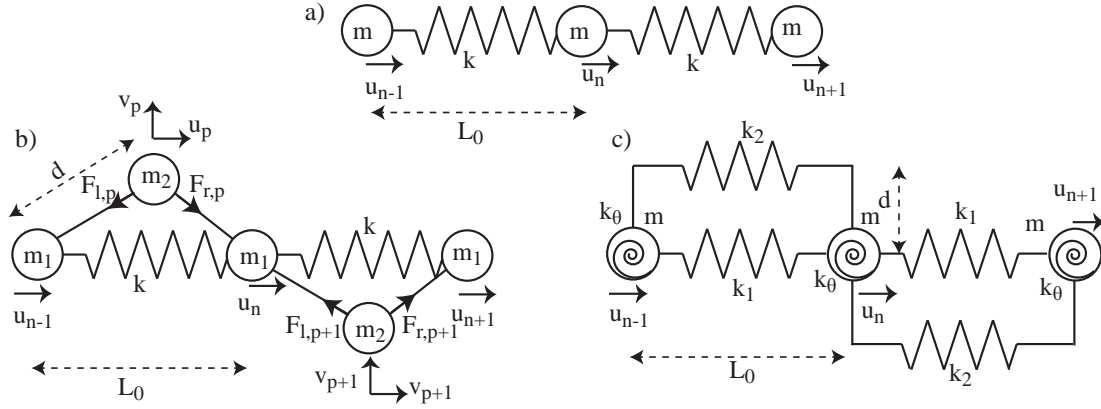


Figure 3.2: Simple mass-spring chain (a) accounting for transverse-inertial effects (b) or stiffness coupling effects (c).

particle, given by

$$m\ddot{u}_n = P\{\Delta U_R\} - P\{\Delta U_L\}, \quad (3.4)$$

where u_n denotes the displacement of the n^{th} particle of mass m , and $(\ddot{})$ the second derivative with respect to time t . $\Delta U_R = \Delta U_0 + u_{n+1} - u_n$ and $\Delta U_L = \Delta U_0 + u_n - u_{n-1}$ are respectively the variation of the length on the right and left sides, where ΔU_0 is the initial relative displacement between two consecutive masses due to pre-compression, and $P\{\Delta U\}$ the load-displacement relation. If $P\{\Delta U\}$ is linear, Eq. (3.4) can be recast into the linear momentum equation

$$\ddot{u}_n = \frac{C_0^2}{L_0^2} (u_{n-1} + u_{n+1} - 2u_n), \quad (3.5)$$

where L_0 is the distance between two consecutive masses, C_0 is the linear velocity for long wavelengths given by

$$C_0^2 = \frac{P'\{\Delta U_0\}L_0^2}{m}, \quad (3.6)$$

and $P'\{\Delta U_0\} = k$ is the linear stiffness of the spring in the case of Fig. 3.2a. Assuming plane harmonic waves, a solution of the form $u_n = ue^{i(\epsilon n - \omega t)}$ where $\epsilon = kL_0$ is the phase constant, gives the dispersion relation

$$\omega^2 = \frac{4C_0^2}{L_0^2} \sin^2\left(\frac{\epsilon}{2}\right). \quad (3.7)$$

For small wave number, Eq. (3.7) can be recast into polynomial form using Taylor expansion:

$$\left(\frac{\omega}{\omega_0}\right)^2 = \epsilon^2 - \frac{1}{12}\epsilon^4 + \mathcal{O}(\epsilon^6), \quad (3.8)$$

where $\omega_0 = C_0/L_0$. This expansion allows the decomposition of the dispersion equation in several terms. The first term gives the long-wavelength phase velocity and the second term, proportional to ϵ^4 , describes dispersion due to periodicity. Note that contrary to bending waves (Eq. (3.1)), the dispersion is here negative such that the phase speed (slope of the dispersion curve) decreases with increasing frequency, and is referred next as subsonic dispersion type (Fig. 3.1).

Chain of masses and springs accounting for transverse-inertial effects

A more realistic model of the buckled beam is the mass-spring chain with an additional mass m_2 , linked to the masses m_1 with rigid connectors of length d , as shown in Fig. 3.2b. From Fig. 3.2b, the coordinates X_p and Y_p linearized around the equilibrium point are given in terms of u_n and u_{n-1} , and reads

$$X_p - X_0 = \frac{u_n + u_{n-1}}{2}, \quad (3.9a)$$

$$Y_p - Y_0 = \sqrt{d^2 - \left(\frac{L_0 + u_n - u_{n-1}}{2}\right)^2} \simeq \sqrt{d^2 - \left(\frac{L_0}{2}\right)^2} - \frac{L_0(u_n - u_{n-1})}{4\sqrt{d^2 - \left(\frac{L_0}{2}\right)^2}}, \quad (3.9b)$$

where X_0 and Y_0 are constants. The particle acceleration is given by

$$\ddot{u}_p = \ddot{X}_p = \frac{\ddot{u}_n + \ddot{u}_{n-1}}{2}, \quad (3.10a)$$

$$\ddot{v}_p = \ddot{Y}_p = -\sqrt{\alpha} \frac{(\ddot{u}_n - \ddot{u}_{n-1})}{2}, \quad (3.10b)$$

where $\alpha = \left(\left(\frac{2d}{L_0}\right)^2 - 1\right)^{-1} > 0$ is a dimensionless parameter that depends on pre-compression. Note also that $\tan^{-1} \theta = \sqrt{\alpha}$. The momentum equation of the p^{th} mass is (Fig. 3.2b)

$$(F_{r,p} - F_{l,p}) \cos \theta = m_2 \ddot{u}_p, \quad (3.11a)$$

$$-(F_{r,p} + F_{l,p}) \sin \theta = m_2 \ddot{v}_p. \quad (3.11b)$$

Combining the momentum equations of the p^{th} and $p+1^{\text{th}}$ masses, the momentum equation of the n^{th} mass yields

$$\begin{aligned} \ddot{u}_n m_1 &= k(-2u_n + u_{n+1} + u_{n-1}) + F_{l,p+1} \cos \theta - F_{r,p} \cos \theta \\ &= k(-2u_n + u_{n+1} + u_{n-1}) - \frac{m_2}{4} ((2\ddot{u}_n + \ddot{u}_{n+1} + \ddot{u}_{n-1}) + \alpha(2\ddot{u}_n - \ddot{u}_{n+1} - \ddot{u}_{n-1})). \end{aligned} \quad (3.12)$$

Considering plane-harmonic waves with $u_n = ue^{i(\epsilon n - \omega t)}$, Eq. (3.12) can be recast into the dispersion relation:

$$\omega^2 = \frac{4k}{m} \sin^2 \frac{\epsilon}{2} + (1 - \alpha) \frac{4m_2}{m} \omega^2 \sin^2 \frac{\epsilon}{2}, \quad (3.13)$$

where $m = m_1 + m_2$. Using Taylor expansion, Eq. (3.13) reads

$$\left(\frac{\omega}{\omega_0}\right)^2 = \epsilon^2 - \frac{1}{12}\epsilon^4 + (1 - \alpha) \frac{m_2}{m} \left(\frac{\omega}{\omega_0}\right)^2 \epsilon^2 + \mathcal{O}\left(\left(\frac{\omega}{\omega_0}\right)^2 \hat{\epsilon}^4\right) + \mathcal{O}(\hat{\epsilon}^6). \quad (3.14)$$

While the term proportional to ϵ^4 is the dispersive term induced by the periodicity and is identical to Eq. (3.8), the one proportional to $\omega^2 \epsilon^2$ results from transverse-inertial effects. Since $0 < \alpha < \infty$, note that $1 - \alpha$ is negative for $d < L_0/\sqrt{2}$ (masses m_1 and m_2 almost aligned) and positive otherwise. It means that the total dispersion $(-1/12 + (1 - \alpha) m_2/m)$ can be either negative or positive, such that the dispersion behavior can change from subsonic to supersonic type (Fig. 3.1), and it shows the importance of the role played by transverse-inertial effects. Finally, Fig. 3.2b is only a simplified model of the buckled beam, which gives the advantage to explain physical mechanisms resulting in dispersion, without quantifying them.

Chain of masses and springs accounting for stiffness coupling effects

The model presented in Fig. 3.2b is a-posteriori a good model of the guided-supported buckled beams, but is not appropriate for the pinned-support configuration since rotation cannot be transmitted to neighboring masses. In order to capture this effect, a new mass-spring system is proposed in Fig. 3.2c. Note that for the sake of clarity, the transverse masses are not included here. In addition to the different forces shown in Fig. 3.2c, a moment equal to $k_\theta \theta_n$ is applied to each mass. Conservation of axial (u_n) and angular (θ_n) momentum equations are given by

$$m\ddot{u}_n = k(-2u_n + u_{n+1} + u_{n-1}) - k_2 d (\theta_{n+1} - \theta_{n-1}), \quad (3.15a)$$

$$I_\theta \ddot{\theta}_n = -k_2 d (u_{n+1} - u_{n-1}) + k_2 d^2 (-2\theta_n + \theta_{n+1} + \theta_{n-1}) - k_\theta \theta_n, \quad (3.15b)$$

where $k = k_1 + k_2$. Assuming plane-harmonic waves with $u_n/u = \theta_n/\theta = e^{i(\epsilon n - \omega t)}$, the system (3.15) can be recast as

$$\begin{bmatrix} 2k(1 - \cos \epsilon) - \omega^2 m & i2k_2 d \sin \epsilon \\ i2k_2 d \sin \epsilon & 2k_2 d^2 (1 - \cos \epsilon) + k_\theta - \omega^2 I_\theta \end{bmatrix} \begin{Bmatrix} u \\ \theta \end{Bmatrix} = \mathbf{0}. \quad (3.16)$$

The nontrivial solution of this system leads to the dispersion relation

$$\omega^2 = \frac{4kk_\theta + 16k_2^2 d^2}{mk_\theta} \sin^2 \frac{\epsilon}{2} + \frac{16k_1 k_2 d^2}{mk_\theta} \sin^4 \frac{\epsilon}{2} - \frac{4kI_\theta + 4k_2 d^2 m}{mk_\theta} \sin^2 \frac{\epsilon}{2} \omega^2 + \frac{I_\theta}{k_\theta} \omega^4, \quad (3.17)$$

which is recast using Taylor expansion as

$$\begin{aligned} \omega^2 = & \frac{kk_\theta + 4k_2^2 d^2}{mk_\theta} \epsilon^2 + \left(-\frac{1}{12} \frac{kk_\theta + 4k_2^2 d^2}{mk_\theta} + \frac{k_1 k_2 d^2}{mk_\theta} \right) \epsilon^4 - \frac{4kI_\theta + 4k_2 d^2 m}{mk_\theta} \epsilon^2 \omega^2 + \frac{I_\theta}{k_\theta} \omega^4 \\ & + \mathcal{O}\left(\left(\frac{\omega}{\omega_0}\right)^4 \hat{\epsilon}^2\right) + \mathcal{O}\left(\left(\frac{\omega}{\omega_0}\right)^2 \hat{\epsilon}^4\right) + \mathcal{O}(\hat{\epsilon}^6). \end{aligned} \quad (3.18)$$

The first comment arising from Eq. (3.18) is that contrary to Eq. (3.14), in addition to periodicity-induced dispersion, ϵ^4 also depends on dispersion resulting from stiffness coupling between rotations and axial displacements. Moreover, Eq. (3.18) possess additional dispersion terms ($\omega^2\kappa^2$ and ω^4) similar to those encountered in Eq. (3.3), which highlights the notion of coupling (ω^4 is non-Newtonian and results from the combination of two momentum equations). Finally, this model, as the previous one with transverse masses, provides dispersion equations for which physical mechanisms are identified without being quantified. In order to obtain numerical values of the mass and stiffness coefficients, the semi-analytical dispersion equation, derived from the Bloch theorem, is developed next.

3.3 Bloch theorem

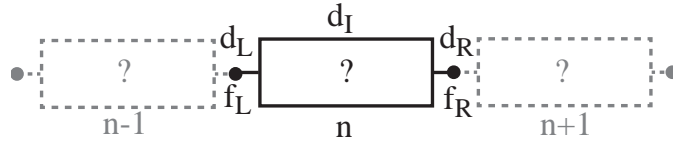


Figure 3.3: The unit cell in a periodic structure with end displacements and loads.

Linear wave propagation in periodic structures can be investigated through the analysis of a unit cell (Fig. 3.3) and the application of Bloch theorem [Phani et al., 2006, Spadoni et al., 2009, Brillouin, 1946]. The motion of a linear periodic domain resulting from uniaxial wave propagation may be expressed as follows:

$$\mathbf{d}_n = e^{-\mu n} \mathbf{d}_0, \quad (3.19)$$

where \mathbf{d}_n denotes the displacement vector (multiple displacement components are possible) of cell n within the periodic assembly, and \mathbf{d}_0 is the displacement vector within the reference cell. The propagation constant μ is a complex number ($\mu = \delta + i\epsilon$) where the real part and the imaginary part represent respectively the attenuation and phase constants ($i = \sqrt{-1}$). Given the periodicity, the propagation constant μ is equal to the wave number κ multiplied by the spatial period $2L_0$ (Fig. 3.4) such that $\mu = 2L_0\kappa$, $\delta = 2L_0\text{Re}(\kappa)$, and $\epsilon = 2L_0\text{Im}(\kappa)$. Eq. (3.19) however is only valid for linear fields, while interest is in wave propagation of finite amplitude in buckled structures. We proceed here to justify the conditions of Eq. (3.19).

The discretized equations of motion from finite elements (FE), given for the nodal displacement vector \mathbf{D} defined by $\mathbf{D} = \mathbf{D}_0 + \mathbf{d}$, with \mathbf{D}_0 the displacement at the equilibrium point (buckled configuration) are [Cook and Malkus, 2002]

$$\mathbf{M}(\mathbf{D})\ddot{\mathbf{D}} + \mathbf{K}(\mathbf{D})\mathbf{D} = \mathbf{F}. \quad (3.20)$$

\mathbf{M} and \mathbf{K} are respectively the mass and stiffness matrices of one unit cell, while \mathbf{F} is the

nodal-force vector. Eq. (3.20) can be linearized about the equilibrium \mathbf{D}_0 , leading to

$$\begin{aligned} \mathbf{K}(\mathbf{D})\mathbf{D} &\simeq \mathbf{K}(\mathbf{D}_0)\mathbf{D}_0 + \left. \frac{\partial \mathbf{K}(\mathbf{D})\mathbf{D}}{\partial \mathbf{D}} \right|_{\mathbf{D}_0} \mathbf{d} = \mathbf{K}(\mathbf{D}_0)\mathbf{D}_0 + \mathbf{K}_T(\mathbf{D}_0)\mathbf{d}, \\ \mathbf{M}(\mathbf{D}) &\simeq \mathbf{M}(\mathbf{D}_0), \end{aligned} \quad (3.21)$$

where

$$\mathbf{K}_T(\mathbf{D}_0) = \mathbf{K}(\mathbf{D}_0) + \mathbf{D}_0 \left. \frac{\partial \mathbf{K}(\mathbf{D})}{\partial \mathbf{D}} \right|_{\mathbf{D}_0}$$

is the tangent stiffness matrix. Substituting Eq. (3.21) into Eq. (3.20) and using the relation $\mathbf{F} = \mathbf{K}(\mathbf{D}_0)\mathbf{D}_0 + \mathbf{f}$ leads to the linearized governing equation which is only valid for small \mathbf{d} :

$$\mathbf{M}(\mathbf{D}_0)\ddot{\mathbf{d}} + \mathbf{K}_T(\mathbf{D}_0)\mathbf{d} = \mathbf{f}, \quad (3.22)$$

where \mathbf{d} and \mathbf{f} are the displacement and forces around the equilibrium defined by $\mathbf{d} = \{\mathbf{d}_L^T \mathbf{d}_I^T \mathbf{d}_R^T\}^T$ and $\mathbf{f} = \{\mathbf{f}_L^T \mathbf{f}_I^T \mathbf{f}_R^T\}^T$. The subscripts $(\)_L$, $(\)_I$ and $(\)_R$ respectively denote the left, internal and right displacements/forces of a unit cell. Assuming harmonic motion, Eq. (3.22) gives

$$\mathbf{D}(\omega)\mathbf{d} = \mathbf{f}, \quad (3.23)$$

where $\mathbf{D}(\omega) = \mathbf{K}_T(\mathbf{D}_0) - \omega^2\mathbf{M}(\mathbf{D}_0)$ is the dynamic stiffness matrix. For the sake of clarity, the subscript T in \mathbf{K}_T is going to be omitted next.

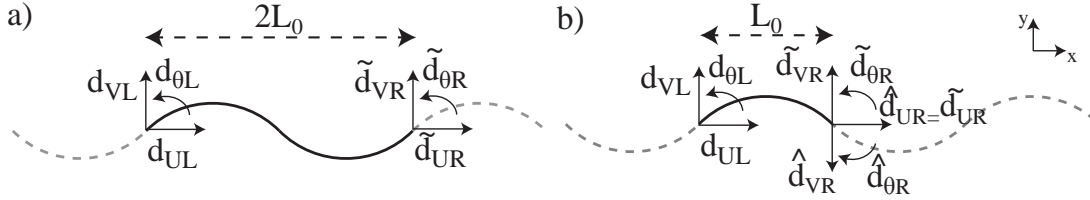


Figure 3.4: Unit cell in full line in terms of the classical Bloch theorem (a) and the reduced version taking into account glide reflection (b).

The unit cell showed in Fig. 3.4a reproduces the infinite structure by translation symmetry. The same unit cell however has intrinsic glide-reflection symmetry (axial-reflection coupled to translation). Glide-reflection can be exploited and the unit cell of Fig. 3.4b is used instead, where transverse displacement and rotation degrees of freedom (dof) of the right side are opposite to those of the left side. To differentiate the different variables defined for the half period and the full period, the superscripts $\hat{\ }$ and $\tilde{\ }$ denote the reduced and the full unit cell, respectively.

Using the full period (Fig. 3.4a) and imposing periodicity conditions on the generalized dis-

placement and equilibrium conditions on the generalized forces yields

$$\begin{Bmatrix} \mathbf{d}_L \\ \mathbf{f}_L \end{Bmatrix} = e^{-\tilde{\mu}} \begin{Bmatrix} \tilde{\mathbf{d}}_R \\ -\tilde{\mathbf{f}}_R \end{Bmatrix}, \quad (3.24)$$

where $\tilde{\mu} = 2L_0\text{Im}(\kappa)$. The equivalent relation for the half period (Fig. 3.4b) is

$$\begin{Bmatrix} \mathbf{d}_L \\ \mathbf{f}_L \end{Bmatrix} = e^{-\hat{\mu}} \begin{Bmatrix} \hat{\mathbf{d}}_R \\ -\hat{\mathbf{f}}_R \end{Bmatrix} = e^{-\hat{\mu}} \begin{bmatrix} R_x & \mathbf{0} \\ \mathbf{0} & R_x \end{bmatrix} \begin{Bmatrix} \tilde{\mathbf{d}}_R \\ -\tilde{\mathbf{f}}_R \end{Bmatrix}, \quad (3.25)$$

where $\mathbf{0}$ is the zero matrix, $\hat{\mu} = L_0\text{Im}(\kappa) = \tilde{\mu}/2$, and R_x is a orthogonal ($R_x^{-1} = R_x^T$) change of basis matrix from $\tilde{\mathbf{d}}_R$ to $\hat{\mathbf{d}}_R$ (Fig. 3.4b). Since our system is conservative and time-symmetric, Eq. (3.25) or its inverse is equivalent. For a structure corresponding to Fig. 3.4b with no supports, the change of basis is an axial reflection about x such that:

$$R_x = \begin{bmatrix} 1 & 0 & 0 \\ 0 & -1 & 0 \\ 0 & 0 & -1 \end{bmatrix}. \quad (3.26)$$

The modifications due the fact that the period used is half of the translational periodicity are explained in Sec. 3.3.3. Before proceeding further, the direct and inverse methods of the reduced Bloch theorem including the matrix R_x have to be introduced.

3.3.1 Direct method

Using Eq. (3.25), $\tilde{\mathbf{d}} = \{\mathbf{d}_L^T \mathbf{d}_I^T \tilde{\mathbf{d}}_R^T\}^T$ can be expressed in terms of a reduced displacement vector $\mathbf{d}^{(r)} = \{\mathbf{d}_L^T \mathbf{d}_I^T\}^T$:

$$\tilde{\mathbf{d}} = \hat{A} \mathbf{d}^{(r)}, \quad (3.27)$$

where

$$\hat{A} = \begin{bmatrix} I_n & \mathbf{0} \\ \mathbf{0} & I_p \\ R_x^T e^{\hat{\mu}} & \mathbf{0} \end{bmatrix}, \quad (3.28)$$

and I the identity matrix of size defined by subscripts; n is the number of dofs at one boundary and p is the number of internal dofs. Substituting Eq. (3.27) into Eq. (3.23) and multiplying both sides by \hat{A}^H where H denotes the conjugate transpose gives

$$\hat{D}^{(r)}(\omega, \hat{\mu}) \mathbf{d}^{(r)} = \mathbf{f}^{(r)}, \quad (3.29)$$

where $\hat{D}^{(r)}(\omega, \hat{\mu}) = \hat{A}^H \hat{D}(\omega) \hat{A}$, $\mathbf{f}^{(r)} = \hat{A}^H \tilde{\mathbf{f}}^{(r)}$, $\tilde{\mathbf{f}} = \{\mathbf{f}_L^T \mathbf{f}_I^T \tilde{\mathbf{f}}_R^T\}^T$, and $\mathbf{f}^{(r)} = \{\mathbf{f}_L^T \mathbf{f}_I^T\}^T$. In the case of a propagating wave without attenuation, $\hat{\mu} = i\hat{c}$ is purely imaginary and if no internal

forces exist ($\mathbf{f}_I = \mathbf{0}$),

$$\widehat{\mathbf{D}}^{(r)}(\omega, \widehat{\mu}) \mathbf{d}^{(r)} = \mathbf{0}. \quad (3.30)$$

Given the periodicity of the medium, $\widehat{\epsilon} = \text{Im}(\widehat{\mu}) \in [-\pi, \pi]$, and associated values of ω are found by solving the eigenvalue problem of Eq. (3.30).

3.3.2 Inverse method

Instead of fixing the wave number and looking for the associated frequency, one can fix the frequency and compute the propagation constant $\widehat{\mu}$ for 1D problems [Romeo and Paolone, 2007]. This technique has been extended to 2D problems for portions of the irreducible Brillouin zone [Spadoni et al., 2009], and more recently for the entire first Brillouin zone [Collet et al., 2011, Farzbod and Leamy, 2011]. With $\widehat{\mu}$ in hand, the propagation and attenuation constants are obtained. The inverse method is used as a starting point to develop semi-analytical dispersion relations.

Eq. (3.23) can be expanded as follows:

$$\begin{bmatrix} \widehat{\mathbf{D}}_{LL} & \widehat{\mathbf{D}}_{LI} & \widehat{\mathbf{D}}_{LR} \\ \widehat{\mathbf{D}}_{IL} & \widehat{\mathbf{D}}_{II} & \widehat{\mathbf{D}}_{IR} \\ \widehat{\mathbf{D}}_{RL} & \widehat{\mathbf{D}}_{RI} & \widehat{\mathbf{D}}_{RR} \end{bmatrix} \begin{Bmatrix} \mathbf{d}_L \\ \mathbf{d}_I \\ \tilde{\mathbf{d}}_R \end{Bmatrix} = \begin{Bmatrix} \mathbf{f}_L \\ \mathbf{f}_I \\ \tilde{\mathbf{f}}_R \end{Bmatrix}. \quad (3.31)$$

In absence of internal forces, Eq. (3.31) can be recast as a new reduced dynamic stiffness:

$$\widehat{\mathcal{D}}(\omega) \begin{Bmatrix} \mathbf{d}_L \\ \tilde{\mathbf{d}}_R \end{Bmatrix} = \begin{bmatrix} \widehat{\mathcal{D}}_{LL} & \widehat{\mathcal{D}}_{LR} \\ \widehat{\mathcal{D}}_{RL} & \widehat{\mathcal{D}}_{RR} \end{bmatrix} \begin{Bmatrix} \mathbf{d}_L \\ \tilde{\mathbf{d}}_R \end{Bmatrix} = \begin{Bmatrix} \mathbf{f}_L \\ \tilde{\mathbf{f}}_R \end{Bmatrix}, \quad (3.32)$$

with $(\{X, Y\} \in \{L, R\})$

$$\widehat{\mathcal{D}}_{XY} = \widehat{\mathbf{D}}_{XY} - \widehat{\mathbf{D}}_{XI} \widehat{\mathbf{D}}_{II}^{-1} \widehat{\mathbf{D}}_{IY}. \quad (3.33)$$

Eq. (3.32) can be rearranged to define a relation between opposite sides of the unit cell:

$$\begin{Bmatrix} \tilde{\mathbf{d}}_R \\ -\tilde{\mathbf{f}}_R \end{Bmatrix} = \widehat{T} \begin{Bmatrix} \mathbf{d}_L \\ \mathbf{f}_L \end{Bmatrix}, \quad (3.34)$$

where the transfer matrix \widehat{T} is

$$\widehat{T} = \begin{bmatrix} -\widehat{\mathcal{D}}_{LR}^{-1} \widehat{\mathcal{D}}_{LL} & \widehat{\mathcal{D}}_{LR}^{-1} \\ \widehat{\mathcal{D}}_{RR} \widehat{\mathcal{D}}_{LR}^{-1} \widehat{\mathcal{D}}_{LL} - \widehat{\mathcal{D}}_{RL} & -\widehat{\mathcal{D}}_{RR} \widehat{\mathcal{D}}_{LR}^{-1} \end{bmatrix}. \quad (3.35)$$

Combining Eqs. (3.25) and (3.34) gives

$$\left[[I_2 \otimes R_x] \widehat{T} - I_{2n} e^{\widehat{\mu}} \right] \begin{Bmatrix} \mathbf{d}_L \\ \mathbf{f}_L \end{Bmatrix} = \mathbf{0}, \quad (3.36)$$

where \otimes is the Kronecker product. Eq. (3.36) is an eigenvalue problem which gives $2n$ complex conjugate eigenvalues $e^{\hat{\epsilon}}$ corresponding to frequency ω .

3.3.3 Reduced Bloch method

Bloch theorem is applicable to systems with translational symmetry and allows analyzing a single unit cell, in our case the cell of Fig. 3.5a with periodicity $2L_0$. This unit cell however has internal glide-reflection symmetry, and can be further simplified as in Fig. 3.5b with period L_0 . This reduces computational cost and produces band structures that are easier to interpret. The phase constant for the full unit cell is $\tilde{\epsilon} = 2L_0 \text{Im}(\kappa)$, whereas when the period in the reduced Bloch theorem is L_0 , $\hat{\epsilon} = L_0 \text{Im}(\kappa)$. The period of the reduced cell in the wavenumber space is then π , while it is 2π for the full unit cell, as shown in Figs. 3.5c-d.

The band structure for the full unit cell (Fig. 3.5c) gives dispersion curves belonging to the interval $\tilde{\epsilon} = [-\pi \ \pi]$. However, $\tilde{\epsilon}$ is not restricted to this interval and the full dispersion is obtained by shifting the curves in full line by $2q\pi$ ($q \in \mathbb{N}$) resulting in the dashed lines in Fig. 3.5c [Brillouin, 1946]. Dashed lines however do not provide any additional information given the periodicity of the dispersion relations. In the dispersion from the reduced Bloch version (Fig. 3.5d), the interval is still $\hat{\epsilon} = [-\pi \ \pi]$ but the period is π . This means that when full lines are shifted by the period $q\pi$, new roots appear in the interval $\hat{\epsilon} = [-\pi \ \pi]$ (dashed line). Taking into account these new roots, one recovers the dispersion using the full periodicity (Fig. 3.5c) using $\hat{\epsilon} = \tilde{\epsilon}/2$. Analysis taking advantage of internal glide-reflection symmetries are referred next as the reduced Bloch method.

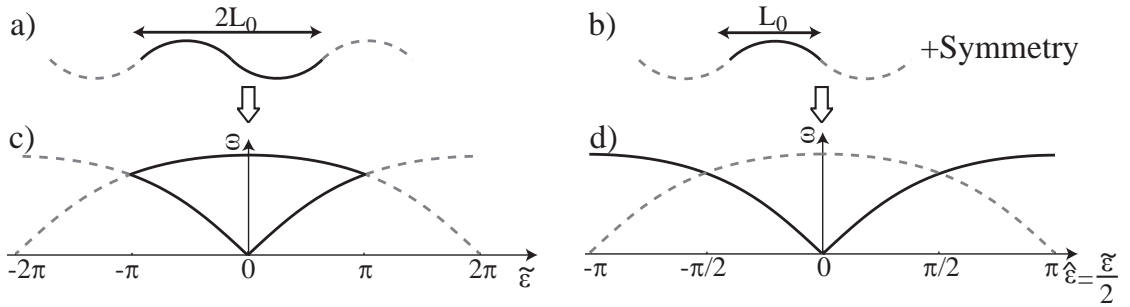


Figure 3.5: Repercussions of glide symmetry on dispersion relations. Full (a) and reduced (b) unit cells with respective band structures (c) and (d). Full lines denote the solution in the first Brillouin zone, while dashed lines denote solutions in the second Brillouin zone.

As a side note, but not presented in this manuscript, Bloch theorem has been generalized also to screw symmetric structures [Maurin, 2015] where the general proof is demonstrated. In addition to the aforementioned advantages, the revisited Bloch method is applicable to structures as the Boerdijk-Coxeter helix that does not possess purely-translational symmetries for which the classical method is not applicable.

3.4 Semi-analytical dispersion relations

The semi-analytical dispersion equation can be derived for both the classical and reduced Bloch theorem so for the sake of clarity, the notations $\langle \cdot \rangle$ and $\langle \cdot \rangle$ are omitted in this section.

The methods in Sec. 3.3 are easily evaluated with a FE discretization of a representative cell to obtain ω - κ curves, but no analytical equation is obtained. We intend to connect certain features of the band structure to specific deformation mechanisms and physical phenomena. In order to achieve this, the method proposed by Mead in [Mead, 1975a,b, Singh and Dhoopar, 1979] is extended to waves in beams with periodic boundary conditions (e.g. railway tracks). For straight beams, Mead employs analytical receptance functions of a single periodic element, explicitly expressed as a function of ω , which are used to link the nodal displacement to the nodal forces of the element extremities. The propagation constant is introduced using Eq. (3.25). However, in the present structure, the mass and the stiffness matrices are found only numerical, given the curvature are not constant. Noting that the receptance matrix is the inverse of the reduced dynamic stiffness matrix $\mathcal{D}(\omega)$ (Eq. (3.32)), the same method can be used, except that in our case, the coefficients \mathcal{D}_{XY} do not contain ω explicitly.

By linearizing receptance-function components \mathcal{D}_{XY} (Eq. (3.33)), one can obtain explicit expressions in terms of ω . For low frequency, one can write:

$$\mathcal{D}_{II}^{-1} = (\mathbf{K}_{II} - \omega^2 \mathbf{M}_{II})^{-1} \simeq \mathbf{K}_{II}^{-1} + \omega^2 \mathbf{K}_{II}^{-1} \mathbf{M}_{II} \mathbf{K}_{II}^{-1}. \quad (3.37)$$

Then using a lumped mass matrix ($\mathbf{M}_{XY} = \mathbf{0}$ if $X \neq Y$), the coefficients of $\mathcal{D}(\omega)$ from Eq. (3.33) are expressed explicitly in terms of ω as:

$$\mathcal{D}_{XY} \simeq \mathcal{K}_{XY} - \omega^2 \mathcal{M}_{XY}. \quad (3.38)$$

The effective stiffness \mathcal{K}_{XY} and mass \mathcal{M}_{XY} matrix components are defined by:

$$\begin{aligned} \mathcal{K}_{XY} &= \mathbf{K}_{XY} - \mathbf{K}_{XI} \mathbf{K}_{II}^{-1} \mathbf{K}_{IY}, \\ \mathcal{M}_{XY} &= \mathbf{M}_{XY} + \mathbf{K}_{XI} \mathbf{K}_{II}^{-1} \mathbf{M}_{II} \mathbf{K}_{II}^{-1} \mathbf{K}_{IY}. \end{aligned} \quad (3.39)$$

Substituting Eq. (3.25) into Eq. (3.32) and given that R_x is orthogonal gives

$$\begin{bmatrix} \mathcal{D}_{LL} & \mathcal{D}_{LR} \\ \mathcal{D}_{RL} & \mathcal{D}_{RR} \end{bmatrix} \begin{Bmatrix} \mathbf{d}_L \\ e^{\mu} R_x^T \mathbf{d}_L \end{Bmatrix} = \begin{Bmatrix} \mathbf{f}_L \\ -e^{\mu} R_x^T \mathbf{f}_L \end{Bmatrix}. \quad (3.40)$$

Finally, the solution of this system is

$$\det [\mathcal{D}_{LL} + R_x \mathcal{D}_{RR} R_x^T + e^{\mu} \mathcal{D}_{LR} R_x^T + e^{-\mu} R_x \mathcal{D}_{RL}] = 0. \quad (3.41)$$

Plugging Eq. (3.38) into Eq. (3.41), the semi-analytical dispersion relation is found by comput-

ing the determinant of this new $n \times n$ matrix. The following expression is obtained:

$$\sum_{i=0}^n \sum_{j=-n}^n c_{i,j} \omega^{2i} e^{\mu j} = 0, \quad (3.42)$$

where $c_{i,j}$ are numerical coefficients given by the components of the stiffness and mass matrix only. Since the propagation of linear-elastic waves in periodic structures is symmetric in the wave number argument, the dispersion relation Eq. (3.42) has to be invariant with respect to $\pm\mu$ leading to the equality $c_{i,j} = c_{i,-j}$. Note also that $c_{0,0} = 0$ if the beam is not supported on elastic foundations (i.e. $\omega \rightarrow 0$ as $\epsilon \rightarrow 0$). The term semi-analytical is employed here to indicate that μ and ω are related explicitly, but the coefficients $c_{i,j}$ are numerical. An important remark is that the semi-analytical solution only approximates the acoustic branch of the dispersion relation and is not valid for optical branches. This is because Eq. (3.37) assumes small frequencies. This method can be used for any 1D periodic structure as long as the number of boundary dofs is small.

3.4.1 Semi-analytical relations including transverse-reflection symmetry

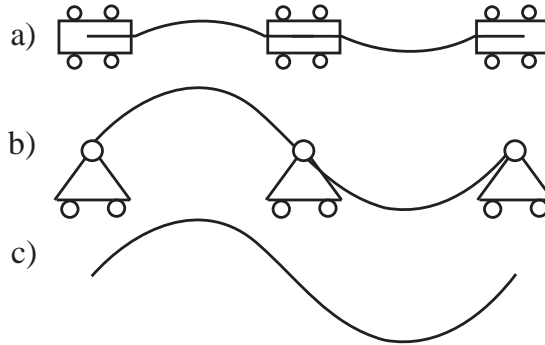


Figure 3.6: Shape of the beam after buckling with guided (a), pinned (b) and free (no) (c) supports. Geometry of the beam with pinned and free supports is identical although the configuration without supports is unstressed.

Semi-analytical dispersion relations can be further simplified using the fact that the reduced cell also possesses reflection symmetry about y , as shown in Fig. 3.7. Therefore, the left and right terms of the stiffness and mass matrices are linked by the following relations:

$$\begin{aligned} \widehat{\mathbf{K}}_{LL} &= R_y^T \widehat{\mathbf{K}}_{RR} R_y, \\ \widehat{\mathbf{K}}_{LR} &= R_y^T \widehat{\mathbf{K}}_{RL} R_y, \\ \widehat{\mathbf{K}}_{LI} &= R_y^T \widehat{\mathbf{K}}_{RI}, \\ \widehat{\mathbf{K}}_{IL} &= \widehat{\mathbf{K}}_{IR} R_y, \\ \widehat{\mathbf{M}}_{LL} &= R_y^T \widehat{\mathbf{M}}_{RR} R_y. \end{aligned} \quad (3.43)$$

The reflection matrix R_y about y is given by

$$R_y = \begin{bmatrix} -1 & 0 & 0 \\ 0 & 1 & 0 \\ 0 & 0 & -1 \end{bmatrix}. \quad (3.44)$$

Plugging Eq. (3.43) into Eq. (3.38) leads to

$$\begin{aligned} \widehat{\mathcal{D}}_{LL} &= R_y^T \widehat{\mathcal{D}}_{RR} R_y, \\ \widehat{\mathcal{D}}_{LR} &= R_y^T \widehat{\mathcal{D}}_{LR} R_y. \end{aligned} \quad (3.45)$$



Figure 3.7: Additional symmetries of buckled beams: the half period possesses a reflection in the y direction also.

For guided ($n = 1, d_U$), pinned ($n = 2, d_U, d_\theta$) and free supports ($n = 3, d_U, d_V, d_\theta$) (Figs. 3.6 and 3.4), Eq. (3.42) is developed using Eq. (3.45). In order to further simplify Eq. (3.42), attenuation is neglected, that is $\widehat{\delta} = 0$. The semi-analytical equations for each kind of support are shown below.

Guided supports

$$\widehat{\mathcal{D}}_{LR} \cos \epsilon + \widehat{\mathcal{D}}_{LL} = 0. \quad (3.46)$$

Pin supports

$$\begin{aligned} &(\widehat{\mathcal{D}}_{LR12}^2 - \widehat{\mathcal{D}}_{LR11} \widehat{\mathcal{D}}_{LR22}) \cos^2 \epsilon + \\ &(\widehat{\mathcal{D}}_{LR11} \widehat{\mathcal{D}}_{LL22} - \widehat{\mathcal{D}}_{LR22} \widehat{\mathcal{D}}_{LL11}) \cos \epsilon + \\ &(\widehat{\mathcal{D}}_{LL11} \widehat{\mathcal{D}}_{LL22} - \widehat{\mathcal{D}}_{LR12}^2) = 0, \end{aligned} \quad (3.47)$$

where the notation \mathcal{D}_{XYij} is the abbreviation for $\mathcal{D}_{XY}(i, j)$ ($i \in \{1, \dots, n\}, j \in \{1, \dots, n\}$).

Free supports

$$A_0(\omega) + A_1(\omega) \cos \epsilon + A_2(\omega) \cos^2 \epsilon + A_3(\omega) \cos^3 \epsilon, \quad (3.48)$$

where:

$$\begin{aligned}
 A_0(\omega) &= \widehat{\mathcal{D}}_{LL11}\widehat{\mathcal{D}}_{LL22}\widehat{\mathcal{D}}_{LL33} + 2\widehat{\mathcal{D}}_{LL12}\widehat{\mathcal{D}}_{LR13}\widehat{\mathcal{D}}_{LR23} \\
 &\quad - \widehat{\mathcal{D}}_{LL11}\widehat{\mathcal{D}}_{LR23}^2 - \widehat{\mathcal{D}}_{LL33}\widehat{\mathcal{D}}_{LL12}^2 - \widehat{\mathcal{D}}_{LL22}\widehat{\mathcal{D}}_{LR13}^2, \\
 A_1(\omega) &= -\widehat{\mathcal{D}}_{LL11}\widehat{\mathcal{D}}_{LL22}\widehat{\mathcal{D}}_{LR33} - \widehat{\mathcal{D}}_{LL11}\widehat{\mathcal{D}}_{LL33}\widehat{\mathcal{D}}_{LR22} + \widehat{\mathcal{D}}_{LL22}\widehat{\mathcal{D}}_{LL33}\widehat{\mathcal{D}}_{LR11} \\
 &\quad + \widehat{\mathcal{D}}_{LR33}\widehat{\mathcal{D}}_{LL12}^2 - \widehat{\mathcal{D}}_{LR11}\widehat{\mathcal{D}}_{LR23}^2 + \widehat{\mathcal{D}}_{LR22}\widehat{\mathcal{D}}_{LR13}^2 \\
 &\quad + 2\widehat{\mathcal{D}}_{LR12}(\widehat{\mathcal{D}}_{LL12}\widehat{\mathcal{D}}_{LL33} - \widehat{\mathcal{D}}_{LR13}\widehat{\mathcal{D}}_{LR23}), \\
 A_2(\omega) &= \widehat{\mathcal{D}}_{LL11}(\widehat{\mathcal{D}}_{LR22}\widehat{\mathcal{D}}_{LR33} + \widehat{\mathcal{D}}_{LR23}^2) - \widehat{\mathcal{D}}_{LL22}(\widehat{\mathcal{D}}_{LR11}\widehat{\mathcal{D}}_{LR33} - \widehat{\mathcal{D}}_{LR13}^2) \\
 &\quad - \widehat{\mathcal{D}}_{LL33}(\widehat{\mathcal{D}}_{LR11}\widehat{\mathcal{D}}_{LR22} + \widehat{\mathcal{D}}_{LR12}^2) - 2\widehat{\mathcal{D}}_{LL12}(\widehat{\mathcal{D}}_{LR12}\widehat{\mathcal{D}}_{LR33} + \widehat{\mathcal{D}}_{LR13}\widehat{\mathcal{D}}_{LR23}), \\
 A_3(\omega) &= \widehat{\mathcal{D}}_{LR11}\widehat{\mathcal{D}}_{LR22}\widehat{\mathcal{D}}_{LR33} + 2\widehat{\mathcal{D}}_{LR12}\widehat{\mathcal{D}}_{LR13}\widehat{\mathcal{D}}_{LR23} \\
 &\quad + \widehat{\mathcal{D}}_{LR11}\widehat{\mathcal{D}}_{LR23}^2 + \widehat{\mathcal{D}}_{LR33}\widehat{\mathcal{D}}_{LR12}^2 - \widehat{\mathcal{D}}_{LR22}\widehat{\mathcal{D}}_{LR13}^2.
 \end{aligned}$$

Note that if one uses the full translational period as the unit cell, equivalent equations can be derived replacing Eq. (3.43) by $\widetilde{\mathcal{K}}_{LL} = R_x^T R_y^T \widetilde{\mathcal{K}}_{RR} R_y R_x$, $\widetilde{\mathcal{K}}_{LR} = R_x^T R_y^T \widetilde{\mathcal{K}}_{RL} R_y R_x$, $\widetilde{\mathcal{K}}_{LI} = R_x^T R_y^T \widetilde{\mathcal{K}}_{RI}$, $\widetilde{\mathcal{K}}_{IL} = \widetilde{\mathcal{K}}_{IR} R_y R_x$, and $\widetilde{\mathcal{M}}_{LL} = R_x^T R_y^T \widetilde{\mathcal{M}}_{RR} R_y R_x$.

3.4.2 Polynomial expression of the semi-analytical equation

Assuming small phase constant, Eqs. (3.42), (3.46), (3.47) or (3.48) can be expanded in Taylor series up to order ϵ^{2m} , and rewritten as a polynomial:

$$\sum_{i=0}^n \sum_{j=0}^m \bar{a}_{2i,2j} \omega^{2i} \epsilon^{2j} + \mathcal{O}(\epsilon^{2m+1}) = 0, \quad (3.49)$$

In the present case, $\bar{a}_{00} = 0$ ($\mathcal{K}_{LR11} = -\mathcal{K}_{LL11}$ since there is no elastic foundation). Defining ω_0 by

$$\omega_0 = \frac{C_0}{L_0}, \quad (3.50)$$

it is possible to further simplify Eq. (3.49):

$$\left(\frac{\omega}{\omega_0}\right)^2 = \sum_{i=2}^n \left(a_{2i,0} \left(\frac{\omega}{\omega_0}\right)^{2i} \right) + \sum_{i=0}^n \sum_{j=1}^m \left(a_{2i,2j} \left(\frac{\omega}{\omega_0}\right)^{2i} \epsilon^{2j} \right) + \mathcal{O}(\epsilon^{2m+1}), \quad (3.51)$$

with

$$a_{2i,2j} = -\frac{\omega_0^{2i-2}}{\bar{a}_{2,0}} \bar{a}_{2i,2j}. \quad (3.52)$$

Eq. (3.51) now has explicit terms in ω and ϵ , and it is particularly useful to analyze the physical meaning of coefficients $a_{2i,2j}$ as done next for the guided and pinned-support case.

3.4.3 Semi-analytical dispersion equation of buckled beams

Guided supports

Substituting the coefficients of Eq. (3.38) into Eq. (3.46), and using trigonometric identities gives

$$\omega^2 = \frac{\widehat{\mathcal{K}}_{LL11} + \widehat{\mathcal{K}}_{LR11}}{\widehat{\mathcal{M}}_{Tot11}} - 2 \frac{\widehat{\mathcal{K}}_{LR11}}{\widehat{\mathcal{M}}_{Tot11}} \sin^2\left(\frac{\widehat{\epsilon}}{2}\right) + \frac{2\widehat{\mathcal{M}}_{LR11}}{\widehat{\mathcal{M}}_{Tot11}} \omega^2 \sin^2\left(\frac{\widehat{\epsilon}}{2}\right), \quad (3.53)$$

which can be recast using the equality $\widehat{\mathcal{K}}_{LL11} = -\widehat{\mathcal{K}}_{LR11}$ (unit cell not linked to the ground)

$$\omega^2 = \frac{\widehat{\mathcal{K}}_{Tot11}}{\widehat{\mathcal{M}}_{Tot11}} \sin^2\left(\frac{\widehat{\epsilon}}{2}\right) + \frac{2\widehat{\mathcal{M}}_{LR11}}{\widehat{\mathcal{M}}_{Tot11}} \omega^2 \sin^2\left(\frac{\widehat{\epsilon}}{2}\right), \quad (3.54)$$

where $\widehat{\mathcal{K}}_{Tot11} = 2\widehat{\mathcal{K}}_{LL11}$ and $\widehat{\mathcal{M}}_{Tot11} = \widehat{\mathcal{M}}_{LL11} + \widehat{\mathcal{M}}_{LR11}$. Note that this equation is similar to Eq. (3.13) describing wave dispersion in a mass-spring system accounting for transverse-inertial effects (Fig. 3.2b). Actually it can be used to find the numerical values of the spring stiffness and the two masses using the relation $\widehat{\mathcal{K}}_{LL11} = 2k$, $\widehat{\mathcal{M}}_{LL11} = m_1 + (1 + \alpha)m_2/2$ and $\widehat{\mathcal{M}}_{LR11} = (1 - \alpha)m_2/2$. Eq. (3.54) can also be recast in the form of Eq. (3.51) using Taylor expansion:

$$\left(\frac{\omega}{\omega_0}\right)^2 = a_{0,2}\widehat{\epsilon}^2 + a_{0,4}\widehat{\epsilon}^4 + a_{2,2}\left(\frac{\omega}{\omega_0}\right)^2 \widehat{\epsilon}^2 + \mathcal{O}\left(\left(\frac{\omega}{\omega_0}\right)^2 \widehat{\epsilon}^4\right) + \mathcal{O}(\widehat{\epsilon}^6), \quad (3.55)$$

with the non-dimensional terms $a_{0,2} = \frac{\widehat{\mathcal{K}}_{Tot11}}{4\omega_0^2 \widehat{\mathcal{M}}_{Tot11}} = 1$, $a_{0,4} = -\frac{1}{12}a_{0,2} = -\frac{1}{12}$, and $a_{2,2} = \frac{\widehat{\mathcal{M}}_{LR11}}{2\widehat{\mathcal{M}}_{Tot11}}$. From the analogy with the mass-spring system, the terms $a_{0,4}$ and $a_{2,2}$ describe dispersion due to periodicity and transverse-inertial effects, respectively. As a side note, $a_{2,2}$ is equivalent to the rotary-inertia term in the Rayleigh-beam formulation [Ghosh, 1984].

Pinned supports

Plugging the coefficients of Eq. (3.38) into Eq. (3.47) and using the equality $\widehat{\mathcal{K}}_{LL11} = -\widehat{\mathcal{K}}_{LR11}$, Eq. (3.47) reads

$$\begin{aligned} \omega^2 = & \left(\frac{\widehat{\mathcal{K}}_{Tot11}}{\widehat{\mathcal{M}}_{Tot11}} - \frac{4\widehat{\mathcal{K}}_{LR12}^2}{\widehat{\mathcal{M}}_{Tot11}\widehat{\mathcal{K}}_{Tot22}} \right) \sin^2\left(\frac{\widehat{\epsilon}}{2}\right) + 4 \frac{\widehat{\mathcal{K}}_{LL11}\widehat{\mathcal{K}}_{LR22} + \widehat{\mathcal{K}}_{LR12}^2}{\widehat{\mathcal{M}}_{Tot11}\widehat{\mathcal{K}}_{Tot22}} \sin^4\left(\frac{\widehat{\epsilon}}{2}\right) \\ & + \left(\frac{2\widehat{\mathcal{M}}_{LR11}}{\widehat{\mathcal{M}}_{Tot11}} - \frac{2\widehat{\mathcal{K}}_{LR22}}{\widehat{\mathcal{K}}_{Tot22}} + \frac{8\widehat{\mathcal{K}}_{LR12}\widehat{\mathcal{M}}_{LR12} - \widehat{\mathcal{K}}_{Tot11}\widehat{\mathcal{M}}_{Tot22}}{\widehat{\mathcal{M}}_{Tot11}\widehat{\mathcal{K}}_{Tot22}} \right) \omega^2 \sin^2\left(\frac{\widehat{\epsilon}}{2}\right) \\ & + \frac{\widehat{\mathcal{M}}_{Tot22}}{\widehat{\mathcal{K}}_{Tot22}} \omega^4 + \mathcal{O}\left(\left(\frac{\omega}{\omega_0}\right)^4 \widehat{\epsilon}^2\right) + \mathcal{O}\left(\left(\frac{\omega}{\omega_0}\right)^2 \widehat{\epsilon}^4\right) + \mathcal{O}(\widehat{\epsilon}^6), \end{aligned} \quad (3.56)$$

where $\widehat{\mathcal{K}}_{Tot11} = 2\widehat{\mathcal{K}}_{LL11}$, $\widehat{\mathcal{M}}_{Tot11} = \widehat{\mathcal{M}}_{LL11} + \widehat{\mathcal{M}}_{LR11}$, $\widehat{\mathcal{K}}_{Tot22} = \widehat{\mathcal{K}}_{LL22} - \widehat{\mathcal{K}}_{LR22}$ and $\widehat{\mathcal{M}}_{Tot22} = \widehat{\mathcal{M}}_{LL22} - \widehat{\mathcal{M}}_{LR22}$. Note that neglecting the transverse-inertial effects ($\widehat{\mathcal{M}}_{LR11} = \widehat{\mathcal{M}}_{LR22} = 0$),

Eq. (3.56) turns out to be equivalent to Eq. (3.17) using the equalities $\widehat{\mathcal{K}}_{LL11} = 2(k_1 + k_2)$, $\widehat{\mathcal{K}}_{LR12} = 2k_2 d$, $\widehat{\mathcal{K}}_{LR22} = 2k_2 d^2$, $\widehat{\mathcal{K}}_{LL22} = k_\theta + 2k_2 d^2$, $\widehat{\mathcal{M}}_{Tot11} = m$, and $\widehat{\mathcal{M}}_{Tot22} = I_\theta$. Similarly to the guided-support case, the semi-analytical dispersion equation can be used to find the mass and stiffness values of the mass-spring problem of Fig. 3.2c. Conversely, Fig. 3.2c can be used to describe the physical mechanisms of the semi-analytical dispersion equation coefficients. Eq. (3.56) can be also recast in the form of Eq. (3.51) using Taylor series with the first coefficients $a_{2i,2j}$ ($\{i, j\} \in \mathbb{N}$) given by

$$\begin{aligned}
 a_{0,2} &= \frac{1}{\omega_0^2} \left(\frac{\widehat{\mathcal{K}}_{Tot11}}{4\widehat{\mathcal{M}}_{Tot11}} - \frac{\widehat{\mathcal{K}}_{LR12}^2}{\widehat{\mathcal{M}}_{Tot11}\widehat{\mathcal{K}}_{Tot22}} \right) = 1, \\
 a_{0,4} &= -\frac{1}{12} a_{0,2} + \frac{\widehat{\mathcal{K}}_{LL11}\widehat{\mathcal{K}}_{LR22} + \widehat{\mathcal{K}}_{LR12}^2}{4\omega_0^2\widehat{\mathcal{M}}_{Tot11}\widehat{\mathcal{K}}_{Tot22}} = -\frac{1}{12} + \frac{\widehat{\mathcal{K}}_{LL11}\widehat{\mathcal{K}}_{LR22} + \widehat{\mathcal{K}}_{LR12}^2}{\widehat{\mathcal{K}}_{Tot11}\widehat{\mathcal{K}}_{Tot22} - 4\widehat{\mathcal{K}}_{LR12}^2}, \\
 a_{2,2} &= \frac{\widehat{\mathcal{M}}_{LR11}}{2\widehat{\mathcal{M}}_{Tot11}} - \frac{\widehat{\mathcal{K}}_{LR22}}{2\widehat{\mathcal{K}}_{Tot22}} + \frac{8\widehat{\mathcal{K}}_{LR12}\widehat{\mathcal{M}}_{LR12} - \widehat{\mathcal{K}}_{Tot11}\widehat{\mathcal{M}}_{Tot22}}{4\widehat{\mathcal{M}}_{Tot11}\widehat{\mathcal{K}}_{Tot22}}, \\
 a_{4,0} &= \frac{\widehat{\mathcal{M}}_{Tot22}}{\widehat{\mathcal{K}}_{Tot22}} \omega_0^2 = \frac{\widehat{\mathcal{M}}_{Tot22}}{\widehat{\mathcal{M}}_{Tot11}} \left(\frac{\widehat{\mathcal{K}}_{Tot11}}{4\widehat{\mathcal{K}}_{Tot22}} - \frac{\widehat{\mathcal{K}}_{LR12}^2}{\widehat{\mathcal{K}}_{Tot22}^2} \right).
 \end{aligned} \tag{3.57}$$

As done for the guided and pinned-support configurations, Eq. (3.48) modeling dispersion in the free-support beam can be also recast in terms of a Taylor expansion. However, the resulting series is much more complex to analyze and restriction is made in the next part to qualitative observations. The free-support configuration is anyway unstable and is only going to be used to show the influence of the supports on dispersion curves.

3.5 Dispersion of buckled beams

In Chapter 2, it is shown that buckled deformations normalized by the critical load are parametrized only in terms of the slenderness parameter λ and the initial imperfection w_0 . Moreover, if $1/\lambda$ and w_0 are sufficiently small, the buckling behavior is only changed for small pre-compression levels ($\chi_0 = \Delta U_0/L < 0.1$), and in order to remain within this assumption, as the previous chapter, $\lambda = 520$ and $w_0 = 10^{-3}$.

While this normalization holds for the load-displacement relation, the same procedure can be applied to the linear speed C_0 . Indeed, from the semi-analytical dispersion equation (Eqs. (3.54) and (3.56)), the linear speed is defined by

$$C_{0,G}^2 = \frac{\widehat{\mathcal{K}}_{Tot11}}{4\widehat{\mathcal{M}}_{Tot11}} L_0^2 \quad \text{and} \quad C_{0,P}^2 = \left(\frac{\widehat{\mathcal{K}}_{Tot11}}{4\widehat{\mathcal{M}}_{Tot11}} - \frac{\widehat{\mathcal{K}}_{LR12}^2}{\widehat{\mathcal{M}}_{Tot11}\widehat{\mathcal{K}}_{Tot22}} \right) L_0^2, \tag{3.58}$$

for respectively guided and pinned supports, and each effective stiffness term is proportional to the first derivative of $P\{\Delta U\}$. Defining the normalizing linear speed C'_0 using Eq. (3.6) with

$P\{\Delta U\}$ derived from elastica (Eq. (2.30)), one reads

$$C_0'^2 = C_0^2 \{\Delta U_0\} \Big|_{\Delta U_0 \rightarrow 0} = \frac{P' \{\Delta U_0\} L_0^2}{m} \Big|_{\Delta U_0 \rightarrow 0} = \frac{1}{2} \frac{EI_z \pi^2}{\rho A L_{eff}^2}, \quad (3.59)$$

where $L_{eff} = L$ and $L_{eff} = L/2$, respectively in the case of the pinned and guided supports (Eq. (2.44)). L and L_0 are respectively the distance between two constitutive supports before and after applying the pre-compression.

The normalized linear speed is plotted in Fig. 3.8 and is found identical whatever the support configuration, in agreement with self-similarities between these two geometries (Fig. 2.8c). The linear speed is found decreased when pre-compression increases, with an important change in the curvature for $\chi_0 \approx 0.02$. Indeed, for this compression level, the initial imperfection creates a smooth but fast transition between axial and bending deformations, for which different mechanisms and so wave speeds operate. This explains why C_0 does not converge to C_0' when $\chi_0 \rightarrow 0$.

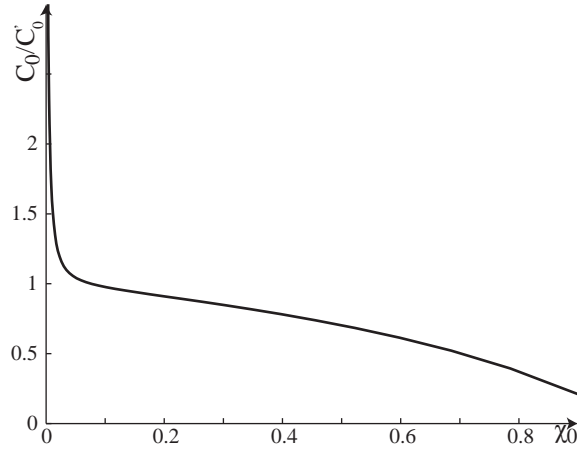


Figure 3.8: Normalized long-wavelength linear velocity C_0 in terms of the pre-compression χ_0 , and valid for both support types.

The power of Fig. 3.8 is that it is valid whatever the support configuration, material property and cross-section profile, as long as initial imperfections and the inverse of the slenderness of the beam remain small, or the pre-compression is large. Moreover, from the equality $C_{0,G}/C_{0,G}' = C_{0,P}/C_{0,P}'$, one get $C_{0,P} = C_{0,G}/2$. While this is true for the linear speed, it is shown next that the dispersion depends on the support type, even when normalized by

$$\omega_0' = \frac{C_0'}{L}. \quad (3.60)$$

3.5.1 Dispersion relation from Bloch theorem

While the goal of this thesis is to investigate nonlinear waves of finite amplitude, linearized analysis of the dispersion is justified *a-posteriori* by comparisons to results of a 2D, discrete Fourier transform. The dispersion is evaluated numerically with the *Matlab* function *FFT2* applied to the nodal displacement history recorded from numerical nonlinear FE simulations, resulting from impulsive boundary (see Chapter 4 for the FE model).

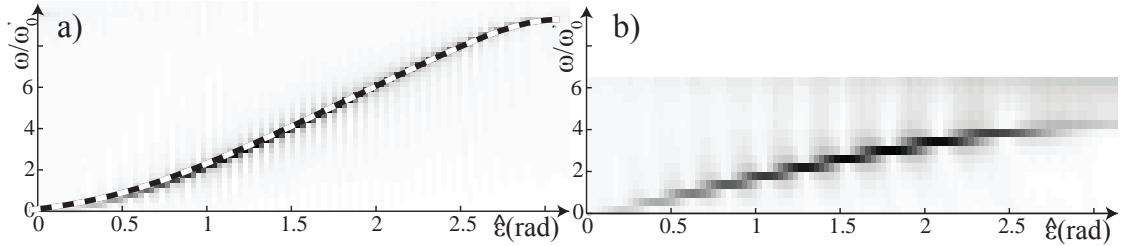


Figure 3.9: Dispersion relation for two different configurations with pinned supports: (a) pre-compression level is $\chi_0 = 0.1$, (b) unstressed configuration with identical geometry as a buckled beam with $\chi_0 = 0.8$ ($\chi_0 = U_0/L$). Linearized dispersion relation computed with the reduced Bloch method (Sec. 3.3.3) in white-dashed lines, and via 2D, discrete Fourier transform of the nodal displacement history recorded from FE simulations in grayscale.

Numerical dispersion relations obtained from the reduced Bloch method are superposed to the amplitude spectrum showing excellent agreement (Fig. 3.9). This justifies the analyses proposed in this chapter whereby dispersion is described by linearized models. Note that for Fig. 3.9 and all the figures that follow, the dispersion is reported for the wavenumber space as shown in Fig. 3.5d and frequency normalized by Eq. (3.60).

Influence of support type on dispersion

Dispersion relations for unstressed buckled beams with the three-support types (Fig. 3.6) are given in Fig. 3.10. By unstressed, the beam is considered buckled until the desire level of compression is reached, and then, the final geometry is modeled with new unstressed elements. This procedure has the advantage to decouple the effects of prestress and curvature, as it will be shown next, while in the present case, it allows the obtaining of dispersion curves from the free-support configuration, which is originally unstable.

In the guided-support case (Fig. 3.10a), the phase velocity decreases with frequency. This tendency is similar to the periodicity effects, but when compared to the equation describing dispersion due to periodicity alone (Eq. (3.7)), the two models agree only at low frequencies. Indeed, as shown in the semi-analytical dispersion equation (Eq. (3.54)), Eq. (3.7) does not account for transverse-inertial effects and explains this difference. For the pinned-support configuration, dispersion curves show that the phase velocity increases with frequency, a characteristic of bending waves. However, as it will be discussed in Sec. 3.5.3, the analyze of the wavemodes indicates that bending waves cannot propagate in the presence of the

supports. In the free-support case, two propagation constants $\hat{\epsilon}$ exist for a given frequency in the acoustic branch. Low values of $\hat{\epsilon}$ are well described by periodicity effects, while for values near π , dispersion is due to bending. Moreover, the second branch matches Eq. (3.1) which is derived for a straight beam and this is explained by the fact that in Fig. 3.10, pre-compression is small. Note that these results are similar to the one obtained in [Trainiti et al., 2015] where free-supported undulated beam are investigated. Finally, note from Fig. 3.10 that classical axial waves with constant phase velocity are not found, and it can be explained by the presence of dispersion induced by the curvature.

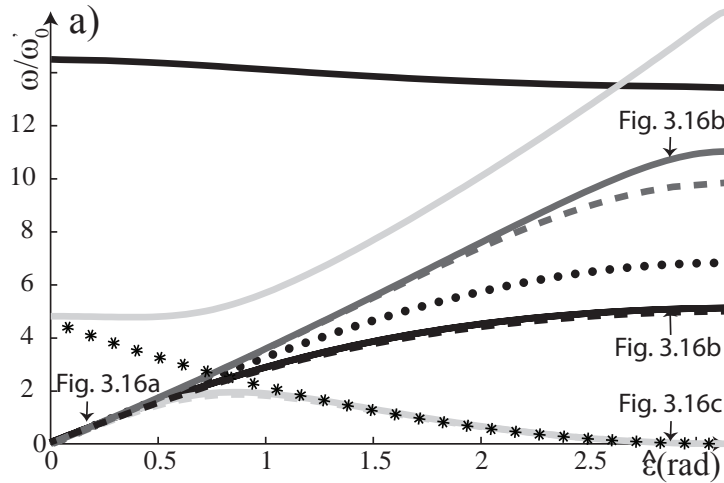


Figure 3.10: Influence of the support type on dispersion relations for guided (dark), pinned (dark gray), and free (light gray) supports, and for pre-compression $\chi_0 = 0.1$ which is then unstressed. Direct reduced-Bloch-theorem dispersion in solid lines, semi-analytical dispersion in dashed lines (Eqs. (3.46), (3.47), and (3.48)), periodicity-induced dispersion (Eq. (3.7)) in dotted line, and bending-induced dispersion (Eq. (3.1)) in star line.

Influence of internal stress on dispersion

To show the influence of the stress independently of the curvature, unstressed and stressed dispersion relations are shown in Fig. 3.11 for the case of the guided and pinned supports (free-support configuration not shown since unstable if stressed). It is found that increasing prestress decreases the phase speed, which is a softening effect, in agreement with the results reported in [Bigoni et al., 2008, Gei et al., 2009].

Influence of dissipation on dispersion and evanescent modes

So far, only dispersion relations obtained with the direct method ($\hat{\delta} = 0$) are discussed. However, additional evanescent modes ($\hat{\delta} \neq 0$) exist and are investigated using the inverse method.

In Fig. 3.12, the phase and attenuation constants are given for the stressed configurations, limiting the analyze to guided and pinned supports. In the guided-support case (Fig. 3.12a-b),

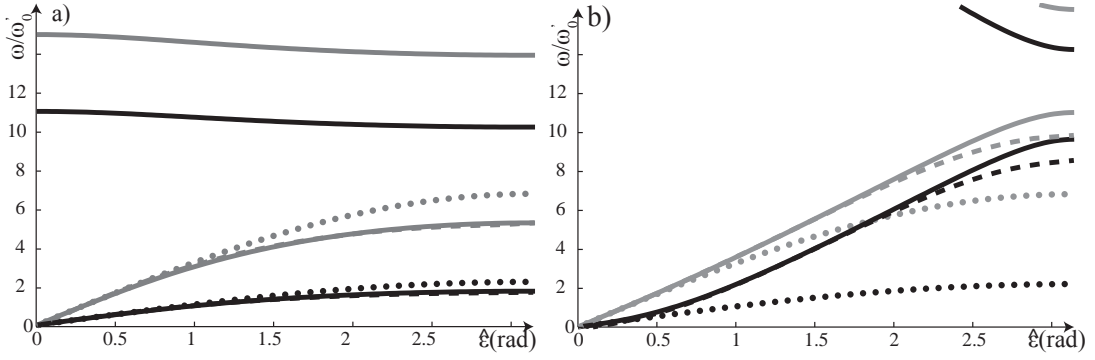


Figure 3.11: Influence of internal stress on dispersion relations for guided (a) and pinned (b) supports, and for pre-compression level $\chi_0 = 0.1$ (black) which is then unstressed (gray). Direct reduced-Bloch-theorem dispersion in solid lines, semi-analytical dispersion in dashed lines (Eqs. (3.46) and (3.47)), and periodicity-induced dispersion (Eq. (3.7)) in dotted lines.

all wavemodes belonging to the acoustic branch are not attenuated ($\widehat{\delta} = 0$) under the first band gap ($\omega/\omega'_0 \approx 2$). Then, for each band gap, an evanescent mode is present. In the pinned-support case, both propagating and evanescent modes are present at low frequency, whereas the two propagating modes are evanescent inside the band gaps (Fig. 3.12c-d).

The power of the inverse method of the Bloch theorem is that dissipation can be accounted for, simply by updating the dynamic stiffness matrix (Eq. (3.23)) with $D(\omega) = K + i\omega C - \omega^2 M$, where C is the damping matrix. In the present case, C models axial frictions of the supports, such that C is the zero matrix except for $C_{LL11} = C_{RR11} = \mu$, where μ is the coefficient of friction arbitrary chosen as $\mu = 0.5$. As shown with the gray lines of Fig. 3.12, dissipation has for effect to convert both non-attenuated and evanescent modes in hybrid, attenuated modes, meaning that the wavenumber has both a real and imaginary part; purely propagating waves and band gaps do not exist in presence of dissipation.

Influence of support added-stiffness on dispersion

Additional dispersion effects of linear springs linking the different support to the ground are investigated and two configurations are considered: axial or rotary springs, with respectively stiffness denoted $k_{Support}$ and $k_{\theta,Support}$. In the case of axial springs, the dispersion relation is shown in Fig. 3.13 for both guided and pinned supports, and frequency is normalized by the updated Eq. (3.60) such that

$$\omega'_0{}^2 = \frac{1}{2} \frac{EI_z \pi^2}{mLL_{eff}^2} + \frac{1}{2} \frac{k_{Support}}{mL}, \quad (3.61)$$

where $m = \rho AL$. For both support types, when $k_{Support} \neq 0$, a low frequency cut-off is present (dark-gray lines of Fig. 3.13). Indeed, from Eq. (3.39), noting that $k_{Support}$ is contained only into the diagonal axial external dof ($\widehat{\mathcal{K}}_{LL11}$ only), Eq. (3.55) is no longer valid and one should

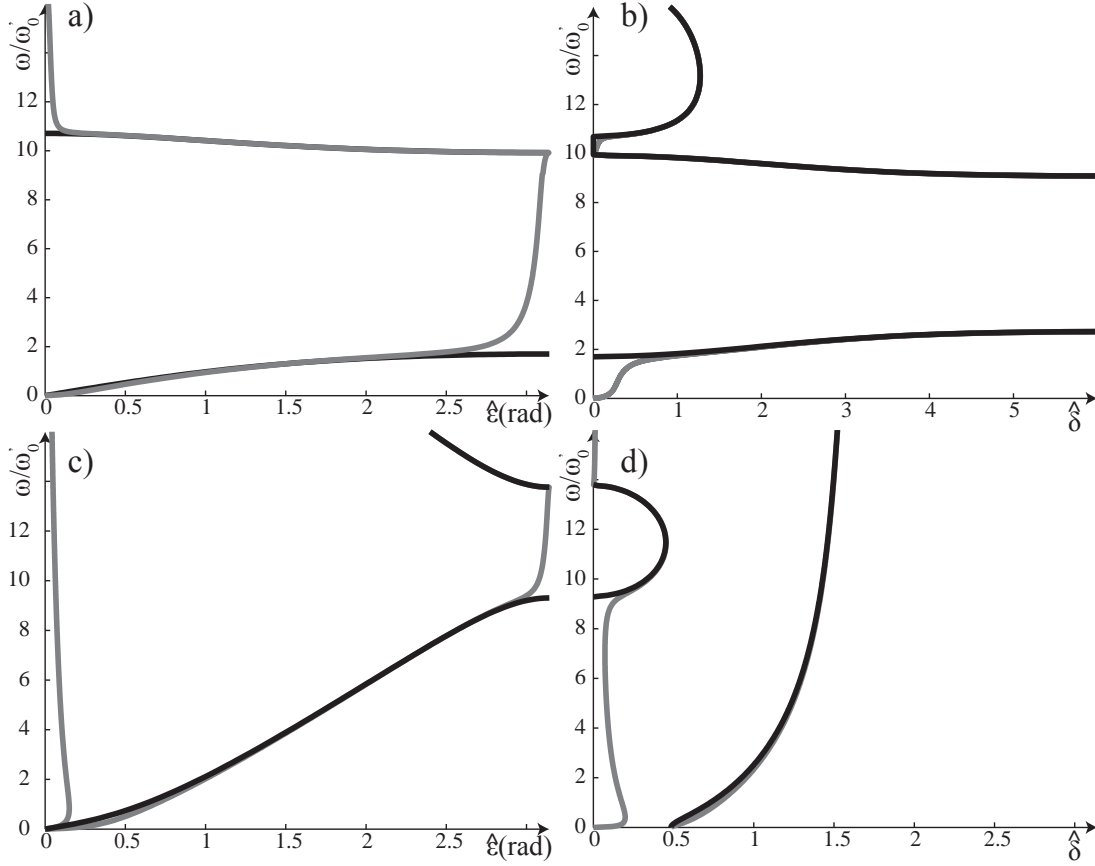


Figure 3.12: Influence of dissipation on dispersion relations for guided (a and b) and pinned (c and d) supports, with $\chi_0 = 0.1$ obtained from inverse reduced-Bloch-theorem dispersion. Imaginary (a and c) and real (b and d) part of the propagation constant.

consider instead Eq. (3.53), which has been derived before the introduction of the assumption $\widehat{\mathcal{K}}_{LL11} = -\widehat{\mathcal{K}}_{LR11}$. From Eq. (3.53), the frequency cut-off is

$$\omega^2|_{\kappa=0} = \frac{\widehat{\mathcal{K}}_{LL11} + \widehat{\mathcal{K}}_{LR11}}{\widehat{\mathcal{M}}_{Tot11}} = \frac{k_{Support}}{\widehat{\mathcal{M}}_{Tot11}}, \quad (3.62)$$

and is verified numerically.

Considering now the pinned-support configuration with rotary springs, when the stiffness $k_{\theta,Support}$ increases, it is expected to get back to the guided-support configuration and indeed, as shown with the light-gray curve of Fig. 3.13b, the dispersion behavior is similar to the dark curve of Fig. 3.13a; the difference in amplitude is explained by the fact that ω_0^2 depends on the support configuration. Moreover, these results can be also founded from the semi-analytical dispersion relation since for $\widehat{\mathcal{K}}_{Tot22} \rightarrow \infty$, Eq. (3.54) is identical to Eq. (3.56) ($k_{\theta,Support}$ is contained only into $\widehat{\mathcal{K}}_{Tot22}$). Note also that from Eq. (3.57), increasing $k_{\theta,Support}$ increases asymptotically ω_0 and so also the linear speed C_0 until $\omega_0^2 = \widehat{\mathcal{K}}_{Tot11}/4\widehat{\mathcal{M}}_{Tot11}$. While influence

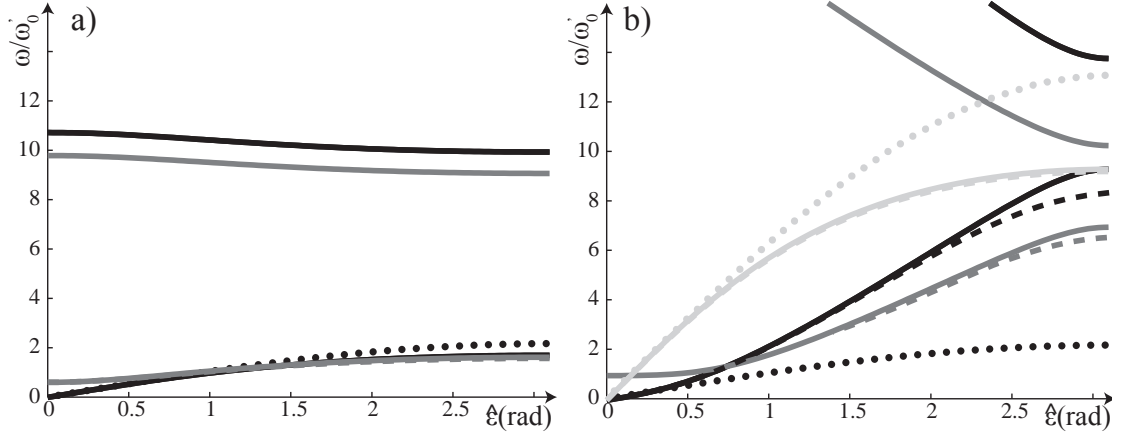


Figure 3.13: Influence of support added-stiffness on dispersion relations for guided (a) and pinned (b) supports with $\chi_0 = 0.1$. Configuration without added stiffness in dark, with axial added stiffness ($k_{Support} = EI_z \pi^2 / (10mLL_{eff}^2)$) in dark gray and with rotary added stiffness ($k_{\theta,Support} \rightarrow \infty$) in light gray. Direct reduced-Bloch-theorem dispersion in solid lines, semi-analytical dispersion in dashed lines (Eqs. (3.46), and (3.47)), and periodicity-induced dispersion (Eq. (3.7)) in dotted lines.

of added stiffness has been addressed here, the same investigations are conducted on added mass.

Influence of support added-mass on dispersion

Up to this point, the buckled beam has been considered without taking into account the mass of the supports. However, experimentally, the support mass is two orders of magnitude larger than the mass of a beam portion, and plays an important role in the dispersion. In the case of the guided supports (Fig. 3.14a), the added mass $m_{Support}$ increases the dispersion such that its curve reaches asymptotically Eq. (3.1) when $m_{Support} \rightarrow \infty$. Indeed, from the semi-analytical dispersion equation, knowing that $m_{Support}$ is only contained into $\widehat{\mathcal{M}}_{LL11}$, increasing $m_{Support}$ will only decrease the effect of transverse-inertial effects ($a_{2,2} = \widehat{\mathcal{M}}_{LR11} / (2\widehat{\mathcal{M}}_{To11})$). Note that Fig. 3.14 is normalized using Eq. (3.61) and $m = \rho AL + m_{Support}$.

For the pinned-support case, it is assumed the rotary inertia to be proportional to the mass of the support such that

$$I_{Support} = r m_{Support}, \quad (3.63)$$

where r is for example, in the case of a full cylinder of radius R : $r = R^2/2$. Noting that $m_{Support}$ and $I_{Support}$ are contained only respectively into $\widehat{\mathcal{M}}_{LL11}$ and $\widehat{\mathcal{M}}_{LL22}$ (Eq. (3.39)), the total

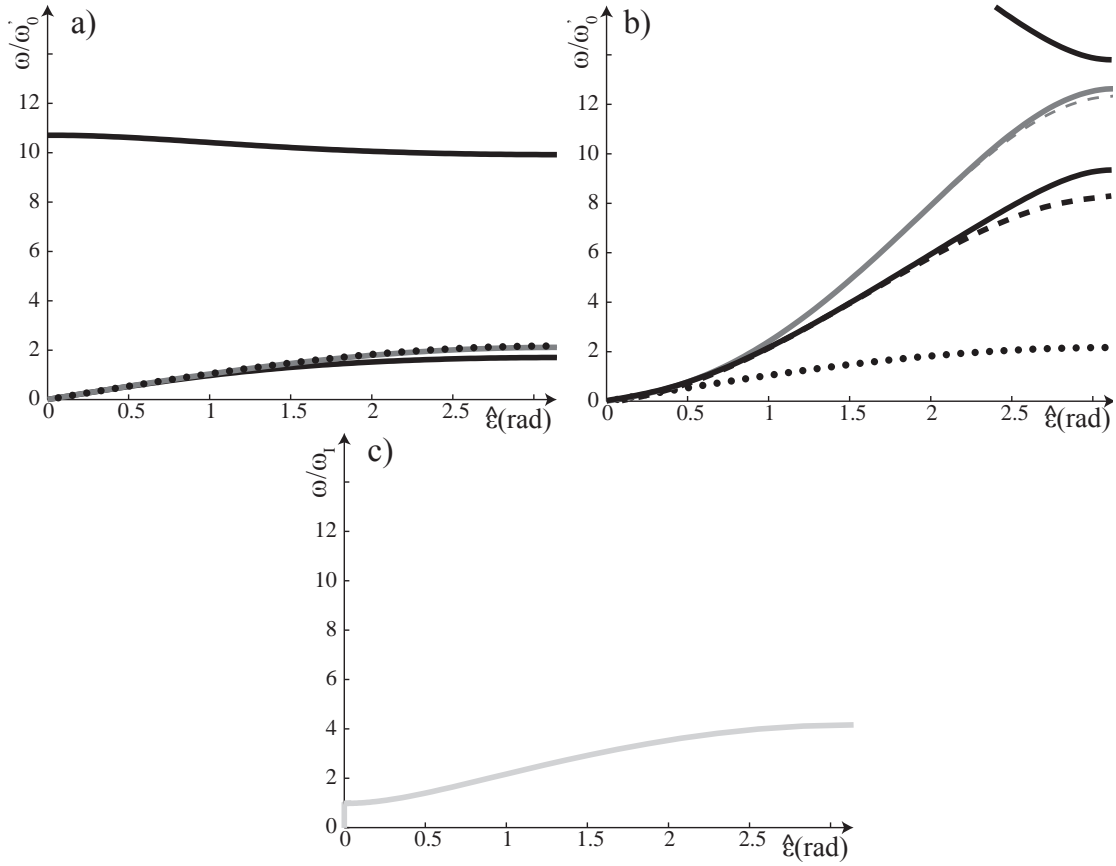


Figure 3.14: Influence of support added-mass on dispersion relations for guided (a) and pinned (b and c) supports with $\chi_0 = 0.1$. Configuration without added mass in dark (a and b), with axial added mass ($m_{Support} \rightarrow \infty$) in dark gray (a and b) and rotary added mass ($r \rightarrow \infty$) in light gray (c). Direct reduced-Bloch-theorem dispersion in solid lines, semi-analytical dispersion in dashed lines (Eqs. (3.46), and (3.47)), and periodicity-induced dispersion (Eq. (3.7)) in dotted lines.

dimensionless dispersion ($a_4 = a_{0,4} + a_{2,2} + a_{4,0}$) using Eq. (3.57) reads

$$\begin{aligned}
 a_4 &= \frac{\widehat{\mathcal{M}}_{LR11}}{2\widehat{\mathcal{M}}_{Tot11}} + \frac{2\widehat{\mathcal{K}}_{LR12}\widehat{\mathcal{M}}_{LR12}}{\widehat{\mathcal{M}}_{Tot11}\widehat{\mathcal{K}}_{Tot22}} - \frac{\widehat{\mathcal{M}}_{Tot22}\widehat{\mathcal{K}}_{LR12}^2}{\widehat{\mathcal{M}}_{Tot11}\widehat{\mathcal{K}}_{Tot22}^2} + Cte \\
 &\approx \frac{\widehat{\mathcal{M}}_{LR11}}{2m_{Support}} + \frac{2\widehat{\mathcal{K}}_{LR12}\widehat{\mathcal{M}}_{LR12}}{m_{Support}\widehat{\mathcal{K}}_{Tot22}} - r \frac{\widehat{\mathcal{K}}_{LR12}^2}{\widehat{\mathcal{K}}_{Tot22}^2} + Cte,
 \end{aligned} \tag{3.64}$$

where Cte is a constant that does not depend on either $m_{Support}$ or r , and the approximation is valid for $m_{Support} \gg \rho AL$. Now, for a fix value of r , increasing $m_{Support}$ converges to a "bounded" solution (see Fig. 3.14b). Alternatively, for a fix value of $m_{Support}$, increasing r decrease the phase speed (a_4) such that when $r \rightarrow \infty$, the dispersion curve converges to zero. While this last observation is verified numerically but not shown here, results are instead

found convergent when normalized by the frequency

$$\omega_I^2 = \frac{\widehat{\mathcal{K}}_{LL22}}{2I_{Supports}}. \quad (3.65)$$

Indeed, as shown in Fig. 3.14c, a frequency threshold is present for $\omega/\omega_I^2 = 1$ meaning that when the rotary inertia is extremely large, the rotary masses are acting as resonators.

3.5.2 Semi-analytical dispersion equation coefficients and pre-compression

While semi-analytical models are proposed in Eqs. (3.46), (3.47), and (3.48), numerical evaluations are in excellent agreement with exact dispersion relations (Figs. 3.10, 3.11, 3.13, and 3.14) and the two models expectedly diverge at high frequencies resulting from the small-frequency approximation of Eq. (3.37).

The advantage arising from these semi-analytical equations is that instead of investigating dispersion curves which are given for a specific pre-compression, the semi-analytical dispersion coefficients, which predict the dispersion behavior, can be directly plotted in terms of the pre-compression χ_0 , as shown in Fig. 3.15.

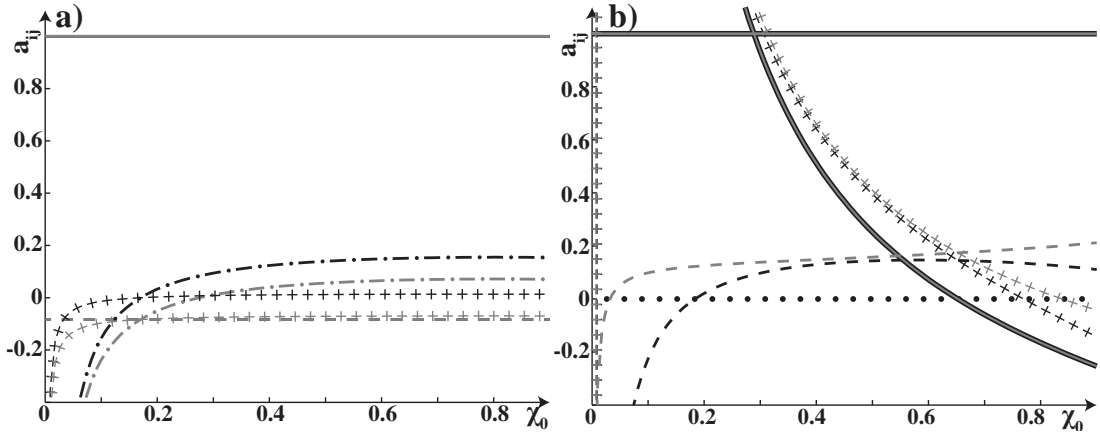


Figure 3.15: Coefficients $a_{2i,2j}$ of Eq. (3.51) in terms of the initial compressive strain χ_0 for guided (a) and pinned (b) supports. Configuration without added mass in dark and with axial added mass ($m_{Support} \rightarrow \infty$ and $r = 0$) in gray.

For the guided-support case (Fig. 3.15a), $a_{0,2} = 1$ and $a_{0,4} = -1/12$ in agreement with Eq. (3.55). Concerning $a_{2,2}$, $a_{2,2} \rightarrow -\infty$ asymptotically for $\chi \rightarrow 0$, becomes greater than zero for $\chi \approx 0.1$, and converges asymptotically to a finite positive value for χ_0 large. $a_{2,2}$ is in agreement with the description of $(1 - \alpha)$ from the mass spring model of Fig. 3.2b (Sec. 3.2.2).

For the pinned-support case (Fig. 3.15b), the trend of $a_{2,2}$ is similar to the guided-support configuration whereas $a_{4,0}$ is not constant anymore. Indeed, as shown in Eq. (3.57), $a_{0,4}$ is composed now of two terms; the dispersive one due to periodicity ($-1/12$) and an additional

dominating one arising from stiffness coupling. Concerning $a_{4,0}$, it is found not significant with respect to the other dispersive terms.

In addition to $a_{0,4}$, $a_{2,2}$ and $a_{4,0}$, the total dimensionless dispersion $a_4 = a_{0,4} + a_{2,2} + a_{4,0}$ is plotted and gives directly the acoustic properties of the medium (Fig. 3.1). For guided supports with small and moderated pre-compression, $a_4 < 0$ whereas $a_4 > 0$ for $\chi_0 > 0.5$. On the contrary, in the pinned-support case, $a_4 > 0$ only for strongly-compressed beam ($\chi_0 > 0.8$). In other words, the guided supports lead to dispersion of supersonic type for small pre-compression compared to subsonic dispersion for large buckling levels. Conversely, for the pinned-support configuration, dispersion is subsonic and supersonic for respectively small and large pre-compression.

Concerning the effects of support added-mass, the semi-analytical coefficients for $m_{Support} \rightarrow \infty$ and $r = 0$ are plotted in gray lines in Fig. 3.15, and the global trend is found unchanged. The effect of additional mass is to decrease $a_{2,2}$ in the guided-support case, whereas it is the opposite effect in the case of pinned supports, as already described in Sec. 3.5.1.

Finally, Fig. 3.15 gives the dispersion behavior for the guided and pinned-support configurations for any pre-compression level, material property and cross-section profile, as long as initial imperfections and the inverse of the slenderness of the beam remain small or the pre-compression is large. Moreover, concerning the added mass, any configuration with r small can be considered since it will be bounded between the curves of $m_{Support} = 0$ and $m_{Support} \rightarrow \infty$.

Up to this point, it has been shown that semi-analytical dispersion relations provide an equation for which the frequency and the wavenumber are explicitly linked and where the coefficients are found using FE. Moreover, the use of mass-spring systems allows physical interpretation of these coefficients and Fig. 3.15 gives good approximations of their values. Wavemodes corresponding to Figs. 3.10-3.14 are discussed next.

3.5.3 Wavemodes

The deformed shapes of propagating wavemodes for the three different configurations are given by the eigenvectors of Eq. (3.36). These modes can be classified in three groups only, shown in Fig. 3.16. In Fig. 3.10 it is also indicated the occurrence of each wavemodes. As a first remark based on geometric considerations, weakly-compressed beams deform mainly in the transverse direction (Fig. 3.16b) whereas strongly-buckled beams deform mainly in the axial direction (Fig. 3.16a). Results are similar regardless of the support type or the state of stress. This means that wavemodes are only dependent on the buckled geometry, determined by the pre-compression. Indeed, in the case of strongly-buckled beams, the top of the beam is already at its maximum with respect to the range of possible deformations in transverse direction; therefore, deformation in this direction is small. Considering strongly-compressed beams as a waveguide, propagating modes can be classified as axial (Figs. 3.16a,d) and barreling

3.6. From dispersion equation to linear wave equation

(Figs. 3.16b,e) types. In the case of unsupported configurations only, a bending wavemode (Figs. 3.16c,f) characterizes propagation for $\hat{\epsilon} > \pi/2$. This finding is in agreement with the discussion in Sec. 3.5.1, where dispersion is found to be described by Eq. (3.1).

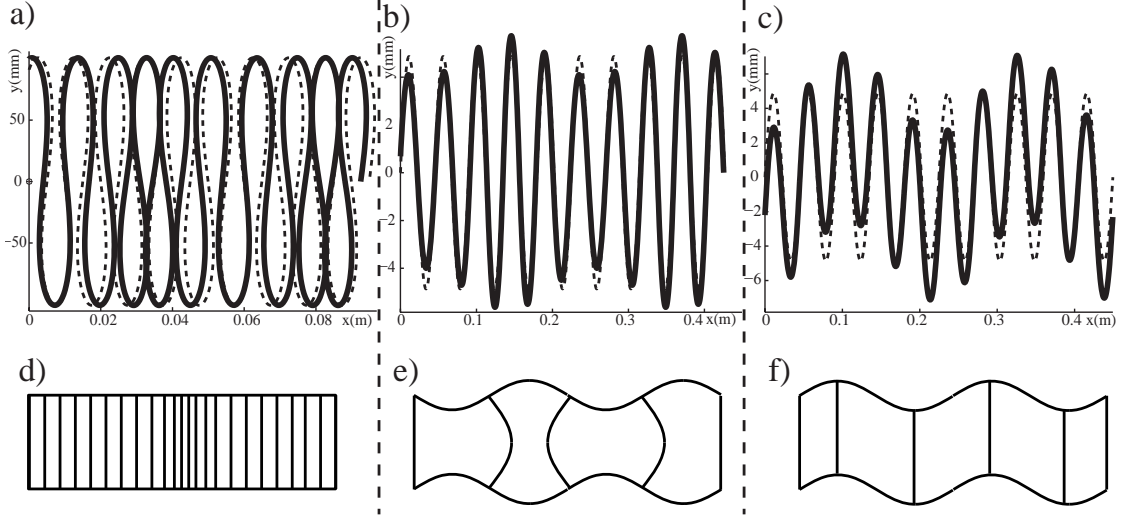


Figure 3.16: Propagating wavemodes for configurations with pinned supports (a, b, $\hat{\epsilon} = 0.4$) and no supports (c, $\hat{\epsilon} = 3$). Weak (a, c, $\chi_0 = 0.1$) and strong (b, $\chi_0 = 0.8$) pre-compression. Deformed configurations (full line) are superposed to undeformed ones (dashed lines). Equivalent-waveguide modes described as axial (d), barreling (e), and bending (f) modes.

3.6 From dispersion equation to linear wave equation

Assuming harmonic waves ($u = e^{i(\kappa x - \omega t)}$), a partial differential equation (PDE) is looked for whose dispersion relation corresponds to the semi-analytical dispersion relation Eq. (3.51), and for linear waves, the unique solution is [Whitham, 1974]

$$u_{tt} = C_0^2 u_{xx} - a_{0,4} L_0^2 C_0^2 u_{xxxx} - a_{2,2} L_0^2 u_{xxtt} - a_{4,0} \frac{L_0^2}{C_0^2} u_{tttt}. \quad (3.66)$$

A review of such linear waves with different dispersive terms can be found in [Berezovski et al., 2011]. In the next chapter, Eq. (3.66) will be the starting point to investigate nonlinear waves.

3.7 Conclusions

In this chapter, both direct and indirect-Bloch methods with FE are used to compute dispersion relations with guided, pinned, and free supports. Starting from the indirect method of the Bloch theorem, a novel method is derived to obtain an analytical approximated equation of the dispersion relation in the acoustic branch: the semi-analytical dispersion relation. Moreover, simplified mass-spring models are proposed to describe physical mechanisms of the dispersion relations.

Chapter 3. Dispersion Of Periodic Buckled Beams

Dispersion analyses show that the initial curvature (pre-compression level) plays an important role in the behavior of the dispersion. Indeed, in the case of the guided supports, for small pre-compression levels, the phase speed decrease for increasing frequency whereas for strong pre-compression levels, the phase speed increase with frequency. For pinned supports, the opposite is true.

Concerning the analysis of the waveguide modes, they are found also mainly dependent to the curvature. For low pre-compression levels, symmetric barreling modes are present whereas axial modes dominate for large curvatures. In addition, in the free-support configuration, bending modes exist at small pre-compression levels only. Added mass and stiffness can be used as tuning tools to modify the dispersion relation characteristics. While axial added stiffness creates a threshold in the dispersion relation, increasing the rotary stiffness changes the dispersion behavior from supersonic to subsonic type, leading to the guided-support configuration in the asymptote. Added mass decreases the transverse-inertial effects by increasing the periodicity-induced dispersion in the guided-support case, whereas pinned supports provide opposite effects. Concerning the rotary inertia, its increase, relative to the added mass, decreases the phase speed such that for extremely large values, particles are acting as resonators and no propagation is possible at the resonance frequency.

Since only the case of added mass is going to be considered in the next chapter, a really important point is that Fig. 3.15 gives dispersion estimation for any configuration, whatever the support type, level of compression, and mass of the support. The only restriction that applies at small pre-compression level for which, the slenderness parameter and the imperfection amplitude have to be respectively large and small. This means that the wave-speed behavior (supersonic or subsonic) can be directly obtained from Fig. 3.15 and will be useful in the next chapter to determine the soliton type. This work leads to the derivation of linear homogenized-continuum models, nonlinear ones are investigated in the next chapter.

4 Nonlinear Wave Propagation In Buckled Beam: Models And Simulations

4.1 Introduction

In the two previous chapters, it has been shown that buckled beams possess a geometrically-nonlinear load-deformation behavior and intrinsic dispersion sources, two characteristics necessary to stationary waves forming. It is the goal of the present chapter to derive nonlinear wave models and validate them by comparison to numerical finite-element (FE) simulations of the structure.

One of the simplest nonlinear dispersive equations, modeling in particular wave propagation in discrete systems, is the Boussinesq equation given by:

$$\xi_{\bar{t}\bar{t}} = \xi_{\bar{x}\bar{x}} + \frac{1}{12}\xi_{\bar{x}\bar{x}\bar{x}\bar{x}} + \frac{1}{2}(\xi^2)_{\bar{x}\bar{x}}, \quad (4.1)$$

where ξ is the strain and \bar{x} and \bar{t} are respectively the dimensional space and time variables. However, as it will be shown in Sec. 4.3, the dispersion is not correctly captured with the simple Boussinesq equation and one should instead consider the double-dispersion Boussinesq equation

$$\xi_{\bar{t}\bar{t}} = \xi_{\bar{x}\bar{x}} - a_{0,4}\xi_{\bar{x}\bar{x}\bar{x}\bar{x}} - a_{2,2}\xi_{\bar{x}\bar{x}\bar{t}\bar{t}} + \frac{1}{2}(\xi^2)_{\bar{x}\bar{x}}, \quad (4.2)$$

where $a_{0,4}$ and $a_{2,2}$ are two dimensionless constants modeling dispersion. For $a_{2,2} = 0$, Eq. (4.2) is the bad Boussinesq equation (bad refers to the ill-posed dispersion relation of this equation when linearized) whereas for $a_{0,4} = 0$, Eq. (4.2) is the improved (or regularized) long-wave Boussinesq equation [Christov et al., 2007]. The full Eq. (4.2) is the double-dispersion equation which is found when describing waves in microstructure solids [Engelbrecht et al., 2011, Delsanto, 2006, Berezovski et al., 2013], in rods [Samsonov and Maugin, 2001, Porubov, 2003, Christov et al., 2007], or in the Cauchy problem [Wang and Chen, 2006, Liu and Xu, 2008, Erbay et al., 2015, Kutev et al., 2014].

For nonlinear wave propagation with large amplitude or small pre-compression, the gener-

alized Boussinesq equation based on local approximations of the load-displacement curve by a second-degree polynomial is no longer valid. To this end, a model based on power law nonlinearities similar to the one used for wave propagation in pre-compressed granular media [Nesterenko, 2001] is proposed in Sec. 4.4.2. Existing solution techniques are extended to account for the additional dispersion sources and for the case of a power law with a negative power coefficient. In addition to the power law nonlinearity, a method based on the exact load-displacement curve is also derived. Finally, numerical FE simulations are then used to validate the homogenized models in Sec. 4.5. Discussions and conclusions follow.

4.2 Geometric, material and FE properties

Before investigating nonlinear wave propagation, the different properties used in this chapter are introduced here. Values of the different parameters correspond to the physical ones used in experiments (see Chapter 5). The beam has a rectangular cross section of area $A = bt$ and area-moment of inertia $I_z = bt^3/12$ where $t = 0.4$ mm and $b = 12.7$ mm. The material is steel assumed to be linear and elastic with $E = 190$ GPa and $\rho = 7600$ Kg m⁻³. The interspace between two consecutive supports is initially $L = 60$ mm and the mass of one support is $m_{Support} = 24$ g. The initial imperfection (see Fig. 4.2b) is chosen as $w_0/L = 10^{-3}$.

For numerical simulations, the selected beam formulation is the co-rotational model [Batini, 2002] which is limited to small strain (linear elastic material) but applicable to finite displacements and rotations. Since the beam is assumed slender, this formulation neglects shear. A super-convergent beam formulation is discussed in Chapter 6, but given the need to use Lagrange multipliers to enforce boundary conditions, co-rotational formulation is preferred here for simplicity. Each wavelength is composed of 30 or 8 elements and a total of $p = 300$ or $p = 1200$ wavelengths are used for respectively the guided and pinned-support configurations. Simulations are divided into two steps; the first one in load control where the structure is statically buckled after applying the desired load for the pre-compression, and a second one, in displacement control, where a dynamic pulse is generated at the left boundary. Both static and dynamic simulations are divided into 5000 steps (in the static case this is done to ensure resolution in the load-displacement curve) and the convergence criterion for the Newton-Raphson scheme [Cook and Malkus, 2002] is defined by $\|R_i\|_\infty/\|R_0\|_\infty < 10^{-5}$ or $\|R_i\|_\infty < 10^{-10}$ where R_0 is the residual due to the external forces and R_i is the residual at the i^{th} convergence iteration (see Chapter 6). For the time integration scheme, the generalized- α method is used and can be second-order accurate in time and unconditionally stable for linear problems [Chung and Hulbert, 1993]. Details on the implementation and the choice of parameters can be found in [Raknes et al., 2013], and in the present thesis, the high-frequency dissipation parameter is chosen as $\rho_\infty = 0.9$.

4.3 Wave propagation described by the simple Boussinesq model

4.3.1 From the simple mass-spring chain to the Boussinesq equation

An idealized model for periodic buckled beam is constructed as a chain of masses and nonlinear springs like that shown in Fig. 4.1. Beam segments are replaced by discrete masses $m = \rho AL + m_{Support}$ and nonlinear springs defined by nonlinear load-deformation relation $P\{\Delta U\}$ (see Chapter 2) such that dynamic deformations between supports are neglected.

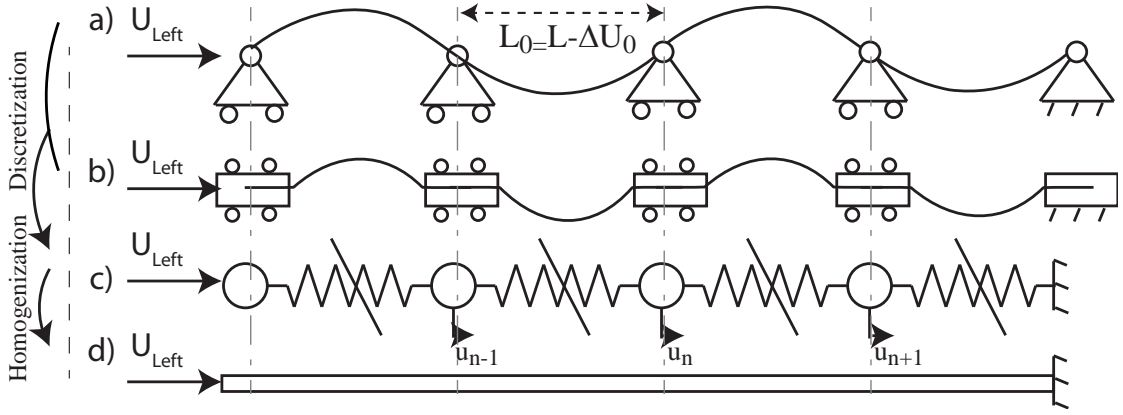


Figure 4.1: Guided (only axial displacement allowed) (a) and pinned (both axial displacement and rotation free) (b) support configurations composed of $p = 4$ cells and modeled by a discrete chain of masses and nonlinear springs (c), and long-wavelength homogenization (d).

Conservation of linear momentum for particle of the n^{th} requires:

$$\ddot{u}_n = \frac{1}{m} (P\{\Delta U_0 - u_n + u_{n-1}\} - P\{\Delta U_0 - u_{n+1} + u_n\}), \quad (4.3)$$

where $\ddot{(\)}$ denotes differentiation in time, u_n is the displacement of n^{th} mass about its equilibrium, ΔU_0 is the initial displacement due to static compression, and the nonlinear load-displacement relation $P\{\Delta U\}$ already analyzed in Chapter 2 is recalled in Fig. 4.2. Assuming the dynamic wave small with respect to the pre-compression ($\Delta u_n = u_n - u_{n+1} \ll \Delta U_0$), Taylor expansion of $P\{\Delta U\}$ reads:

$$P\{\Delta U\} = P\{\Delta U_0\} + P'\{\Delta U_0\}(\Delta U - \Delta U_0) + \frac{1}{2}P''\{\Delta U_0\}(\Delta U - \Delta U_0)^2 + \mathcal{O}(u^3), \quad (4.4)$$

such that the momentum equation (4.3) can be recast as

$$\ddot{u}_n = \frac{P'\{\Delta U_0\}}{m} (u_{n-1} + u_{n+1} - 2u_n) + \frac{P''\{\Delta U_0\}}{2m} (u_{n-1} + u_{n+1} - 2u_n)(u_{n-1} - u_{n+1}). \quad (4.5)$$

Finite differences in Eq. (4.5) are replaced by an equivalent continuous displacement $\tilde{u}(x, t)$ as

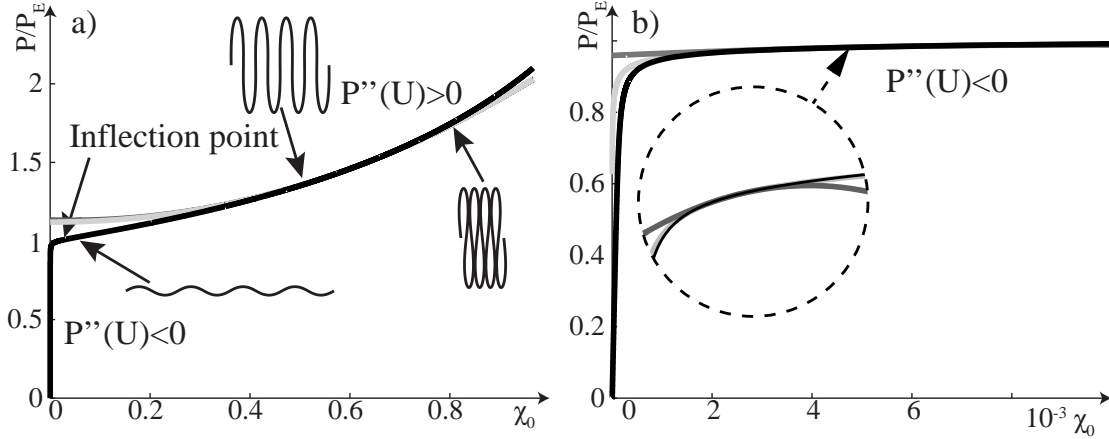


Figure 4.2: Load-displacement $P\{\Delta U\}$ relation in black lines obtained numerically from FE, and normalized by the critical Euler buckling load P_E (Eq. (2.44)). The figure is plotted in terms of the large (a) and small (b) buckling level $\chi_0 = \Delta U_0/L$. Approximation of the $P\{\Delta U\}$ curve at $\chi_0 = 0.6$ (a) and $\chi_0 = 5 \times 10^{-3}$ (see inset for details) (b) by a polynomial of degree two (Eq. (4.4)) in dark gray and by a power law (Eq. (4.27)) in light gray.

$$\begin{aligned} u_{n+1} - u_{n-1} &= 2L_0 \tilde{u}_x + \mathcal{O}(L_0^3), \\ u_{n-1} + u_{n+1} - 2u_n &= L_0^2 \tilde{u}_{xx} + \frac{L_0^4}{12} \tilde{u}_{xxxx} + \mathcal{O}(L_0^6), \end{aligned} \quad (4.6)$$

where $L_0 = L - \Delta U_0$, and subscripts of $\tilde{u}(x, t)$ indicate partial derivatives. Substituting Eq. (4.6) into Eq. (4.5), neglecting terms higher than order $\mathcal{O}(L_0^4)$, and dropping the notation $(\tilde{\cdot})$ for conciseness, one obtains

$$u_{tt} = C_0^2 u_{xx} + 2C_0 \gamma u_{xxxx} - \sigma u_{xx} u_x, \quad (4.7)$$

where

$$C_0^2 = \frac{P'(\Delta U_0) L_0^2}{m}, \quad \sigma = \frac{P''(\Delta U_0) L_0^3}{m} \quad \text{and} \quad \gamma = \frac{C_0 L_0^2}{24}, \quad (4.8)$$

are respectively the coefficient of linear speed, nonlinearity, and periodicity-induced dispersion. Note that at a first approximation, for moderated buckling levels, using Eq. (2.31), $C_0^2 = P_E L_0^2 / (2mL\delta_0^3)$ and $\sigma = 3P_E L_0^3 / (8mL^2\delta_0^4)$ where $\delta_0 = 1 - \frac{\Delta U_0}{4L}$.

Eq. (4.7) can be recast in terms of total compressive strain $\xi = -U_x = -u_x - \chi_0$ given in the initially deformed configuration ($\chi_0 = \Delta U_0/L$ is the initial strain):

$$\xi_{tt} = C_0^2 \xi_{xx} + 2C_0 \gamma \xi_{xxxx} + \frac{\sigma}{2} (\xi^2)_{xx}. \quad (4.9)$$

Eq. (4.9) is the Boussinesq equation [Ablowitz, 2011] and admits the solitary-wave solutions

4.3. Wave propagation described by the simple Boussinesq model

called solitons:

$$\Delta\xi = \Delta\xi_m \operatorname{sech}^2 \{ \Lambda^{-1}(x - Vt) \}, \quad (4.10)$$

where $\Delta\xi = \xi - \chi_0$, $\Delta\xi_m = \xi_m - \chi_0$ and ξ_m is the maximum strain. Note that the dynamic wave amplitude $\Delta\xi_m$ can be positive (compressive soliton) or negative (tensile or rarefaction soliton) such that $\operatorname{sgn}(\Delta\xi_m) = \operatorname{sgn}(\gamma)\operatorname{sgn}(\sigma)$ and is a very important characteristic that will be revisited in the following sections. The soliton phase speed V is:

$$V = \sqrt{C_0^2 + \sigma\Delta\xi_m/3}, \quad (4.11)$$

which is supersonic for $\gamma > 0$, the case of pure periodicity dispersion, and is subsonic for $\gamma < 0$. The characteristic width Λ is

$$\Lambda = \sqrt{24C_0\gamma/(\sigma\Delta\xi_m)}, \quad (4.12)$$

and is linked to the width at half maximum $\Lambda_{1/2}$ by the relation $\Lambda_{1/2} = 2\cosh^{-1}\{\sqrt{2}\}\Lambda \approx 1.7627\Lambda$.

As a side note, assuming $a_{0,4}^2 \ll 1$, $\bar{\sigma}^2 \ll 1$ and $\bar{\sigma} \sim a_{0,4}$, Eq. (4.9) can be simplified, following [Kunin, 1982], into the Korteweg–de Vries (KdV) equation:

$$\xi_t + C_0\xi_x + \gamma\xi_{xxx} + \frac{\sigma}{2C_0}\xi\xi_x = 0. \quad (4.13)$$

Eq. (4.13) also admits the soliton solution Eq. (4.10) and differs only by the definition of the speed ($V = C_0 + \sigma\Delta\xi_m/(6C_0)$) [Maurin and Spadoni, 2014b].

In order to validate the Boussinesq model, results are next compared to FE simulations of the structure.

4.3.2 Comparison between the simple Boussinesq model and FE simulations

Numerical simulations are performed using the parameters given in Sec. 4.2 imposing the dynamic displacement on the left extremity of the beam U_{Left} (Fig. 4.1), obtained after integrating Eq. (4.10) in space such that:

$$U_{Left} = \Delta\xi_m\Lambda(\tanh\{\Lambda^{-1}V(t_0 - t)\} + 1) + p\Delta U_0, \quad (4.14)$$

where t_0 is chosen arbitrarily as $t_0 = 5\Lambda/V$. The total time of the dynamic simulation is given by $t_f = pL/V$.

Numerical comparisons are performed for the pinned-supported weakly ($\chi_0 = 0.1$) and strongly ($\chi_0 = 0.9$) buckled beam, and propagating waves are shown in Fig. 4.3. Note that for $\chi_0 \geq 0.1$, $P'\{\Delta U_0\} > 0$.

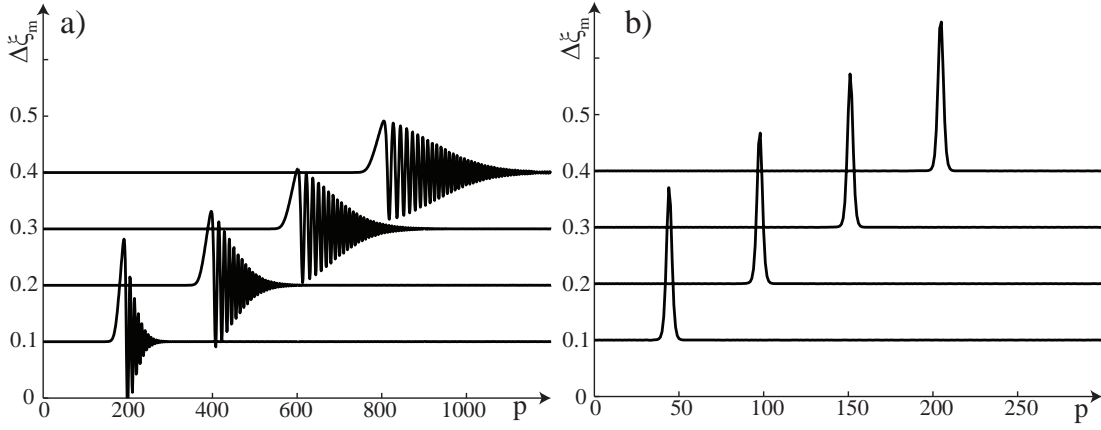


Figure 4.3: Snapshots at times multiple of $t_i = 3/20t_f$ of the maximum strain wave $\Delta\xi_m$ vs support number (p) for weakly pinned-supported ($\chi_0 = 0.1$) (a) and strongly ($\chi_0 = 0.9$) (b) buckled beam obtained by numerical FE simulations of the structure.

For the case of the strongly-buckled beam, the wave propagates keeping its shape and speed whereas for the case of the weakly-buckled configuration, the propagation does not stabilize. Moreover, while periodicity-induced dispersion results to the creation of a tail (if not balanced), in the present case, a front is permanently created which is contrary to the simple mass-spring model presented in Fig. 4.1c (see Fig. 3.1). Indeed, as discussed in Chapter 3, the sign of the dispersive term is dominated by coupling effects which are neglected here. In order to improve the current model, it is necessary to include the dispersion analysis derived in the previous chapter to the nonlinear model.

4.4 Solitary waves including mass and stiffness coupling

4.4.1 The double-dispersion Boussinesq model

In the previous chapter, it has been shown assuming harmonic waves ($u = u_m e^{i(\kappa x - \omega t)}$) that the unique PDE having for dispersion relation Eq. (3.51) is Eq. (3.66) which is here recast in terms of the strain ξ :

$$\xi_{tt} = C_0^2 \xi_{xx} - a_{0,4}^{(1)} L_0^2 C_0^2 \xi_{xxxx} - a_{2,2}^{(1)} L_0^2 \xi_{xxtt} - a_{4,0}^{(1)} \frac{L_0^2}{C_0^2} \xi_{tttt}, \quad (4.15)$$

where the superscripts $()^{(1)}$ refer to the coefficients derived in Chapter 3 (Eq. (3.57)). For the guided-support configuration ($a_{4,0}^{(1)} = 0$), since the supports allow only axial translations, there is no displacement coupling at the support location (see Fig. 3.2a). In order to include nonlinearities, the nonlinear term from Eq. (4.9) is added to Eq. (4.15) describing axial waves

4.4. Solitary waves including mass and stiffness coupling

such that Eq. (4.15) becomes the double-dispersion Boussinesq equation:

$$\xi_{tt} = C_0^2 \xi_{xx} - a_{0,4}^{(1)} L_0^2 C_0^2 \xi_{xxxx} - a_{2,2}^{(1)} L_0^2 \xi_{xxtt} + \frac{\sigma}{2} (\xi^2)_{xx}. \quad (4.16)$$

In the case of pinned supports, both axial displacement U and rotation θ are allowed at the support location, so that Eq. (4.15) is the result of two coupled PDEs. Since the nonlinear term cannot simply be added to Eq. (4.15) as done for the guided-support case, it is the goal here to find the two coupled original PDEs (momentum equations).

Combining Eqs. (3.32) and (3.25), one gets:

$$\begin{bmatrix} D_{11} & D_{12} \\ D_{12} & D_{22} \end{bmatrix} \begin{Bmatrix} U_m \\ \theta_m \end{Bmatrix} = \mathbf{0}. \quad (4.17)$$

where U_m and θ_m are respectively the amplitude of the harmonic axial strain and rotation waves such that $U = U_m e^{i(\kappa x - \omega t)}$ and $\theta = \theta_m e^{i(\kappa x - \omega t)}$, and

$$\begin{aligned} D_{11} &= \mathcal{D}_{LL11} + \mathcal{D}_{LR11} \cosh L_0 \kappa \\ &= \mathcal{K}_{LL11} (1 - \cosh L_0 \kappa) - \mathcal{M}_{Tot11} \omega^2 - \mathcal{M}_{LR11} (\cosh L_0 \kappa - 1) \omega^2, \\ D_{12} &= i \mathcal{D}_{LR12} \sinh L_0 \kappa \\ &= i (\mathcal{K}_{LR12} - \mathcal{M}_{LR12} \omega^2) \sinh L_0 \kappa, \\ D_{22} &= \mathcal{D}_{LL22} - \mathcal{D}_{LR22} \cosh L_0 \kappa \\ &= \mathcal{K}_{Tot22} + \mathcal{K}_{LR22} (1 - \cosh L_0 \kappa) - \mathcal{M}_{Tot22} \omega^2 + \mathcal{M}_{LR22} (\cosh L_0 \kappa - 1) \omega^2. \end{aligned}$$

Eq. (4.17) results from a system of two linear harmonic coupled equations given by:

$$U_{\bar{t}\bar{t}} = U_{\bar{x}\bar{x}} - \frac{1}{12} U_{\bar{x}\bar{x}\bar{x}\bar{x}} + \frac{\mathcal{M}_{LR11}}{2\mathcal{M}_{Tot11}} U_{\bar{x}\bar{x}\bar{t}\bar{t}} + 2 \frac{\mathcal{K}_{LR12}}{\mathcal{K}_{LL11}} \theta_{\bar{x}} - \frac{\mathcal{M}_{LR12}}{\mathcal{M}_{Tot11}} \theta_{\bar{x}\bar{t}\bar{t}} - \frac{\mathcal{K}_{LR12}}{3\mathcal{K}_{LL11}} \theta_{\bar{x}\bar{x}\bar{x}}, \quad (4.18a)$$

$$\theta = -\frac{\mathcal{K}_{LR12}}{\mathcal{K}_{Tot22}} U_{\bar{x}} + \frac{\mathcal{K}_{LR12}}{6\mathcal{K}_{Tot22}} U_{\bar{x}\bar{x}\bar{x}} + \frac{C_0^2}{L_0^2} \frac{\mathcal{M}_{LR12}}{\mathcal{K}_{Tot22}} U_{\bar{x}\bar{t}\bar{t}} - \frac{\mathcal{K}_{LR22}}{2\mathcal{K}_{Tot22}} \theta_{\bar{x}\bar{x}} + \frac{C_0^2}{L_0^2} \frac{\mathcal{M}_{Tot22}}{\mathcal{K}_{Tot22}} \theta_{\bar{t}\bar{t}}, \quad (4.18b)$$

where $\bar{x} = x/L_0$ and $\bar{t} = tC_{0,G}/L_0$ are respectively the dimensional space and time and high-order terms of Eq. (4.18b) have been neglected. Eqs. (4.18a) and (4.18b) are respectively the momentum equations describing axial deformations and rotations. The exact solution of this system, up to order four is Eq. (4.15). However, instead of working with Eq. (4.15), the axial nonlinear term is added to the axial momentum equation and the new system of coupled

PDEs given in terms of the strain ($\xi = -U_x$) and rotation θ reads:

$$\xi_{\bar{t}\bar{t}} = \xi_{\bar{x}\bar{x}} - \frac{1}{12} \xi_{\bar{x}\bar{x}\bar{x}\bar{x}} + \frac{\mathcal{M}_{LR11}}{2\mathcal{M}_{Tot11}} \xi_{\bar{x}\bar{x}\bar{t}\bar{t}} + \frac{1}{L_0} \left(2 \frac{\mathcal{K}_{LR12}}{\mathcal{K}_{LL11}} \theta_{\bar{x}\bar{x}} - \frac{\mathcal{M}_{LR12}}{\mathcal{M}_{Tot11}} \theta_{\bar{x}\bar{x}\bar{t}\bar{t}} - \frac{\mathcal{K}_{LR12}}{3\mathcal{K}_{LL11}} \theta_{\bar{x}\bar{x}\bar{x}\bar{x}} \right), \quad (4.19a)$$

$$\frac{\theta}{L_0} = -\frac{\mathcal{K}_{LR12}}{\mathcal{K}_{Tot22}} \xi + \frac{\mathcal{K}_{LR12}}{6\mathcal{K}_{Tot22}} \xi_{\bar{x}\bar{x}} + \frac{C_{0,G}^2}{L_0^2} \frac{\mathcal{M}_{LR12}}{\mathcal{K}_{Tot22}} \xi_{\bar{t}\bar{t}} - \frac{1}{L_0} \left(\frac{\mathcal{K}_{LR22}}{2\mathcal{K}_{Tot22}} \theta_{\bar{x}\bar{x}} - \frac{C_{0,G}^2}{L_0^2} \frac{\mathcal{M}_{Tot22}}{\mathcal{K}_{Tot22}} \theta_{\bar{t}\bar{t}} \right). \quad (4.19b)$$

Similarly to the asymptotic procedure used in [Delsanto, 2006, Berezovski et al., 2013], under the long-wave assumption, as a first approximation, one get from Eq. (4.19b):

$$\frac{\theta}{L_0} = \frac{\mathcal{K}_{LR12}}{\mathcal{K}_{Tot22}} \xi, \quad (4.20)$$

such that Eq. (4.19b) can be recast as

$$\frac{\theta}{L_0} = \frac{\mathcal{K}_{LR12}}{\mathcal{K}_{Tot22}} \xi - \left(\frac{1}{6} \frac{\mathcal{K}_{LR12}}{\mathcal{K}_{Tot22}} + \frac{1}{2} \frac{\mathcal{K}_{LR12}\mathcal{K}_{LR22}}{\mathcal{K}_{Tot22}^2} \right) \xi_{\bar{x}\bar{x}} - \frac{C_{0,G}^2}{L_0^2} \left(\frac{\mathcal{M}_{LR12}}{\mathcal{K}_{Tot22}} - \frac{\mathcal{K}_{LR12}\mathcal{M}_{Tot22}}{\mathcal{K}_{Tot22}^2} \right) \xi_{\bar{t}\bar{t}}. \quad (4.21)$$

Plugging Eq. (4.21) into Eq. (4.19a), one get:

$$\xi_{\bar{t}\bar{t}} = C_{0,p}^2 \xi_{\bar{x}\bar{x}} - a_{0,4}^{(2)} L_0^2 C_{0,p}^2 \xi_{\bar{x}\bar{x}\bar{x}\bar{x}} - a_{2,2}^{(2)} L_0^2 \xi_{\bar{x}\bar{x}\bar{t}\bar{t}} + \frac{\sigma}{2} (\xi^2)_{\bar{x}\bar{x}}, \quad (4.22)$$

where the dimensionless dispersive constants are

$$a_{0,4}^{(2)} = -\frac{1}{12} + \frac{\mathcal{K}_{LL11}\mathcal{K}_{LR22} + \mathcal{K}_{LR12}^2}{\mathcal{K}_{Tot11}\mathcal{K}_{Tot22} - 4\mathcal{K}_{LR12}^2} - \frac{\mathcal{K}_{LR22}}{2\mathcal{K}_{Tot22}}, \quad (4.23)$$

$$a_{2,2}^{(2)} = \frac{1}{2} \frac{\mathcal{M}_{LR11}}{\mathcal{M}_{Tot11}} + 2 \frac{\mathcal{M}_{LR12}\mathcal{K}_{LR12}^2}{\mathcal{M}_{Tot11}\mathcal{K}_{Tot22}} - \frac{\mathcal{M}_{Tot22}\mathcal{K}_{LR12}^2}{\mathcal{M}_{Tot11}\mathcal{K}_{Tot22}^2}.$$

Because Eq. (4.22) is different than Eq. (4.15), the dispersion is not exactly captured. However, note that the total dimensionless dispersion $a_4 = a_{0,4}^{(2)} + a_{2,2}^{(2)} = a_{0,4}^{(1)} + a_{2,2}^{(1)} + a_{4,0}^{(1)}$ remains unchanged. For a sake of clarity, the simplified notation is used next; for the guided-support case, $a_{0,4} = a_{0,4}^{(1)}$ and $a_{2,2} = a_{2,2}^{(1)}$, whereas for the pinned-support case, $a_{0,4} = a_{0,4}^{(2)}$ and $a_{2,2} = a_{2,2}^{(2)}$.

Eq. (4.22) is the double-dispersion Boussinesq equation which also describes axial waves in straight rods [Porubov, 2003, Samsonov and Maugin, 2001, Christov et al., 2007]. It is not exactly integrable in the sense of the inverse scattering transform [Soerensen, 1984] and its solution is derived following the same procedure as for the Boussinesq equation [Remoissenet, 1995], with solution given by Eq. (4.10) but the dispersive term γ is now:

$$\gamma = -\frac{L_0^2}{2C_0} (a_{0,4}C_0^2 + a_{2,2}V^2). \quad (4.24)$$

4.4. Solitary waves including mass and stiffness coupling

For solitary waves in discrete media, an important characteristic is the wavelength at half amplitude ($\Lambda_{1/2}$) with respect to the period of the medium. Assuming small amplitude waves ($V \approx C_0$), the characteristic width (Eq. (4.12)) normalized by the distance between two supports reads

$$\frac{\Lambda_{1/2}}{L_0} = \frac{1.7627\Lambda}{L_0} \approx 1.7627 \sqrt{\frac{-12C_0^2 a_4}{\sigma \Delta \xi_m}} = 1.7627 \sqrt{\frac{-12P'\{\chi_0\} a_4}{(1-\chi_0)P''\{\chi_0\} \Delta \xi_m}}. \quad (4.25)$$

Using the load displacement relation derived in Chapter 2 (Eq. (2.43)), in a first approximation, $P''\{\chi_0\}/P'\{\chi_0\}$ is found dependent only to the strain χ_0 and the initial imperfection (for small buckling levels), but not on material neither on the cross-section properties. Moreover, from Fig. 3.15, it is shown that $a_4 \approx a_4\{\chi_0\}$ (the role of $m_{Support}$ on a_4 can be neglected in a first approximation) and is dimensionless. Finally, the ratio $\Lambda_{1/2}/L_0$ depends almost only on the compression level χ_0 and the wave amplitude.

In order to compare nonlinearity to dispersion, Eq. (4.22) is recast into a dimensionless form:

$$\xi_{\bar{t}\bar{t}} = \xi_{\bar{x}\bar{x}} + a_{0,4}\xi_{\bar{x}\bar{x}\bar{x}\bar{x}} + a_{2,2}\xi_{\bar{x}\bar{x}\bar{t}\bar{t}} + \bar{\sigma}(\xi^2)_{\bar{x}\bar{x}}, \quad (4.26)$$

with $\bar{\sigma} = \frac{\sigma}{2C_0^2}$, $\bar{x} = \frac{x}{L_0}$ and $\bar{t} = \frac{C_0}{L_0} t$. For both support types, the coefficients of the semi-analytical dispersion equation ($a_{0,4}$, $a_{2,2}$, and a_4) as well as the dimensionless nonlinear term $\bar{\sigma}$ are plotted in Fig. 4.4 in terms of the pre-compression χ_0 .

For the case of guided supports, the first comment due in Fig. 4.4a is that the main contribution to the total dispersion (a_4) is the transverse inertia ($a_{2,2}$) for small buckling level and periodicity ($a_{0,4}$) otherwise. The sign of a_4 is important in that it determines the wave speed in the case of guided supports which is supersonic ($a_4 < 0$). For the pinned-support configuration, the main contribution to a_4 is from $a_{0,4}$ which accounts for both dispersion induced by periodicity and coupling effects. However, since the dimensionless periodicity dispersion is $-1/12$ (see Eq. (4.23)) and is really different from $a_{0,4}$ (Fig. 4.4b), coupling effects are dominant. Noting now that a_4 is positive except for extremely large compression, subsonic and supersonic solitary waves are respectively expected for $\chi_0 > \chi_\gamma$ and $\chi_0 < \chi_\gamma$ (see Table 4.1), where $\chi_\gamma \approx 0.85$.

Concerning nonlinearity, its sign also influences the type of solitary wave since $\text{sgn}(\Delta \xi_m) = -\text{sgn}(a_4)\text{sgn}(\bar{\sigma})$, where $\bar{\sigma}$ is found negative for $\chi_0 < \chi_\sigma$ and positive for $\chi_0 > \chi_\sigma$ whatever the support configuration (see Fig. 4.4), and $\chi_\sigma \approx 0.081$ is the level of pre-compression for which there is an inflection in the load-displacement curve (Fig. 4.2).

Combining the sign of dispersive and nonlinear terms, four kinds of waves are possible: compressive supersonic, compressive subsonic, rarefaction supersonic, and rarefaction subsonic waves. What is particularly interesting with buckled beams is that varying the level of the pre-compression and the support type, a configuration for each of the four different wave types can be obtained, as shown in Table 4.1. Furthermore, with pinned supports, simply

Chapter 4. Nonlinear Wave Propagation In Buckled Beam: Models And Simulations

varying pre-compression gives three different wave types.

Table 4.1: Solitary waves characteristics in terms of the sign of the nonlinear $\bar{\sigma}$ and dispersive a_4 terms (Fig. 4.4).

$\text{sgn}(\bar{\sigma})$	$\text{sgn}(a_4)$	Shape behavior	Speed behavior	Configurations	Symbol
+	-	Compression	Supersonic	Guided: $\chi_0 > \chi_\sigma$ Pinned: $\chi_0 > \chi_\gamma$	\nearrow
-	-	Rarefaction	Supersonic	Guided: $\chi_0 < \chi_\sigma$	\searrow
+	+	Rarefaction	Subsonic	Pinned: $\chi_\sigma < \chi_0 < \chi_\gamma$	\swarrow
-	+	Compression	Subsonic	Pinned: $\chi_0 < \chi_\sigma$	\nwarrow

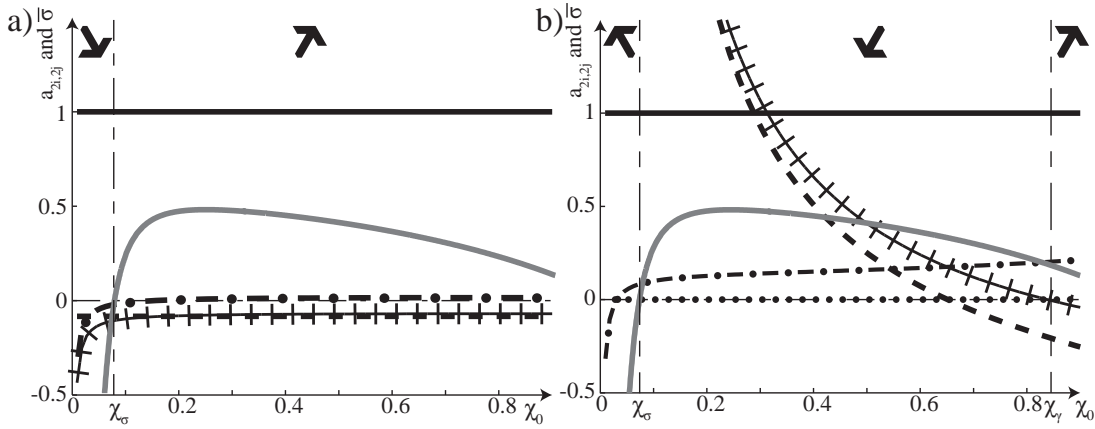


Figure 4.4: Dimensionless nonlinear and dispersive coefficients, in terms of the pre-compressive strain χ_0 for the guided (a) and pinned (b) support configurations. $a_{0,2} = 1$ in full, $a_{0,4}$ in dashed, $a_{2,2}$ in dashed-dotted, a_4 in + dark, and $\bar{\sigma}$ in full gray lines. See Table 4.1 for arrow notation.

However, the amplitude range $\Delta\xi_m$ for which solitary waves are expected is limited by two phenomena. Indeed, the dynamic wave cannot cross the snapping point ($\chi_0 = 0$) or the inflection point ($\chi_0 = \chi_\sigma$) either in compression or in tension, since the static curve $P\{\Delta U_0\}$ is not defined for $\chi_0 < 0$ and is linear for $\chi_0 = \chi_\sigma$. The second constraint applies only for a_4 positive (pinned-support configuration with $\chi_0 < \chi_\gamma$) and is such that the subsonic wave speed has to remain real (see Eq. (4.11)). While the equations governing the constraints on $\Delta\xi_m$ are given in Table 4.2, numerical results are shown in Fig. 4.5.

To conclude, it has been shown here that updating dispersion by including mass and stiffness coupling leads again to a solitary wave. The variety of wave types in buckled-beams is evident in that four different waves (rarefaction/compression shapes and supersonic/subsonic speeds) can be obtained changing only the support-type and the pre-compression level (Table 4.1). The goal is next to investigate nonlinear wave propagation for large amplitude or small pre-compression, where the Boussinesq model is not valid.

4.4. Solitary waves including mass and stiffness coupling

Table 4.2: Constraints on the upper bound of the wave amplitude $|\Delta\xi_m|$ given by the fact that the dynamic wave cannot cross the snapping point ($\chi_0 = 0$) or the inflection point ($\chi_0 = \chi_\sigma$) and also limited by the fact that the subsonic speed cannot be imaginary.

Configuration	$P\{\Delta U_0\}$	Speed real (Eq. (4.11))
Guided: $\chi_0 < \chi_\sigma$	$ \Delta\xi_m < \chi_0 L/L_0$	\emptyset
Guided: $\chi_0 > \chi_\sigma$	\emptyset	\emptyset
Pinned: $\chi_0 < \chi_\sigma$	$ \Delta\xi_m < (\chi_\sigma - \chi_0) L/L_0$	$ \Delta\xi_m < 3C_0^2/\sigma$
Pinned: $\chi_\sigma < \chi_0 < \chi_\gamma$	$ \Delta\xi_m < (\chi_0 - \chi_\sigma) L/L_0$	$ \Delta\xi_m < 3C_0^2/\sigma$
Pinned: $\chi_0 > \chi_\gamma$	\emptyset	\emptyset

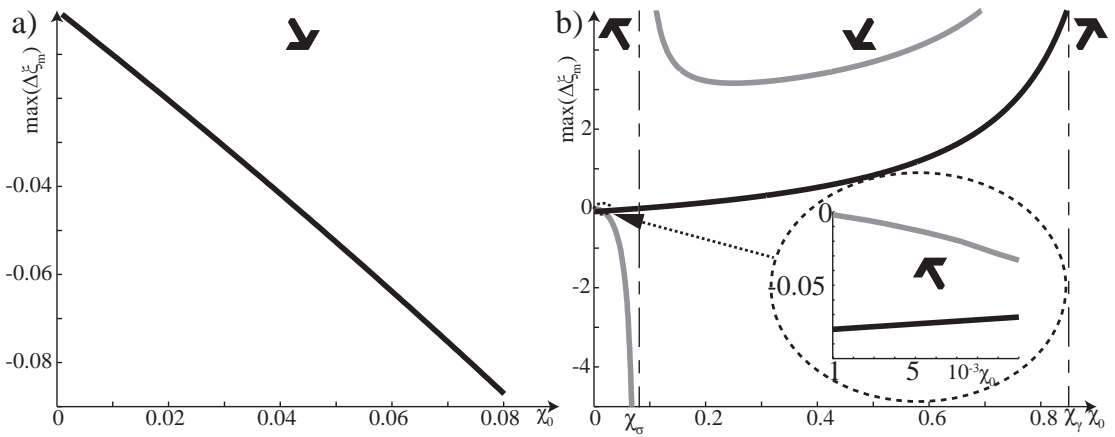


Figure 4.5: Maximum value of $\Delta\xi_m$ for the guided (a) and pinned-support (b) configurations in terms of the pre-compression χ_0 computed using the rules given in Table 4.2. Limitations arising from the load-deformation behavior shown in black lines, and real speed in gray lines. See Table 4.1 for arrow notation.

4.4.2 Strongly nonlinear models

For nonlinear waves with large amplitude or small pre-compression, the approximation of the load-displacement $P\{\Delta U\}$ by a second degree polynomial (Eq. (4.4)) is not accurate (see Fig. 4.2) but is used in the derivation of the generalized Boussinesq model. In this section, it is proposed the approximation of $P\{\Delta U\}$ by a power law. Where a power law or polynomial are not sufficient, $P\{\Delta U\}$ is retained as a general function.

Nonlinearity described by power law

Wave propagation in nonlinear media where the nonlinearity can be described locally by a power law

$$P\{\Delta U\} = a\Delta U^n + b, \quad (4.27)$$

is quite common and arises for example in describing wave propagation in granular media [Nesterenko, 2001, Sen et al., 2008] with $n = 3/2$ for spheres (Hertz law), and any $n > 0$ when the contact surfaces are not elliptical (Hertz-like law [Sun et al., 2011]). Here, the coefficients of Eq. (4.27) are given in terms of the local derivatives of the load-displacement such that $a = \frac{1}{m} \frac{P'\{\Delta U_0\}}{nU_0^{n-1}}$, $n = 1 + \Delta U_0 \frac{P''\{\Delta U_0\}}{P'\{\Delta U_0\}}$ and $b = P\{\Delta U_0\} - a\Delta U_0^n$, and note that $\text{sgn}(n) = \text{sgn}(a)$. Note also that as in Eq. (4.4), these coefficients refer up to the second derivative of $P\{\Delta U\}$. Nesterenko [Nesterenko, 2001] shows that chains of masses and nonlinear springs (Fig. 4.1c,

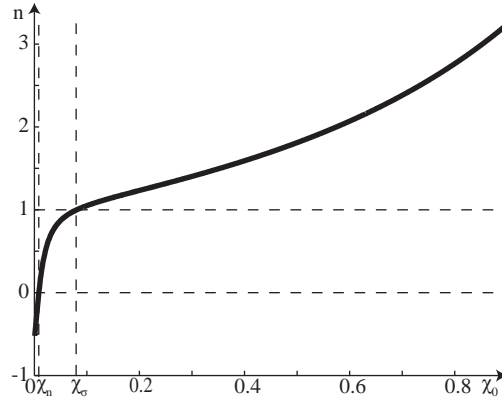


Figure 4.6: Power n of Eq. (4.27) in terms of the pre-compression χ_0 . Note that $n > 1$ for $\chi_0 > \chi_\sigma$, $n < 0$ for $\chi_0 < \chi_n$ and $n \in [0 1]$ otherwise.

and Eq. (4.3)) with the load-displacement $P\{\Delta U\}$ given by Eq. (4.27) are capable of hosting solitary waves for $n > 0$. However, as shown in Fig. 4.6 where the power n is plotted in terms of the pre-compression, for $\chi_0 < \chi_n = 8.8 \times 10^{-3}$, n and a are both negative and mathematical analyses for this case are not available. In this thesis, in addition to extending the work in [Nesterenko, 2001] to the case of $n < 0$, we will also consider adding terms to account for the additional dispersion sources. For the case of a buckled beam on guided supports ($a_{0,4} = -1/12$) modeled by a chain of nonlinear springs and masses, with the nonlinearity described by a power law, the momentum equation governing the n^{th} particle is:

$$\ddot{u}_n = \frac{a}{m} \left((U_{i-1} - U_i)^n - (U_i - U_{i+1})^n \right) - L_0^2 a_{2,2} U_{i,xxtt}, \quad (4.28)$$

where the first part of the right hand side accounts for nonlinearity and periodicity dispersion whereas the last term accounts for dispersion due to transverse inertial effects. In the long wave approximation, Eq. (4.28) can be homogenized into a strongly nonlinear wave equation [Nesterenko, 2001]:

$$\xi_{tt} = C_n^2 \left(\xi^n - a_{0,4} L_0^2 \frac{2n}{n+1} \xi^{\frac{n-1}{2}} \left(\xi^{\frac{n+1}{2}} \right)_{xx} \right) - L_0^2 a_{2,2} \xi_{xxtt}, \quad (4.29)$$

4.4. Solitary waves including mass and stiffness coupling

where $C_n^2 = \frac{a}{m} L_0^{n+1}$ and $\xi = -U_x$. Using the regularization $\xi_{tt} \approx C_n^2 (\xi^n)_{xx}$, Eq. (4.29) can be recast in:

$$\xi_{tt} = C_n^2 \left(\xi^n - a_{0,4} L_0^2 \frac{2n}{n+1} \xi^{\frac{n-1}{2}} \left(\xi^{\frac{n+1}{2}} \right)_{xx} - a_{2,2} L_0^2 (\xi^n)_{xx} \right)_{xx}. \quad (4.30)$$

Using the transformation

$$(\xi^n)_{xx} = \frac{2n}{n+1} \xi^{\frac{n-1}{2}} \left(\xi^{\frac{n+1}{2}} \right)_{xx} + \frac{n(n-1)}{2} \xi^{n-2} \xi_x^2, \quad (4.31)$$

Eq. (4.30) can be rewritten into two different forms:

$$\xi_{tt} = C_n^2 \left(\xi^n - a_4 L_0^2 \frac{2n}{n+1} \xi^{\frac{n-1}{2}} \left(\xi^{\frac{n+1}{2}} \right)_{xx} - a_{2,2} L_0^2 \frac{n(n-1)}{2} \xi^{n-2} \xi_x^2 \right)_{xx} \quad (4.32)$$

$$= C_n^2 \left(\xi^n - a_4 L_0^2 (\xi^n)_{xx} + a_{0,4} L_0^2 \frac{n(n-1)}{2} \xi^{n-2} \xi_x^2 \right)_{xx}. \quad (4.33)$$

However, contrary to [Nesterenko, 2001], due to the additional term in $a_{2,2}$, Eqs. (4.32) or (4.33) cannot be recast exactly into potential form, and it is necessary to neglect the last terms of these equations. Justification of this assumption will be given a posteriori by showing that results from truncated forms of Eqs. (4.32) and (4.33) are similar. In addition, for $|a_4| \gg |a_{2,2}|$, neglecting $a_{2,2}$ in Eq. (4.33) leads to Eq. (4.32) without its last term. Similarly, the use of the assumption $|a_4| \gg |a_{0,4}|$ in Eq. (4.32) leads to the truncated form of Eq. (4.33). Since the ratio $|a_{2,2}/a_{0,4}|$ is large for weakly buckled beams and small otherwise (Fig. 4.4), both equations are considered next.

Potential for Eq. (4.32)

Neglecting the last term of Eq. (4.32), this equation becomes identical to the one studied in [Nesterenko, 2001], and for $n > 1$ and $0 < n < 1$, respectively compressive and rarefaction solitary waves are possible solutions. However, for $n < 0$, since $a < 0$, $C_n = \sqrt{\frac{a}{m} L_0^{n+1}}$ is purely imaginary. Note that the long wave sound speed $C_0 = j C_n \sqrt{n} \xi_0^{\frac{n-1}{2}}$ with $j = \text{sgn}(n)$, remains real ($\xi_0 = \Delta U_0 / L_0 \neq \chi_0 = \Delta U_0 / L$). In order to recast Eq. (4.32) in form of a potential $W\{z\}$ such that

$$z_{xx} = - \frac{dW\{z\}}{dz}, \quad (4.34)$$

Nesterenko uses the change of variables $z = \xi^{\frac{n+1}{2}} \left(\frac{C_n}{V} \right)^{\frac{n+1}{n-1}}$ but with $n < 0$, z becomes a complex number and the one-to-one relation between z and ξ is lost. In the present work, an update in

the change of variables is proposed and reads:

$$z = \xi^{\frac{n+1}{2}} \left(j \left(\frac{C_n}{V} \right)^2 \right)^{\frac{n+1}{2(n-1)}}. \quad (4.35)$$

In the case of stationary waves, $z = z\{x - Vt\}$ and using the boundary conditions

$$\lim_{x=\pm\infty} \xi = \xi_0 \text{ and } \lim_{x=\pm\infty} \xi_x = \lim_{x=\pm\infty} \xi_{xx} = 0, \quad (4.36)$$

Eq. (4.32) can be rewritten in the form of a potential $W\{z\}$:

$$W\{z\} = -\frac{n+1}{2na_4L_0^2} \left(\frac{1}{2}z^2 - j\frac{n+1}{4}z^{\frac{4}{n+1}} + Cz^{\frac{2}{n+1}} \right). \quad (4.37)$$

Using the fact that $z_{xx}|_{\xi=\xi_0} = 0$, the constant C is

$$C = \frac{n+1}{2} \left(jz_0^{\frac{2}{n+1}} - z_0^{\frac{2n}{n+1}} \right), \quad (4.38)$$

where $z_0 = z\{\xi_0\}$. In order to have localized stationary waves, the potential must have two extremes and following the procedure in [Nesterenko, 2001], C has to comply with Table 4.3 which is validated numerically for the full range of compression levels ($0 < \chi_0 < 0.9$). The

Table 4.3: Constraints on C with $N_1 = \frac{n^2-1}{2}(jn)^{n/(1-n)}$ derived following [Nesterenko, 2001].

$1 < n$	$0 < n < 1$	$-1 < n < 0$	$n < -1$
$0 < C < N_1$	$N_1 < C < 0$	$C < N_1$	$N_1 < C$

shape of the solitary wave is obtained by recasting Eq. (4.34) into an elliptical integral

$$x = \int_z^{z_m} \frac{dz}{\sqrt{2(W\{z_0\} - W\{z\})}}, \quad (4.39)$$

which is solved numerically and $z_m = z\{\xi_m\}$ where ξ_m is the maximum strain. In order to compare the wavelength of this solitary wave to simulations, the width of the wave at half of its amplitude is used and reads:

$$\Lambda_{1/2} = 2 \int_{\frac{z_0+z_m}{2}}^{z_m} \frac{dz}{\sqrt{2(W\{z_0\} - W\{z\})}}. \quad (4.40)$$

Using the fact that $W\{\xi_m\} = W\{\xi_0\}$, the solitary wave speed is:

$$V = \frac{C_n}{|\xi_m - \xi_0|} \left(2 \frac{n\xi_0^{n+1} + \xi_m^{n+1} - (n+1)\xi_0^n \xi_m}{n+1} \right)^{1/2}. \quad (4.41)$$

Potential for Eq. (4.33)

The same procedure developed in Sec. 4.4.2 can be applied to Eq. (4.33) using the change of variable:

$$z = \xi^n \left(j \left(\frac{C_n}{V} \right)^2 \right)^{\frac{n}{n-1}}. \quad (4.42)$$

Eq. (4.33) can be rewritten in potential form:

$$W\{z\} = -\frac{1}{a_4 L_0^2} \left(\frac{1}{2} z^2 - j \frac{n}{n+1} z^{\frac{n+1}{n}} + Cz \right), \quad (4.43)$$

where the constant $C = jz_0^{1/n} - z_0$ has to fulfill the conditions given in Table 4.4 which are validated numerically for the compression level $0 < \chi_0 < 0.9$. The shape of the solitary wave is

Table 4.4: Constraints on C with $N_2 = (n-1)(jn)^{n/(1-n)}$.

$1 < n$	$0 < n < 1$	$n < 0$
$0 < C < N_2$	$C < N_2 < 0$	$C < N_2$

given by Eq. (4.39) and the solitary wave speed is:

$$V = C_n |\xi_m^n - \xi_0^n| \left(\frac{n+1}{2(\xi_0^{n+1} + n\xi_m^{n+1} - (n+1)\xi_0\xi_m^n)} \right)^{1/2}. \quad (4.44)$$

For the sake of clarity, up to this point, we have restricted ourselves to the case of guided supports (see Eq. (4.28)). Pinned-support configurations can be considered as well but the $z = z\{\xi\}$ relation is not invertible analytically anymore. As a consequence, it is not possible to get analytical expressions for the potential or the phase speed, so that the simplicity of using the power law approximation compared to the use of the general relation $P\{\Delta U\}$ is lost, as it will be shown in next section.

Nonlinearity described by general function

Instead of approximating the load-displacement relation by an analytical equation (second degree polynomial Eq. (4.4) or power law Eq. (4.27)), in this section this relation is kept general. The momentum equation of the n^{th} particle of the chain is:

$$\ddot{u}_n = \frac{1}{m} (P\{U_{i-1} - U_i\} - P\{U_i - U_{i+1}\}) - L_0^2 \left(a_{0,4}^{\text{No}C_0} C_0^2 U_{i,xxxx} + a_{2,2} U_{i,xtt} \right), \quad (4.45)$$

where the first part of the right hand side accounts for nonlinearity and dispersion proportional to the linear speed, whereas the following two terms account for the rest of the dispersion

sources with

$$a_{0,4} = a_{0,4}^{C_0} + a_{0,4}^{\text{No}C_0}, \quad (4.46)$$

and $a_{0,4}^{C_0} = -\frac{1}{12} \cdot a_{0,4}^{\text{No}C_0}$ is null for the case of the guided supports and defined by Eq. (4.4) for the case of the pinned supports. This equation, in the case of dispersion induced purely by periodicity ($a_{0,4}^{\text{No}C_0} = a_{2,2} = 0$), has been already analyzed in [Nesterenko, 2001] and following the same procedure, Eq. (4.45) is homogenized into a nonlinear wave equation:

$$\xi_{tt} = \frac{1}{\rho_0} \left(P - a_{0,4}^{C_0} L_0^2 \sqrt{P'} \left(\int_{\xi_0}^{\xi} (P')^{1/2} d\xi \right)_{xx} \right)_{xx} - L_0^2 \left(a_{0,4}^{\text{No}C_0} C_0^2 \xi_{xxxx} + a_{2,2} \xi_{xxtt} \right), \quad (4.47)$$

where $\rho_0 = \frac{m}{L_0}$, $P = P\{L_0\xi\}$ and $(\cdot)'$ denotes now the derivative with respect to ξ . Using the equality $C_0^2 = \frac{P'}{\rho_0}$ where $P_0 = P\{L_0\xi\}|_{\xi=\xi_0}$, the regularization method ($\xi_{tt} \approx P_{xx}/\rho_0$) leads to:

$$\xi_{tt} = \frac{L_0^2}{\rho_0} \left(\frac{P}{L_0^2} - a_{0,4}^{C_0} \sqrt{P'} \left(\int_{\xi_0}^{\xi} (P')^{1/2} d\xi \right)_{xx} - a_{2,2} P_{xx} - a_{0,4}^{\text{No}C_0} P'_0 \xi_{xx} \right)_{xx}. \quad (4.48)$$

Note that using the change of variable $\xi = \xi_0 + \Delta\xi$, expansion of Eq. (4.30) into series assuming $\Delta\xi$ small gives back the generalized Boussinesq equation (Eq. (4.22)). Using the transformations

$$P_{xx} = \sqrt{P'} \left(\int_{\xi_0}^{\xi} (P')^{1/2} d\xi \right)_{xx} + \frac{P''}{2} \xi_x^2, \quad (4.49)$$

and

$$\xi_{xx} = \sqrt{P'} \left(\int_{\xi_0}^{\xi} (P')^{-1/2} d\xi \right)_{xx} + \frac{P''}{2P'} \xi_x^2, \quad (4.50)$$

Eq. (4.48) can be recast into two different forms:

$$\begin{aligned} \xi_{tt} &= \frac{L_0^2}{\rho_0} \left(\frac{P}{L_0^2} - \sqrt{P'} \left(\left(a_{2,2} + a_{0,4}^{C_0} \right) \int_{\xi_0}^{\xi} (P')^{1/2} d\xi + a_{0,4}^{\text{No}C_0} P'_0 \int_{\xi_0}^{\xi} (P')^{-1/2} d\xi \right)_{xx} \right. \\ &\quad \left. - \xi_x^2 \left(a_{2,2} \frac{P''}{2} + a_{0,4}^{\text{No}C_0} \frac{P'_0 P''}{2P'} \right) \right)_{xx} \end{aligned} \quad (4.51)$$

$$= \frac{L_0^2}{\rho_0} \left(\frac{P}{L_0^2} - \left(\left(a_{2,2} + a_{0,4}^{C_0} \right) P + a_{0,4}^{\text{No}C_0} P'_0 \xi \right)_{xx} + a_{0,4} \frac{P''}{2} \xi_x^2 \right)_{xx}. \quad (4.52)$$

In order to recast these equations into potential form, the last term of Eqs. (4.51) or (4.52) has to be neglected, as done in Sec. 4.4.2 and is justified a posteriori.

Using the variable transformation $z = \left(a_{2,2} + a_{0,4}^{C_0} \right) \int_{\xi_0}^{\xi} (P')^{1/2} d\xi + a_{0,4}^{\text{No}C_0} P'_0 \int_{\xi_0}^{\xi} (P')^{-1/2} d\xi$ for Eq. (4.51) or $z = \left(a_{2,2} + a_{0,4}^{C_0} \right) P + a_{0,4}^{\text{No}C_0} P'_0 \xi$ for Eq. (4.52), in the case of stationary waves

$z = z\{x - Vt\}$, and using the boundary conditions of Eq. (4.36),

$$\frac{dW\{z\}}{dz} = -\frac{1}{L_0^2 F} (V^2 \rho_0 (\xi - \xi_0) - (P - P_0)), \quad (4.53)$$

where $\xi = \xi\{z\}$ and $F = \sqrt{P'}$ or $F = 1$, respectively for Eq. (4.51) and Eq. (4.52). The speed is derived using the equality $W\{\xi_m\} = W\{\xi_0\}$ and reads:

$$V^2 = \frac{1}{\rho_0} \frac{\int_{z_0}^{z_m} \frac{P-P_0}{F} dz}{\int_{z_0}^{z_m} \frac{\xi-\xi_0}{F} dz}, \quad (4.54)$$

where $z_0 = z\{\xi_0\}$, $z_m = z\{\xi_m\}$, and the shape of the solitary wave is obtained using Eq. (4.39). Note that contrary to the case of the power-law nonlinearity (Sec. 4.4.2), even for the guided-supports case ($a_{0,4}^{N_0 C_0} = 0$), the relation $z = z\{\xi\}$ is not invertible analytically meaning that the expression of the speed can be obtained only using numerical integration (Eq. (4.54)). The validity of these different models is investigated using FE simulations, which are introduced next.

4.5 Results and discussion

4.5.1 Comparison of the Boussinesq model to FE simulations

Guided-supported beam

Snapshots of the strain wave propagating through the guided-support beam for several levels of compression are shown in Fig. 4.7 where the input is either a compressive or a rarefaction wave, depending on the compression level (Table 4.1). In Figs. 4.7c,f, the wave propagates without any change in shape, in agreement with the stationary properties of solitary waves. In Figs. 4.7a-d, a small tail is present and propagates more slowly than the main wave, in agreement with the supersonic properties predicted by the Boussinesq model (Table 4.1). The fact that the input does not lead directly to the asymptotic solution shows that the Boussinesq model for such levels of compression is not accurate. This is particularly true in Fig. 4.7d where the initial guess splits into two distinct waves.

Additionally, in order to check if stationary waves are indeed nonlinear, the dependency of speed and wavelength on amplitude is shown in Fig. 4.8 in terms of the compression χ_0 and the dynamic-amplitude $\Delta\xi_m$. Figs. 4.8a,b show that the speed indeed increases whereas the wavelength decreases with the absolute amplitude, in agreement with the Boussinesq model. However, for weakly-compressed beams or large wave amplitudes, the values of the speed and wavelength extracted from FE simulations are not in agreement with the Boussinesq equation (Eq. (4.9)). This is due to the fact that for certain conditions, approximation of the load-displacement curve by a polynomial of degree two (Eq. (4.4)) is not accurate. Focusing

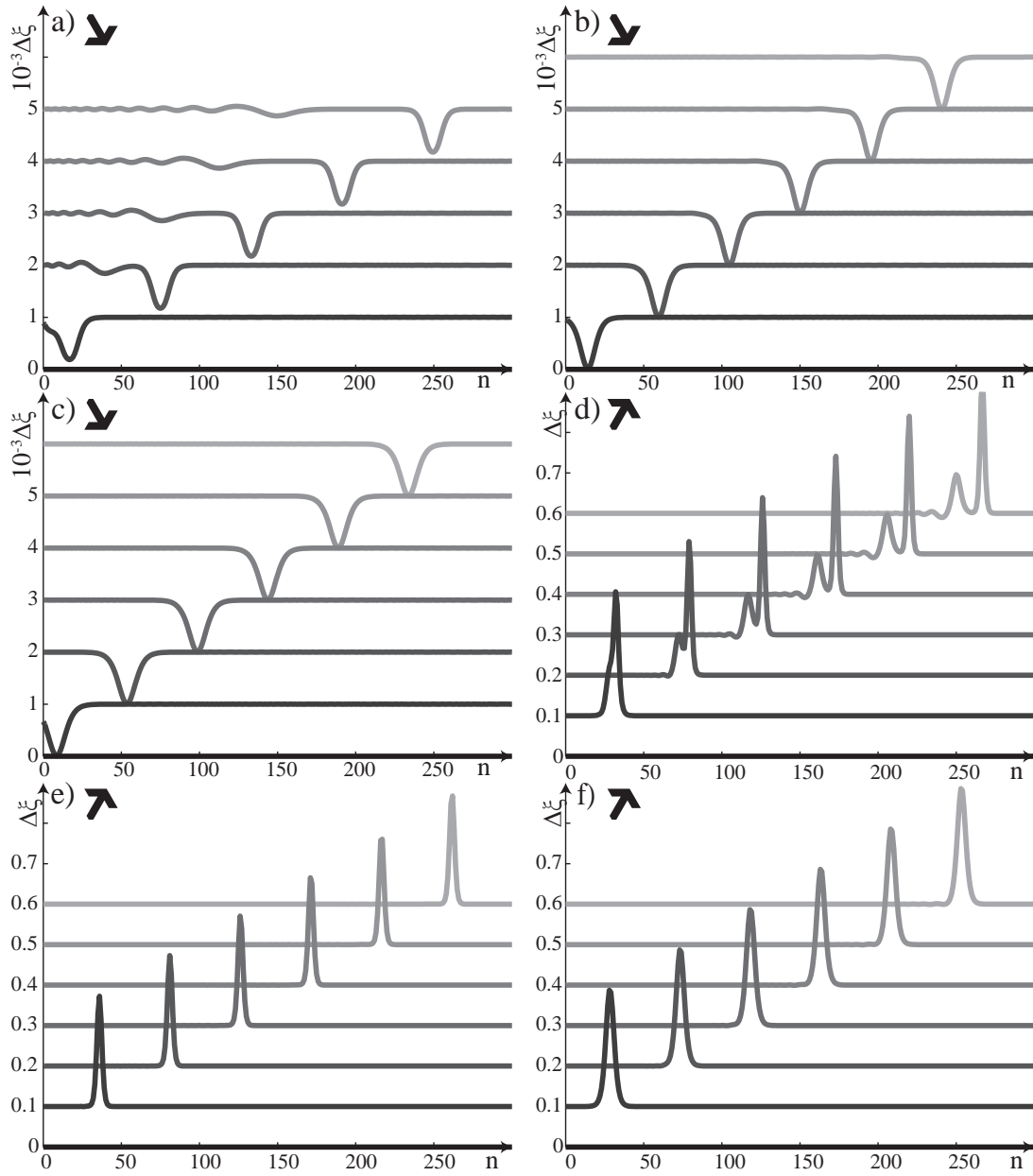


Figure 4.7: Snapshots at times multiple of $t_i = 3/20t_f$ of the strain wave propagating in the guided-supported buckled beam with the pre-compression $\chi_0 = 1 \times 10^{-3}$ (a), $\chi_0 = 5 \times 10^{-3}$ (b), $\chi_0 = 10 \times 10^{-3}$ (c), $\chi_0 = 0.1$ (d), $\chi_0 = 0.5$ (e) and $\chi_0 = 0.9$ (f), with dynamic input rarefaction $\Delta\xi_m = -1 \times 10^{-3}$ (a,b,c) and compressive $\Delta\xi_m = 0.3$ (e,f,g) waves. See Table 4.1 for arrow notation.

now on the wavelength, it is found that the characteristic width decreases when the dynamic wave amplitude increases and that the FE results match the Boussinesq model (Figs. 4.8c,d).

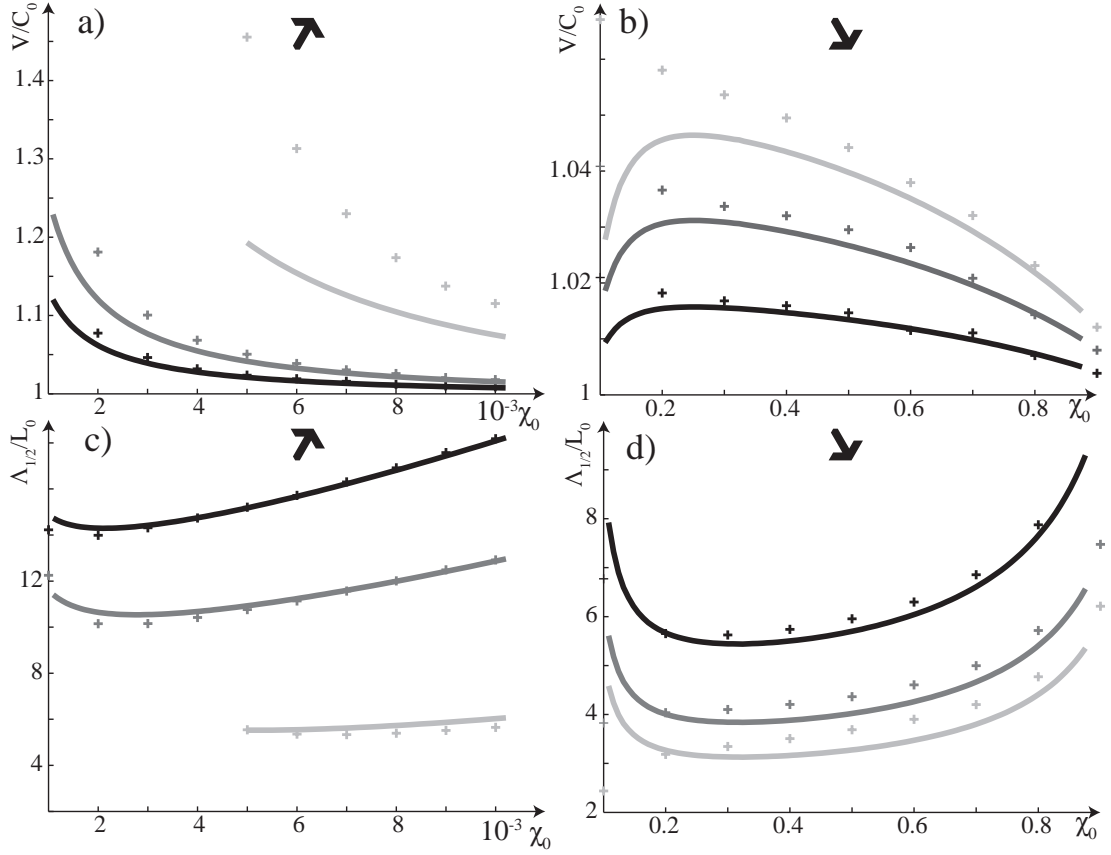


Figure 4.8: Normalized wave speed V/C_0 (Eq. (4.11)) (a,b) and normalized width at half amplitude $\Lambda_{1/2}/L_0$ (Eq. (4.12)) (c,d) in terms of the pre-compression χ_0 for the guided-support configuration, computed from the Boussinesq equation (full lines) or from simulations (+) with $\Delta\xi_m = -[0.5 \ 1 \ 5] \times 10^{-3}$ (a,c) and $\Delta\xi_m = [0.1 \ 0.2 \ 0.3]$ (b,d) respectively from dark to light gray. Note that no simulations were performed for the highest dynamic amplitude ($\Delta\xi_m = -5 \times 10^{-3}$) and small buckling level ($\chi_0 < 5 \times 10^{-3}$) since the dynamic wave cannot cross the snapping point ($\chi_0 = 0$), as shown in Fig. 4.5a. See Table 4.1 for arrow notation.

Pinned-supported beam

Simulations for wave propagation in pinned-support configurations using Eq. (4.14) as input are performed for several levels of compression and snapshots of the strain are shown in Fig. 4.9.

For $\chi_0 < \chi_\sigma$ (Fig. 4.9a-c), the input wave is compressive and a small front is present, in agreement with subsonic properties of the pinned-support beam for such level of compression (Table 4.1). This argument holds also for $\chi_\sigma < \chi_0 < \chi_\gamma$ (Fig. 4.9d,e) where a front is present too with a rarefaction wave. Finally, for $\chi_0 > \chi_\gamma$ (Fig. 4.9f), the input is in compression, but contrary to Fig. 4.9a-c, a tail is present, in agreement with the supersonic properties of strongly compressed pinned-support beams (Table 4.1).

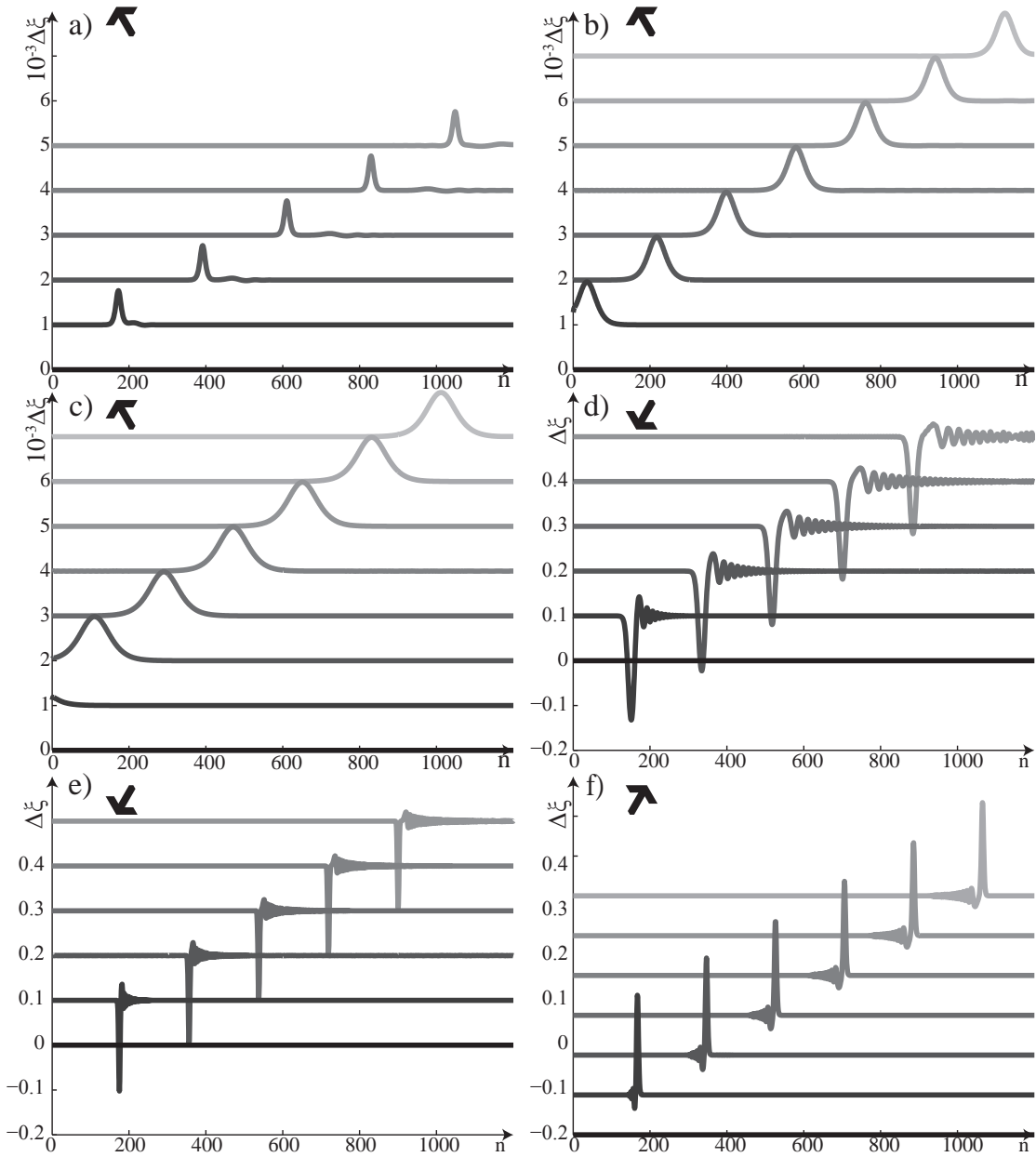


Figure 4.9: Snapshots at times multiple of $t_i = 3/20t_f$ of the strain wave propagating in the pinned-supported buckled beam with the pre-compression $\chi_0 = 1 \times 10^{-3}$ (a), $\chi_0 = 5 \times 10^{-3}$ (b), $\chi_0 = 10 \times 10^{-3}$ (c), $\chi_0 = 0.3$ (d), $\chi_0 = 0.8$ (e) and $\chi_0 = 0.9$ (f) with $\Delta\xi_m = 1 \times 10^{-3}$ (a,b,c), $\Delta\xi_m = -0.3$ (d,e) or $\Delta\xi_m = 0.3$ (f). See Table 4.1 for arrow notation.

The time required to obtain the asymptotic solution is now investigated. For $\chi_0 < \chi_\sigma$ (Fig. 4.9a-c), if a front is initially present, its separates quite readily from the main wave, in agreement with the subsonic properties of the solitary wave model. Note now that the number of unit cells compared to the guided-support configuration has been increased by a factor 4 due to the fact that for a given compression ΔU_0 , the linear speed in the pinned-support configuration

is 4 times smaller ($C_0^2 = P'\{\Delta U_0\}L_0^2/m$ and see $P\{\Delta U_0\}$ curve in Fig. 4.2). However, for $\chi_0 > \chi_\sigma$ (Fig. 4.9d-f), despite this extension, the length of the beam is just enough to see the beginning of the wave splitting but it is not immediately clear why the solitary wave takes so long to reach its asymptotic characteristics. In particular, if the wave propagation in the pinned configuration is compared to the one in the guided configuration for the same pre-compression $\chi_0 = 0.9$ (Figs. 4.7f and 4.9f), this phenomenon is present only in the case of pinned supports, whereas predicted wave behavior, nonlinearity, and wave amplitude are the same. The dispersion is also almost the same for this level of compression (Fig. 4.4). Nonlinear coupling between rotations and axial displacement, which is neglected, is weak so that any perturbation would require a large time to separate from the asymptotic solution.

The solitary wave speed and wavelength are plotted in Fig. 4.10 and compared to the Boussinesq solution. For $\chi_0 > \chi_\gamma$, the speed increases with the amplitude such that propagating waves are supersonic (Figs. 4.10b). On the contrary, for $\chi_0 < \chi_\gamma$, the waves are subsonic since the speed decreases when the amplitude increases (Figs. 4.10a,b). Finally, the computed wavelength trend is in agreement with the Boussinesq model although values do not match perfectly (Figs. 4.10c,d).

As before, although the trend of the wave speed and wavelength are in agreement with the Boussinesq equation, numerical values are not perfectly recovered specifically when increasing the amplitude for a fixed χ_0 or decreasing χ_0 for a fixed amplitude. Again this is explained by the fact that the local approximation of the load-displacement relation by a polynomial of degree two is not always appropriate. However, although the input does not correspond directly to the asymptotic solution, the conclusion of this part is that compressive supersonic, rarefaction supersonic, compressive subsonic and rarefaction subsonic solitary waves are obtained.

Soliton collisions

Solitary waves that are insensitive to collisions, beyond a phase shift are termed solitons and result from PDEs which are exactly integrable as the Boussinesq equation [Ablowitz, 2011]. However, the improved, the double-dispersive Boussinesq equations are only nearly integrable PDEs, and numerical simulations of such PDEs show some radiation after wave collisions [Bogolubsky, 1977, Soerensen, 1984]. Here, wave collision is obtained by exciting the left and right boundary of the structure with waves such that $U_{Right} = -U_{Left}$ (Eq. (4.14)). Snapshots of these waves are shown in Fig. 4.11 for the four different wave types described in Table 4.1. Solitary waves are found unchanged by collisions in Figs. 4.11a-c, whereas for Fig. 4.11d the presence of a front before the collision discredits direct observations. However, for this last example but not shown here, a single wave propagating in one direction only will give the same wave as the one propagating in Fig. 4.11d after the collision. The fact that elastic collisions are observed means either that the radiation is not perceptible or that the Boussinesq-type model is not accurate to describe wave propagation in buckled structures for a certain support type and pre-compression level.

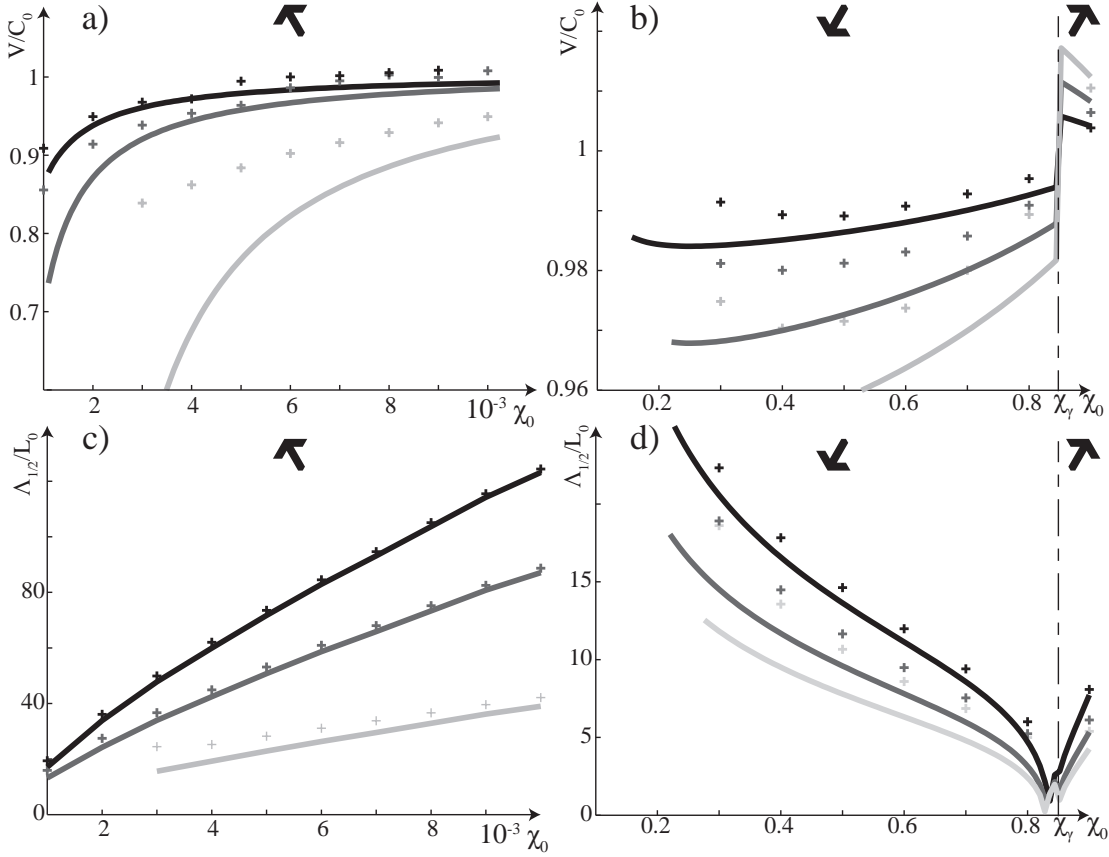


Figure 4.10: Normalized wave speed V/C_0 (Eq. (4.11)) (a,b) and normalized width at half amplitude $\Lambda_{1/2}/L_0$ (Eq. (4.12)) (c,d) in terms of the pre-compression χ_0 for the pinned-support configuration, computed from the Boussinesq equation (full lines) or from simulations (+) with $\Delta\xi_m = [0.5 \ 1 \ 5] \times 10^{-3}$ (a,c) and $|\Delta\xi_m| = [0.1 \ 0.2 \ 0.3]$ (b,d) respectively from dark to light gray. Note that no simulations were performed for the highest dynamic amplitude ($\Delta\xi_m = 5 \times 10^{-3}$) and small buckling level ($\chi_0 < 3 \times 10^{-3}$) since the wave speed cannot be imaginary (Fig. 4.5b). See Table 4.1 for arrow notation.

4.5.2 Comparison of the strongly nonlinear models to FE simulations

The phase speed in terms of the dynamic amplitude for solitary waves with different levels of compression is shown in Fig. 4.12. The speed V increases with amplitude, in agreement with supersonic properties of buckled beams with guided supports.

Expectedly, Eq. (4.54) based on the general relation $P\{\Delta U\}$ provides the best agreement with FE results. Models based on the power law approximation (Eqs. (4.41) and (4.44)) are generally acceptable except for moderated buckling levels, since $P\{\Delta U\}$ is not well approximated in this region (Fig. 4.2). For the Boussinesq model, the speed V is almost linear in $\Delta\xi_m$ ($\Delta\xi_m \ll 3C_0^2/\sigma$) and only the tangent at $V = C_0$ is in agreement with FE results. For increasing $\Delta\xi_m$, results differ and this is explained again by the fact that the load-displacement relation cannot be described by a second degree polynomial (Fig. 4.2). For strong pre-compression (Fig. 4.12f),

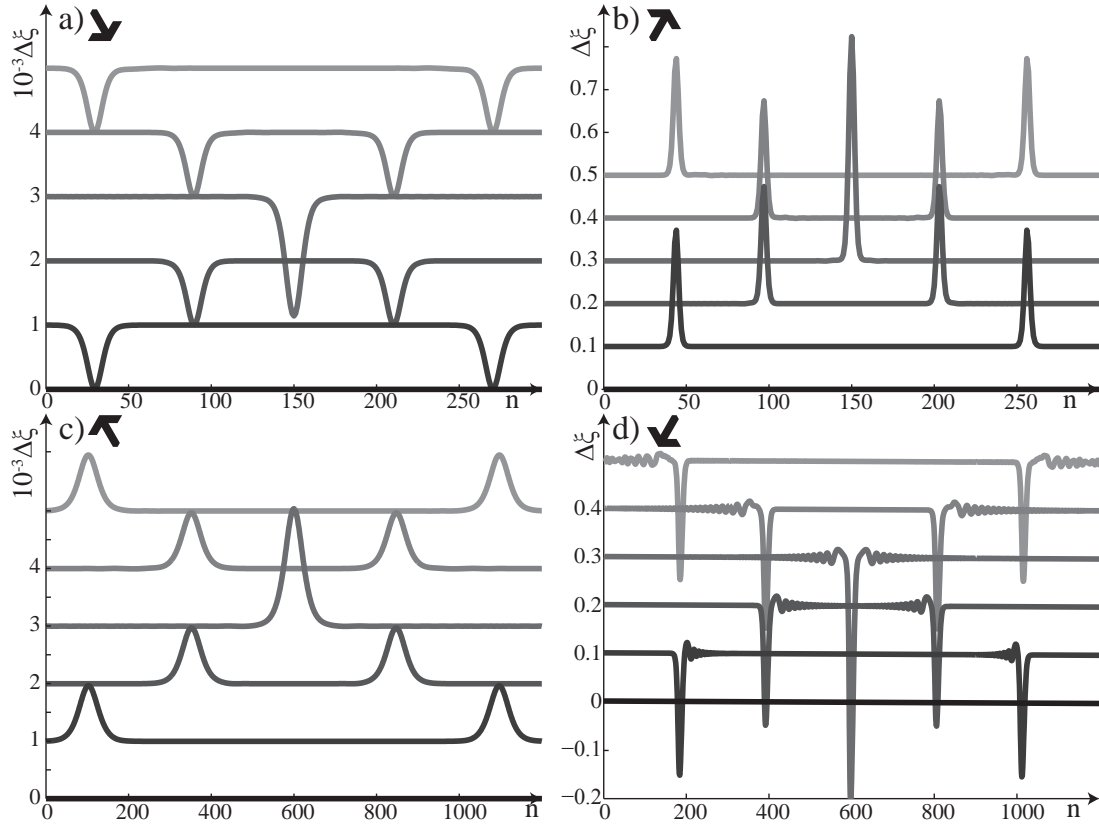


Figure 4.11: Snapshots of the collision of supersonic rarefaction (a), supersonic compressive (b), rarefaction subsonic (c) and compressive subsonic (d) strain waves given that the pre-compression is $\chi_0 = 5 \times 10^{-3}$ (a,c), $\chi_0 = 10 \times 10^{-3}$ (b,d), and the dynamic amplitude is $|\Delta\xi_m| = 1 \times 10^{-3}$ (a,c) and $|\Delta\xi_m| = 0.3$ (b,d). Time of snapshots is in multiples of 0.1137s (a), 0.0736s (b), 1.0403s (c) and 1.4613s (d) such that the fourth snapshot corresponds to the time with the maximum amplitude. See Table 4.1 for arrow notation.

all models are in agreement with FE results. This is explained by the fact that for such level, the dynamic amplitude of the wave relative to the pre-compression strain is small, justifying Eq. (4.4) or Eq. (4.27). Finally, note that the two models based on the power law (Eq. (4.32) and (4.33)) or the two models based on the general function (Eq. (4.51) and (4.52)) are similar validating the assumption to neglect the last terms of Eqs. (4.32), (4.33), (4.51) and (4.52). Since both models are similar, the ratio $|a_{2,2}/a_{0,4}|$ and so the choice of the model to use is not significant. Results for the case of pinned supports are not given since they provide similar conclusions.

Wavelength is less sensitive to $\Delta\xi_m$ (Fig. 4.13) compared to the speed (Fig. 4.12). Indeed, both the Boussinesq and the power law models disagree with FE simulations only for the case of $\chi_0 = 0.1$ (Fig. 4.13d), and this is explained by the fact that λ is mostly determined by C_0 .

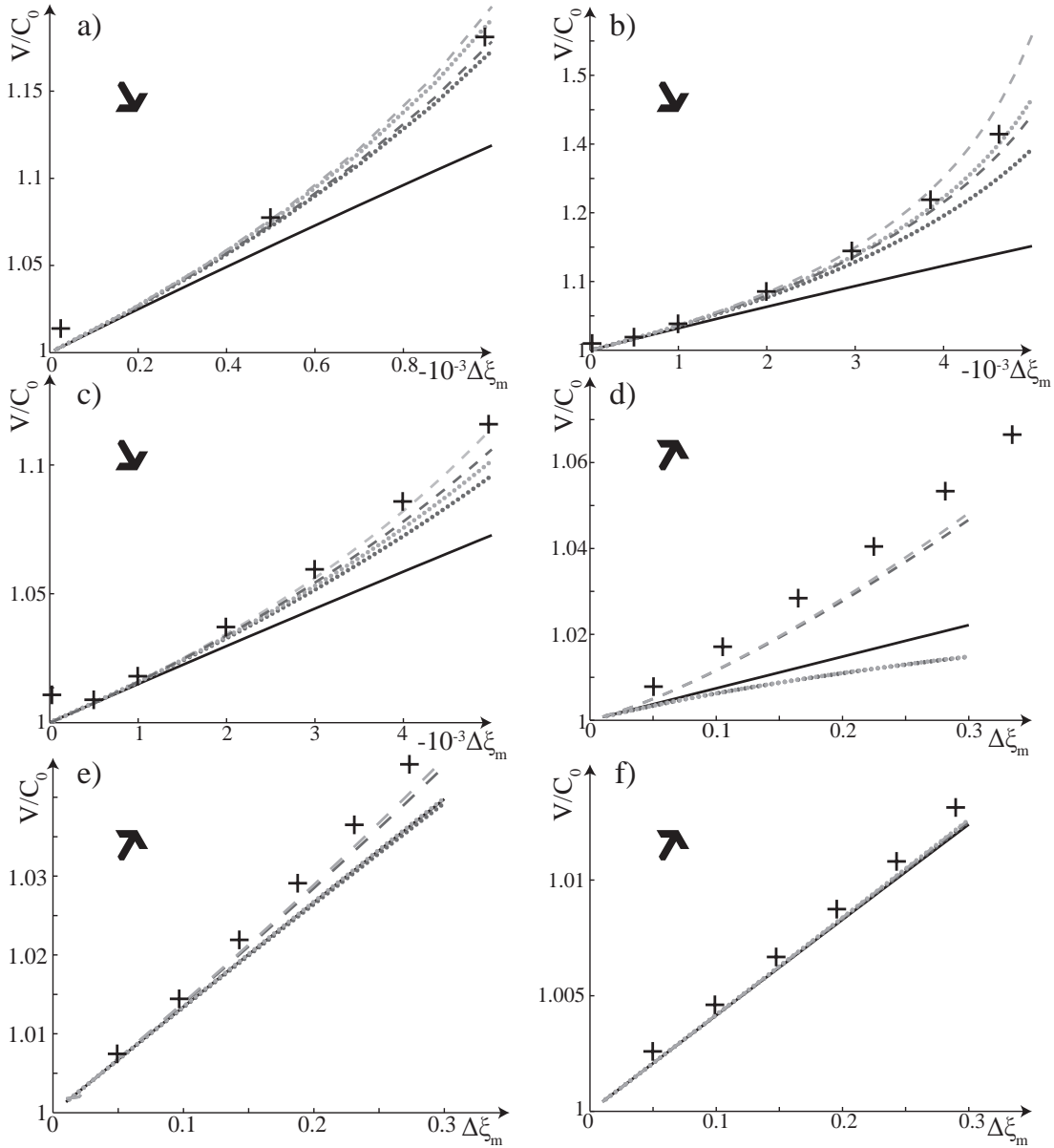


Figure 4.12: Normalized solitary wave speed V/C_0 in terms of the wave amplitude $|\Delta\xi_m|$ for the guided-support configuration with pre-compression $\chi_0 = 2 \times 10^{-3}$ (a), $\chi_0 = 6 \times 10^{-3}$ (b), $\chi_0 = 10 \times 10^{-3}$ (c), $\chi_0 = 0.1$ (d), $\chi_0 = 0.5$ (e) and $\chi_0 = 0.9$ (f). Results from FE simulations with (+), improved Boussinesq model Eq. (4.11) in full dark lines, power law with Eq. (4.32) in dark-gray dotted lines, power law with Eq. (4.33) in light-gray dotted lines, general function with Eq. (4.51) in dark-gray dashed lines and general function with Eq. (4.52) in light-gray dashed lines. See Table 4.1 for arrow notation.

4.6 Conclusions

Wave propagation in buckled beams is investigated and it is found that depending on the pre-compression and dynamic amplitude, various homogenized PDEs describe the propagation of

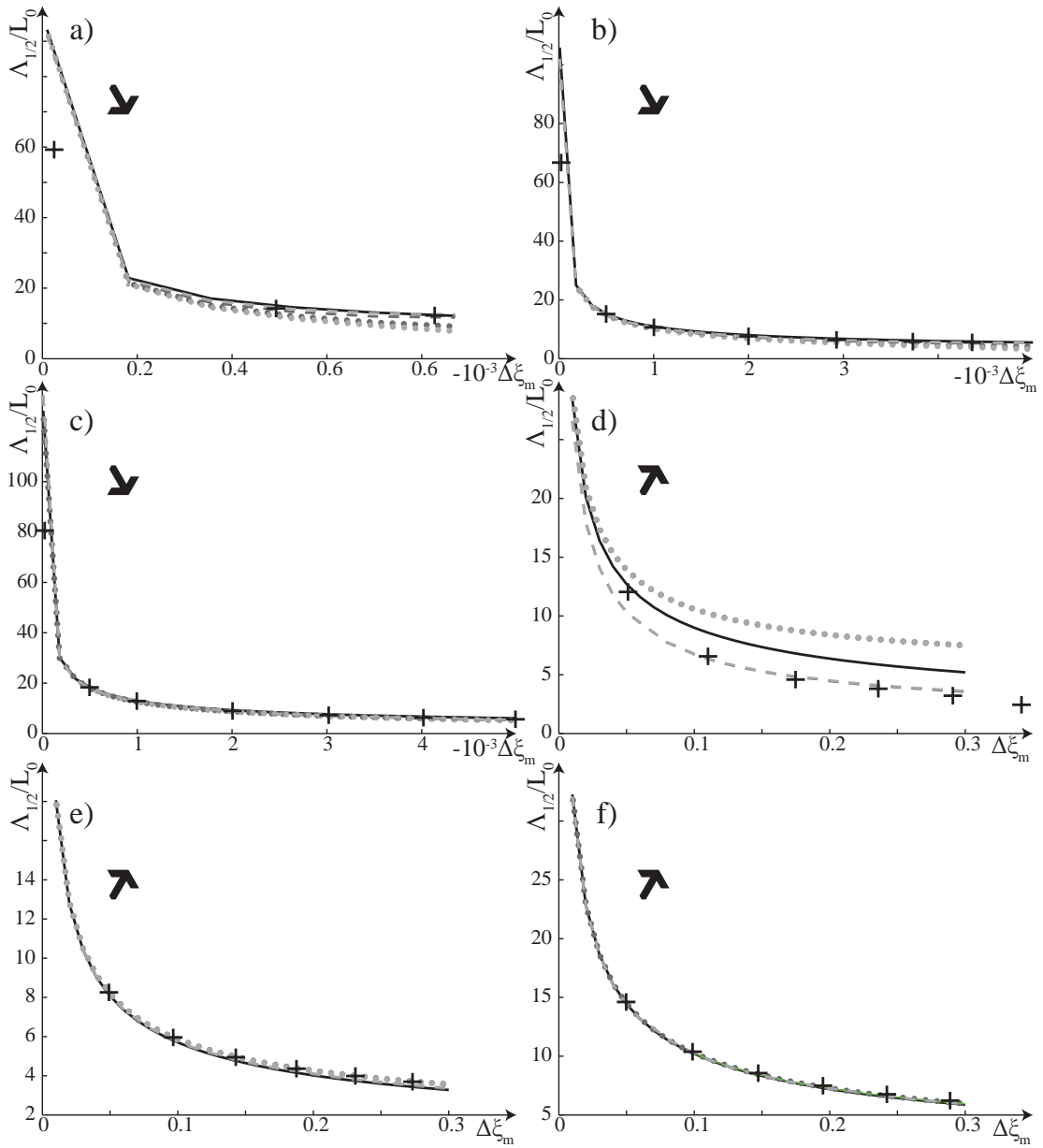


Figure 4.13: Normalized solitary wavelength $\Lambda_{1/2}/L_0$ in terms of the wave amplitude $|\Delta\xi_m|$ for the guided-support configuration with pre-compression $\chi_0 = 2 \times 10^{-3}$ (a), $\chi_0 = 6 \times 10^{-3}$ (b), $\chi_0 = 10 \times 10^{-3}$ (c), $\chi_0 = 0.1$ (d), $\chi_0 = 0.5$ (e) and $\chi_0 = 0.9$ (f). Results from FE simulations with (+), improved Boussinesq model Eq. (4.11) in full dark lines, power law with Eq. (4.32) in dark-gray dotted lines, power law with Eq. (4.33) in light-gray dotted lines, general function with Eq. (4.51) in dark-gray dashed lines and general function with Eq. (4.52) in light-gray dashed lines. See Table 4.1 for arrow notation.

stationary, non-linear waves. Where the load-deformation can be described by a polynomial of degree two, the Boussinesq equation can be employed. Even though the fidelity of predicted velocity and wavelength depend on appropriate representation of the load-displacement

Chapter 4. Nonlinear Wave Propagation In Buckled Beam: Models And Simulations

relation, the pre-compression level and support type furthermore determine dispersion characteristics of the resulting medium. This leads to the double-dispersion Boussinesq equation, from which it is shown that four types of solitary waves are possible. Namely combination of subsonic, supersonic, compressive and rarefaction waves. Where power-law and general load-displacement relations are required, strongly nonlinear PDEs results from homogenization. Existing techniques are extended here for solitary-wave solutions based on equivalent potentials. Finite element simulations validate analytical models. In conclusion, a qualitative prediction for the type of propagating wave, its speed and shape, various forms of the Boussinesq equation are the simplest model to implement and use. Homogenized PDEs based on the exact load-displacement relation provide best results but require numerical integration. For small buckling level and guided-supports, the model based on power law nonlinearities is also a good alternative.

5 Nonlinear Wave Propagation In Buckled Beam: Experiments

5.1 Introduction

In the previous chapter, it has been shown analytically and numerically that periodic buckled beams host stationary nonlinear waves. Moreover, by varying the pre-compression level and changing the support type, four different waves are possible, namely compressive supersonic, rarefaction supersonic, compressive subsonic and rarefaction subsonic solitary waves. While finite-element (FE) simulations of the structure have been performed validating the derived models, the aim of the proposed chapter is to repeat this work experimentally.

Although the support type changes the speed behavior (supersonic or subsonic medium) and the solitary wave type (compressive or rarefaction), in the present chapter, only guided supports are investigated since they are easier to realize experimentally.

From material considerations, an experimental limitation is the maximum reachable buckling level. While it has been shown that wave characteristics are also dependent on pre-compression, experimentally, only small buckling levels can be tested for metallic structures. Indeed, when the buckling is too high such that the material reaches its yield limit, plastic hinges occur and the structure collapses [Ehrlich and Armero, 2004]. Hyperelastic materials can be used to avoid plasticity [Bower, 2009], but are not investigated here.

This chapter is organized as follows: the experimental setup is presented and details on the signal acquisition and synchronization are given in Sec. 5.2. Results are presented in Sec. 5.3, investigating first static buckling and focusing then on the wave profile and its characteristics. Discussion and conclusion follow.

5.2 Experimental setup and signal acquisition

5.2.1 Experimental setup

A 2 m long continuous steel ribbon is periodically supported by 30 trolleys such that the supports are of guided type (Fig. 5.1). The ribbon (reference number *162830.0500* from *Brütsch-Rüegger*) is modeled as a beam and the following notation and numerical values are used: the cross-section area is A ($b = 12.7 \text{ mm} \times t = 0.4 \text{ mm}$) and the area-moment of inertia is $I_z = bt^3/12$; $E = 190 \text{ GPa}$ and $\rho = 7600 \text{ Kg m}^{-3}$ are respectively the measured Young modulus and density. Each trolley (model *SELB10* from *Misumi*) provides an additional mass of $2.4 \times 10^{-2} \text{ Kg}$ and the free distance between them is 60 mm.

The experiment is divided into two parts; a static one, where the pre-compression is applied and a dynamic one, where a wave is sent through the structure. The static load is applied with a screw (model *NSE5-SN* from *Nozag*) at the left side and carried at the right side by a spring (reference *8101-084928* from *Kubo*, with nominal rigidity of $K_{\text{spring}} = 7.9 \text{ Nmm}^{-1}$ and length of $L_{\text{spring}} = 41 \text{ mm}$). The load-displacement relation of one unit cell is then obtained after averaging the displacement between the screw and the spring, measured via two identical linear systems (*S System LIN*, $2 \mu\text{m}$ accurate, from *Sylvac*), and the force computed from the spring compression.

To generate a wave at the right extremity, a shaker is used and is directly connected to the spring (last trolley). The shaker model is *LDS V406M4* from *Brüel & Kjaer* and has internal axial stiffness $K_{\text{shaker}} = 12.3 \text{ Nmm}^{-1}$. The shaker is connected after applying the static load such that all the pre-compression is carried by the spring and not the shaker. Its displacement is recorded by a LVDT (model *WI/5mm-T* and a signal conditioner *MP55* from *HBM*).

The wave propagation throughout the structure was originally measured with accelerometers, but due to the problem arising from time integration and low frequency noise, a laser which give directly the speed is used instead (compact laser vibrometer *CLV 2534* from *Polytec*). Since the laser can record the speed at one point only, it is mounted on a positioning system (model *BiSlide* by *Velmex*) which can move along the beam. Note that in order to do so, the experiment is assumed reproducible.

5.2.2 Signal acquisition in *LabView*

In this thesis, all physical quantities measured experimentally are analogical. However, nowadays, analogical signals are no longer directly plotted analogically but they are stored and post-processed under numerical form. This requires the use of digital to analog converter (DAC) and the data acquisition system (DAQ) from *National Instruments (NI)* is used with the *NI PXIe-6368* and the *NI PXIe-4492* cards plugged into the *NI PXIe-1073* chassis. In addition, the *S System LIN Sylvac* sensor integrates its own DAC and communicates with the computer via a *RS – 232* serial standard.

5.2. Experimental setup and signal acquisition

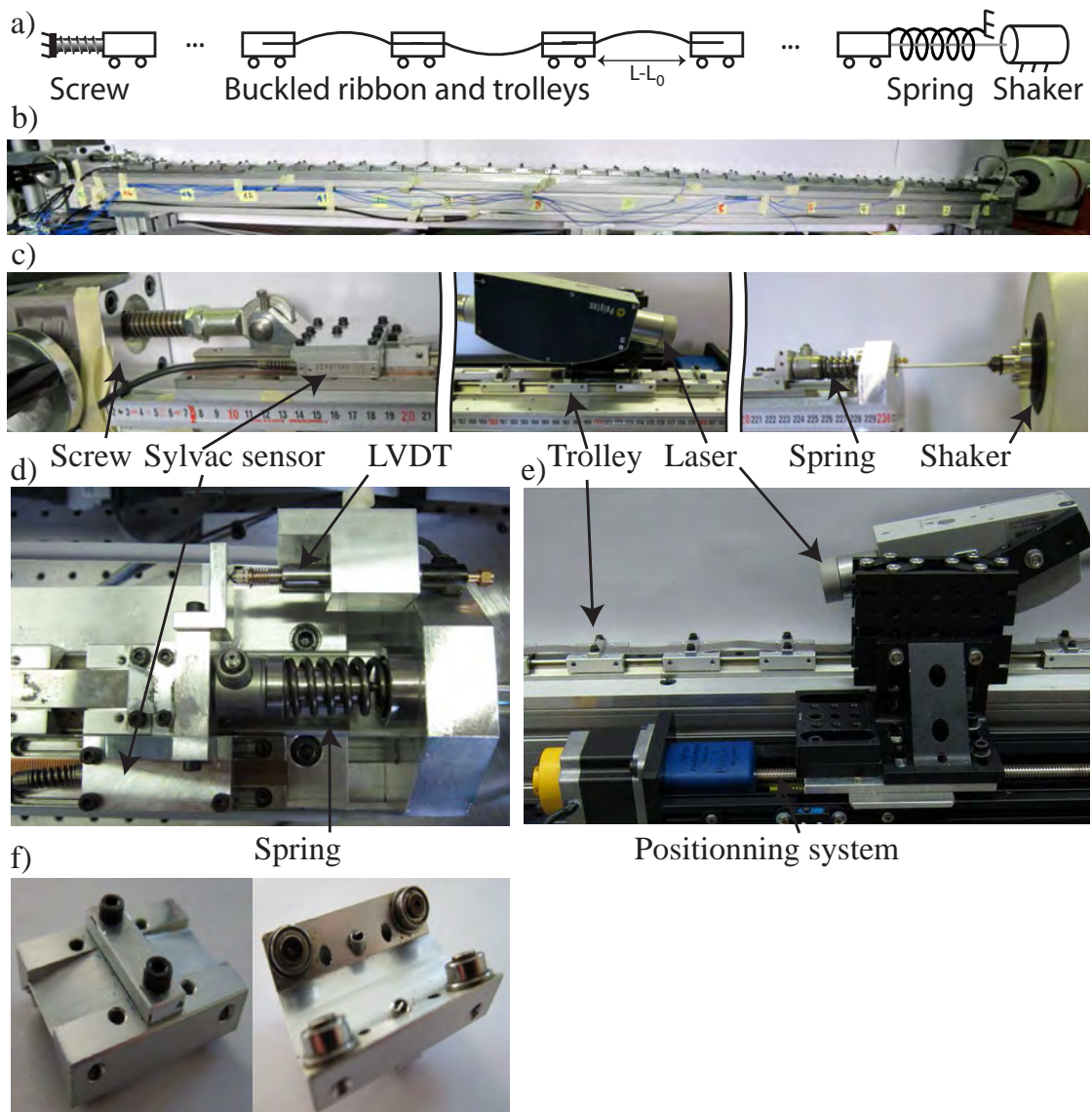


Figure 5.1: Experimental model (a) and full setup (b) with detailed views of the face (c), top right (d), back center (e), and trolley (f).

While all signals are recorded and post-processed via *LabView*, some challenges have been encountered to synchronize acquisition between the different signals and to establish the *RS-232* communication; it is the goal of this part to provide details and solutions to these issues. For this part, it is assumed the reader to have basic knowledge in *LabView* and data acquisitions.

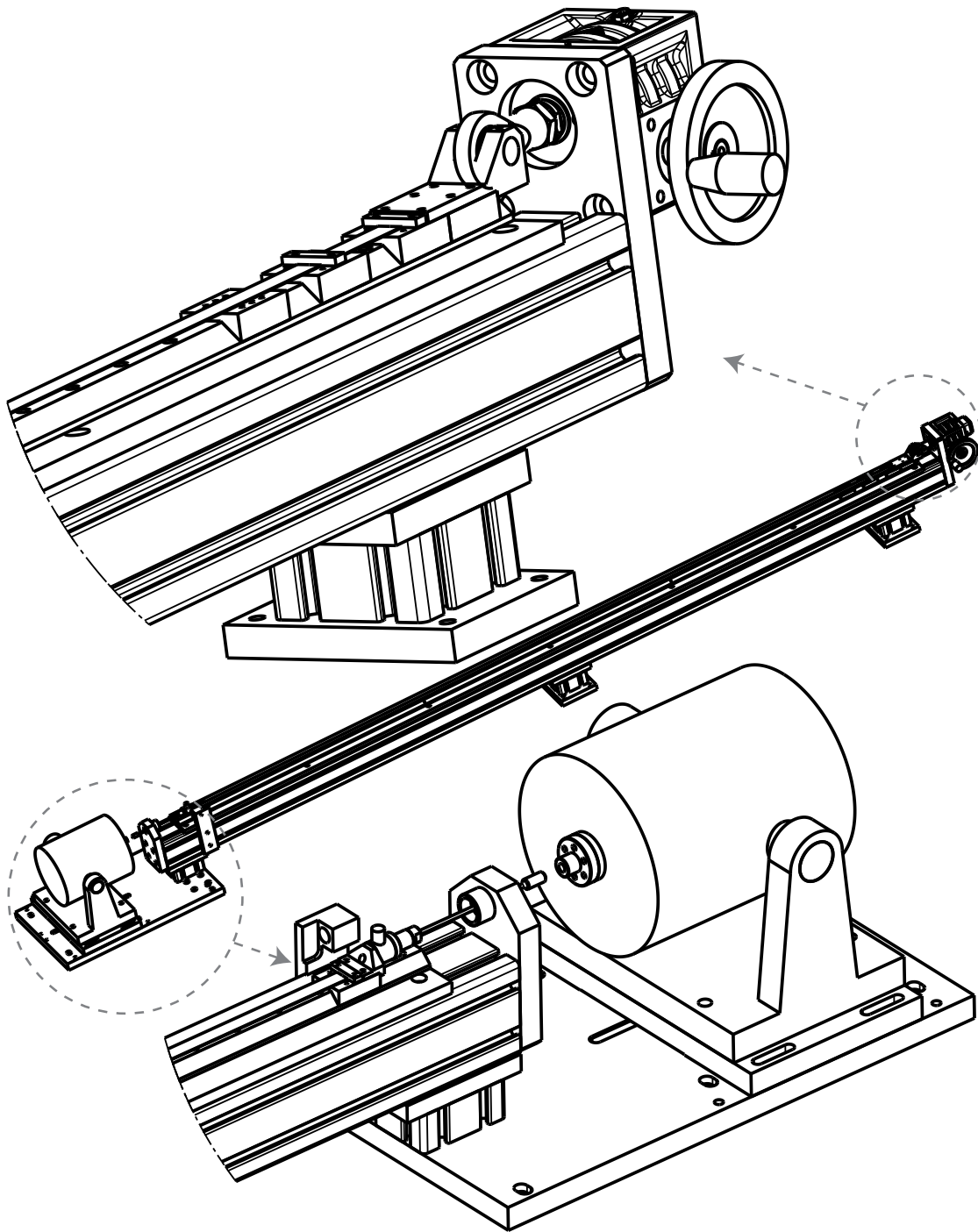


Figure 5.2: Isometric view with details area of the setup plan.

5.2.3 Synchronization of *NI* cards from different series via *LabView*

The displacement and speed measured via the LVDT and laser sensors are both analogical voltage inputs which are acquired via the *NI PXIe-6368* card. This card is also used to generate

5.2. Experimental setup and signal acquisition

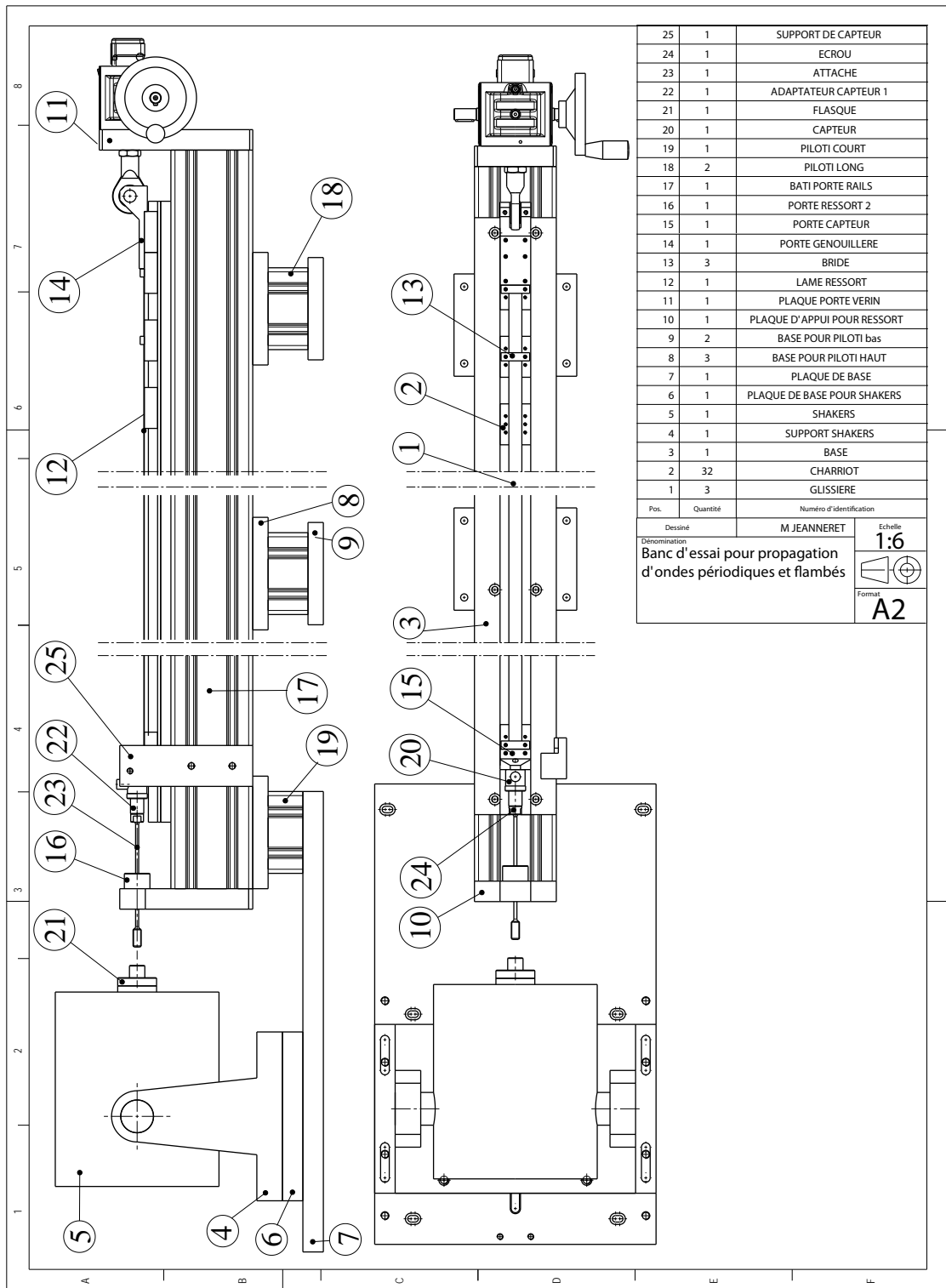


Figure 5.3: Face and top views of the setup plan.

Chapter 5. Nonlinear Wave Propagation In Buckled Beam: Experiments

the analogical voltage sent to the shaker. On the contrary, the *NI PXIe-4492* card is specific to the acquisition of analogical signals from sensors which are power amplified and use the integrated electronics piezo electric (IEPE) standard. This is the case of the accelerometers and load cell which were used in the first experimental investigations.

LabView provides direct access to *NI* acquisition cards via *DAQmx* libraries, which allow writing and read time signals. These operations are called tasks and three of them are defined:

- read voltage in the *NI PXIe-6368* card (measured by LVDT and laser sensors).
- write voltage in the *NI PXIe-6368* card (output signal sent to the shaker).
- read voltage in the *NI PXIe-4492* card from IEPE sensors (accelerometers and load cell).

Note that a task can be multichannel (e.g. several accelerometers) and the synchronization between its different channels is automatic.

The idea of synchronization between different tasks in *LabView* is to define a master and slaves. The master triggering setting is defined first, recorded and used next as a triggering source for slaves. The tasks are then started in the opposite order since the slaves have to be ready before the master operates (see Figs. 5.4 and 5.5 for implementation details).

While the order of the operation is imposed by the error dataflow (Fig. 5.4), synchronization between different tasks requires also the use of a common reference clock. If the different tasks are on the same card, they share the same reference clock while the same is not true for cards from different series (e.g. *NI PXIe-6368* and *NI PXIe-4492* cards). Instead of using the card clocks, the *NI PXIe-1073* chassis clock is used and is based on the communication bus PCI. Moreover, the “e” of “PXIe” stands for express (100 MHz) which is 10 times faster than the simple PCI version (10 MHz). However, although the internal clock of the *NI PXIe-6368* card is 100 MHz and is in agreement with the card reference, the one from the *NI PXIe-4492* is only 10 MHz. This means that *RefClk.Src* parameter have to be set to the minimum frequency (10 MHz) using the command *PXI_Clk10* (see Fig. 5.5). This limitation is not problematic since the sampling frequency is in the order of KHz.

5.2.4 *Sylvac* sensor and RS-232 communications in *LabView*

The *S System LIN Sylvac* sensor is different than classical sensors since the DAC is directly integrated into the sensor and is plugged to the computer via the *DB9* connector (also called port COM) and use the serial communication standard *RS – 232*.

LabView provides a library for serial communication called *VISA* and is working into three steps: the first one consist one the initialization of the connection, given parameters as the baud rate, the parity, the data bits, the termination character etc. which can be found in *Sylvac* documentation and which are given in Fig. 5.6a. Once initialized, writing and reading

5.2. Experimental setup and signal acquisition

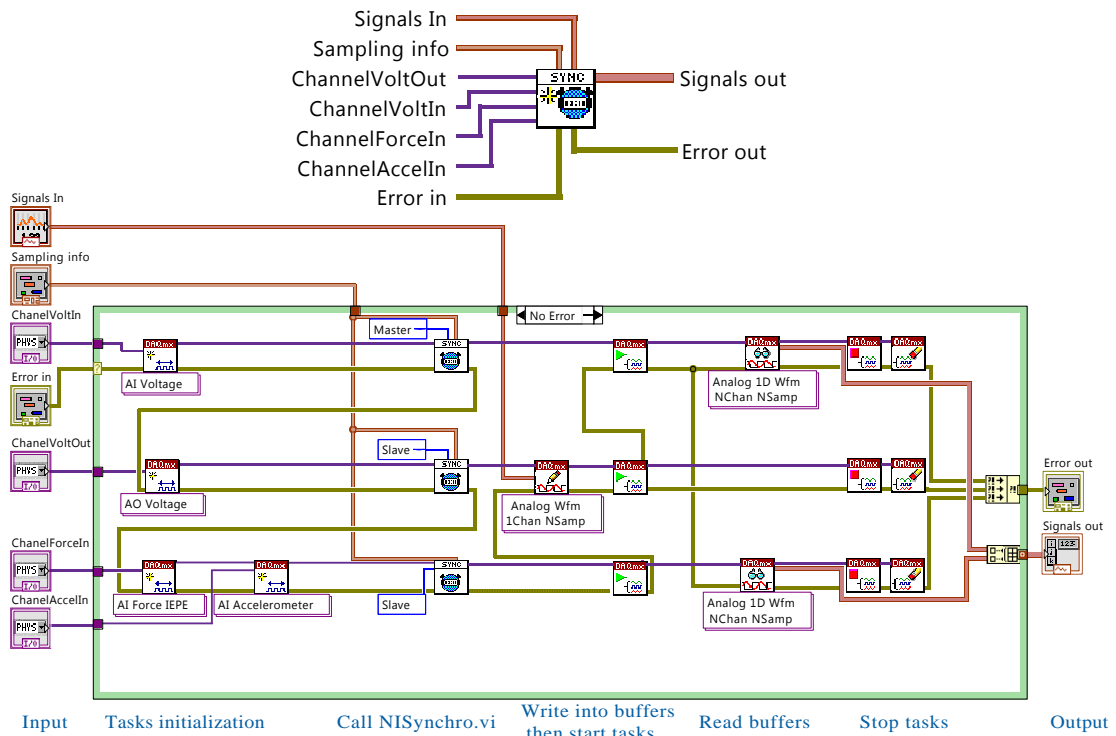


Figure 5.4: LabView VI to read or write tasks. The synchronization operation order is given by the error dataflow. Note also that for the output task, it is necessary to fill the buffer (write) before starting the task. For a shake of clarity, the properties of “DAQmx Create Channel” as max/min values, units, sensitivity etc., and the sampling properties of “DAQmx Read” have been removed.

operations in hexadecimal with the sensors is possible such that the sensor always answer to a single command at the time. Among all commands, the most important ones are the string “SET” which reset the displacement to zero, and the string “?” which request the relative displacement (Fig. 5.6b). Each time that the displacement is measured correctly, the answer of the sensor is coded under 10 bytes. If the sensor is too far from the magnetic strip or the displacement speed is too fast, the answer from the sensor is for example “ERROR” which is different than 10 bytes and is used as an error detection (Fig. 5.6b). The last step of VISA protocol consists in closing and cleaning the connection.

Finally, in order to plot continuously the displacement in time, the operation write and read is repeated into a while loop (Fig. 5.6c). The frequency (around 20Hz) is limited by the sensor which do not used buffer and it is the reason with the *Sylvac* sensor is used only for static experiments whereas LVDT sensors are preferred for dynamic acquisitions. However, *Sylvac* sensor operates in a much larger displacement range without any lost in the accuracy which justify its use.

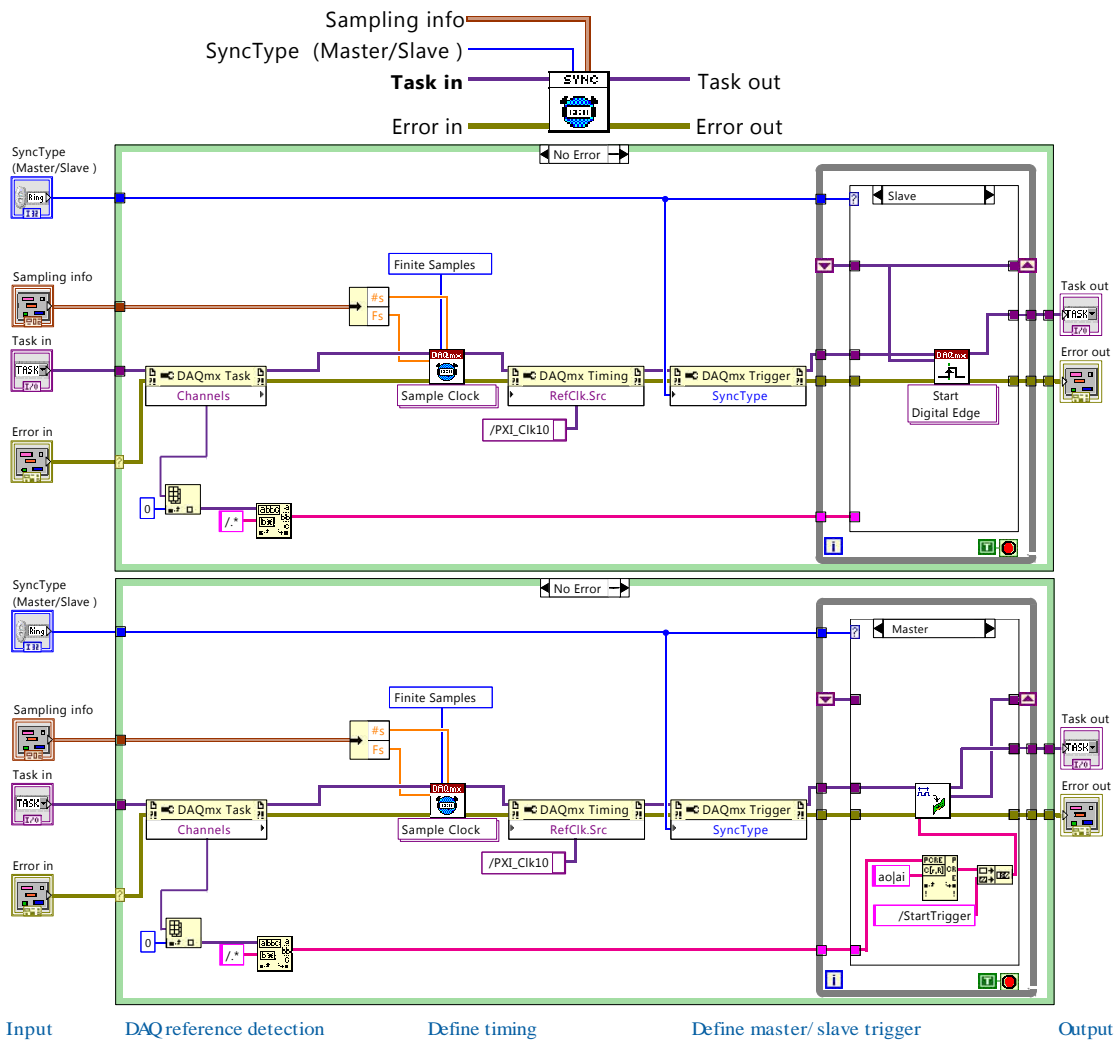


Figure 5.5: LabView VI to synchronize slave or master tasks. Note the use of a shift register as global variable to store the master trigger source reference which is used next by slaves.

5.3 Experimental results

In this section, experimental results are given, starting from static considerations and then analyzing wave propagation.

5.3.1 Static buckling pattern

When a beam with equispaced pinned supports is buckled, the buckling pattern alternates between positive and negative transverse deformations and is explained by the fact that when one trolley starts to turn, a moment in the opposite direction is created on the next trolley, which turns in the opposite direction and so on. For the guided-support configuration, since only axial displacements are allowed, the buckling is expected to be random, depending

5.3. Experimental results

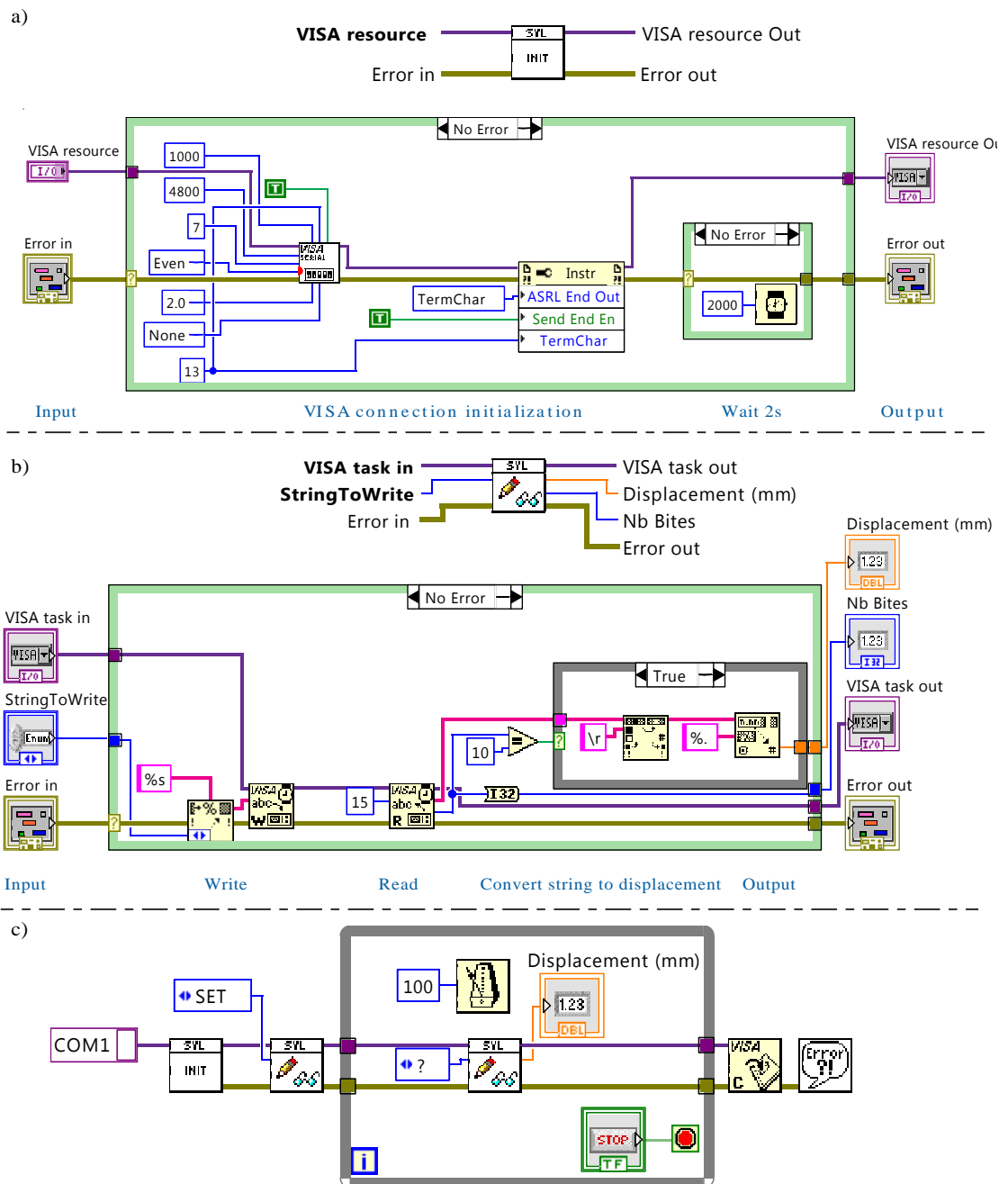


Figure 5.6: LabView VI to initialize (a), read and write (b), and display (c) the displacement using the serial communication standard RS – 232.

only on initial imperfections. If gravity is not negligible, the deformations are expected to be unidirectional. However, as shown in Fig. 5.7a, the buckling direction is neither random nor uniform, and alternates between up and down, similarly to the pinned-support case. This distribution can be explained by the fact that the trolleys possess a small play in rotation, such that a similar deformation mechanism as the pinned-support configuration occurs. Moreover,

as shown in Fig. 5.7a, the buckling in the top direction is more significant in the bottom one, which is opposite to gravity effects but is explained by the residual strain in the beam. Indeed, the beam is originally received coiled in a curved box (Fig. 5.7b) and once placed on a flat surface, the residual curvature is evident (Fig. 5.7c). Note that if the beam is flipped, the preferred direction is also changed.

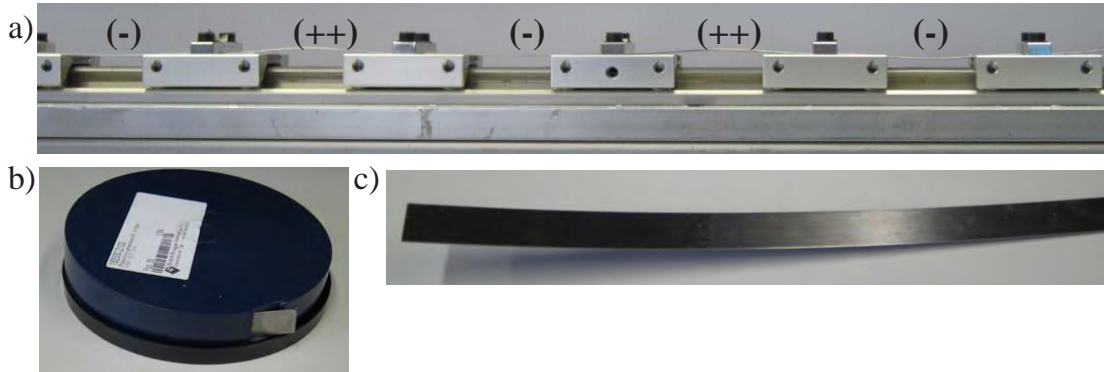


Figure 5.7: Beam alternating with up-down deformations due to small play in the trolley allowing small rotation (a). Beam in its originally package (b) that possess some residual stress after uncoiling since the extremities of the beam are not in contact with the flat surface (c). The (++) indicates large positive deformations whereas (-) indicates small negative deformations.

Since the pre-buckling level is not homogeneous whereas the model assumes a periodic pattern, the averaged value is used, as presented next for the load-displacement relation.

5.3.2 Static load-displacement relation

The load-displacement ($P\{\Delta U\}$) curve from experiments, averaged over the full beam, is given in Fig. 5.8 and compared to the FE results. While results are in good agreement for the weakly-buckled beam (Fig. 5.8a), the beam becomes plastic and collapses around $\chi_0 = 0.05$ (Fig. 5.8b). For this reasons, only small strain is considered.

For the aforementioned parameters, small initial buckling ($\chi_0 < 0.08$) and guided supports, supersonic waves are expected (see Chapter 4).

5.3.3 Wave input

A classical way to see if a structure can hold solitary waves is to excite it with a delta function and observe if there is creation of a solitary train [Nesterenko, 2001]. However, the present setup is limited to 30 trolleys which is not long enough to see the wave propagating and splitting. In this work, it is proceeded in the opposite manner. The structure is excited with a guessed solitary solution and the propagating wave is observed. If the resulting wave is unchanged, solitary waves are obtained whereas if a front or a tail is present, the input guess is

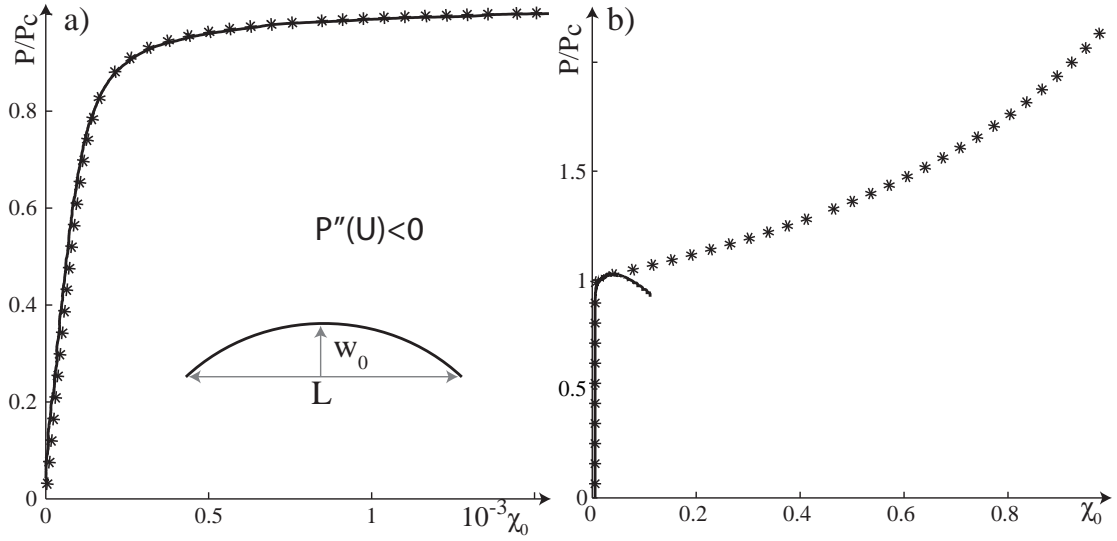


Figure 5.8: Normalized load displacement relation ($P\{\Delta U\}/P_C$ where $P_C = 4EI\pi^2/L^2$) in terms of the small (a) and large (b) buckling level χ_0 . Experiments in full lines (becoming plastic) and FE (assuming linear elastic material) with *. FE results are given for an initial imperfection of sinusoidal form and has its maximum transverse amplitude $w_0 = 10^{-3}L$ such that using this value, both curves in (a) overlaps.

not the correct one, and the measured wave is discarded. This operation is repeated iteratively keeping the wave amplitude constant and varying only the period input, until no tail or front is present.

However, this procedure is working only for displacement control whereas the shaker works on force control. To work on displacement control, piezo-stack actuator would be a good alternative, but no configuration for the desired displacement and dynamic range is available. In order to use the shaker in displacement control, the proportional-integral-derivative (PID) method has been implemented, but works only for slow dynamics, far from the desired frequencies. Finally, the input is tuned by hand as follows.

Knowing that the shaker works in force control, its delivered force is of form:

$$F_{Shaker} = M_{eff}\ddot{U} + K_{eff}U + F_{Soliton}\{U\}, \quad (5.1)$$

where M_{eff} and K_{eff} are effective mass and stiffness. K_{eff} is defined easily and is such that:

$$K_{eff} = K_{Shaker} + K_{Spring}. \quad (5.2)$$

M_{eff} involves however the mass of the different trolleys which do not constitute a rigid body such that its determination analytically is too difficult. U and its derivatives in time are

obtained from the strain solution (Eq. (4.10)) such that:

$$\begin{aligned} U &= U_m (\tanh\{-tT^{-1}\} + 1), \\ \dot{U} &= -U_m T^{-1} \operatorname{sech}^2\{-tT^{-1}\}, \\ \ddot{U} &= -2U_m T^{-2} \operatorname{sech}^2\{-tT^{-1}\} \tanh\{-tT^{-1}\}, \end{aligned} \quad (5.3)$$

where $U_m = \Delta\xi_m\Lambda$ is the wave amplitude in displacement, and $T = \Lambda V^{-1}$ its characteristic width in time that is referred next as period. $F_{Soliton}(U)$ is assumed proportional to the strain wave that is also proportional to the wave-speed profile such that:

$$F_{Soliton}(U) = F_{eff}\dot{U}. \quad (5.4)$$

Finally, for each combination of U_m and T , the two unknowns M_{eff} and F_{eff} have to be determined, and they are tuned manually by varying iteratively their values until the displacement of the first trolley, measured by the LVDT sensor, correspond to the desired one.

5.3.4 Stationary wave profile

For a given initial compression, the initial input is parametrized by U_m and T . However, for solitary waves, given the amplitude U_m , only one solution T result to a stationary wave. In order to find these different combinations, a grid from the parameters $\{U_m, T\}$ is constructed and experiments are run for each grid combination.

For a given U_m , the corresponding value of T is found when the resulting wave propagates maintaining its shape. For example, in Fig. 5.9a-c, the wave speed in time of the first 5 even trolleys is shown for three different values of T , fixing χ_0 and U_m . In Fig. 5.9a, the period T is initially too large and decreases while propagating, meaning that the input is not correct. In Fig. 5.9c, the period seems to remain constant but a tail appears, which is contrary to stationary waves. Finally, in Fig. 5.9b, the period is constant and there is a flat part before the reflection meaning that there is no creation of tail and that the solution is approximately stationary.

Since variations of the period are hardly detectable due to limitation in the setup size, selection of the corresponding period T is based on the tail behavior. Indeed, as shown in Fig. 5.9d, where the 10th trolley speed $V_p\{t\}$ is plotted for U_m constant and several values of T , the retained value of T corresponding to a stationary wave is the first one before the appearance of a tail (see dotted line in Fig. 5.9d). As a general remark, front has not been observed in this structure, in agreement with the dispersion characteristics of the weakly-buckled guided-supported beam.

Once the combinations $\{U_m, T\}$ are determined, the wave profile at each trolley is recorded and profiles are shown in Fig. 5.10a-c for three pre-compression levels. In Fig. 5.10d, FE simulations of the structure using the same parameters as in Fig. 5.10b is given, and comparison shows

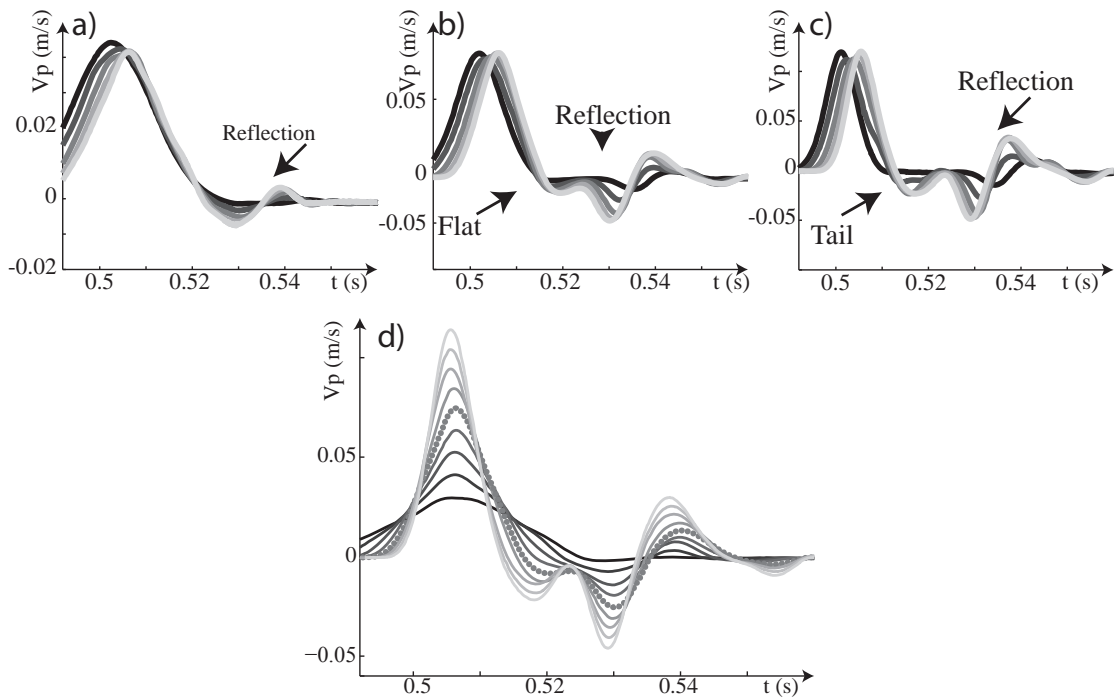


Figure 5.9: Speed of the trolleys V_p in terms of the time t of the first 5 even trolleys, for $\chi_0 = 1.72 \times 10^{-3}$, $U_m = 0.5$ mm and $T^{-1} = 70$ s $^{-1}$ (a), $T^{-1} = 140$ s $^{-1}$ (b), and $T^{-1} = 150$ s $^{-1}$ (c). Speed at the 10th trolley for $U_m = 0.5$ mm and $T^{-1} = \{70, 90, 110, 130, 150, 170, 190, 210, 230\}$ s $^{-1}$, respectively from dark to light gray lines. The experiment resulting to stationary solution is in dotted line ($T^{-1} = 150$ s $^{-1}$).

some discrepancies. In order to carry out a quantitative comparison, the wave phase-speed and its period are investigated next.

5.3.5 Phase speed

As shown in Chapter 4, for guided supports and a slightly-buckled beam, the medium is supersonic meaning that nonlinear waves travel faster than linear ones and the phase-speed of the former increases. It is this characteristic that is intended to demonstrate in this section. The speed between each trolley is computed by measuring the time shift between two consecutive trolleys, knowing the distance between them, and using the maximum amplitude of the signal as reference. However, as shown in Fig. 5.11a, this speed is not constant and alternates between high and low values. Indeed, it is possible to make a link between the buckling pattern and the speed since when the beam is highly buckled, the slope of the load-displacement curve is low corresponding to small speed, whereas it is the opposite for small pre-compression.

In order to analyze the influence of amplitude on wave speed, the average speed is used and results are shown in Fig. 5.11b in terms of the amplitude for three pre-compression levels. As expected, the phase-speed increases with amplitude and decreases with the initial

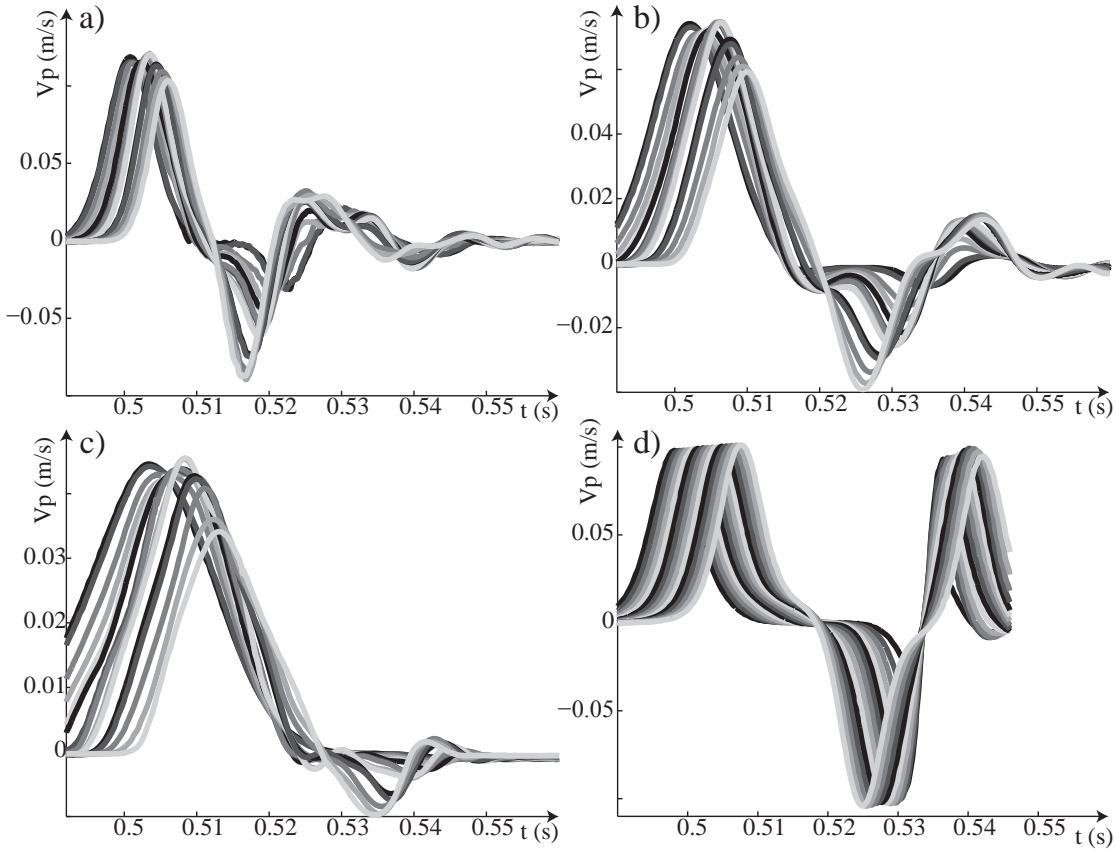


Figure 5.10: Speed V_p of the 15th first trolleys in terms of the time t , for $U_m = 0.5 \times 10^{-3}$ and $\{\chi_0 = 1.14 \times 10^{-3}, T^{-1} = 240 \text{ s}^{-1}\}$ (a), $\{\chi_0 = 1.72 \times 10^{-3}, T^{-1} = 150 \text{ s}^{-1}\}$ (b) and $\{\chi_0 = 3.00 \times 10^{-3}, T^{-1} = 90 \text{ s}^{-1}\}$ (c). FE simulations with the same input as (b) in (d).

compression. Considering measurement, results from Boussinesq model are recovered.

5.3.6 Period and wavelength

After the phase-speed, the selected input period T that leads to a stationary wave is compared to the double-dispersion Boussinesq model in Fig. 5.12. It results that T increases with pre-compression, in agreement with the Boussinesq-type model. However, concerning the experimental values of the input period, T is found too large at small amplitude and too small otherwise. Since the estimation of the phase-speed is found acceptable, an explanation of the fact that the wavelength (or period) is badly predicted could be that all the dispersion sources are not correctly captured. Indeed, the phase-speed (Eq. (4.11)) do not depends on the dispersion, contrary to the wavelength and the period (Eq. (4.12)).

However, since numerical FE simulations are in agreement with the Boussinesq-type model, the error may be on the experimental side. Indeed the phase-speed depends mainly on the medium and is almost independent of the input, whereas it is the opposite for the period when

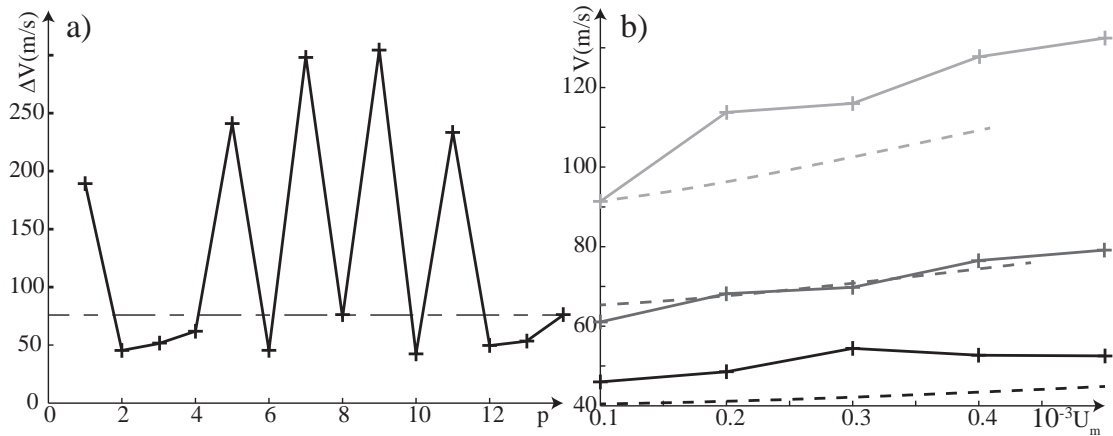


Figure 5.11: Phase speed ΔV between the 15th first trolleys for $\chi_0 = 1.72 \times 10^{-3}$, $T^{-1} = 150 \text{ s}^{-1}$ and $U_m = 0.5 \text{ mm}$ (a), and averaged phase-speed V in terms of the amplitude U_m (b) for $\chi_0 = 1.14 \times 10^{-3}$ (light gray), $\chi_0 = 1.72 \times 10^{-3}$ (dark gray) and $\chi_0 = 3.00 \times 10^{-3}$ (dark), with experimental data in full lines and Boussinesq model in dashed lines.

measured at the first trolleys. The fact that the input is badly selected can find an explanation in its selection criterion. Indeed, for a given U_m , the selected T is based on the tail creation criterion and as it will be shown next, tails can result from heterogeneities.

In conclusion, in order to measure the period independently of the input, longer setup would be required.

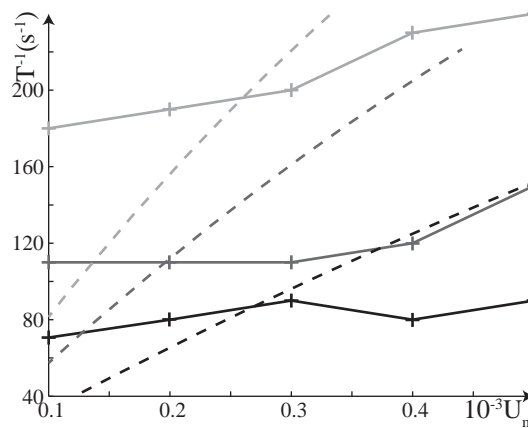


Figure 5.12: Inverse of the period (T^{-1}) in terms of the amplitude U_m (b) for $\chi_0 = 1.14 \times 10^{-3}$ (light gray), $\chi_0 = 1.72 \times 10^{-3}$ (dark gray) and $\chi_0 = 3.00 \times 10^{-3}$ (dark), with experimental data in full lines and Boussinesq model in dashed lines.

5.3.7 Effects of heterogeneities

In Figs. 5.7a and 5.11a, it is shown that the buckling is not homogeneous and effects of heterogeneities are investigated here. While the setup does not allow long-wave observations, investigations are restricted here to numerical FE simulations with a uniformly distributed random imperfections such that:

$$w_{0,p} = w_0 \pm 5\%, \quad (5.5)$$

where $w_{0,p}$ is the midspan transverse displacement of the p^{th} beam portion. The buckled beam is modeled with 100 supports and the propagating wave is shown in Fig. 5.13 and compared to the homogenized structure ($w_{0,p} = w_0, \forall p$). In the presence of heterogeneities, the global trend of the wave profile seems on average to remain unchanged, localized and stationary. Locally, however, effects of periodicity-defects are significant, as observed on the wave amplitude. Note also the presence of a small tail uniquely in the presence of heterogeneities, which confirm that the use of the tail-criterion to choose the selected input (Sec. 5.3.4) is biased by heterogeneities.

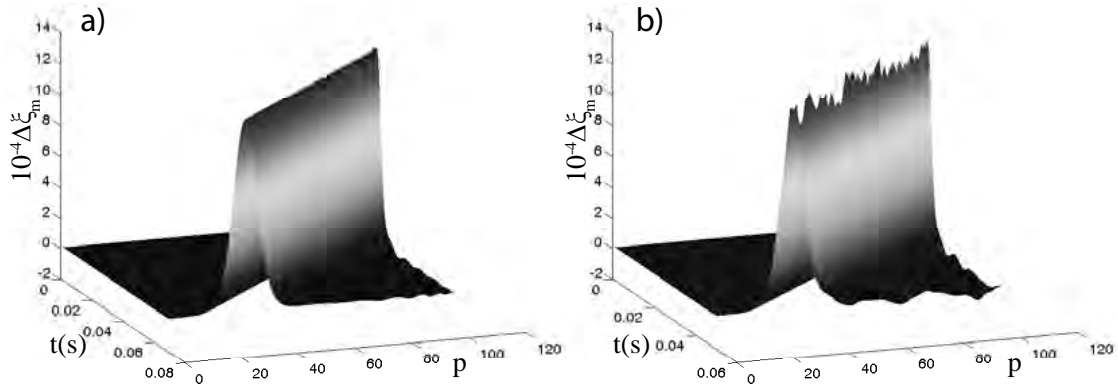


Figure 5.13: Strain wave propagating in a beam uniformly (a) and randomly (b) buckled (Eq. (5.5)) in terms of the support number p and the time t for $\chi_0 = 1.72 \times 10^{-3}$ and $U_m = 0.5 \times 10^{-3}$.

In order to carry out a quantitative comparison, the wave phase-speed and its period are given in Fig. 5.14. The simulation is repeated 25 times with each time a new random distribution, and in addition to the mean and the standard deviation, results are compared to the homogeneous case. Concerning the evolution of the speed and period in terms of the support number, they both converge asymptotically meaning that heterogeneities, which are local phenomena do not play a role in the long-wave propagation, validating the use of homogenized models here for the imperfect structure. In addition to this observation, the convergence rate of the phase-speed (Fig. 5.13a) is much faster than the one of the period (Fig. 5.13b) and is explained again by the fact that the phase-speed is weakly dependent on the input, whereas it is the opposite for the period. This confirms why experimentally, the phase-speed is correctly captured whereas this is not true for the wavelength (period).

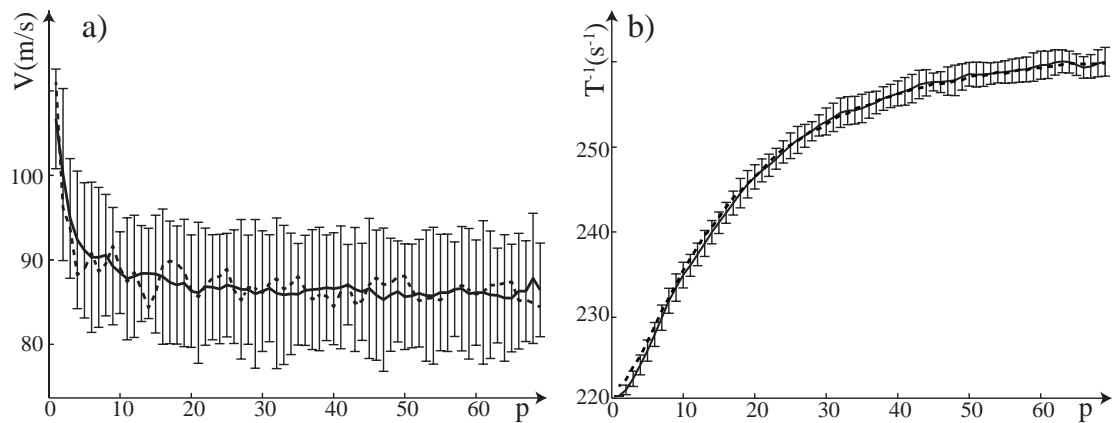


Figure 5.14: Wave speed V (a) and inverse of the period T^{-1} (b) in terms of the support number p for $\chi_0 = 1.72 \times 10^{-3}$ and $U_m = 0.5 \times 10^{-3}$. Mean value and its standard deviation resulting from 25 FE simulations with random imperfections (Eq. (5.5)) in full lines, compared to the FE simulation without heterogeneities in dashed lines.

5.4 Conclusions

Wave propagation in guided-supported, weakly-buckled beams is investigated experimentally and two characteristics predicted by the double-dispersion Boussinesq model are recovered: (i) the medium is supersonic, meaning that the phase-speed increases with amplitude and (ii) if the input is not stationary, there is creation of a tail but never a front. Moreover, the phase-speed decreases with pre-compression and is in agreement with the predicted values. While the wave profile seems stationary, due to limitations in the setup size, the reflected wave appears after few supports and long-wave observations as the wavelength, period, heterogeneity effects, friction-induced decay are not possible.

6 Isogeometric Analysis Of Extensible-Elastica

Sections 6.2 to 6.7 and 6.9 are mostly reprinted from [Maurin et al., 2015] with authorization of the publisher.

6.1 Abstract

For beams undergoing large geometrical deformations, the geometrically-exact beam theory is the most adapted formulation since the strain follows directly from geometrical considerations without approximations. For slender beam structures, as often encountered in buckling problems, shear deformations can be neglected preventing numerical shear-locking issues and in Chapter 2 it has been shown that this formulation is refereed as the extensible-elastica.

If the extensible-elastica formulation is expressed in terms of displacements without rotation, the kinematics involved in the weak form are described by second order derivatives. However the spatial approximation of such high-order PDE cannot be approximated by the classical \mathcal{C}^0 -continuous FE method in the standard Galerkin framework, and in this chapter, NURBS-based isogeometric analysis (IGA) is proposed instead. This work is completed in Sec. 6.8 by a comparison of the present formulation to the co-rotational beam formulation applied to the problem of static and dynamic buckling.

6.2 Introduction

Finite deformation of slender structures are of interest for many problems ranging from buckling of frames to curling of cables, for which linear beam theories based on infinitesimal strain cannot be used. The geometrically-exact beam formulation, firstly introduced by Reissner [Reissner, 1972, 1973], takes into account large nonlinear deformations of bending, axial and shear type; the term exact refers to the fact that the strain follows directly from geometrical considerations without approximations. The finite element (FE) formulation introduced by Simo [Simo, 1985, Simo and Vu-Quoc, 1986] contributed to the popularity of this

theory (see a more recent detailed implementation in [Wriggers, 2008]), and computational aspects arising from new formulations are still of interest [Ghosh and Roy, 2009, Santos et al., 2010, Češarek et al., 2012]. However, the formulation proposed by Simo requires, in addition to the two degrees of freedom (dofs) corresponding to the components of the position vector, the introduction of a third dof describing the local rotation, in order to enforce equilibrium. In addition to increasing the computational cost in dynamic problems, rotary dofs lead to a non-constant mass matrix restricting time-integration schemes to implicit ones [Romero, 2008]. The absolute-nodal-coordinate formulation (ANCF) [Shabana and Yakoub, 2001, Shabana, 2001, Gerstmayr and Shabana, 2006, Gerstmayr et al., 2008] has been developed to improve these drawbacks even if it involves higher-order spatial operators.

For slender structures such as cables or rods, shear deformations can be neglected using the Euler-Bernoulli assumption of beam cross-sections remaining normal to the elastic axis and plane after deformation. This leads to the formulation of extensible-elastica, for which the kinematics are often expressed in terms of trigonometric functions involving one displacement component and the rotation of the cross section of the beam [Magnusson et al., 2001]. If expressed in terms of both displacement components, the kinematics are mathematically represented by high-order partial differential equations (PDEs), specifically a fourth order spatial differential operator is involved. As consequence, in the weak formulation, the problem involves second-order derivatives for which a numerically-approximated solution based on the standard Galerkin method requires the use of at least globally \mathcal{C}^1 -continuous basis functions. Conversely, when considering FE approximations based on Lagrangian polynomials which are globally C^0 -continuous in the computational domain, the use of mixed formulations with auxiliary variables represents one of the most viable approaches. A similar problem arises in linear beam theory, where the curvature, proportional to the moment, is given by the second derivative of the transverse displacement. This problem is often solved by using \mathcal{C}^1 -continuous cubic Hermite basis functions with the addition of an explicit dof physically corresponding to the rotation [Reddy, 2004]. However, this approach cannot be used for the rotation-free extensible-elastica, since second derivatives of displacements are not physically meaningful quantities. In the literature, different techniques have been used to solve the rotation-free extensible-elastica formulation. In [Saje, 1990], the Hu-Washizu variational principle is employed for which the rotation is numerically approximated with the aim of removing the second-order derivative. More recently, this problem has been solved by the quaternion-based method [Zhao and Ren, 2012], and the weak-form quadrature element method [Zhang and Zhong, 2013].

Isogeometric analysis (IGA), firstly introduced by Hughes et al. [Cottrell et al., 2009], aims at filling the gap existing between computational mechanics for engineering applications and computational geometry, specifically computer aided design (CAD) systems. The key feature of IGA consists in generalizing the FE method by considering an isoparametric approach for which the same basis functions used to represent the geometry are then used for the approximation of the unknown solution field of the PDEs. As a consequence, the representation of the computational domain is encapsulated in the numerical approximation of the governing

PDEs. Since non-uniform rational B-splines (NURBS) are especially used in CAD systems, we will consider NURBS-based IGA for the approximation of the PDEs. A crucial property of NURBS basis functions is the possibility to increase their degree of continuity through the k -refinement procedure [Dedè and Santos, 2012]. The smoothness of the NURBS basis functions leads in many cases to better accuracy and reduced computational cost compared to the standard FE method [Cottrell et al., 2009]. In addition, in vibration analysis, IGA based on smooth NURBS basis functions improves the representation of optical branches of the frequency spectrum [Cottrell et al., 2006, Weeger et al., 2013]. In this chapter, we take advantage of properties of the basis functions to solve the shear-free, high-order-formulation problem in the standard Galerkin framework in a computational domain representing a beam with a single NURBS patch. Even if we consider single NURBS patches, we remark that for multiple NURBS patches (typical of problems with piece-wise continuous geometry), the rotation-free extensible-elastica formulation cannot be directly used for which, rigid constrains or stiff simplified elements (bending strip method [Raknes et al., 2013]) between patches need to be added.

In the field of nonlinear isogeometric beams, available formulations in literature are based on elastica [Dedè and Santos, 2012] and nonlinear Euler-Bernoulli [Weeger et al., 2013, Raknes et al., 2013, Nagy et al., 2010] theories. Beam models including shear are proposed in [Beirão da Veiga et al., 2012, Bouclier et al., 2012] for Timoshenko beams and in [Li et al., 2013] for the third-order, shear-deformation theory (TSDT). For isogeometric nonlinear plates and shells, we refer the reader to [Greco and Cuomo, 2013, 2014] for Kirchhoff-Love rods, to [Kiendl et al., 2009, 2010, Benson et al., 2011] for Kirchhoff-Love shells, to [Benson et al., 2010, 2013] for Reissner-Mindlin shells, and to [Echter et al., 2013] for modified Reissner-Mindlin shells including variable thickness.

A isogeometric method for slender beams undergoing large deformations and free of shear is proposed in [Raknes et al., 2013]. With respect to this work, our formulation differs in the choice of the constitutive material model. In order to explain this difference, we recall that Irschik and Gerstmayr [Irschik and Gerstmayr, 2009] presented an interpretation of the strain measures and stress resultants of the extensible-elastica formulation in terms of nonlinear continuum mechanics. A linear relation between the second Piola-Kirchhoff stress and the Green-Lagrange strain, as given by the Saint Venant-Kirchhoff model, results in a nonlinear relationship between stress resultants (axial force and moment) and strain (axial strain and curvature), thus introducing a nonlinear material model. The former is the formulation considered in [Raknes et al., 2013]. Conversely, in this chapter, we consider a linear constitutive law between Biot Stress and Biot strain resulting in a linear material model. Indeed, the axial force and moment are only a function of axial strain and curvature, respectively [Irschik and Gerstmayr, 2009] (see [Humer, 2011] for a comparison with the Saint Venant-Kirchhoff model). Such linear constitutive law at the beam level is a key feature of the extensible-elastica theory [Magnusson et al., 2001], allowing closed-form solutions of simple nonlinear beam problems with coupled axial and transverse displacements (the term closed-form refers to the fact that solutions are expressed in terms of known functions such as elliptical integrals). Closed-form

solutions of known problems provide an ideal setting to evaluate the numerical performance of the IGA formulation, which we consider by using “patch tests”. Static analytical solutions for the extensible-elastica method have already been applied to buckling [Magnusson et al., 2001, Humer, 2013], variable-length beams under concentrated/distributed forces [Humer, 2011, Humer and Irschik, 2011], and snap-through buckling [Chen and Tsao, 2013, 2014]. However, to the best of our knowledge, patch tests for initially-curved extensible-elastica have not been considered yet; tests which are currently available differ in the constitutive laws and strain-measurement [Pulngern et al., 2013, Gonzalez and LLorca, 2005]. In the present chapter, we derive a new closed-form solution for a tip-loaded curved cantilever beam using the extensible-elastica to expand available benchmark cases.

Closed-form solutions of patch tests for static beams are used to verify the convergence orders of the errors under h -refinement associated to the IGA approximations using a-priori error estimates [Bazilevs et al., 2006, Beirão da Veiga et al., 2011], including high-order PDEs [Tagliabue et al., 2014, Auricchio et al., 2007]. Despite the fact that the error estimates are derived for linear problems, the same convergence orders are often observed for nonlinear PDEs also (see e.g. [Dedè and Santos, 2012]). Moreover, we remark that the considered formulation is free of shear locking by design even for initially-curved structures [Ishaquddin et al., 2013], but may exhibit membrane locking when beam elements possess very low aspect ratio. This phenomenon is well known in FE formulations [Reddy, 2004, Ibrahimbegovic, 1995] and has received renewed attention in the context of IGA for Timoshenko beam formulations, using different locking-free methods: namely the collocation method [Beirão da Veiga et al., 2012], the selective reduced integration, the reduced integration with hourglass mode control, the \bar{B} strain projection, and the discrete-strain-gap (DSG) method [Bouclier et al., 2012]. Moreover, the IGA formulation can be conveniently used for the spatial approximation of dynamic beam problems, as we illustrate by means of several numerical tests: the propagation of solitons (nonlinear waves) in post-buckled beams [Maurin and Spadoni, 2014b,a], and snap-through buckling of a pinned beam that is axially buckled before transverse loading [Chen and Tsao, 2014].

This chapter is organized as follows. In Sec. 6.3, the rotation-free extensible-elastica formulation is recalled and the different terms of the weak formulation and its linearization are given; the isogeometric concept is applied to the present problem. Closed-form solutions for different static beam problems are presented and derived in Sec. 6.4; then, the a-priori error estimates are recalled in Sec. 6.5. In Sec. 6.6, static beam problems are solved, and convergence order is numerically estimated and compared with the a-priori error estimates. In Sec. 6.7, dynamic problems are solved. Conclusions follow.

6.3 Rotation-free extensible-elastica formulation

6.3.1 Strain measurement and constitutive law

The derivation of the rotation-free extensible-elastica formulation follows from the geometrically exact beam theory including shear and is described in [Wriggers, 2008]. However, contrarily to [Wriggers, 2008], the beam formulation is provided in the global coordinate frame allowing initial deformations and is not rotated back to the local frame in order to compute strain and stress resultants [Zhang and Zhong, 2013] (Fig. 6.1). Indeed, the rotation to a local frame is not compatible with rotation-free formulations.

In the initial configuration of the beam, $\mathbf{r}_0 \in \mathbb{R}^2$ is referred to as the position vector of a material point of the beam; $\mathbf{e}_{0,i}$, $i = 1, 2$ is an orthonormal basis vector of the Euclidean space \mathbb{R}^2 such that $\mathbf{e}_{0,1}$ represents the normal direction of the cross-section and $\theta_0 \in \mathbb{R}$ the orientation angle of the initial configuration with respect to the reference configuration. We indicate with $s_0 \in \mathbb{R}$ the arc-length parameter of the elastic axis of the beam (i.e. the curvilinear coordinate) and with l_0 its total length. Correspondingly, \mathbf{r} , \mathbf{e}_i , θ and s represent the position vector, the orthonormal basis vectors, the rotation, and the curvilinear coordinate in the current configuration of the beam, respectively. These quantities are shown in Fig. 6.1 and are defined as:

$$\begin{aligned} \mathbf{r}_0 &= \{r_{0,x}, r_{0,y}\}^T, & \mathbf{r} &= \{r_x, r_y\}^T, \\ \mathbf{e}_{0,1} &= \{\cos\theta_0, \sin\theta_0\}^T, & \mathbf{e}_1 &= \{\cos\theta, \sin\theta\}^T, \\ \mathbf{e}_{0,2} &= \{-\sin\theta_0, \cos\theta_0\}^T, & \mathbf{e}_2 &= \{-\sin\theta, \cos\theta\}^T. \end{aligned} \quad (6.1)$$

where $\mathbf{r}_0 = \mathbf{r}_0(s_0)$, $\mathbf{r} = \mathbf{r}(s)$, $\mathbf{e}_{0,i} = \mathbf{e}_{0,i}(s_0)$, $\mathbf{e}_i = \mathbf{e}_i(s)$, $\theta_0 = \theta_0(s_0)$, and $\theta = \theta(s)$.

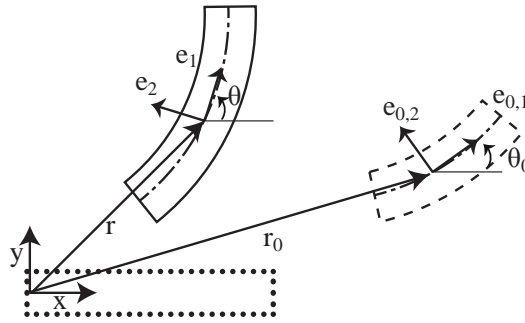


Figure 6.1: Beam kinematics: reference (dotted lines), initial (dashed lines), and current configuration (full lines).

The strain relation proposed by Reissner [Reissner, 1972] extended to global coordinates reads:

$$\begin{aligned}
 \epsilon &= r'_x \cos \theta + r'_y \sin \theta - (r'_{0,x} \cos \theta_0 + r'_{0,y} \sin \theta_0), \\
 \gamma &= r'_y \cos \theta - r'_x \sin \theta - (r'_{0,y} \cos \theta_0 - r'_{0,x} \sin \theta_0), \\
 \kappa &= \theta' - \theta'_0.
 \end{aligned} \tag{6.2}$$

where ϵ is the axial strain, γ the shear strain, and κ the curvature. The notation $()'$ denotes the derivative with respect to the initial curvilinear coordinate s_0 (Lagrange formulation). The Euler-Bernoulli beam model assumes that the cross section remains planar and normal to the tangent of the elastic axis of the beam after deformation, which corresponds to assuming that the shear γ is identically zero. By substituting the rotations θ and θ_0 in Eq. (6.2), the axial strain ϵ and the curvature κ can be rewritten in terms of \mathbf{r}_0 , \mathbf{r} , and their derivatives¹:

$$\begin{aligned}
 \epsilon &= \|\mathbf{r}'\|_2 - \|\mathbf{r}'_0\|_2, \\
 \kappa &= \frac{\mathbf{r}''^T \Theta \mathbf{r}'}{\|\mathbf{r}'\|_2^2} - \frac{\mathbf{r}''_0{}^T \Theta \mathbf{r}'_0}{\|\mathbf{r}'_0\|_2^2},
 \end{aligned} \tag{6.3}$$

where $\|\mathbf{r}'\|_2 = \sqrt{r_x'^2 + r_y'^2}$ is the Euclidean norm and Θ is a 90° rotation matrix given by:

$$\Theta = \begin{bmatrix} 0 & -1 \\ 1 & 0 \end{bmatrix}. \tag{6.4}$$

By assuming that the strain is finite but small, even for large displacements, it is possible to describe material behavior by Hooke's law. By using the Young modulus E , the constitutive law between the force and the strain after the integration over the cross section of the beam is [Reissner, 1972, Wriggers, 2008, Irschik and Gerstmayr, 2009]:

$$\begin{Bmatrix} N_\epsilon \\ N_\kappa \end{Bmatrix} = \begin{bmatrix} EA & 0 \\ 0 & EI_z \end{bmatrix} \begin{Bmatrix} \epsilon \\ \kappa \end{Bmatrix}, \tag{6.5}$$

where A and I_z are the area and moment of inertia of the beam, respectively; N_ϵ and N_κ indicate the internal axial force and bending moment, respectively. The constitutive law Eq. (6.5) is equivalent in continuum mechanics to the linear relationship between the Biot's stress and strain. For an overview of alternative constitutive laws, see [Irschik and Gerstmayr, 2009].

6.3.2 The weak formulation

The weak formulation of the equilibrium equation is obtained from the principle of virtual work and is expressed in terms of the current configuration $\mathbf{r} = \mathbf{r}_0 + \mathbf{u}$, where $\mathbf{u} = \{u_x \ u_y\}^T$

¹ $\mathbf{r}''^T \Theta \mathbf{r}'$ is sometimes expressed as a norm of a cross product $\|\mathbf{r}' \times \mathbf{r}''\|_2$ (e.g. [Zhang and Zhong, 2013]); however, in this convention, the sign is lost.

6.3. Rotation-free extensible-elastica formulation

is the displacement vector, and $\delta \mathbf{u} = \delta \mathbf{r}$ the virtual displacements vector; $\mathbf{f} \in \mathbb{R}^2$ and $\mathbf{F} \in \mathbb{R}^2$ are the distributed and boundary forces vectors, respectively. The distributed and boundary moments are indicated by $m \in \mathbb{R}$ and $M \in \mathbb{R}$, respectively. Transverse and axial follower loads are not taken into account in our formulation, but can be derived similarly to what is done for the moment. By considering a dynamic problem, the weak formulation of the equilibrium equation is given by [Wriggers, 2008]:

$$\text{find } \mathbf{u} \in \mathcal{V} : G(\mathbf{r}(\mathbf{u}))(\delta \mathbf{u}) = 0 \quad \forall \delta \mathbf{u} \in \mathcal{V}, \quad \forall t \in (0, t_f), \quad (6.6)$$

given suitable initial conditions at the time $t = 0$, with t_f is the final time, and $\mathcal{V} \subset H^2(\Omega)$ ($\Omega \in (0, l_0)$) a suitable subset of the Hilbert function space $H^2(\Omega)$ carrying the essential boundary conditions and:

$$G(\mathbf{r}(\mathbf{u}))(\delta \mathbf{u}) = \int_0^{l_0} (N_\epsilon \delta \epsilon + N_\kappa \delta \kappa) ds_0 - \int_0^{l_0} ((\mathbf{f}^T + \rho A \ddot{\mathbf{u}}^T) \delta \mathbf{u} + m \delta \theta) ds_0 - [\mathbf{F}^T \delta \mathbf{u} + M \delta \theta]_0^{l_0}, \quad (6.7)$$

for which

$$\begin{aligned} \delta \epsilon &= \mathbf{R}_{\epsilon'} \delta \mathbf{u}', \\ \delta \kappa &= \mathbf{R}_{\kappa'} \delta \mathbf{u}' + \mathbf{R}_{\kappa''} \delta \mathbf{u}'', \\ \delta \theta &= \mathbf{R}_{\theta'} \delta \mathbf{u}', \end{aligned} \quad (6.8)$$

where:

$$\begin{aligned} \mathbf{R}_{\epsilon'} &:= \frac{\mathbf{r}'^T}{\|\mathbf{r}'\|_2}, \\ \mathbf{R}_{\kappa'} &:= \frac{\mathbf{r}''^T \Theta [\|\mathbf{r}'\|_2^2 I - 2\mathbf{r}' \mathbf{r}'^T]}{\|\mathbf{r}'\|_2^4}, \\ \mathbf{R}_{\theta'} &:= \mathbf{R}_{\kappa''} = \frac{\mathbf{r}'^T \Theta^T}{\|\mathbf{r}'\|_2^2}, \end{aligned} \quad (6.9)$$

with I the identity matrix and Θ the rotation matrix (Eq. (6.4)); ρ is the density, and $(\ddot{\cdot})$ denotes the second derivative with respect to time. Since there are no rotation dofs in the current formulation, we do not include rotary-inertia terms in Eq. (6.7), thus avoiding mass matrices with possibly bad conditioning [Reddy, 2004]. Note also that in Eq. (6.7), we have omitted for simplicity the explicit dependency of the unknown \mathbf{u} on the time variable t . The equilibrium equation (6.7) is nonlinear in the first argument, for which, in order to solve the problem, the Newton-Raphson scheme is used [Reddy, 2004]. The linearization of the functional $G(\mathbf{r}(\mathbf{u}))(\delta \mathbf{u})$ reads:

$$DG(\mathbf{r}(\mathbf{u}))(\delta \mathbf{u}, \delta \mathbf{v}) = \int_0^{l_0} \left((EA + N_\epsilon) \widehat{\delta \epsilon} + (EI_z + N_\kappa) \widehat{\delta \kappa} - m \widehat{\delta \theta} \right) ds_0 - [M \widehat{\delta \theta}]_0^{l_0} \quad (6.10)$$

where:

$$\begin{aligned}\widehat{\delta\epsilon} &= (\delta\mathbf{u}')^T G_{\epsilon'\epsilon'} \delta\mathbf{v}', \\ \widehat{\delta\kappa} &= (\delta\mathbf{u}')^T G_{\kappa'\kappa'} \delta\mathbf{v}' + (\delta\mathbf{u}'')^T G_{\kappa''\kappa'} \delta\mathbf{v}' + (\delta\mathbf{u}')^T G_{\kappa'\kappa''} \delta\mathbf{v}'', \\ \widehat{\delta\theta} &= (\delta\mathbf{u}')^T G_{\theta'\theta'} \delta\mathbf{v}',\end{aligned}\tag{6.11}$$

and:

$$\begin{aligned}G_{\epsilon'\epsilon'} &:= \frac{\|\mathbf{r}'\|_2^2 I - \mathbf{r}'\mathbf{r}'^T}{\|\mathbf{r}'\|_2^3}, \\ G_{\kappa'\kappa'} &:= -2 \frac{[\mathbf{r}'\mathbf{r}''^T \Theta + \Theta^T \mathbf{r}''\mathbf{r}'^T] \|\mathbf{r}'\|_2^2 + [\|\mathbf{r}'\|_2^2 I - 4\mathbf{r}'\mathbf{r}'^T] \mathbf{r}''^T \Theta \mathbf{r}'}{\|\mathbf{r}'\|_2^6}, \\ G_{\theta'\theta'} &:= G_{\kappa'\kappa''} = G_{\kappa''\kappa'} = \frac{\Theta [\|\mathbf{r}'\|_2^2 I - 2\mathbf{r}'\mathbf{r}'^T]}{\|\mathbf{r}'\|_2^4},\end{aligned}\tag{6.12}$$

being $\Theta [\|\mathbf{r}'\|_2^2 I - 2\mathbf{r}'\mathbf{r}'^T]$ a symmetric matrix. Note that although the proposed formulation is valid for large deformations, inertia term are independent of the deformed configuration so no inertia terms appear in Eq. (6.10). The finite dimensional approximation of Eq. (6.6) reads:

$$\text{find } \mathbf{u}_h \in \mathcal{V}_h : G(\mathbf{r}_h(\mathbf{u}_h))(\delta\mathbf{u}_h) = 0 \quad \forall \delta\mathbf{u}_h \in \mathcal{V}_h, \quad \forall t \in (0, t_f),\tag{6.13}$$

given suitable initial conditions at the time $t = 0$, and \mathcal{V}_h is a finite dimensional subspace of \mathcal{V} , such that $\mathcal{V}_h \subset \mathcal{V}$. We remark that the spatial approximation of problem (6.13) by means of the standard Galerkin method requires basis functions which belong to the space $\mathcal{V} \subset H^2(\Omega)$, a requirement that is satisfied when considering globally \mathcal{C}^1 -continuous functions across the mesh elements in the choice of the functions space $\mathcal{V}_h \subset \mathcal{V}$. Contrarily to classical FE methods, NURBS-based IGA can be successfully used to match this requirement.

6.3.3 Isogeometric formulation

We consider the representation of the geometry of a curved beam by means of NURBS [Cottrell et al., 2009]. We say that the geometry mapping \mathbf{r}_0 possesses a p -degree NURBS representation when there exist $n \in \mathbb{N}$ control points $\mathbf{B}_i \in \mathbb{R}^2$, weights $w_i \in \mathbb{R}$, $i = 1, \dots, n$, and a set of knots $\Xi = \{0 = \xi_1 \leq \dots \leq \xi_{n+p+1} = 1\}$ such that:

$$\mathbf{r}_0(\xi) = \sum_{i=1}^n R_{i,p}(\xi) \mathbf{B}_i,\tag{6.14}$$

where $R_{i,p}(\xi)$ is the NURBS basis defined at $\xi \in (0, 1)$ by:

$$R_{i,p}(\xi) = \frac{N_{i,p}(\xi) w_i}{\sum_{j=1}^n N_{j,p}(\xi) w_j},\tag{6.15}$$

with $N_{i,p}(\xi)$ the i -th B-spline basis function defined by the Cox-De Boor recursive formula [Piegl and Tiller, 1997]:

$$N_{i,0}(\xi) = \begin{cases} 1 & \text{if } \xi_i \leq \xi < \xi_{i+1}, \\ 0 & \text{otherwise,} \end{cases} \quad (6.16)$$

$$N_{i,p}(\xi) = \frac{\xi - \xi_i}{\xi_{i+p} - \xi_i} N_{i,p-1}(\xi) + \frac{\xi_{i+p+1} - \xi}{\xi_{i+p+1} - \xi_{i+1}} N_{i+1,p-1}(\xi), \quad \text{for } p \geq 1.$$

The use of weights w_i for $i = 1, \dots, n$ allows the exact representation of conical sections. The so-called knot vector Ξ defines a partition of the parameter domain $(0, 1)$ similar to the classic FE subdivision yielding the so-called mesh of the parametric domain. A non-uniform knot vector and repeated knots are the key of the NURBS flexibility, allowing locally-refined, geometric descriptions and reduced continuity of the basis functions. In particular, a knot of multiplicity q such that $1 \leq q \leq p$ yield basis functions \mathcal{C}^{p-q} -continuous across the knot. In the present chapter, for the purposes of the proposed formulation, at least globally \mathcal{C}^{p-q} basis functions are used with $1 \leq q \leq p-1$ for $p \geq 2$.

For the sake of simplicity, the independent variable ξ is omitted in the rest of the chapter. The first and second derivatives of NURBS basis functions are given by:

$$\frac{dR_{i,p}}{d\xi} = \frac{1}{W} \left(\frac{dN_{i,p}}{d\xi} w_i - R_{i,p} \frac{dW}{d\xi} \right), \quad (6.17)$$

$$\frac{d^2 R_{i,p}}{d\xi^2} = \frac{1}{W} \left(\frac{d^2 N_{i,p}}{d\xi^2} w_i - 2 \frac{dR_{i,p}}{d\xi} \frac{dW}{d\xi} - R_{i,p} \frac{d^2 W}{d\xi^2} \right), \quad (6.18)$$

where $W = \sum_{j=1}^n N_{j,p} w_j$. Derivatives of NURBS basis functions with respect to the initial curvilinear coordinate s_0 are:

$$R'_{i,p} = \frac{1}{\|J_0\|_2} \frac{dR_{i,p}}{d\xi}, \quad (6.19)$$

$$R''_{i,p} = \frac{1}{\|J_0\|_2^2} \frac{d^2 R_{i,p}}{d\xi^2} - \frac{J_0^T \mathbf{H}_0}{\|J_0\|_2^4} \frac{dR_{i,p}}{d\xi}, \quad (6.20)$$

where $\mathbf{H}_0 = \frac{dJ_0}{d\xi}$ and the Jacobian $J_0 = \frac{dr_0}{d\xi}$ is such that:

$$s_0 = \int_0^\xi \|J_0\|_2 d\xi. \quad (6.21)$$

The main idea of the isogeometric approach is to use the same basis functions that represented

the geometry also for the approximation of displacement field as:

$$\mathbf{r} = \sum_{i=1}^n R_{i,p}(\mathbf{B}_i + \mathbf{u}_i), \quad (6.22)$$

where \mathbf{u}_i is the discretized displacement for which in Eq. (6.13) we set $\mathcal{V}_h = \mathcal{V} \cap \text{span}\{R_{i,p}, i = 1, \dots, n\}$. Note that in dynamics, the control variables $\mathbf{u}_i = \mathbf{u}_i(t)$ are time dependent.

The integrals involved in the weak formulation (6.7) are involved in the parametric space using the change of variable given in Eq. (6.21). Their evaluation can be done numerically by using suitable Gauss-quadrature rules (more efficient quadrature rules can be eventually used for NURBS-based IGA [Hughes et al., 2010]). For dynamic beam problems, the generalized- α method is employed as the time integration scheme, which can be second-order accurate and unconditionally stable in linear problems [Chung and Hulbert, 1993]. This method is implemented in the form of a predictor-multicorrector algorithm [Hughes, 1987]. Specifically, we consider the parameters used for the method as dependent on $\rho_\infty \in [0, 1]$, which is the high-frequency dissipation parameter. We refer the reader to [Raknes et al., 2013] for the details of the method and choice of the parameters. Moreover it has been shown in [Espath et al., 2013] that for dynamic problems solved with the generalized- α scheme, k -refinement speeds up the convergence and improves energy conservation.

6.4 Set of static problems and exact/closed-form solutions

We consider a set of static extensible-elastica classical problems, found in the literature, for which exact or closed-form solutions are known [Magnusson et al., 2001, Zhang and Zhong, 2013, Humer, 2013, Humer and Irschik, 2011]. In addition, we propose the closed-form solution of a clamped extensible-elastica initially curved under a transverse tip load.

6.4.1 Test A: straight beam under pure-axial load with non-constant Young modulus

The first problem we propose is a cantilever beam stretched by an axial force P taken as $P = 3EA$. All the properties of the beam are assumed constant except the Young modulus, which is chosen as $E(s_0) = E/(1 + 0.5 \sin(2\pi s_0/l_0))$, with l_0 the length of the beam. The strain equation (6.3) is pure-axial and becomes linear:

$$\begin{aligned} \epsilon &= r'_x - 1, \\ \kappa &= 0, \end{aligned} \quad (6.23)$$

and the weak form (Eq. (6.7)) only involves first-order derivatives. The exact solution for the displacement is:

$$\begin{aligned} u_x(s_0) &= \frac{P}{EA} \left(s_0 - \frac{1}{4\pi} \left(\cos\left(\frac{2\pi s_0}{l_0}\right) - 1 \right) \right), \\ u_y(s_0) &= 0. \end{aligned} \quad (6.24)$$

6.4.2 Tests B: straight and curved beams with pure-bending

We consider two similar problems where a clamped beam initially straight or curved is subjected to a moment M applied at the tip (Fig. 6.2). This problem is of pure-bending type and the curvature remains homogeneous along the beam [Zhang and Zhong, 2013]. In the first problem (test B₁), the initially-straight beam is bent until a quarter of a circle is obtained, while for the second problem (test B₂), the initially-curved beam is bent until a straight beam is obtained. The applied moment to obtain the final configuration reads:

$$M = \pm \frac{EI_z}{R_0} = \pm \frac{\pi EI_z}{2l_0}, \quad (6.25)$$

where the sign + and – indicate tests B₁ and B₂, respectively. The strain equation (6.3) simplifies:

$$\begin{aligned} \epsilon &= 0, \\ \kappa &= \frac{1}{R} - \frac{1}{R_0}, \end{aligned} \quad (6.26)$$

where R and R_0 are the current and initial radius of the beam, respectively. Since κ is a constant through the radius R , the weak formulation (6.7) involves only the first-order operator. The displacement is given by:

$$\begin{aligned} u_x(s_0) &= \pm \left(\frac{2l_0}{\pi} \sin\left(\frac{\pi s_0}{2l_0}\right) - s_0 \right), \\ u_y(s_0) &= \pm \frac{2l_0}{\pi} \cos\left(\frac{\pi s_0}{2l_0}\right). \end{aligned} \quad (6.27)$$

6.4.3 Test C: cantilever straight beam under transverse tip load

The cantilever straight beam under transverse tip load (Fig. 6.3) induces both axial and bending components. The force applied at the extremity is chosen as $P = 2EI_z/l_0^2$. By rewriting the weak form in terms of θ gives with the extensible-elastica method [Humer and Irschik, 2011]:

$$\frac{d\theta}{ds_0} = -\sqrt{\frac{P}{EI_z}} \sqrt{(\sin\theta - \sin\theta_l) \left(2 - \frac{P}{EA} (\sin\theta + \sin\theta_l) \right)}, \quad (6.28)$$

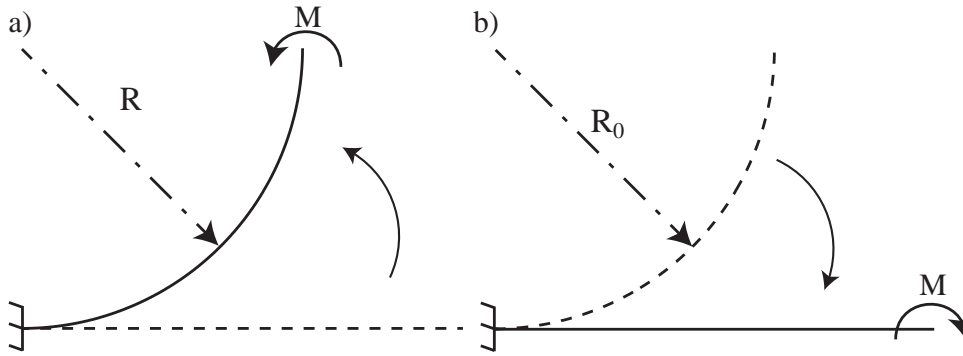


Figure 6.2: Straight (test B₁) (a) and quarter circle beam (test B₂) (b); the moment M is applied to obtain a quarter circle and a straight beam, respectively.

where θ_l , the angle at the tip of the beam, is determined by integration of:

$$l_0 = \int_0^{l_0} ds_0 = \int_0^{\theta_l} \frac{ds_0}{d\theta} d\theta. \quad (6.29)$$

Similarly, the angle in the deformed (current) configuration θ is linked to the original curvilinear coordinate s_0 as:

$$s_0 = \int_0^{s_0} ds_0 = \int_0^{\theta} \frac{ds_0}{d\theta} d\theta. \quad (6.30)$$

The displacement is given by:

$$\begin{aligned} u_x(s_0) &= \int_0^{\theta} \left(\cos\theta + \frac{P}{EA} \cos\theta \sin\theta \right) \frac{ds_0}{d\theta} d\theta - s_0, \\ u_y(s_0) &= \int_0^{\theta} \left(\sin\theta + \frac{P}{EA} \sin^2\theta \right) \frac{ds_0}{d\theta} d\theta. \end{aligned} \quad (6.31)$$

Note that l_0 and s_0 are evaluated by means of numerical integration, alternatively, they can be expressed in terms of incomplete elliptical integrals as in [Humer and Irschik, 2011].

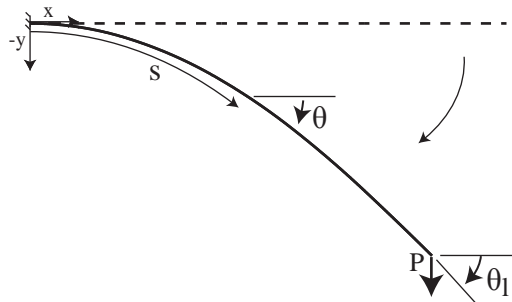


Figure 6.3: Test C: cantilever straight beam under transverse tip load.

6.4.4 Test D: buckling of a pinned-roller beam

Beam buckling is another test involving axial and bending deformations (Fig. 6.4). The applied load is taken as $P = 1.4P_c$ where P_c , the critical load, is defined as:

$$P_c = \frac{\pi^2 EI_z}{l_0^2}. \quad (6.32)$$

In order to follow the stable path from the initial configuration without adding any initial imperfections to the geometry, a second load P' ($P' \ll P$) is applied in the middle of the beam until $P \leq P_c$ and removed afterwards. The analytical closed-form solution of this problem has been derived using again the extensible-elastica equation and can be found in [Magnusson et al., 2001, Humer, 2013].

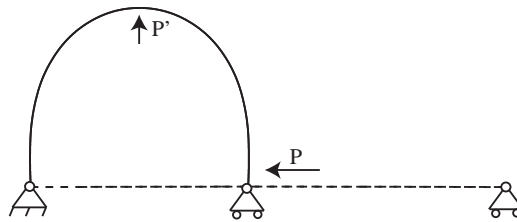


Figure 6.4: Test D: buckling of a pinned-roller beam.

6.4.5 Test E: clamped arc under a transversal tip load

A clamped, curved beam under concentrated load is used to test the formulation for curved beams with axial and bending deformations (Fig. 6.5). By using the same method as [Magnusson et al., 2001, Humer, 2013] for beam buckling, or the straight beam under transverse loads [Humer and Irschik, 2011], we derive the extensible-elastica equation for an initially-curved beam. By inserting Eq. (6.3), expressed in terms of θ and r'_x , into Eq. (6.7), and by using the constitutive law (6.5), we obtain:

$$\frac{d\theta}{ds_0} = \sqrt{\frac{1}{R_0^2} + \frac{2P}{EI_z} (\cos\theta_l - \cos\theta) + \frac{P^2}{EAEI_z} (\cos^2\theta_l - \cos^2\theta)}, \quad (6.33)$$

where the angles θ_l and θ in terms of l_0 and s_0 are found using Eqs. (6.29) and (6.30), respectively. The displacement is given by:

$$\begin{aligned}
 u_x(s_0) &= \int_0^{s_0} r'_x ds_0 - r_{0,x} \\
 &= \int_0^\theta \left(\cos\theta + \frac{P}{EA} \cos^2\theta \right) \frac{ds_0}{d\theta} d\theta - R_0 \sin\theta_0, \\
 u_y(s_0) &= \int_0^{s_0} r'_y ds_0 - r_{0,y} \\
 &= \int_0^\theta \left(\sin\theta + \frac{P}{EA} \cos\theta \sin\theta \right) \frac{ds_0}{d\theta} d\theta - R_0(1 - \cos\theta_0).
 \end{aligned} \tag{6.34}$$

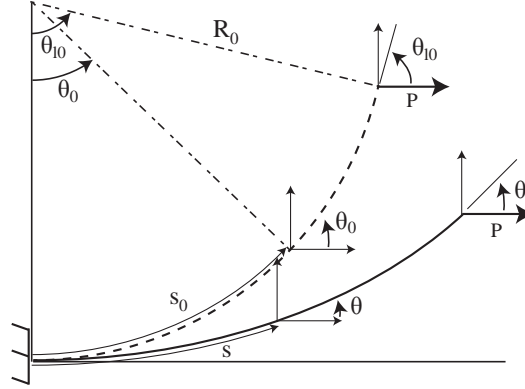


Figure 6.5: Test E: clamped arc under a transversal tip load.

6.5 A-priori error estimation: convergence order

Since the exact/closed-form solutions for the considered static problems are now detailed, the efficiency of the IGA formulation can be verified by using a-priori error estimates under h -refinement [Tagliabue et al., 2014]. We consider the convergence orders of the errors in Hilbert spaces by ensuring that numerical quadrature errors in Eqs. (6.29) and (6.30) are negligible compared to the approximation error of the Galerkin method. Similarly, we consider a “sufficiently”-small tolerance for the convergence criterion of the Newton-Raphson method used to solve the tangent problem associated to Eq. (6.13).

6.5.1 Error norms

Convergence plots of the curve under h -refinement are obtained by computing the approximated solution and the exact ones. The standard error in norm L^2 ($L^2(\Omega) \equiv H^0(\Omega)$), where

$\Omega = (0, l_0)$, reads:

$$\|\mathbf{u} - \mathbf{u}_h\|_{L^2(\Omega)} = \left(\int_0^{l_0} (\mathbf{u} - \mathbf{u}_h)^2 ds_0 \right)^{1/2}. \quad (6.35)$$

When considering high-order PDEs, namely of order $2m$ with $m \geq 1$, the Hilbert norm for $\sigma \geq 1$ is given by:

$$\|\mathbf{u} - \mathbf{u}_h\|_{H^\sigma(\Omega)} = \left(\|\mathbf{u} - \mathbf{u}_h\|_{H^{(\sigma-1)}(\Omega)}^2 + \int_0^{l_0} \left(\frac{d^\sigma}{ds_0^\sigma} (\mathbf{u} - \mathbf{u}_h) \right)^2 ds_0 \right)^{1/2}. \quad (6.36)$$

6.5.2 A-priori error estimation

The a-priori error estimate in the norm H^σ for linear high-order elliptic PDEs provides the convergence order of the errors under h -refinement; we refer the reader to [Tagliabue et al., 2014] for the derivation. Specifically, the error in the Hilbert norm H^σ can be estimated as:

$$\|\mathbf{u} - \mathbf{u}_h\|_{H^\sigma(\Omega)}^2 \leq Ch^\beta \|\mathbf{u}\|_{H^r(\Omega)}, \quad (6.37)$$

if $\mathbf{u} \in \mathcal{V} \cap H^r(\Omega)$, where h is the characteristic mesh size of the elements, and C a constant independent of \mathbf{u} and h ; β is the order of convergence defined as $\beta = \min\{\delta - \sigma, 2(\delta - m)\}$ with $\delta = \min\{r, p + 1\}$ and p the NURBS degree.

We remark that the a-priori error estimates have been derived for linear problems, which is not the case of Eq. (6.7). However, in several instances, the convergence order of the error is often achieved also for nonlinear problems as e.g. in [Dedè and Santos, 2012]. Therefore, we will use the a-priori error estimate (Eq. (6.37)) for verification purposes.

6.6 Static numerical results and discussion

For all tests presented in Sec. 6.4, we assume that the beam has a square cross section ($A = k_0^2$ and $I_z = k_0^4/12$) of thickness $k_0 = 0.02$ m, length $l_0 = 1$ m, and Young modulus $E = 200$ GPa. The stopping criterion for the solution of the nonlinear problem with the Newton-method is defined by $\|\mathcal{R}_j\|_2 / \|\mathcal{R}_0\|_2 < 10^{-8}$ where \mathcal{R}_j is the residual vector at the Newton iteration j . Numerical quadrature is performed using $p + 1$ Gauss-Legendre quadrature points per element.

The geometry representing the beam in the initial configuration is h -refined starting from a straight or a quarter circle and exactly represented by globally \mathcal{C}^1 -continuous NURBS associated to the knot vector $\Xi = \{0, 0, 0, 1, 1, 1\}$. The control points and weights for both geometries are given in Table 6.1. Note that we arbitrarily expressed the straight beam in terms of two parameters associated to the second control point: η ($0 < \eta < 2$) and w_η ($w_\eta > 0$),

which are taken equal to 1 to yield a linearly geometrical map. This is the case for all tests with initially-straight geometry (tests A, B₁, C, and D), with the exception of test B₁^{*}, defined from test B₁, for which $\eta \neq 1$ and/or $w_\eta \neq 1$ are considered.

Table 6.1: Control points $\mathbf{B} = \{\mathbf{B}_x \ \mathbf{B}_y\}^T$ and weights w of the straight (tests A, B₁, B₁^{*}, C and D) and quarter of circle (tests B₂ and E) geometries with globally \mathcal{C}^1 -continuous NURBS corresponding to the knot vector $\Xi = \{0, 0, 0, 1, 1, 1\}$.

Geometry	Straigth			Quarter of circle		
\mathbf{B}_x	0	$\frac{l_0}{2}\eta$	l_0	0	0	R_0
\mathbf{B}_y	0	0	0	0	R_0	R_0
w	1	w_η	1	1	$\frac{1}{\sqrt{2}}$	1

6.6.1 Convergence orders

We verify by means of numerical tests that the convergence orders of the errors under h -refinement are in agreement with expected theoretical ones. Plots of the errors vs. the mesh size h are reported for each norm H^σ with $0 \leq \sigma \leq m$ for globally \mathcal{C}^{p-q} -continuous NURBS basis of degree $p \in \{2, 3, 4\}$, and $1 \leq q \leq p - 1$. Theses plots are given in Figs. 6.6, 6.7 and 6.8 for pure-axial (test A), pure-bending (tests B₁, B₂, and B₁^{*}) and mixed constraints (tests C, D, and E), respectively.

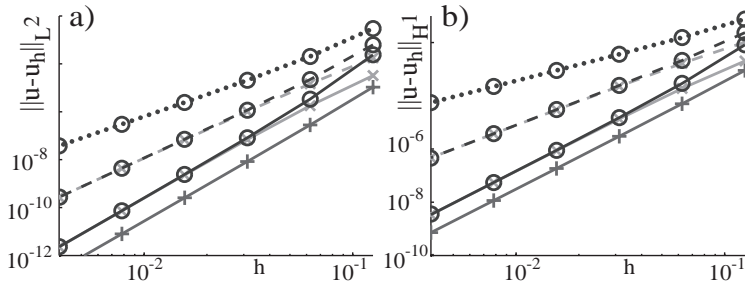


Figure 6.6: Error vs. mesh size h for test A in norms L^2 (a) and H^1 (b). NURBS basis of degree $p \in \{2, 3, 4\}$ are represented by dotted, dashed, and full lines, respectively, and globally \mathcal{C}^{p-q} -continuous basis functions with $q \in \{1, 2, 3\}$ are represented by $\{\circ, \times, +\}$, respectively.

When the mesh size h is decreased, the error decreases linearly in the log-log scale for h “sufficiently” small. The convergence order α_X with $X \in \{A, B_1, B_2, B_1^*, C, D, E\}$ for the different tests, is estimated by using the two last points of the convergence curves presented in Figs. 6.6, 6.7 and 6.8, and are given in Table 6.2. The convergence order β of Eq. (6.37) is evaluated by considering $r \geq p + 1$ since the exact/closed form solutions of the tests under considerations are “sufficiently” smooth. The theoretical-convergence order β for $m = 1$ (β_1) and $m = 2$ (β_2) are also given in Table 6.2 where $2m$ is the order of the differential spatial operator in the strong form of the PDE.

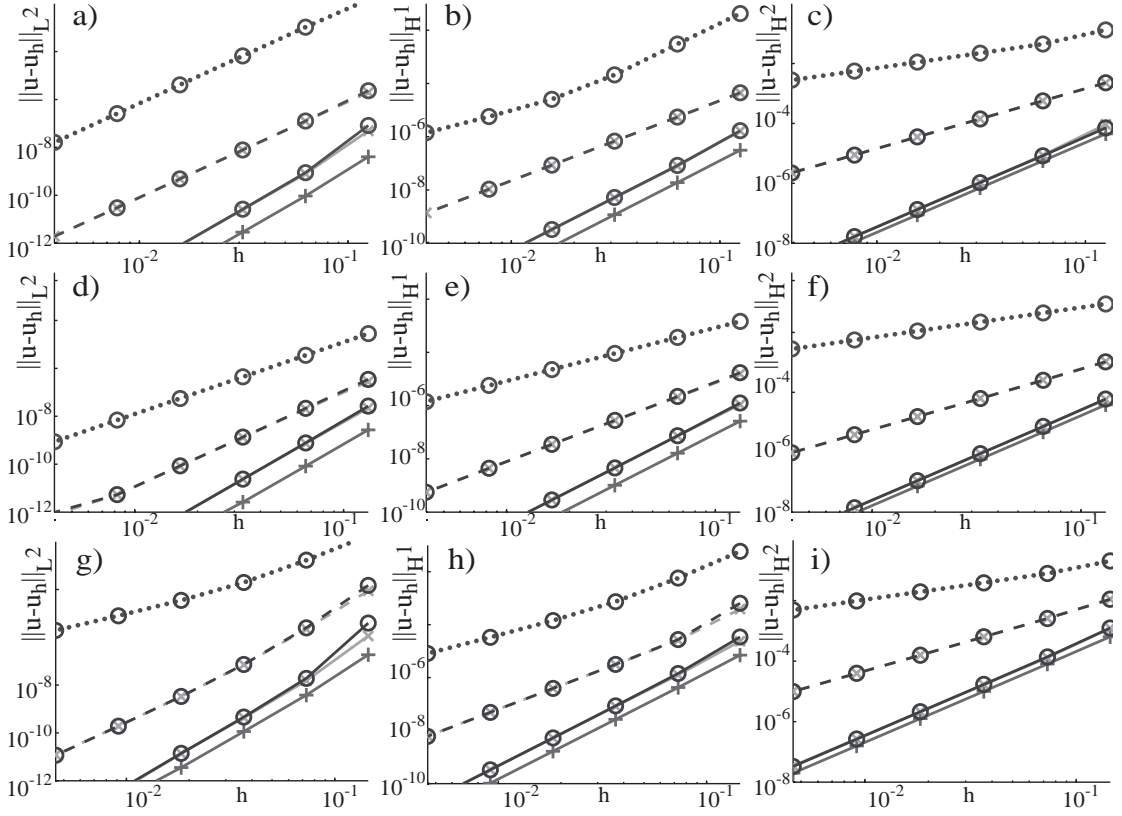


Figure 6.7: Error vs. mesh size h for tests B₁ (a, b, c), B₂ (d, e, f) and B₁^{*} (g, h, i) in norms L^2 (a, d, g), H^1 (b, e, h) and H^2 (c, f, i). NURBS basis of degree $p \in \{2, 3, 4\}$ are represented by dotted, dashed, and full lines, respectively, and globally \mathcal{C}^{p-q} -continuous basis functions with $q \in \{1, 2, 3\}$ are represented by {o, x, +}, respectively.

By focusing on the case of pure-axial deformations (test A), the problem is a first-order, linear problem ($m = 1$) and we deduce $\alpha_A \simeq \beta_1$ from Table 6.2, in agreement with Eq. (6.37).

For problems in pure-bending (Sec. 6.4.2), we have shown that the exact weak form involves only first-order operators. However, this is not the case for approximated solutions since discretization leads to spurious axial terms and non-constant curvature. For tests B₁ and B₂, the convergence orders are $\alpha_{B_1} \simeq \alpha_{B_2} \simeq \beta_2$, except for curves in the norm L^2 with NURBS of degree $p = 2$. Indeed, the convergence orders are higher than expected ($\beta_2 = 2$), being $\alpha_{B_1} \simeq 4$ and $\alpha_{B_2} \simeq 3$ yielding a convergence order higher than the expected one. For test B₁^{*}, the results are obtained for $\eta = 1$ and $w_\eta = \frac{1}{\sqrt{2}}$ but can be extended to any case with $\eta \neq 1$ and/or $w_\eta \neq 1$. We find that $\alpha_{B_1^*} \simeq \beta_2$ even for $p = 2$ in the norm L^2 .

For the results where both axial and bending terms are activated (tests C, D, and E), we have from Table 6.2 that $\alpha_C \simeq \alpha_D \simeq \alpha_E \simeq \beta_2$.

In passing, we emphasize that for a given NURBS basis degree p and a fixed mesh size h , increasing the continuity increases the error. Indeed, for the same mesh size, smoother basis

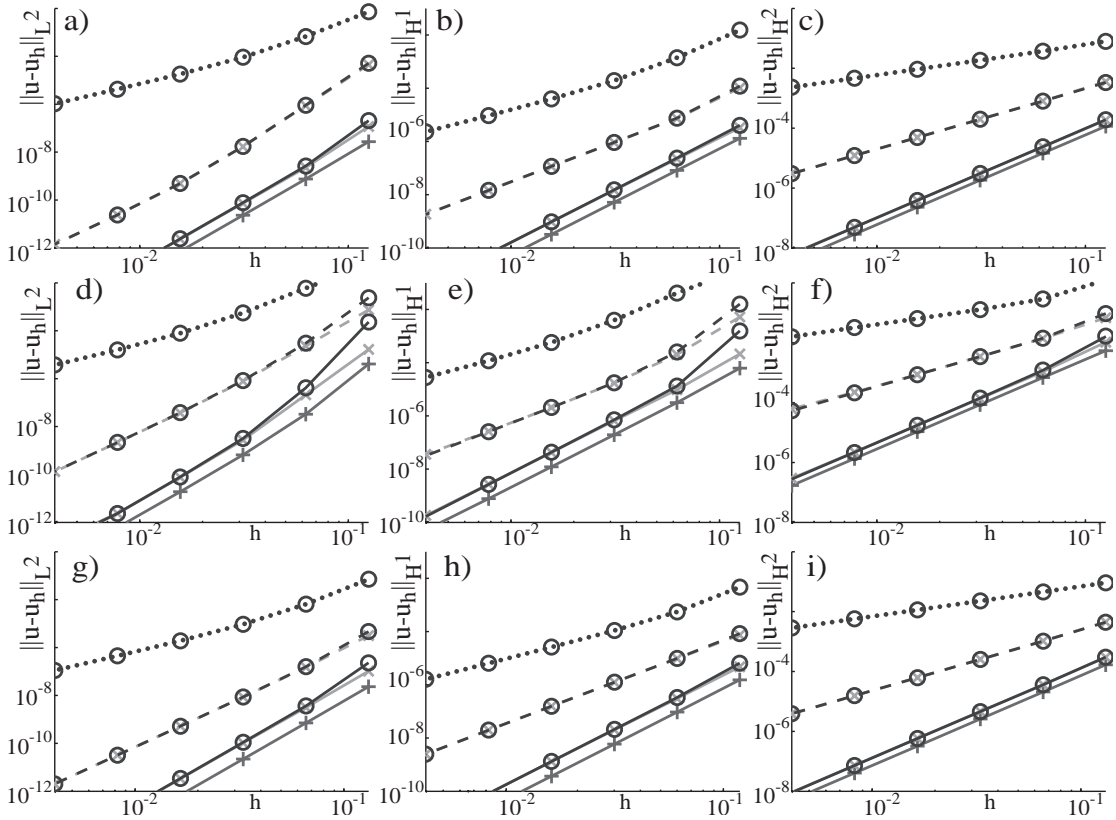


Figure 6.8: Error vs. mesh size h for tests C (a, b, c), D (d, e, f) and E (g, h, i) in norms L^2 (a, d, g), H^1 (b, e, h) and H^2 (c, f, i). NURBS basis of degree $p \in \{2, 3, 4\}$ are represented by dotted, dashed, and full lines, respectively, and globally \mathcal{C}^{p-q} -continuous basis functions with $q \in \{1, 2, 3\}$ are represented by $\{\circ, \times, +\}$, respectively.

functions use less dofs than the basis with lower continuity, which have more degrees of freedom to fit the solution.

6.6.2 Membrane locking

The formulation considered in this chapter is free of shear locking by design based on Euler-Bernoulli-beam assumptions [Ishaquddin et al., 2013], but not of membrane locking. Membrane locking is attributed to the inability of the basis functions to reproduce the inextensible bending due to the appearance of spurious axial (membrane) terms that constitute the major part of the strain energy. Indeed, in Eq. (6.3), the axial strain ϵ is composed of two terms of different order which are integrated using the same Gauss rule, leading, in the case of pure-bending, to the inability to satisfy exactly $\epsilon = 0$. This is also the reason for which the discretized weak form cannot be simplified to a first-order problem in the case of pure-bending. By

Table 6.2: Convergence order α for the different tests compared to the estimated convergence orders β_1 or β_2 in norm H^σ , for globally \mathcal{C}^{p-q} -continuous NURBS basis of degree p .

Norm	L^2						H^1						H^2					
	2		3		4		2		3		4		2		3		4	
\mathcal{C}^{p-q}	\mathcal{C}^1	\mathcal{C}^1	\mathcal{C}^2	\mathcal{C}^1	\mathcal{C}^2	\mathcal{C}^3	\mathcal{C}^1	\mathcal{C}^1	\mathcal{C}^2	\mathcal{C}^1	\mathcal{C}^2	\mathcal{C}^3	\mathcal{C}^1	\mathcal{C}^1	\mathcal{C}^2	\mathcal{C}^1	\mathcal{C}^2	\mathcal{C}^3
β_1	3	4	4	5	5	5	2	3	3	4	4	4						
α_A	3.01	3.99	4.00	5.01	4.99	4.99	2.00	2.99	3.00	4.01	4.00	4.00						
β_2	2	4	4	5	5	5	2	3	3	4	4	4	1	2	2	3	3	3
α_{B_1}	4.00	4.00	4.00	4.97	5.01	5.00	2.01	3.99	3.00	3.99	3.99	4.00	1.00	1.99	2.00	3.00	3.00	3.00
α_{B_2}	3.00	3.99	3.99	5.00	5.01	5.01	2.00	2.99	3.00	4.00	4.00	4.00	1.00	2.00	2.00	3.00	3.00	3.00
$\alpha_{B_1^*}$	2.04	3.99	4.04	5.01	4.99	5.04	2.03	2.98	3.00	3.99	3.98	4.00	1.00	1.98	2.00	3.98	3.00	3.00
α_C	2.03	4.09	4.06	4.96	5.00	5.00	2.02	2.99	3.00	3.95	4.00	3.98	1.00	2.00	2.01	3.00	2.99	2.99
α_D	2.09	4.03	4.03	4.99	4.96	5.05	2.08	2.96	3.00	3.96	3.97	4.00	1.00	1.96	2.00	2.97	2.99	3.01
α_E	2.02	4.00	4.00	4.96	5.00	5.00	2.00	2.99	3.00	3.96	3.99	4.00	1.00	2.01	2.00	2.99	2.99	3.00

defining the slenderness parameter as:

$$\lambda = \sqrt{\frac{I_z}{Al_0^2}}, \quad (6.38)$$

the membrane-locking phenomenon is shown for test B_2 in Fig. 6.9 by setting $\lambda = k_0 / (l_0 \sqrt{12}) = 0.001 / \sqrt{12}$ (k_0 is now $k_0 = 0.001$). This phenomenon does not occur for the test in Fig. 6.7d where $\lambda = 0.02 / \sqrt{12}$. Membrane locking appears when the slenderness is small since the membrane and bending terms are proportional to k_0 and k_0^3 , respectively. Contrarily to the Timoshenko beam [Beirão da Veiga et al., 2012, Bouclier et al., 2012], membrane locking is present also for initially-straight beams since the constant terms of ϵ in Eq. (6.3) are not zero. As shown in Fig. 6.9, the increased NURBS degree alleviates membrane locking as it has been already observed in FE and IGA [Reddy, 2004, Bouclier et al., 2012, Ibrahimbegovic, 1995]. However, by increasing the degree p , the number of dofs and the computational cost increases; we remark that for NURBS-based IGA, the dof number only moderately increases when increasing p and the smoothness of the basis function (k -refinement). Alternative methods completely free of locking are presented in [Beirão da Veiga et al., 2012, Bouclier et al., 2012] in the framework of isogeometric Timoshenko beams.

Finally, even though shear-free assumptions are violated for large thickness ratio (for $k_0 \approx 1$ we have $\lambda \approx 1 / \sqrt{12}$), we have analyzed convergence rates for such conditions. We find that the computed convergence order is reduced with respect to the one expected for linear PDEs (Eq. (6.37)). This phenomenon is not due to membrane locking but appears to be sensitive to the NURBS basis global continuity, and deserves further investigations.

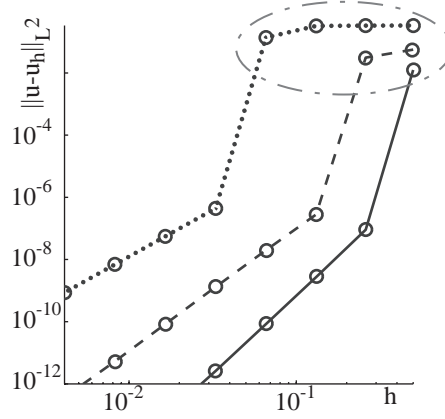


Figure 6.9: Error vs. mesh size h for test B_1 in norms L^2 . Globally \mathcal{C}^{p-1} -continuous NURBS basis of degree $p \in \{2, 3, 4\}$ are represented by dotted, dashed, and full lines, respectively. The slenderness is $\lambda = 0.001/\sqrt{12}$. The simulations for which membrane locking happens are highlighted with a dashed ellipse.

6.7 Dynamic problems

We consider now two different dynamic beam problems.

6.7.1 Solitons propagating in post buckled beams

Post-buckled beams (Fig. 6.10a) possess a geometrically-nonlinear load-displacement relationship ($P(\Delta U)$; see Fig. 6.10c) and dispersion sources for which the phase velocity decreases with frequency, such that these structures are capable of hosting solitons (nonlinear stationary waves) [Maurin and Spadoni, 2014b,a]. In [Maurin and Spadoni, 2014a] it is shown that these conditions on the dispersion (phase speed decreases with frequency) are only valid for some configurations depending on the buckling level, type of supports (necessary to ensure the stability), and curvature. This is the case of the highly-buckled beam on roller supports [Maurin and Spadoni, 2014b].

The numerical simulation of these beam problems is obtained by the application of two distinct steps: a static one in load control, where the beam, with a large number of unit cells (q), is buckled (Fig. 6.10a), and a dynamic one, in displacement control, where a pulse is sent through the buckled structure (Fig. 6.10b). We define the axial displacement of the support j by $U_j = u_x(\xi_j) = \sum_{i=1}^n R_i(\xi_j) u_{i,x}$, where ξ_j is the position of the pinned-support in the knot vector. The strain ζ_j at the support j is defined as the variation of the distance between two supports, and taken positive in compression such that:

$$\zeta_j = \frac{U_j - U_{j+1}}{L_0} = \frac{\Delta U_j}{L_0}, \quad \text{for } j = 1, \dots, q-1, \quad (6.39)$$

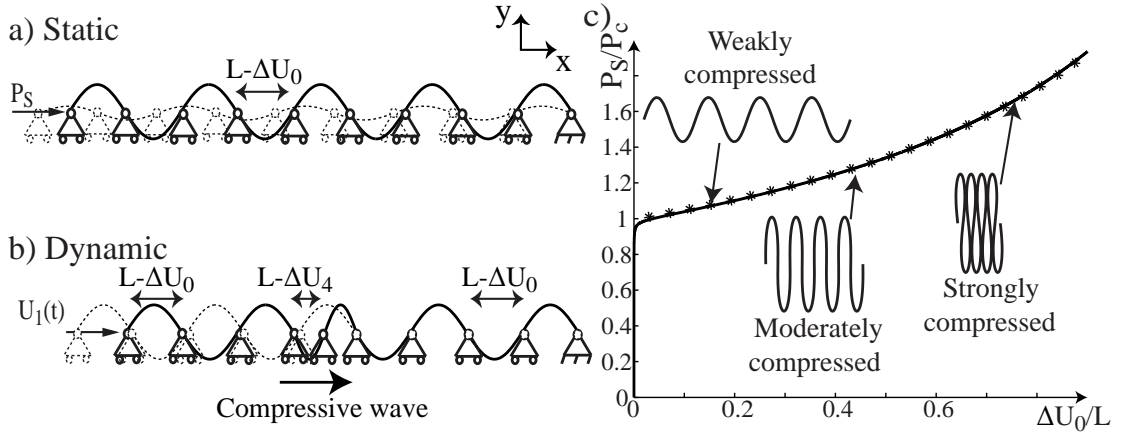


Figure 6.10: (a, b) Schematic post buckled beam with $q = 9$ unit cells. (a) Initial (dashed line) and post-buckled (solid line) configurations after applying the static load $P_S = P(\Delta U_0)$. (b) Displacement control $U_1(t)$ (Eq. (6.41)) resulting in a propagating compressional wave (solid line). (c) Nonlinear load displacement-relationship $P(\Delta U_0)$ with elastica solution [Maurin and Spadoni, 2014b] (*) and results obtained by a static simulation using the present formulation (full line).

where $L_0 = L - \Delta U_0 = L(1 - \zeta_0)$, and L is the length between two supports before buckling; ΔU_0 and ζ_0 are constant after the static buckling along the beam and are the relative displacement between two consecutive supports and strain, respectively. By modeling the structure by a series of alternating masses and nonlinear springs, and approximating locally the load-displacement by a second order polynomial, it is shown in [Maurin and Spadoni, 2014b] that the homogenization of the discrete system leads to the Boussinesq equation ([Remoissenet, 1995]) admitting a soliton as solution, reading:

$$\Delta\zeta = \Delta\zeta_m \operatorname{sech}^2(\Lambda^{-1}(x - Vt)), \quad (6.40)$$

where $\Delta\zeta = \zeta - \zeta_0$ is the dynamic strain wave and $\Delta\zeta_m$ its amplitude; in addition, $V^2 = C_0^2 + \sigma\Delta\zeta_m / (3C_0)$ is the soliton phase velocity and $\Lambda = \sqrt{24C_0\gamma / (\sigma\Delta\zeta_m)}$ its characteristic width, where $C_0^2 = P'(\Delta U_0)L_0^2/m$, $\sigma = P''(\Delta U_0)L_0^3/m$, $\gamma = C_0L_0^2/24$, and $m = \rho AL$. The dynamic displacement applied at the left extremity of the beam is obtained by integrating Eq. (6.40):

$$U_1(t) = \Delta\zeta_m \Lambda (\tanh(\Lambda^{-1}V(t - t_0)) + 1) + q\Delta U_0, \quad (6.41)$$

where t_0 is arbitrary chosen as $t_0 = 5\Lambda V^{-1}$. Note that in the present case, it is restricted to the post-buckled beam compressed with a really strong pre-compression, such that contrary to previous chapters, one can use the simple Boussinesq model instead of the double-dispersion one (dispersion only resulting from periodicity when pre-compression is really large, see Fig. 4.4).

In order to get buckling, instead of considering additional loads as done in Sec. 6.4.4, initial imperfections in the configuration of the beam are used. The procedure used to construct the

initial geometry with imperfections reads:

- build a straight beam with globally \mathcal{C}^1 -continuous NURBS basis of degree $p = 2$ as defined in Table 6.1 with $\eta = 1$ and $l_0 = qL$;
- h -refine the knot vector to get q equispaced mesh elements;
- modify the y coordinates of the $q + 1$ control points such that:

$$B_{j,y} = \begin{cases} 0 & \text{if } j = \{1, q + 1\}, \\ (-1)^j e & \text{otherwise,} \end{cases} \quad (6.42)$$

where $0 < e \ll L_0$ is the parameter characterizing the imperfection amount (Fig. 6.11a);

- perform order elevations and then additional knots insertions without repeating existing knots (Figs. 6.11a, b) such that the NURBS basis remains globally \mathcal{C}^1 -continuous.

The applied boundary conditions are illustrated in Fig. 6.10a. However, since the NURBS basis functions are globally \mathcal{C}^1 -continuous, the control points which are not at the extremities of the beam do not lay on the geometry. For each support $j = 2, \dots, q - 1$, the y displacement is fixed by enforcing the condition:

$$r_y(\xi_j) = \sum_{i=1}^n R_i(\xi_j)(B_{i,y} + u_{i,y}) = \sum_{i=1}^n R_i(\xi_j) u_{i,y} = \mathbf{C}_j \mathbf{u} = 0, \quad (6.43)$$

where the position of the support in the knot vector is given by $\xi_j = j/q$ and \mathbf{C}_j is a vector which has for length the number of dofs, built from shape functions, and completed by zeros. In order to enforce these conditions, $q - 1$ Lagrange multipliers λ_j [Wriggers and Nackenhorst, 2006] are introduced, thus resulting in a coupled system of two equations:

$$G(\mathbf{r}(\mathbf{u}))(\delta \mathbf{u}) + \sum_{j=1}^{q-1} \lambda_j \mathbf{C}_j \delta \mathbf{u} = 0, \quad (6.44)$$

$$\sum_{j=1}^{q-1} \mathbf{C}_j \mathbf{u} \delta \lambda_j = 0. \quad (6.45)$$

Eq. (6.44) represents the virtual work (see Eq. (6.7)) and Eq. (6.45) is the variation of the force necessary to constrain the displacement of the supports along y .

For the numerical simulation, the following parameters are used: number of unit cells $q = 150$, rectangular cross section of the beam width $b_0 = 12$ mm and thickness $k_0 = 0.4$ mm, $L = 0.06$ m, $E = 200$ GPa, and $\rho = 8000$ Kg m⁻³. The initial imperfection is $e = 0.1$ mm, the initial buckling compression $\Delta U_0/L = 0.8$ (Fig. 6.10c), and the amplitude of the dynamic strain wave $\Delta \zeta_m = 0.1$. Each span (unit cell) is divided into $n_e/q = 14$ mesh elements, and the degree of the NURBS basis is $p = 3$, such that these parameters give a good approximation of the

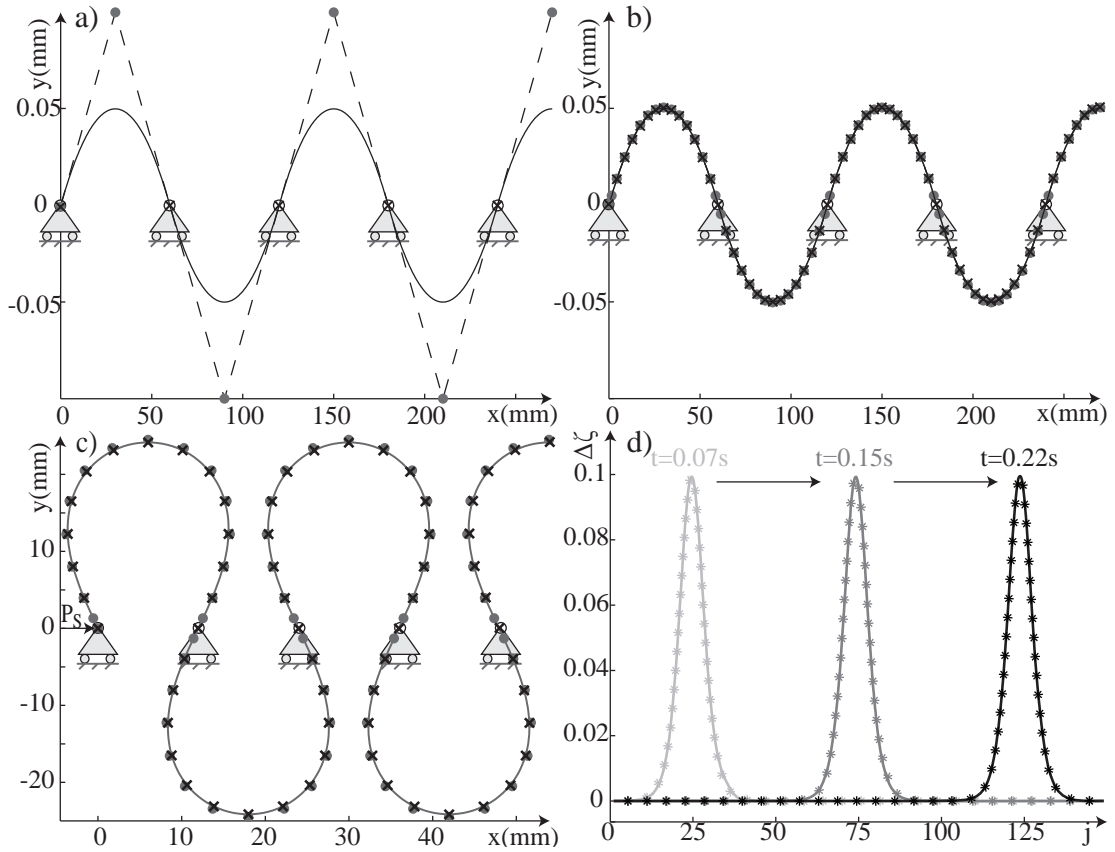


Figure 6.11: (a, b, c) Four first unit cells (a) before and (b, c) after the refinement, and (a, b) before and (c) after the static buckling. Control points and knots locations are represented by • and ×, respectively. (d) Snapshots at time $t = \{0.07, 0.15, 0.22\}$ s of the strain wave $\Delta\zeta$ vs. the support number j resulting from simulation (full lines), and compared with the analytical soliton (Eq. (6.40)) (curves with *).

analytical elastica equation [Maurin and Spadoni, 2014b] (see Fig. 6.10c). In the static part, the load is incrementally applied in 1000 steps, while in the dynamic part 1000 time steps are used with a total integration time $t_f = qL_0V$ and $\rho_\infty = 0.9$. The resulting strain wave is shown in Fig. 6.11. While propagating, the wave preserves its shape. Moreover, the strain wave overlaps very well with the approximated analytical equation describing solitons (Eq. (6.40)). This example shows that our formulation can be conveniently adapted to nonlinear wave propagation problems in slender structures undergoing large dynamic deformations.

6.7.2 Dynamic snap-through buckling

We consider the snap-through buckling of a transversally-loaded arch, which is obtained from the buckling of an initially straight beam (see Figs. 6.12a, b). This problem is particularly interesting because it involves internal resonances [Nayfeh et al., 1999], and thus is good candidate to demonstrate the robustness of the proposed methods. In particular, we are

interested in the transient response of a buckled beam laterally loaded in its center by a step load, as already studied in [Chen and Tsao, 2014], and we aim at reproducing the findings of [Chen and Tsao, 2014]: the critical load is (i) smaller in dynamics than in statics and (ii) it decreases with extensibility (the extensibility is inversely proportional to the slenderness parameter λ defined in Eq. (6.38)). The construction of the initial geometry with the initial imperfections follows the method presented in Sec. 6.7.1 with a single unit cell ($q = 1$). The beam is divided into $n_e = 150$ mesh elements and the degree of the NURBS basis is $p = 3$ with NURBS basis functions which are \mathcal{C}^2 -continuous. The material and geometrical parameters are the same as in Sec. 6.7.1 except the initial length of the beam defined by $l_0 = \sqrt{I_z/A}/\lambda$. We choose $\lambda = 0.01$ and 0.02 to compare the influence of extensibility. The time step is $\Delta t = 0.001T$, where $T = l_0^2 \sqrt{\rho A/EI_z}$, and $\rho_\infty = 0.9$.

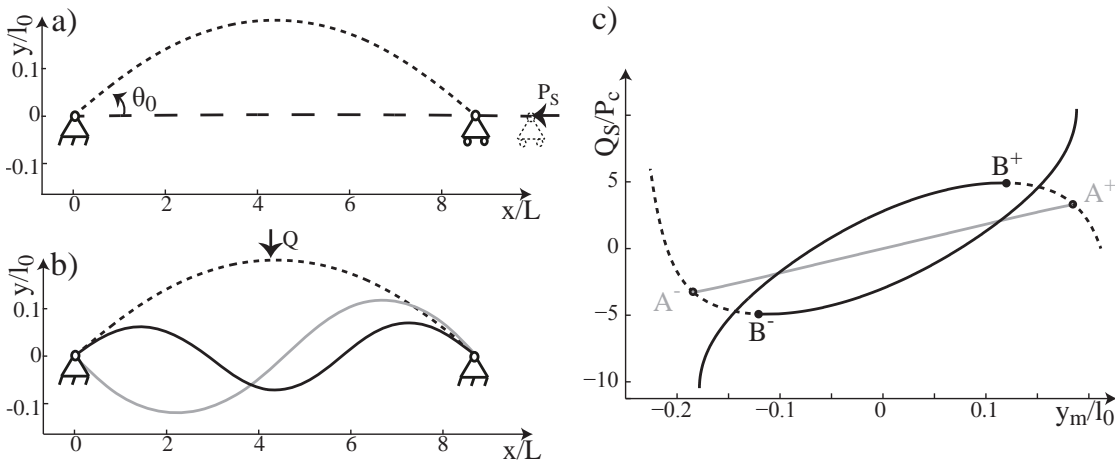


Figure 6.12: (a) Straight beam (large dashes) statically buckled (small dashes) and (b) snap-through its second (gray line) or third (black line) mode after the application of a load (Q) along the y axis at the mid span. (c) Resulting load (Q_S) midpoint-displacement (y_m) curve. Points A and B are the static critical load of the second and third modes, respectively; the $()^+$ and $()^-$ give the sign of the initial angle θ_0 . We set $\theta_0 = 40^\circ$ and $\lambda = 0.01$.

The static snapping critical load for the beam is obtained from the non-monotonic load-displacement curve (Fig. 6.12c), computed using the arc-length method [Schweizerhof and Wriggers, 1986]. If the beam is perfectly symmetric and the load is applied in its center, the second mode (asymmetric) is not excited and the deformed beam “jumps” (point B in Fig. 6.12c) directly to the third mode (symmetric); whereas, if asymmetric imperfections are present (e.g. the load is not perfectly applied in the center), snapping occurs at point A (see Fig. 6.12c) with deformation given by the second mode (Figs. 6.12a,b). Values of the normalized critical load (Q_S/P_C) are reported in Table 6.3 where we can already conclude that the critical load is smaller in dynamics than in statics, in agreement with [Chen and Tsao, 2014].

In Fig. 6.13a, the midpoint deflection history of the beam under a dynamic step load $Q_D(t) =$

6.8. Comparison to co-rotational beam formulation

Table 6.3: Nondimensional static critical load Q_S/P_c (P_c defined in Eq. (6.32)) for snapping through the second and third bucking modes and for two different levels of beam slenderness λ . Results are compared to [Chen and Tsao, 2014], if available.

λ	0.01	0.02
Mode 2	3.31 (3.31 [Chen and Tsao, 2014])	3.21
Mode 3	4.92	4.65

$H(t)Q_D$ is reported, where $H(t)$ is the Heaviside function and $Q_D = 4P_c$ is chosen between the static critical load (Q_S) of the second and third mode (see Table 6.3). Both configurations of slenderness (λ) are considered. Although the dynamic load is smaller than the static critical load, snapping occurs directly through the third mode for the most extensible beam ($\lambda = 0.02$) (see deformed shapes in Fig. 6.13d) showing that the dynamic critical load is smaller than the static one. Conversely, in the case $\lambda = 0.01$, the beam does not have enough energy to snap directly through the excited mode (mode three). The beam starts oscillating (Fig. 6.13b), then snaps through the second mode (Fig. 6.13c). For the same load $Q_D(t)$, since only the most extensible beam snaps directly through the third mode, dynamic critical load values become smaller and smaller for increasing values of extensibility, in agreement with [Chen and Tsao, 2014].

Although we recover the same results, the point here is to compare both methods. Indeed, in [Chen and Tsao, 2014], the extensible-elastica concept based on the same strain kinematics and constitutive law is used, similarly to the proposed formulation. Solutions of the extensible-elastica are presented in terms of rotation and axial displacements in [Chen and Tsao, 2014], while we report in this chapter x and y -displacement components. Accordingly, the main difference lies in discretization of the problem; finite differences associated to the second-order Crank-Nicolson time integration scheme are used in [Chen and Tsao, 2014], whereas the formulation presented here considers NURBS-based IGA with the second-order generalized- α scheme. Even if direct comparisons of the results are not possible, since the smoothness of the displacement field and rotation is ensured by the NURBS basis functions which are globally \mathcal{C}^1 -continuous, a small number of mesh elements and time steps is required in the present work, leading to significant gains in computational efforts.

6.8 Comparison to co-rotational beam formulation

The rotation-free extensible-elastica formulation allows large geometrical displacements, rotations and strains, and the strain follows directly from geometrical considerations without approximations. In the previous section, it has been shown that the extensible-elastica can be solved numerically using NURBS-based IGA, but alternative approximated methods exist and it is the goal here to compare their efficiency in terms of error and computational cost.

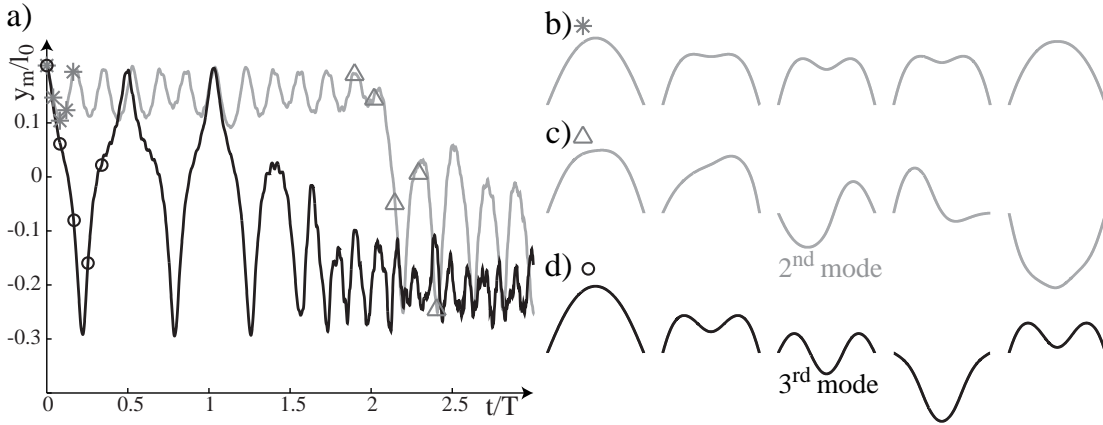


Figure 6.13: Dynamic snap-through buckling of a beam with initial angle $\theta_0 = 40^\circ$, of slenderness $\lambda = 0.01$ (gray) and $\lambda = 0.02$ (black) laterally loaded in its center by a step load ($Q_D/P_c = 4$). (a) Time history of the normalized center deflection y_m/l_0 and (b, c, d) snapshots of the deformed shape. For the less extensible case, the beam oscillates around its first mode (b) and snaps through its second buckling mode after $t/T \approx 2$ (c), whereas for the most extensible case, the beam snaps directly to its third mode (d). Snapshots starts at time $t/T = 0$ (b, d) and $t/T = 2.2$ (c) with a time step between each snapshots of $\Delta t/T = 0.04$ (b), $\Delta t/T = 0.13$ (c) and $\Delta t/T = 0.08$ (d), and are represented in (a) by *, Δ , and \circ , respectively. $l_0 = [0.0289, 0.0144]$ m, $P_C = [197.3921, 789.5684]$ N and $T = [5.8095, 1.4524] \times 10^{-4}$ s for $\lambda = [0.01, 0.02]$, respectively.

We focus here on the co-rotational beam that decomposes the motion into rigid body and pure deformation [Battini, 2002, Borst et al., 2012]. Each element is rotated back to its local original frame and this allows an artificial separation of the material and geometrical nonlinearities. However, this limits the strain to small levels since geometrical deformations are not considered in the local frame. In counterpart, the resulting implementation into FE codes turns out to be simplified and does not require the use of IGA. Moreover, small strain deformations can be approximated by small-degree polynomial shape-function such that the minimum of integration point per element is only one. Note however that as for classical FE beams, in addition to the two dofs per node modeling the displacement, an additional one is required for the rotation.

To sum up, the rotation-free formulation is more accurate than the co-rotational one, but is much more complex to implement and requires loops over integration points. On the contrary, in order to have results of the same accuracy, it is necessary to choose the co-rotational formulation with a finer mesh, and added to the fact that it requires an extra dof per node for the rotation, the total number of dofs in the co-rotational formulation is more important than the one in the rotation-free formulation. This means that on one side, the formulation is more complex (tangent stiffness complexed to build), whereas on the other side the problem is larger (time inversion increased) and the question is which formulation is the fastest for a given accuracy?

To answer to this question, the pinned-supported buckled beam analyzed in Sec. 6.7.1 is

simulated using both IGA and co-rotational methods with several levels of discretization, and the error in terms of the computation time is given in Fig. 6.14. Both computation times of the static and dynamic simulations are shown, but the error is based only from the static solution from which an exact solution exist (see Sec. 6.4).

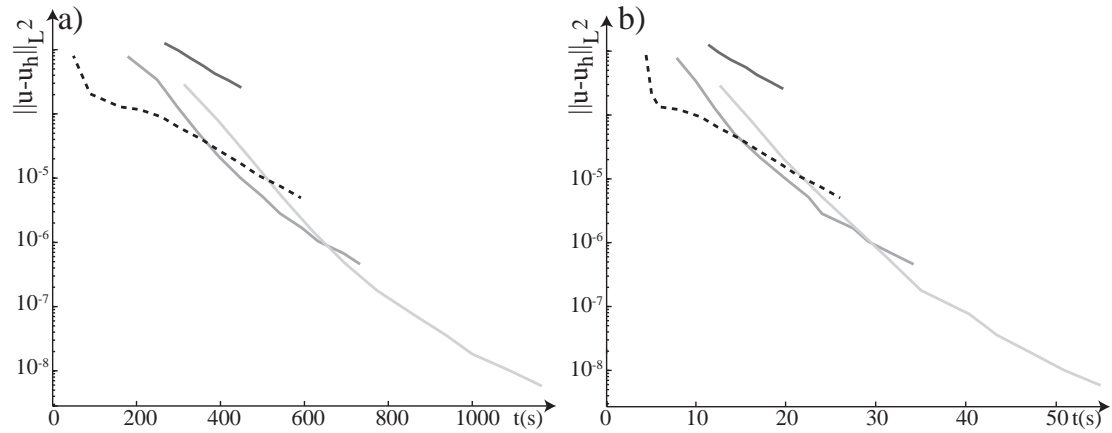


Figure 6.14: Error in norms L^2 in terms of the computation time of the simulation in static (a) and dynamic (b) of the pinned-support buckled beam with 50 supports. NURBS basis are globally \mathcal{C}^{p-1} -continuous and are of degree $p \in \{1, 2, 3, 4\}$ represented from dark to light-gray lines ($p = 1$ also in dashed lines is equivalent to classical FE). Note that these results are computed using *Matlab*, considering sparse matrices and MEX-Files.

The first comment arising from Fig. 6.14 is that both static and dynamic simulations give similar results. In terms of computational cost, the co-rotational formulation used as a first approximation is found faster, whereas if high-resolution results are required, the rotation-free formulation provides results more quickly.

Moreover, these plots are given using the Newton-Raphson algorithm to solve the nonlinear problem. This means that at each load increment, $i \geq 1$ Newton-Raphson iterations are run involving i tangent stiffness matrix computations and i problem inversions. Alternatively (but not implemented here), the modified Newton-Raphson algorithm considers $j \geq i$ problem inversions whereas the tangent stiffness matrix is computed only once at the beginning of the step but is not updated during the Newton-Raphson iterative process. Defining now N as the number of dofs, the time to the problem inversion is proportional to N^3 whereas the one for the matrix assembling is only proportional to N . It is clear that the modified Newton-Raphson method will be more efficient with the rotation-free extensible-elastica formulations, whatever the accuracy required.

6.9 Conclusions

Rotation-free extensible-elastica formulations involves fourth order spatial derivatives of displacements that are not available in classical FE methods, and we propose the use of

IGA based on NURBS with high-degree continuous basis functions for the finite-element approximation. The performance of the discretized model has been verified by means of a-priori error estimates based on several static test problems for which an analytical solution is known. In addition to problems available in literature, a closed-form solution based on the extensible-elastica theory for the initially-curved, clamped beam under transverse load is also derived. We remark that the formulation under consideration may suffer from membrane locking when elements have small thickness ratio. Another advantage is the reduced number of degrees of freedom involved, since the formulation is rotation-free. The absence of the rotary degree of freedom is of great interest in dynamics, leading to constant mass terms which contain the computational cost and allowing the simulation of complex beam problems.

In addition, it is shown that the computational cost of the present formulation is smaller than the co-rotational formulation, as soon as high-accuracy is required. The only reason justifying why the co-rotational formulation has been preferred in previous chapters is that it does not require the implementation of Lagrange multipliers, facilitating the manipulation of the different vector quantities in *Matlab*.

7 Conclusions

7.1 Summary of the results

The research presented in this work investigates periodic buckled structures that possess geometrical nonlinearities and intrinsic dispersive sources. The main finding is to show that these structures host solitary waves.

More specifically, starting from the extensible-elastica, static stability and geometrical nonlinearities are investigated, and a new approximated equation describing the nonlinear load-displacement behavior between extremities of a pinned or guided-supported buckled beam with initial geometrical imperfections is derived. This equation is valid for post-buckled regimes, where bending deformations are dominant and for weakly-buckled states, where imperfections and axial deformations dominate. Moreover, this equation shows that the second derivative of the load-displacement relation is negative for weakly pre-compression levels (softening behavior), whereas it is positive otherwise (hardening behavior).

The linear dispersion is analyzed employing the semi-analytical dispersion equation, a newly method that explicitly relates the frequency to the propagation constant of the acoustic branch. This allows the identification and the numerical quantification of the different dispersion sources and it is found that in addition to periodicity, transverse inertial effects are playing a dominant role for small pre-compression levels. In the case of the pinned-supported configuration, in addition to the aforementioned dispersion sources, stiffness coupling between rotations and axial displacements are dominant. The main conclusion of the dispersion analysis is that the dispersion behavior (sign of the total dispersion) changes with the pre-compression level and the support type. While for the guided-supported beam, dispersion behavior is of type supersonic whatever the pre-compression level, in the case of the pinned-supported configuration, dispersion behavior is of type supersonic only for strong compression and it is otherwise of type subsonic.

Modeling the system by a mass-spring chain and accounting for additional dispersion sources, it is shown in Chapter 4 that homogenization of the discrete system and the use of asymptotic

methods to couple momentum equations lead to the double-dispersion Boussinesq equation, which admits solitary wave solutions. By combining the signs of the nonlinear and dispersive terms, four different waves are possible, namely compressive supersonic, tensile supersonic, compressive subsonic and tensile subsonic solitary waves. What is particularly interesting with buckled beams is that by varying the pre-compression level and the support type, these four wave types are present. Moreover, for the pinned-supported configuration, only varying the pre-compression level changes the medium behavior from subsonic to supersonic.

The double-dispersion Boussinesq equation is derived by approximating the load-displacement relation by a second order polynomial. However, for waves with large amplitudes or for small levels of pre-compression, models based on strongly nonlinear PDEs are more appropriate and the approximation of the load-displacement relation by a power law is proposed, as often used in granular media. Alternatively, the load-displacement relation can be kept general (not approximated by a function) but the results are not analytical and require the use of numerical integrations. Both strong nonlinear PDEs are updated to account for additional dispersion sources, and solitary solutions are found using the potential method. Analytical model results are then compared to finite-element simulations of the structure and are found in excellent agreement.

Experiments about the weakly-buckled guided-supported beam are also investigated. The setup is a 2 m long beam which is buckled into 30 ripples. While the pre-compression is applied on one side through a screw, dynamic pulses are sent at the other side through a shaker. It is found that the medium is supersonic, meaning that the phase-speed increases with amplitude and if the input is not stationary, there is creation of a tail but never a front, in agreement with the supersonic properties expected. Moreover, the phase-speed is in agreement with the predicted values and it is recovered that the speed decreases with pre-compression. While the wave profile seems stationary, due to limitations in the setup size, the reflected wave appears after few supports and long-wave observations as the wavelength, period, heterogeneity effects, and friction-induced decay are not possible. These challenges are left open for future works.

7.2 Novel methods developed in the thesis

The research presented in this thesis provides some novel methods applicable to structures other than the periodically buckled beam:

- For complex periodic structures, dispersion curves can be obtained using the Bloch theorem after the discretization of one periodic unit cell. However, this method provides only numerical results. The semi-analytical dispersion equation has been developed here to obtain analytical approximated expression of the dispersion curves. While the wavenumber and the frequency are expressed explicitly, coefficients of the expression are numerical and are expressed in terms of the dynamic stiffness matrix components.

7.3. Limitations of the present research and recommendations for future work

This method assumes the frequency to be small such that in general, only the acoustic branch is well approximated. The semi-analytical dispersion relation can be applied to any discretized periodic structures, as long as the number of degrees of freedom at the boundary remains small.

- For periodic structures by translation with additional glide symmetries, dispersion curves fold in the first Brillouin zone and the information is repeated. In this thesis, it is shown that in such a case, the minimum unit cell to use is half of the one by translation and changes into the Bloch theorem concern only boundary conditions which are reflected. Advantages of the reduced unit cell are that the dispersion curves are easier to interpret and computational costs/errors reduced.

As a side note, but not presented in this manuscript, Bloch theorem has been generalized also to screw symmetric structures [Maurin, 2015] where the general proof is demonstrated. In addition to the aforementioned advantages, the revisited Bloch method is applicable to structures as the Boerdijk-Coxeter helix that do not possess purely-translational symmetries for which the classical method is not applicable.

- Finally, the last contribution concerns finite-element simulations of any slender planar-beam structures under large geometrical nonlinear deformations and for which shear deformations can be neglected. While for such elements the most appropriated formulation is the extensible-elastica, Galerking method applied to this formulation involves second order derivatives for which at least \mathcal{C}^1 -continuous basis functions are required, whereas classical finite-element methods are maximum \mathcal{C}^0 -continuous through the geometry. It is proposed in this thesis the use of NURBS-based isogeometric analysis (IGA) that solves this issue, and allows the exact geometrical representation of curved beams. Moreover, the proposed formulation is shear-looking free and has the advantage to require a limited number of degrees of freedom, allowing efficient numerical solution of the discrete problem. Performances are validated using convergence of static “patch-test” and dynamic problems.

7.3 Limitations of the present research and recommendations for future work

In this thesis, assumptions have been made and limitations have been encountered. Possible directions of further researches include the following.

7.3.1 High frequencies

Wave propagation in buckled beams has been investigated only under the long wave assumption, neglecting any high-frequency phenomena. Indeed, to derive the semi-analytical dispersion relation, linearization of the reduced dynamic stiffness with respect to the frequency is necessary, limiting dispersion to the acoustic branch for which the wavelength is

larger than a period. Since the solitary wavelengths are known to be much larger than the lattice size, this assumption does not provide a limitation to the proposed work.

Nevertheless, numerical results of the Bloch theorem that account for high frequencies show the presence of band gaps resulting from resonant modes. This means that buckled beam at high frequency acts as a resonator, phenomenon already investigated for granular media [Bonanomi et al., 2015]. Since these band gaps and more generally speaking the dispersion curves depend on the buckling level, one could consider building an analytical filter with its properties changing simply by varying the pre-compression level.

7.3.2 Limitation in the wave amplitude: the case of snapping

In Fig. 4.5, it has been shown that the amplitude of the nonlinear wave is limited by some geometrical factors. For example, in the guided support configuration, the amplitude of the rarefaction (tension) wave is limited by the fact that the total strain cannot be negative. However, if an input wave with an amplitude higher than the limit given in Fig. 4.5a is sent, once the strain reaches zero, the beam snaps to the opposite direction due to the transverse inertia, as shown in Fig. 7.1.

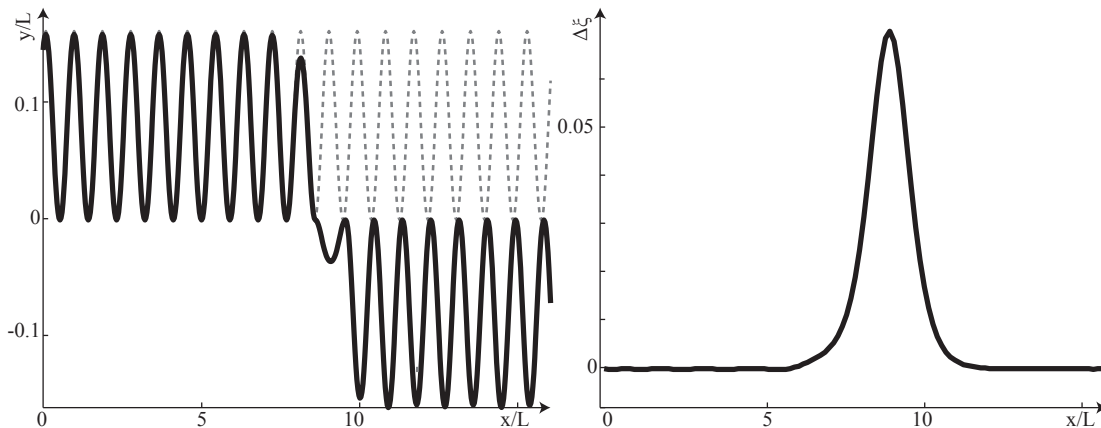


Figure 7.1: Structure snapping from one equilibrium state to the other one (a), such that the interpolated strain wave resulting from this transition is a solitary wave (b). In (a), initial geometry in dashed line and deformed geometry in full line. Parameters are exactly the same than in Chapter 4 with guided supports. The wave is moving from the right to the left side.

This figure is interesting since it shows that buckled beams can jump from an equilibrium configuration to the other one, and this transfer of energy takes the form of a solitary wave. Moreover, the amplitude of snapping (amplitude of the wave) is imposed by the initial geometry which means that it is independent to the input (the only condition on the input is that it should have enough energy to excite snapping of the first cell). Since the different models present in this thesis are not valid for snapping, this problem remains open for future work.

7.3.3 Experiments

Experiments have validated some characteristics of the expected waves such as the supersonic properties of the weakly-buckled guided-supports beam, but some limitations arise on the observation of long-wave propagation. Indeed, the setup size is 2 m long, but possesses only 30 periods, which turns out to be the order of the expected wavelength, meaning that reflection happens before the wave get time to propagate. As shown in Chapter 4, the characteristic wavelength normalized by the period of the medium depends only on the precompression levels, whereas it is independent to the material and the cross-section properties (Eq. (4.25)). In order to improve the setup, for additional research, a longer setup or a smaller periodicity should be considered. Note that in order to consider a smaller periodicity, smaller supports have to be considered as well.

Experimental investigations were limited to the case of the weakly-buckled beam. To consider other regimes as large post-buckling level, different solutions exist: select a material with higher Yield limits, choose a beam with thinner cross-section, increase the distance between supports, etc. However, other considerations have to be taken into account as for example, if a thinner cross-section is selected, the force of the strain wave will be weaker and effects of dissipation forces at the support level might be dominant.

Finally, pinned-supported configurations have not been investigated here experimentally, and the design of such a setup remains a challenging problem.

7.3.4 Dissipation and heterogeneity effects

While heterogeneity effects have been investigated in Chapter 5, this work has only been done numerically. Updating the present analytical models to consider heterogeneities is a challenging problem that requires future work. Similarly, dissipation induced by the support frictions can be included in the proposed analytical models; A possibility to solve this issue is to consider frictional forces as small perturbations such that the wave shape remain a solitary waves that decays in time. The use of the multi-scale method allows the separation between the solitary wave propagation and its decays, and an expression of the decay in terms of time can be found [Ablowitz and Segur, 1981, Scott, 2003].

7.3.5 Application to more complex periodic structures

Finally, the most promising direction of research is the application of this work to other more complex periodically buckled structures, like the one presented in the introduction (Figs. 1.2 and 1.3). These problems involve 2D/3D wave directions, secondary path for wave propagation, interactions between different materials, contacts, dissipations, heterogeneities etc. Understanding how periodic wrinkles affect waves will considerably improve fields like medical or earth-crust imaging, and the capabilities of a structure to host solitary waves can be used for example in phonic transport as a tool to cancel dispersion or nonlinearity effects.

A Load-Displacement Series Derived From The Extensible-Elastica

In this appendix, an approximation of the load-displacement relation is derived starting from the extensible-elastica theory. Knowing that $\chi = \Delta U/L$ is a function in terms of P and q (Eq. (2.24)), and that Eq. (2.21) links P to q , this system of two equations with three unknowns can be recast somehow in the load displacement relation $P\{\chi\}$, and the goal here is to look for such approximated function. Expending $P\{\chi\}$ around the critical point $P = P_c$ in a Taylor series, one reads

$$P\{\chi\} = P_c + \left. \frac{\partial P}{\partial \chi} \right|_{P \rightarrow P_c} (\chi - \chi_c) + \frac{1}{2} \left. \frac{\partial^2 P}{\partial \chi^2} \right|_{P \rightarrow P_c} (\chi - \chi_c)^2 + \mathcal{O}(\chi - \chi_c)^3, \quad (\text{A.1})$$

where $P \rightarrow P_c$ is equivalent to $q \rightarrow 0$ and $\chi_c = P_c/EA$. Since χ is expressed analytically in terms of the two other variables, the derivatives of Eq. (A.1) are expressed in terms of their inverses such that

$$\frac{\partial^{j+1} P}{\partial \chi^{j+1}} = \left(\frac{\partial \chi}{\partial P} \right)^{-1} \frac{\partial}{\partial P} \left(\frac{\partial^j P}{\partial \chi^j} \right), \quad (\text{A.2})$$

where $j \in \mathbb{N}^+$. Since $\chi\{P, q\}$, the chain rule gives

$$\frac{\partial^j \chi}{\partial P^j} = \frac{d}{dP} \left(\frac{\partial^{j-1} \chi}{\partial P^{j-1}} \right) + \frac{d}{dq} \left(\frac{\partial^{j-1} \chi}{\partial P^{j-1}} \right) \frac{\partial q}{\partial P}, \quad (\text{A.3})$$

where from Eq. (2.24),

$$\frac{\partial^0 \chi}{\partial P^0} = \chi = 2 - e + 2eq^2 - 2(1 - e + 2eq^2) \frac{E\{c\}}{K\{c\}}, \quad (\text{A.4})$$

and

$$c = q^2 \frac{1 + eq^2}{1 - e + 2eq^2}. \quad (\text{A.5})$$

Appendix A. Load-Displacement Series Derived From The Extensible-Elastica

Defining a new function \mathcal{P} from Eq. (2.21) as,

$$\mathcal{P}\{P, q\} = \frac{P}{P_E} - \frac{4}{\pi^2} \frac{1}{1 - e + 2eq^2} K\{c\}^2 = 0, \quad (\text{A.6})$$

in Eq. (A.3), $\frac{\partial q}{\partial P}$ reads

$$\frac{\partial q}{\partial P} = - \frac{d\mathcal{P}\{P, q\}}{dP} \left(\frac{d\mathcal{P}\{P, q\}}{dq} \right)^{-1}. \quad (\text{A.7})$$

The successive derivatives of $\frac{\partial q}{\partial P}$ are again given by the chain rule such that:

$$\frac{\partial^{j+1} q}{\partial P^{j+1}} = \frac{d}{dP} \left(\frac{\partial^j q}{\partial P^j} \right) + \frac{d}{dq} \left(\frac{\partial^j q}{\partial P^j} \right) \frac{\partial q}{\partial P}. \quad (\text{A.8})$$

Note that the derivatives of the first and second elliptical integrals with respect to their arguments are given in Eq. (2.29). *Mathematica* is used to derive the successive derivatives of Eq. (A.1) and to find their limits when $P \rightarrow P_c$ and $q \rightarrow 0$. In addition to the expansion in χ , the beam is assumed slender and expansion in $\frac{1}{\lambda^2}$ is also used. Finally, the approximation of the load-displacement for a slender beam with small deformations is

$$\frac{P}{P_E} = 1 + \frac{\pi^2}{\lambda^2} + 2 \frac{\pi^4}{\lambda^4} + \left(\frac{1}{2} + \frac{1}{4} \frac{\pi^2}{\lambda^2} - \frac{11}{8} \frac{\pi^4}{\lambda^4} \right) (\chi - \chi_c) + \left(\frac{9}{32} - \frac{3}{64} \frac{\pi^2}{\lambda^2} - \frac{39}{32} \frac{\pi^4}{\lambda^4} \right) (\chi - \chi_c)^2 + \mathcal{O}(\chi - \chi_c)^3. \quad (\text{A.9})$$

As in the inextensible case, the convergence of Eq. (A.9) is not the best one, and a series which a faster convergence is given by

$$\frac{P}{P_E} = \frac{1}{\left(1 - \frac{1}{2} \frac{\pi^2}{\lambda^2} - \frac{5}{2} \frac{\pi^4}{\lambda^4} - \left(\frac{1}{4} - \frac{1}{4} \frac{\pi^2}{\lambda^2} - \frac{37}{32} \frac{\pi^4}{\lambda^4} \right) (\chi - \chi_c) - \left(\frac{3}{64} - \frac{3}{32} \frac{\pi^2}{\lambda^2} + \frac{27}{512} \frac{\pi^4}{\lambda^4} \right) (\chi - \chi_c)^2 + \mathcal{O}(\chi - \chi_c)^3 \right)^2}. \quad (\text{A.10})$$

Note that when $\lambda \rightarrow \infty$ and $\chi_c \rightarrow 0$, results from inextensible beam are recovered (Eqs. (2.30) and (2.32)).

Bibliography

- M. J. Ablowitz. *Nonlinear Dispersive Waves: Asymptotic Analysis and Solitons*. Cambridge University Press, 2011.
- M. J. Ablowitz and H. Segur. *Solitons and the inverse scattering transform*. SIAM, Philadelphia, 1981.
- B. Audoly and Y. Pomeau. *Elasticity and Geometry: From hair curls to the non-linear response of shells*, volume 2. OUP Oxford, 2010.
- F. Auricchio, L. B. da Veiga, A. Buffa, C. Lovadina, A. Reali, and G. Sangalli. A fully "locking-free" isogeometric approach for plane linear elasticity problems: A stream function formulation. *Computer Methods in Applied Mechanics and Engineering*, 197(1-4):160–172, 2007.
- J. M. Battini. Co-rotational beam elements. Technical report, Royal Institute of Technology, 2002.
- Z. P. Bazant, L. Cedolin, and J. W. Hutchinson. *Stability of Structures: Elastic, Inelastic, Fracture, and Damage Theories*, volume 60. World Scientific, 1993.
- Y. Bazilevs, L. Beirão Da Veiga, J. A. Cottrell, T. J. R. Hughes, and G. Sangalli. Isogeometric analysis: approximation, stability and error estimates for h-refined meshes. *Mathematical Models and Methods in Applied Sciences*, 16(7):1031–1090, 2006.
- L. Beirão da Veiga, A. Buffa, J. Rivas, and G. Sangalli. Some estimates for h-p-k-refinement in Isogeometric Analysis. *Numerische Mathematik*, 118(2):271–305, 2011.
- L. Beirão da Veiga, C. Lovadina, and A. Reali. Avoiding shear locking for the Timoshenko beam problem via isogeometric collocation methods. *Computer Methods in Applied Mechanics and Engineering*, 241-244(0):38–51, 2012.
- D. J. Benson, Y. Bazilevs, M. C. Hsu, and T. J. R. Hughes. Isogeometric shell analysis: The Reissner-Mindlin shell. *Computer Methods in Applied Mechanics and Engineering*, 199(5): 276–289, 2010.
- D. J. Benson, Y. Bazilevs, M. C. Hsu, and T. J. R. Hughes. A large deformation, rotation-free, isogeometric shell. *Computer Methods in Applied Mechanics and Engineering*, 200(13): 1367–1378, 2011.

Bibliography

- D. J. Benson, S. Hartmann, Y. Bazilevs, M. C. Hsu, and T. J. R. Hughes. Blended isogeometric shells. *Computer Methods in Applied Mechanics and Engineering*, 255(0):133–146, 2013.
- A. Berezovski, J. Engelbrecht, and M. Berezovski. Waves in microstructured solids: A unified viewpoint of modeling. *Acta Mechanica*, 220(2):349–363, 2011.
- A. Berezovski, J. Engelbrecht, A. Salupere, K. Tamm, T. Peets, and M. Berezovski. Dispersive waves in microstructured solids. *International Journal of Solids and Structures*, 50(11-12):1981–1990, 2013.
- D. Bigoni, M. Gei, and A. B. Movchan. Dynamics of a prestressed stiff layer on an elastic half space: filtering and band gap characteristics of periodic structural models derived from long-wave asymptotics. *Journal of the Mechanics and Physics of Solids*, 56(7):2494–2520, 2008.
- C. Bisagni. Numerical analysis and experimental correlation of composite shell buckling and post-buckling. *Composites Part B: Engineering*, 31(8):655–667, 2000.
- I. L. Bogolubsky. Some examples of inelastic soliton interaction. *Computer Physics Communications*, 13(3):149–155, 1977.
- L. Bonanomi, G. Theocharis, and C. Daraio. Wave propagation in granular chains with local resonances. *Physical Review E*, 91(3):033208, 2015.
- R. D. Borst, M. A. Crisfield, J. J. C. Remmers, and C. V. Verhoosel. *Nonlinear Finite Element Analysis of Solids and Structures*. Wiley, 2012.
- R. Bouclier, T. Elguedj, and A. Combescure. Locking free isogeometric formulations of curved thick beams. *Computer Methods in Applied Mechanics and Engineering*, 245-246(0):144–162, 2012.
- J. Boussinesq. Théorie des ondes et des remous qui se propagent le long d'un canal rectangulaire horizontal, en communiquant au liquide contenu dans ce canal des vitesses sensiblement pareilles de la surface au fond. *J Math Pures Appl*, 17(2):55–108, 1872.
- A. F. Bower. *Applied Mechanics of Solids*. CRC Press, 2009.
- F. Brau, H. Vandeparre, A. Sabbah, C. Poulard, A. Boudaoud, and P. Damman. Multiple-length-scale elastic instability mimics parametric resonance of nonlinear oscillators. *Nature Physics*, 7(1):56–60, 2010.
- L. Brillouin. *Wave propagation in periodic structures; electric filters and crystal lattices*. Courier Dover Publications, 1946.
- P. F. Byrd and M. D. Friedman. *Handbook of elliptic integrals for engineers and physicists*. Springer Verlag, 1971.

- P. Češarek, M. Saje, and D. Zupan. Kinematically exact curved and twisted strain-based beam. *International Journal of Solids and Structures*, 49(13):1802–1817, 2012.
- A. R. Champneys, G. W. Hunt, and J. M. T. Thompson. *Localization and solitary waves in solid mechanics*. World Scientific, 1997.
- J. S. Chen and H. W. Tsao. Static snapping load of a hinged extensible elastica. *Applied Mathematical Modelling*, 37(18-19):8401–8408, 2013.
- J. S. Chen and H. W. Tsao. Dynamic snapping of a hinged extensible elastica under a step load. *International Journal of Non-Linear Mechanics*, 59:9–15, 2014.
- X. Chen and J. W. Hutchinson. A family of herringbone patterns in thin films. *Scripta Materialia*, 50(6):797–801, 2004.
- J. Chopin and A. Kudrolli. Helicoids, Wrinkles, and Loops in Twisted Ribbons. *Physical Review Letters*, 111(17):174302, 2013.
- J. Chopin, V. Démercy, and B. Davidovitch. Roadmap to the Morphological Instabilities of a Stretched Twisted Ribbon. *Journal of Elasticity*, 119(1-2):137–189, 2014.
- C. I. Christov, G. A. Maugin, and A. V. Porubov. On Boussinesq’s paradigm in nonlinear wave propagation. *Comptes Rendus Mecanique*, 335(9-10):521–535, 2007.
- J. Chung and G. M. Hulbert. A Time Integration Algorithm for Structural Dynamics With Improved Numerical Dissipation: The Generalized- α Method. *Journal of Applied Mechanics*, 60(2):371, 1993.
- B. D. Coleman, E. H. Dill, and D. Swigon. On the dynamics of flexure and stretch in the theory of elastic rods. *Archive for Rational Mechanics and Analysis*, 129(2):147–174, 1995.
- M. Collet, M. Ouisse, M. Ruzzene, and M. N. Ichchou. Floquet-Bloch decomposition for the computation of dispersion of two-dimensional periodic, damped mechanical systems. *International Journal of Solids and Structures*, 48(20):2837–2848, 2011.
- W. R. D. Cook and D. S. Malkus. *Concepts and applications of finite element analysis*. Wiley India Pvt. Limited, 2002.
- J. A. Cottrell, A. Reali, Y. Bazilevs, and T. J. R. Hughes. Isogeometric analysis of structural vibrations. *Computer Methods in Applied Mechanics and Engineering*, 195(41-43):5257–5296, 2006.
- J. A. Cottrell, T. J. R. Hughes, and Y. Bazilevs. *Isogeometric Analysis Toward Intergration of CAD and FEA*. John Wiley & Sons, 2009.
- B. Davidovitch, R. D. Schroll, D. Vella, M. Adda-Bedia, and E. A. Cerda. Prototypical model for tensional wrinkling in thin sheets. *Proceedings of the National Academy of Sciences of the United States of America*, 108(45):18227–32, 2011.

Bibliography

- L. Dedè and H. a. F. a. Santos. B-spline goal-oriented error estimators for geometrically nonlinear rods. *Computational Mechanics*, 49(1):35–52, 2012.
- P. P. Delsanto. *Universality of Nonclassical Nonlinearity*. Springer Science & Business Media, 2006.
- R. Dembitzer. Cambridge Meeting of the British Association for the Advancement of Science. Technical report, 1965.
- M. Destrade and G. Saccomandi. Nonlinear transverse waves in deformed dispersive solids. *Wave Motion*, 45(3):325–336, 2008.
- G. Domokos, P. Holmes, and B. Royce. Constrained euler buckling. *Journal of Nonlinear Science*, 7(3):281–314, 1997.
- J. F. Doyle. *Wave Propagation in Structures-Spectral Analysis Using Fast Discrete Fourier Transforms*. Springer Verlag, 1997.
- B. Duričković, A. Goriely, and G. Saccomandi. Compact waves on planar elastic rods. *International Journal of Non-Linear Mechanics*, 44(5):538–544, 2009.
- R. Echter, B. Oesterle, and M. Bischoff. A hierarchic family of isogeometric shell finite elements. *Computer Methods in Applied Mechanics and Engineering*, 254(0):170–180, 2013.
- D. Ehrlich and F. Armero. Finite element methods for the analysis of softening plastic hinges in beams and frames. *Computational Mechanics*, 35(4):237–264, 2004.
- J. Engelbrecht, A. Salupere, and K. Tamm. Waves in microstructured solids and the Boussinesq paradigm. *Wave Motion*, 48(8):717–726, 2011.
- H. A. Erbay, S. Erbay, and A. Erkip. Existence and Stability of Traveling Waves for a Class of Nonlocal Nonlinear Equations. *Journal of Mathematical Analysis and Applications*, 425(1):307–336, 2015.
- L. F. R. Espath, A. L. Braun, and A. M. Awruch. Energy conserving and numerical stability in nonlinear dynamic using isogeometric analysis. *Mec. Comput. XXXII*, pages 33–62, 2013.
- L. Euler. Methodus Inveniendi Lineas Curvas Maximi Minimive Proprietate Gaudentes. *Lausanne, Genf: Bousquet & Socios*, 1744.
- F. Farzbod and M. J. Leamy. Analysis of Bloch’s Method and the Propagation Technique in Periodic Structures. *Journal of Vibration and Acoustics*, 133(3):031010, 2011.
- E. Fermi, J. Pasta, and S. Ulam. Studies of nonlinear problems. *Los Alamos Report*, 1955.
- F. Fraternali, L. Senatore, and C. Daraio. Solitary waves on tensegrity lattices. *Journal of the Mechanics and Physics of Solids*, 60(6):1137–1144, 2012.

- F. Fraternali, G. Carpentieri, A. Amendola, R. E. Skelton, and V. F. Nesterenko. Multiscale tunability of solitary wave dynamics in tensegrity metamaterials. *Applied Physics Letters*, 105(20):201903, 2014.
- M. Gei, A. B. Movchan, and D. Bigoni. Band-gap shift and defect-induced annihilation in prestressed elastic structures. *Journal of Applied Physics*, 105(6):063507, 2009.
- J. Genzer and J. Groenewold. Soft matter with hard skin: From skin wrinkles to templating and material characterization. *Soft Matter*, 2(4):310, 2006.
- J. Gerstmayr and A. A. Shabana. Analysis of thin beams and cables using the absolute nodal co-ordinate formulation. *Nonlinear Dynamics*, 45(1-2):109–130, 2006.
- J. Gerstmayr, M. K. Matikainen, and A. M. Mikkola. A geometrically exact beam element based on the absolute nodal coordinate formulation. *Multibody System Dynamics*, 20(4):359–384, 2008.
- S. Ghosh. *Theory of vibration with applications, (2nd edition)*, volume 9. CRC Press, 1984.
- S. Ghosh and D. Roy. A frame-invariant scheme for the geometrically exact beam using rotation vector parametrization. *Computational Mechanics*, 44(1):103–118, 2009.
- C. Gonzalez and J. LLorca. Stiffness of a curved beam subjected to axial load and large displacements. *International Journal of Solids and Structures*, 42(5-6):1537–1545, 2005.
- G. M. Grason and B. Davidovitch. Universal collapse of stress and wrinkle-to-scar transition in spherically confined crystalline sheets. *Proceedings of the National Academy of Sciences of the United States of America*, 110(32):12893–8, 2013.
- L. Greco and M. Cuomo. B-Spline interpolation of Kirchhoff-Love space rods. *Computer Methods in Applied Mechanics and Engineering*, 256(0):251–269, 2013.
- L. Greco and M. Cuomo. An implicit G1 multi patch B-spline interpolation for Kirchhoff-Love space rod. *Computer Methods in Applied Mechanics and Engineering*, 269(0):173–197, 2014.
- C. Guo, G. van der Heijden, and H. Cai. Homoclinic complexity in the localised buckling of an extensible conducting rod in a uniform magnetic field. *Physica D: Nonlinear Phenomena*, 284:42–52, 2014.
- B. Haghpanah, J. Papadopoulos, D. Mousanezhad, H. Nayeb-Hashemi, and A. Vaziri. Buckling of regular, chiral and hierarchical honeycombs under a general macroscopic stress state. *Proceedings of the Royal Society A: Mathematical, Physical and Engineering Sciences*, 470(2167):20130856, 2014.
- A. Hasegawa. *Optical Solitons in Fibers*. Springer Science & Business Media, 1998.
- B. E. Hobbs and A. Ord. Localized and chaotic folding: the role of axial plane structures. *Philosophical transactions. Series A, Mathematical, physical, and engineering sciences*, 370(1965):1966–2009, 2012.

Bibliography

- B. Z. Huang and S. N. Atluri. A simple method to follow post-buckling paths in finite element analysis. *Computers & Structures*, 57(3):477–489, 1995.
- T. J. R. Hughes. *The finite element method: linear static and dynamic finite element analysis*. Courier Dover Publications, New Jersey, 1987.
- T. J. R. Hughes, A. Reali, and G. Sangalli. Efficient quadrature for NURBS-based isogeometric analysis. *Computer Methods in Applied Mechanics and Engineering*, 199(5-8):301–313, 2010.
- A. Humer. Elliptic integral solution of the extensible elastica with a variable length under a concentrated force. *Acta Mechanica*, 222(3-4):209–223, 2011.
- A. Humer. Exact solutions for the buckling and postbuckling of shear-deformable beams. *Acta Mechanica*, 224(7):1493–1525, 2013.
- A. Humer and H. Irschik. Large deformation and stability of an extensible elastica with an unknown length. *International Journal of Solids and Structures*, 48(9):1301–1310, 2011.
- J. Hure, B. Roman, and J. Bico. Stamping and Wrinkling of Elastic Plates. *Physical Review Letters*, 109(5):054302, 2012.
- A. Ibrahimbegovic. On Finite Element Implementation Of Geometrically Nonlinear Reissner’s Beam Theory: Three Dimensional Curved Beam Elements. *Computer Methods in Applied Mechanics and Engineering*, 122(1):11–26, 1995.
- H. Irschik and J. Gerstmayr. A continuum mechanics based derivation of Reissner’s large-displacement finite-strain beam theory: The case of plane deformations of originally straight Bernoulli-Euler beams. *Acta Mechanica*, 206(1-2):1–21, 2009.
- M. Ishaquddin, P. Raveendranath, and J. N. Reddy. Coupled polynomial field approach for elimination of flexure and torsion locking phenomena in the Timoshenko and Euler–Bernoulli curved beam elements. *Finite Elements in Analysis and Design*, 65:17–31, 2013.
- S. H. Kang, S. Shan, A. Košmrlj, W. L. Noorduyn, S. Shian, J. C. Weaver, D. R. Clarke, and K. Bertoldi. Complex Ordered Patterns in Mechanical Instability Induced Geometrically Frustrated Triangular Cellular Structures. *Physical Review Letters*, 112(9):098701, 2014.
- K. R. Khusnutdinova and M. R. Tranter. Modelling of nonlinear wave scattering in a delaminated elastic bar. page 20, 2015.
- K. R. Khusnutdinova, A. M. Samsonov, and A. S. Zakharov. Nonlinear layered lattice model and generalized solitary waves in imperfectly bonded structures. *Physical Review E - Statistical, Nonlinear, and Soft Matter Physics*, 79(5):056606, 2009.
- J. M. Kiendl, K. U. Bletzinger, J. Linhard, and R. Wüchner. Isogeometric shell analysis with Kirchhoff-Love elements. *Computer Methods in Applied Mechanics and Engineering*, 198(49):3902–3914, 2009.

- J. M. Kiendl, Y. Bazilevs, M. C. Hsu, R. Wüchner, and K. U. Bletzinger. The bending strip method for isogeometric analysis of Kirchhoff-Love shell structures comprised of multiple patches. *Computer Methods in Applied Mechanics and Engineering*, 199(37):2403–2416, 2010.
- E. Kim, F. Li, C. Chong, G. Theocharis, J. Yang, and P. G. Kevrekidis. Highly Nonlinear Wave Propagation in Elastic Woodpile Periodic Structures. *Physical Review Letters*, 114(11):118002, 2015.
- H. King, R. D. Schroll, B. Davidovitch, and N. Menon. Elastic sheet on a liquid drop reveals wrinkling and crumpling as distinct symmetry-breaking instabilities. *Proceedings of the National Academy of Sciences of the United States of America*, 109(25):9716–20, 2012.
- A. P. Korte, E. L. Starostin, and G. H. M. van der Heijden. Triangular buckling patterns of twisted inextensible strips. *Proceedings of the Royal Society A: Mathematical, Physical and Engineering Sciences*, 467(2125):285–303, 2010.
- D. J. Korteweg and G. de Vries. On the change of form of long waves advancing in a rectangular canal, and on a new type of long stationary waves. *Philosophical Magazine*, 39(240):422–443, 1895.
- K. Krieger. Extreme mechanics: Buckling down. *Nature*, 488(7410):146–7, 2012.
- I. A. Kunin. *Elastic Media with Microstructure*. Springer, 1982.
- N. Kutev, N. Kolkovska, and M. Dimova. Global existence to generalized Boussinesq equation with combined power-type nonlinearities. *Journal of Mathematical Analysis and Applications*, 410(1):427–444, 2014.
- P. Le Grogneac and K. Sad Saoud. Elastoplastic buckling and post-buckling analysis of sandwich columns. *International Journal of Non-Linear Mechanics*, 72:67–79, 2015.
- R. Levien. The elastica: a mathematical history. Technical Report UCB/EECS-2008-103, 2008.
- B. Li, Y.-P. Cao, X.-Q. Feng, and H. Gao. Surface wrinkling of mucosa induced by volumetric growth: Theory, simulation and experiment. *Journal of the Mechanics and Physics of Solids*, 59(4):758–774, 2011a.
- B. Li, F. Jia, Y.-P. Cao, X.-Q. Feng, and H. Gao. Surface Wrinkling Patterns on a Core-Shell Soft Sphere. *Physical Review Letters*, 106(23):234301, 2011b.
- B. Li, Y.-P. Cao, X.-Q. Feng, and H. Gao. Mechanics of morphological instabilities and surface wrinkling in soft materials: a review. *Soft Matter*, 8(21):5728, 2012.
- X. Li, J. Zhang, and Y. Zheng. NURBS-based isogeometric analysis of beams and plates using high order shear deformation theory. *Mathematical Problems in Engineering*, 2013:1–9, 2013.

Bibliography

- E. Lignon, P. Le Tallec, and N. Triantafyllidis. Onset of failure in a fiber reinforced elastomer under constrained bending. *International Journal of Solids and Structures*, 50(2):279–287, 2013.
- Y. Liu and R. Xu. Potential well method for initial boundary value problem of the generalized double dispersion equations. *Communications on Pure and Applied Analysis*, 7(2):63–81, 2008.
- A. Magnusson, M. Ristinmaa, and C. Ljung. Behaviour of the extensible elastica solution. *International Journal of Solids and Structures*, 38(46-47):8441–8457, 2001.
- L. Mahadevan, J. Bico, and G. McKinley. Popliteal rippling of layered elastic tubes and scrolls. *Europhysics Letters (EPL)*, 65(3):323–329, 2004.
- G. A. Maugin. *Nonlinear Waves in Elastic Crystals*. Oxford University Press, 1999.
- F. Maurin. Bloch theorem with Revised Boundary Conditions applied to glide and screw symmetric, quasi-one-dimensional structures. *Wave Motion*, *In press*, doi:10.1016/j.wavemoti.2015.10.008, 2015.
- F. Maurin and A. Spadoni. Wave dispersion in periodic post-buckled structures. *Journal of Sound and Vibration*, 333(19):4562–4578, 2014a.
- F. Maurin and A. Spadoni. Low-frequency wave propagation in post-buckled structures. *Wave Motion*, 51(2):323–334, 2014b.
- F. Maurin, L. Dedè, and A. Spadoni. Isogeometric rotation-free analysis of planar extensible-elastica for static and dynamic applications. *Nonlinear Dynamics*, 2015.
- D. J. Mead. Wave propagation and natural modes in periodic systems: I. Mono-coupled systems. *Journal of Sound and Vibration*, 40(1):1–18, 1975a.
- D. J. Mead. Wave propagation and natural modes in periodic systems: II. Multi-coupled systems, with and without damping. *Journal of Sound and Vibration*, 40(1):19–39, 1975b.
- L. Munteanu and S. Donescu. *Introduction to soliton theory: applications to mechanics*. Kluwer Academic Publishers, 2004.
- A. P. Nagy, M. M. Abdalla, and Z. Gürdal. Isogeometric sizing and shape optimisation of beam structures. *Computer Methods in Applied Mechanics and Engineering*, 199(17-20):1216–1230, 2010.
- A. H. Nayfeh, W. Lacarbonara, and C. M. Chin. Nonlinear normal modes of buckled beams: three-to-one and one-to-one internal resonances. *Nonlinear Dynamics*, 18(3):253–273, 1999.
- V. F. Nesterenko. *Dynamics of Heterogeneous Materials*. Springer, 2001.

- A. S. Phani, J. Woodhouse, and N. A. Fleck. Wave propagation in two-dimensional periodic lattices. *The Journal of the Acoustical Society of America*, 119(4):1995–2005, 2006.
- L. Piegl and W. Tiller. *The NURBS Book*, volume 28. Springer Science & Business Media, 1997.
- A. V. Porubov. *Amplification of nonlinear strain waves in solids*. World Scientific, 2003.
- A. V. Porubov and I. E. Berinskii. Non-linear plane waves in materials having hexagonal internal structure. *International Journal of Non-Linear Mechanics*, 67:27–33, 2014.
- A. V. Porubov and G. A. Maugin. Longitudinal strain solitary waves in presence of cubic non-linearity. *International Journal of Non-Linear Mechanics*, 40(7):1041–1048, 2005.
- T. Pulngern, T. Sudsanguan, C. Athisakul, and S. Chucheepsakul. Elastica of a variable-arc-length circular curved beam subjected to an end follower force. *International Journal of Non-Linear Mechanics*, 49:129–136, 2013.
- S. B. Raknes, X. Deng, Y. Bazilevs, D. J. Benson, K. M. Mathisen, and T. Kvamsdal. Isogeometric rotation-free bending-stabilized cables: Statics, dynamics, bending strips and coupling with shells. *Computer Methods in Applied Mechanics and Engineering*, 263:127–143, 2013.
- J. N. Reddy. *An Introduction to Nonlinear Finite Element Analysis*. OUP Oxford, 2004.
- E. Reissner. On one-dimensional finite-strain beam theory: The plane problem. *Journal of Applied Mathematics and Physics*, 23(5):795–804, 1972.
- E. Reissner. On one-dimensional large-displacement finite-strain beam theory. *Studies in Applied Mathematics*, 52(2):87–95, 1973.
- M. Remoissenet. *Waves Called Solitons: Concepts and Experiments*, volume 63. Springer, 1995.
- D. S. Ricketts and D. Ham. *Electrical Solitons: Theory, Design, and Applications*. CRC Press, 2010.
- F. Romeo and A. Paolone. Wave propagation in three-coupled periodic structures. *Journal of Sound and Vibration*, 301(3-5):635–648, 2007.
- I. Romero. A comparison of finite elements for nonlinear beams: The absolute nodal coordinate and geometrically exact formulations. *Multibody System Dynamics*, 20(1):51–68, 2008.
- K. Sad Saoud and P. Le Grogneq. A unified formulation for the biaxial local and global buckling analysis of sandwich panels. *Thin-Walled Structures*, 82(0):13–23, 2014.
- M. Saje. A variational principle for finite planar deformation of straight slender elastic beams. *International Journal of Solids and Structures*, 26(8):887–900, 1990.
- A. M. Samsonov and G. A. Maugin. *Strain Solitons in Solids and How to Construct Them*, volume 54. CRC Press, 2001.

Bibliography

- A. M. Samsonov, G. V. Dreiden, I. V. Semenova, and A. G. Shvartz. Bulk solitary waves in elastic solids. In *APPLICATION OF MATHEMATICS IN TECHNICAL AND NATURAL SCIENCES: 7th International Conference for Promoting the Application of Mathematics in Technical and Natural Sciences - AMiTaNS'15*, volume 1684, page 020002. AIP Publishing, 2015.
- H. a. F. a. Santos, P. M. Pimenta, and J. P. Moitinho De Almeida. Hybrid and multi-field variational principles for geometrically exact three-dimensional beams. *International Journal of Non-Linear Mechanics*, 45(8):809–820, 2010.
- K. H. Schweizerhof and P. Wriggers. Consistent linearization for path following methods in nonlinear fe analysis. *Computer Methods in Applied Mechanics and Engineering*, 59(3): 261–279, 1986.
- A. C. Scott. A Nonlinear Klein-Gordon Equation. *American Journal of Physics*, 37(1):52, 1969.
- A. C. Scott. *Nonlinear Science: Emergence and Dynamics of Coherent Structures*. Oxford University Press, 2003.
- K. A. Seffen and S. V. Stott. Surface Texturing Through Cylinder Buckling. *Journal of Applied Mechanics*, 81(6):061001, 2014.
- S. Sen, J. Hong, J. Bang, E. Avalos, and R. Doney. Solitary waves in the granular chain. *Physics Reports*, 462(2):21–66, 2008.
- A. A. Shabana. Nodal Coordinate Formulation for Beam Elements : Implementation. *Journal of Mechanical Design*, 123(4):614–621, 2001.
- A. A. Shabana and R. Y. Yakoub. Three Dimensional Absolute Nodal Coordinate Formulation for Beam Elements: Theory. *Journal of Mechanical Design*, 123(4):606, 2001.
- S. Shan, S. H. Kang, P. Wang, C. Qu, S. Shian, E. R. Chen, and K. Bertoldi. Harnessing Multiple Folding Mechanisms in Soft Periodic Structures for Tunable Control of Elastic Waves. *Advanced Functional Materials*, 24(31):4935–4942, 2014.
- E. Sharon, B. Roman, M. Marder, G.-S. Shin, and H. L. Swinney. Mechanics. Buckling cascades in free sheets. *Nature*, 419(6907):579, 2002.
- J. Shim, C. Perdigou, E. R. Chen, K. Bertoldi, and P. M. Reis. Buckling-induced encapsulation of structured elastic shells under pressure. *Proceedings of the National Academy of Sciences of the United States of America*, 109(16):5978–83, 2012.
- J. Simo. A finite strain beam formulation. The three-dimensional dynamic problem. Part I. *Computer Methods in Applied Mechanics and Engineering*, 49(1):55–70, 1985.
- J. Simo and L. Vu-Quoc. A three-dimensional finite-strain rod model. part II: Computational aspects. *Computer Methods in Applied Mechanics and Engineering*, 58(1):79–116, 1986.

- K. Singh and B. L. Dhoopar. Free vibration of circular rings on radial supports. *Journal of Sound and Vibration*, 65(1):297–301, 1979.
- M. P. Soerensen. Solitary waves on nonlinear elastic rods. I. *The Journal of the Acoustical Society of America*, 76(3):871, 1984.
- A. Spadoni, M. Ruzzene, and K. Cunefare. Vibration and Wave Propagation Control of Plates with Periodic Arrays of Shunted Piezoelectric Patches. *Journal of Intelligent Material Systems and Structures*, 20(8):979–990, 2009.
- D. Sun, C. Daraio, and S. Sen. Nonlinear repulsive force between two solids with axial symmetry. *Physical Review E - Statistical, Nonlinear, and Soft Matter Physics*, 83(6):066605, 2011.
- Y. Sun, W. M. Choi, H. Jiang, Y. Y. Huang, and J. A. Rogers. Controlled buckling of semiconductor nanoribbons for stretchable electronics. *Nature nanotechnology*, 1(3):201–207, 2006.
- A. Tagliabue, L. Dedè, and A. Quarteroni. Isogeometric Analysis and error estimates for high order partial differential equations in fluid dynamics. *Computers & Fluids*, 102:277–303, 2014.
- A. Takei, F. Brau, B. Roman, and J. Bico. Stretch-induced wrinkles in reinforced membranes: From out-of-plane to in-plane structures. *EPL (Europhysics Letters)*, 96(6):64001, 2011.
- G. Theocharis, N. Boechler, and C. Daraio. Nonlinear Periodic Phononic Structures and Granular Crystals. In *Acoustic Metamaterials and Phononic Crystals*. Springer Berlin Heidelberg, Berlin, Heidelberg, 2013.
- J. M. T. Thompson, M. Silveira, G. H. M. van der Heijden, and M. Wiercigroch. Helical post-buckling of a rod in a cylinder: with applications to drill-strings. *Proceedings of the Royal Society A: Mathematical, Physical and Engineering Sciences*, 468(2142):1591–1614, 2012.
- S. P. Timoshenko. *History of Strength of Materials: With a Brief Account of the History of Theory of Elasticity and Theory of Structures*. Courier Corporation, 1983.
- G. Trainiti, J. Rimoli, and M. Ruzzene. Wave propagation in periodically undulated beams and plates. *International Journal of Solids and Structures*, 75-76:260–276, 2015.
- J. Valverde and G. H. M. van der Heijden. Magnetically-Induced Buckling of a Whirling Conducting Rod with Applications to Electrodynamical Space Tethers. *Journal of Nonlinear Science*, 20(3):309–339, 2010.
- A. Vaziri. On the buckling of cracked composite cylindrical shells under axial compression. *Composite Structures*, 80(1):152–158, 2007.
- D. Vella, J. Bico, A. Boudaoud, B. Roman, and P. M. Reis. The macroscopic delamination of thin films from elastic substrates. *Proceedings of the National Academy of Sciences of the United States of America*, 106(27):10901–6, 2009.

Bibliography

- D. Vella, A. Ajdari, A. Vaziri, and A. Boudaoud. Wrinkling of Pressurized Elastic Shells. *Physical Review Letters*, 107(17):174301, 2011.
- S. Wang and G. Chen. Cauchy problem of the generalized double dispersion equation. *Nonlinear Analysis: Theory, Methods & Applications*, 64(10371111):159–173, 2006.
- O. Weeger, U. Wever, and B. Simeon. Isogeometric analysis of nonlinear Euler-Bernoulli beam vibrations. *Nonlinear Dynamics*, 72(4):813–835, 2013.
- G. B. Whitham. *Linear and Nonlinear Waves*, volume 28. John Wiley & Sons, 1974.
- P. Wriggers. *Nonlinear finite element methods*. Springer Science & Business Media, 2008.
- P. Wriggers and U. Nackenhorst. *Analysis and Simulation of Contact Problems*, 2006.
- J. Xiong, R. Ghosh, L. Ma, A. Vaziri, Y. Wang, and L. Wu. Sandwich-walled cylindrical shells with lightweight metallic lattice truss cores and carbon fiber-reinforced composite face sheets. *Composites Part A: Applied Science and Manufacturing*, 56:226–238, 2014.
- H. Yasuda, C. Chong, E. G. Charalampidis, P. G. Kevrekidis, and J. Yang. Formation of rarefaction waves in origami-based metamaterials. *arXiv preprint*, 2015.
- J. Yin, Z. Cao, C. Li, I. Sheinman, and X. Chen. Stress-driven buckling patterns in spheroidal core/shell structures. *Proceedings of the National Academy of Sciences of the United States of America*, 105(49):19132–5, 2008.
- N. J. Zabusky and M. D. Kruskal. Interaction of "solitons" in a collisionless plasma and the recurrence of initial states. *Physical Review Letters*, 15(6):240–243, 1965.
- D. Zaccaria, D. Bigoni, G. Noselli, and D. Misseroni. Structures buckling under tensile dead load. *Proceedings of the Royal Society A: Mathematical, Physical and Engineering Sciences*, 467(2130):1686–1700, 2011.
- R. Zhang and H. Zhong. Weak form quadrature element analysis of planar slender beams based on geometrically exact beam theory. *Archive of Applied Mechanics*, 83(9):1309–1325, 2013.
- Z. Zhao and G. Ren. A quaternion-based formulation of Euler-Bernoulli beam without singularity. *Nonlinear Dynamics*, 67(3):1825–1835, 2012.

Curriculum Vitae

Florian Maurin

4 Rue de Véron, 74500 Lurgin, France

Phone: (+41)(0)78 840 70 18

Phone: (+33)(0)6 67 85 68 91

Email: florian.maurin@gmail.com

Born: February 13, 1988

Nationality: French



Education

2015: Ph.D. in mechanical engineering, under the supervision of Prof. W. A. Curtin and Prof. A. Spadoni, EPFL, Lausanne, Switzerland.

2011: M.Sc. in research, Mechanic Power Civil and Acoustics Engineering (MEGA). Project on the implementation of NURBS-based Isogeometric Analysis into *Abaqus* (<http://abqnurbs.insa-lyon.fr/>) under the supervision of Prof. T. Elguedj, LAMCOS, Lyon, France.

2011: M.Sc. in mechanical sciences, Institut National des Sciences Appliquées (INSA), Lyon, France.

Language skills

French: mother tongue

English: good

Teaching

Teaching assistant at EPFL in Solid Mechanics (2011-2013) and Aeroelasticity (2010-2012), and supervision of students under their semester projects.

Publications

Peer-reviewed journal articles

F. Maurin and A. Spadoni. Low-frequency wave propagation in post-buckled structures. *Wave Motion*, 51(2):323–334, 2014.

F. Maurin and A. Spadoni. Wave dispersion in periodic post-buckled structures. *Journal of Sound and Vibration*, 333(19):4562–4578, 2014.

F. Maurin, L. Dedè, and A. Spadoni. Isogeometric rotation-free analysis of planar extensible-elastica for static and dynamic applications. *Nonlinear Dynamics*, 2015.

F. Maurin. Bloch theorem with Revised Boundary Conditions applied to glide and screw symmetric, quasi-one-dimensional structures. *Wave Motion, In Press* (2015), doi:10.1016/j.wavemoti.2015.10.008 .

Conference Proceedings

F. Maurin and A. Spadoni. Wave Propagation in Lightly Post-Buckled Structures. In *Proceedings of the 8th European Nonlinear Dynamics Conference (ENOC)*, Wien, Austria, 2014.

F. Maurin and A. Spadoni. Bloch theorem with revised boundary conditions applied to glide plane and screw axis symmetric, quasi-one-dimensional structures. In *Proceedings of the 5th European Conference on Computational Mechanics (ECCM)*, Barcelona, Spain, 2014.

Conference presentations

Wave propagation in post-buckled structures with unusual dispersion. *The 4th Canadian Conference on Nonlinear Solid Mechanics (CanCNSM)*, Montréal, Canada, 2013.

Wave Propagation in Lightly Post-Buckled Structures. *8th European Nonlinear Dynamics Conference (ENOC)*, Wien, Austria, 2014.

Bloch theorem with revised boundary conditions applied to glide plane and screw axis symmetric, quasi-one-dimensional structures. *5th European Conference on Computational Mechanics (ECCM)*, Barcelona, Spain, 2014.

Geometrically-exact isogeometric formulation for two-dimensional, slender, Euler-Bernoulli beams: Static and dynamic considerations. *5th European Conference on Computational Mechanics (ECCM)*, Barcelona, Spain, 2014.

Wave Propagation in Post-Buckled Structures Buckled ribbon and trolleys. *International Union of Theoretical and Applied Mechanics (IUTAM) symposium: Complexity of Nonlinear Waves*, Tallin, Estonia, 2014.

Wave propagation in buckled-beams. *Advanced Problems in Mechanics (APM)*, St. Petersburg, Russia, 2015.

Invited talks

Etude des solitons dans les milieux périodiques flambés : équation de dispersion semi-analytique et généralisation du théorème de Bloch aux structures périodiques par réflexions glissées ou hélicoïdales. *Séminaire POEMS*, Paris, France, 2015.